Electro-Optic Material Design Criteria Derived from Condensed Matter Simulations Using the Level-of-Detail Coarse-Graining Approach

Andreas F. Tillack

A dissertation

submitted in partial fulfillment of the

requirements for the degree of

Doctor of Philosophy

University of Washington

2015

Reading Committee:

Bruce H. Robinson, Chair

Larry R. Dalton

Lutz G. Maibaum

Program Authorized to Offer Degree:

Department of Chemistry

University of Washington

Abstract

Electro-Optic Material Design Criteria
Derived from Condensed Matter Simulations Using
the Level-of-Detail Coarse-Graining Approach

Andreas F. Tillack

Chair of the Supervisory Committee:
Professor Bruce H. Robinson
Department of Chemistry

Electro-optic materials enable a wide variety of photonics applications such as micro-scale optical sensors, terahertz spectroscopy, photonic computing, quantum key distribution, and high speed data transmission for computing as well as global telecommunications. Organic 2^{nd}-order non-linear optical (ONLO) materials offer several key advantages for photonic devices such as intrinsically higher bandwidth on the order of THz, lower power consumption, and smaller device structures compared to currently used inorganic materials such as lithium niobate. ONLO materials consist of electro-optic chromophores arranged such that overall, acentric dipole order is present in the material. Crucial insight into the acentric ordering of an ensemble of electro-optic chromophores can be provided by computational modeling. Presented in this dissertation is a coarse-graining (CG) Monte Carlo approach, the Level-of-Detail (LoD) method, enabling the systematic determination of CG model parameters with no adjustable parameters from *ab initio* quantum mechanical calculations and fully-atomistic force fields. The LoD method's ability to correctly represent all-atom behavior is demonstrated on a diverse range of condensed molecular systems relevant to different aspects of the simulation of electro-optic materials such as the accurate simulation of π-π interactions, the incorporation of flexible molecular linkers, and the prediction of dielectric behavior. Details of molecular interactions that determine the extent of acentric order are investigated and the observations and conclusions derived in this thesis culminate in a set of design criteria for construction of future molecules by experimentalists.

TABLE OF CONTENTS

LIST OF ABBREVIATIONS

AA	All-Atom
APC	Amorphous polycarbonate
AVA	Adiabatic Volume Adjustment, method to accelerate equilibrium convergence
B3LYP	Becke, three-parameter, Lee-Yang-Parr hybrid DFT functional
CCSD	Coupled-Cluster electronic structure method (alternative to DFT) using Single and Double excitations
CG	Coarse-Graining / Coarse-Grained
cgs	Centimeter-Gram-Seconds system of units, Gaussian units
CHELPG	Charges from Electrostatics Potentials using a Grid-based method
DFT	Density Function Theory
EO	Electro-Optic
FA	Fully-Atomistic
FF	Force Field
GB	Gay-Berne, authors of a type of Lennard-Jones potential
HBFB	1:1 binary mixture of benzene and hexafluorobenzene
IA	Interaction Area, orientation-based method to scale LJ interaction energies
ITO	Indium Tin Oxide, used as a transparent conduction electrode material
LoD	Level-of-Detail, coarse-graining approach used in this work
LJ	Lennard-Jones
MC	Monte Carlo
MD	Molecular Dynamics
NPT	Isothermal-isobaric ensemble
NVT	Canonical ensemble
ONLO	Organic Non-Linear Optical
OPLS-AA	Optimized Potentials for Liquid Simulations All-atom
PCM	Polarizable Continuum Model
PMMA	Poly(methyl methacrylate)
SI	International System of units

SPC	Simple Point Charge water model
TCF	Tricyanofuran, a class of strong electron acceptors
TCP	Tricyanopyrroline, a class of strong electron acceptors
vdW	Van der Waals

Units:

Å	Angström (10^{-10} meters)
atm	atmospheres
cm	centimeters (10^{-2} meters)
cc, cm^3	cubic centimeters
D	Debye
erg	Unit of energy (10^{-7} J)
esu	electrostatic units of first-order hyperpolarizability (cm^5/statcoulomb)
Hz	Hertz, frequency unit (1 per second)
J	Joule, unit of energy
K	Kelvin, unit of temperature
mol	mole
µm	micrometer, micron (10^{-6} meters)
nm	nanometers (10^{-9} meters)
perg	pico-erg (10^{-12} erg = 10^{-19} J)
pm	picometers (10^{-12} meters)
V	Volt

Constants:

c	Speed of light in vacuum
ε_0	Vacuum permittivity
e	Electron charge
h, ħ	Planck's constant, reduced Planck constant
k_B	Boltzmann's constant
m	Electron mass

LIST OF FIGURES

LIST OF TABLES

ACKNOWLEDGEMENTS

I would like to express my sincere thanks for the support and advice received from many outstanding colleagues and friends.

Firstly, I want to thank my advisor Prof. Bruce H. Robinson whose exceptional intellect, ability to think outside the box, patience, and humor has guided this work and inspired me professionally as well as personally. I am deeply grateful to Prof. Larry R. Dalton for his wealth of knowledge, enthusiasm, and encouragement extended not only to me but to all his current and former students. I also thank Prof. Lutz G. Maibaum and Prof. František Tureček for serving on my supervisory committee and for valuable discussions and support along the way.

I thank Dr. Lewis E. v.d.L. Johnson for being an outstanding colleague and great friend. I enjoyed our many discussions and am grateful for his support and continued friendship as well as our current and future scientific collaborations. Thanks to Dr. Dmitry V. Liskin for being an amazing friend, for our many adventures, laughs, and philosophical musings, and also to his wife Dr. Kellie Holzer and daughter Mathilde for making me feel like a family member.

For their ongoing support and many helpful conversations as well as critical questions I thank Dr. Bruce E. Eichinger, Dr. Delwin Elder, Dr. Meghana Rawal, Nathan Sylvain, and Kerry E. Garrett. Furthermore, I would like to thank the many friends met throughout graduate school who made me feel welcome not only in the department but also as an immigrant to the United States of America. Particularly, I want to thank Lewis' parents, Lani and Larry Johnson, for making me feel part of their family, for their encouragement and support since I came here, for many memorable family events, such as my very first Thanksgiving dinner, as well as for countless invitations to fantastic classical music concerts.

I owe special thanks to my girlfriend Lorena Soel Sanchez for her love, commitment, and for making it all work for me. Most importantly, I thank my parents, Ursula and Frank Tillack, and my family for their love, encouragement, and support for as long as I can remember. Thank you!

DEDICATION

In loving memory of my grandparents, Eva-Maria and Wilhelm Bauer.

To my parents, Ursula and Frank Tillack.

1 INTRODUCTION

1.1 GENERAL INTRODUCTION

Since the inception of electronic computers and computer networks, communication demands have continuously increased both in terms of the amount of data as well as data transfer speeds. The amount of global internet data traffic per year is predicted to reach 1 Zettabyte per year (10^{21} bytes = 1 billion Terabytes) by the end of 2016 and approximately 2 Zettabyte per year by 2019.[1,2]

The backbone of the global internet is a dense network of undersea fiber optic cables spanning the globe. This system is a direct descendent of the undersea telegraph cable system of the 19th century.[3] Instead of human operators manually sending and decoding signals, electro-optic modulators are used today increasing bandwidths from a few bits per second to tens of gigabits per second per channel.

An important function of these optical transceivers is the encoding of electrical signals into optical ones. Typically, these transmitters are comprised of multiple Mach-Zehnder type modulators[4–8] which employ the linear electro-optic effect (Pockels effect[9,10]) to change the phase of an incoming light wave using an applied electric field in order to modulate the output light intensity.

Figure 1.1 schematically depicts the working principle of a Mach-Zehnder type modulator. Coherent laser light is split in two optical paths each containing an electro-optic material with electrodes of reversed polarity.

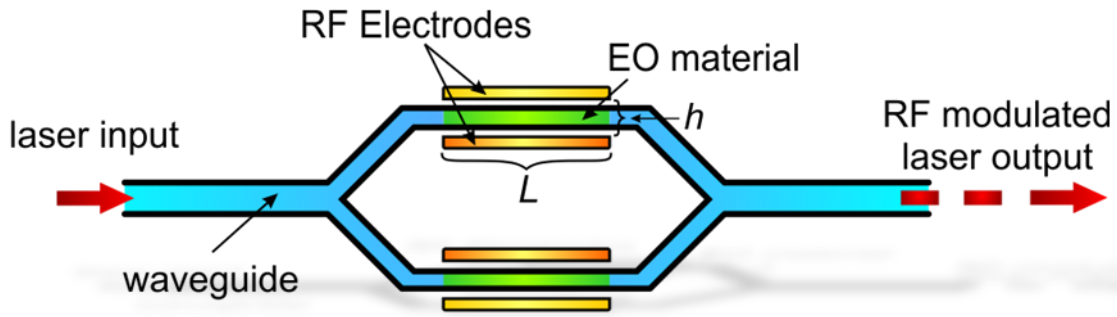

Figure 1.1: Schematic depiction of a Mach-Zehnder type modulator

After passing the electro-optic material, the light fields of both optical paths are combined again and interfere depending on their respective phase shifts due to the applied external field across the electrodes. This enables the output light amplitude to be modulated with the applied field. Application of an external electric field in the z-direction (perpendicular to the direction of light propagation, parallel to its electric field component) alters the refractive index of the electro-optic material by:

$$\Delta n = \frac{1}{2} n_z^3(\omega) r_{33} E \tag{1-1}$$

Here, $n_z(\omega)$ is the field-independent index of refraction at optical frequency ω in z-direction, r_{33} is the electro-optic activity for both the light and the external fields in the z-direction, and E_z is the applied external field magnitude. The electro-optic activity, r_{33}, can be obtained from the following relation:[11–14]

$$r_{33} = -\frac{2\chi^{(2)}_{zzz}(-\omega; 0, \omega)}{n_z(\omega)^4} = \frac{2g(\omega, \varepsilon)}{n_z(\omega)^4} \beta_{zzz}(-\omega; 0, \omega) \rho_N \langle \cos^3 \theta \rangle$$
$$\text{with } g(\omega, \varepsilon) = \frac{\varepsilon(n_0^2 + 2)}{2\varepsilon + n_0^2} \left(\frac{n_\omega^2 + 2}{3} \right)^2 \tag{1-2}$$

Where $\chi_{zzz}^{(2)}$ is the second-order susceptibility, n_z the field-independent index of refraction in z-direction, $g(\omega, \varepsilon)$ the local field factor, β_{zzz} the molecular first-order hyperpolarizability projected onto the dipole axis, ρ_N the number density, and $\langle \cos^3 \theta \rangle$ is the dipole order parameter with respect to the external field. While the molecular first-order hyperpolarizability, β_{zzz}, is a property intrinsic to an individual chromophore, the number density, ρ_N, as well as the average acentric order, $\langle \cos^3 \theta \rangle$, are bulk properties. Therefore, their product, $\rho_N \langle \cos^3 \theta \rangle$, the so called chromophore loading parameter, is an ensemble property that needs to be optimized in addition to the molecular first-order hyperpolarizability in order to maximize the figure of merit for electro-optic device performance, the electro-optic activity, r_{33}.

In a Mach-Zehnder modulator with electrode spacing h and interaction length L, the device drive voltage that causes a phase shift of π (180°) in one arm of the optical paths is inversely proportional to the electro-optic activity:

$$V_\pi = \frac{\lambda h}{n^3 r_{33} L} \tag{1-3}$$

Most current devices utilize crystalline, inorganic non-linear optical materials such as $LiNbO_3$ or silicon. While offering several advantages such as compatibility with integrated circuit technology and well established engineering knowledge of optical properties, these materials offer less room for systematic improvement due to their crystalline nature and possess limited bandwidths on the order of tens of GHz due to a relatively moderate electro-optic activity.[15,16] This dramatically limits their utility to devices with interaction lengths in the range of centimeters, negatively affecting necessary drive voltages, bandwidth, and energy consumption.

On the other hand, organic non-linear optical (ONLO) materials offer several key advantages such as intrinsically higher bandwidth on the order of THz and lower power consumption (lower

drive voltage due to large r_{33}) enabling much smaller device structures.[13,14,17–20] An organic chromophore similar to those discussed in this work, DLD164[21], has recently been employed in an all-plasmonic Mach-Zehnder modulator of 10 µm length demonstrating operation at 70 GHz with a low energy consumption of 25 fJ per bit.[19] A silicon-organic hybrid approach using the electro-optic chromophore DLD164[21] and the binary mixture of YLD124/PSLD41[13,14] (simulation results are discussed in chapter 5) yielded record values for in-device electro-optic activities of about 200 pm/V, directly contributing to operating frequencies of 100 GHz and a low energy consumption of 10 fJ per bit.[20] These results are orders of magnitudes improved compared to similar devices using an all-silicon approach and compared to devices incorporating lithium niobate.[22–24]

Figure 1.2 shows a high-performance organic electro-optic chromophore, YLD124,[14,25–33] consisting of an electron-donating group (substituted diethanolamine) conjugated to an electron-accepting group (tricyanofuran-trifluoromethyl-phenyl, TCF-CF_3-Phenyl[34,35]) via a conjugated bridge with high electron mobility.

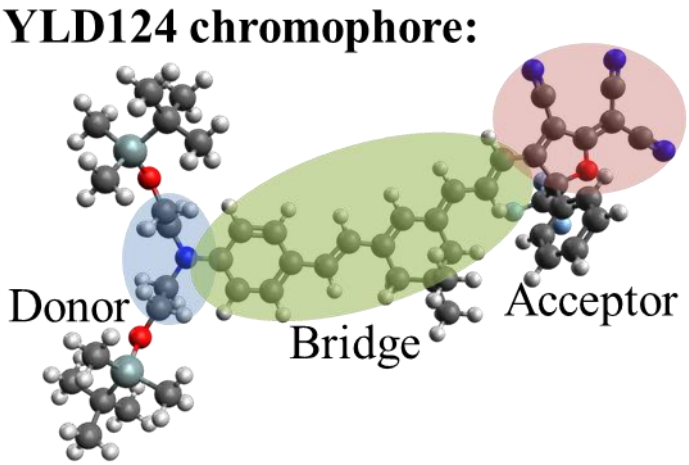

Figure 1.2: YLD124 chromophore as a representative of a typical organic donor-bridge-acceptor type electro-optic chromophore

This so called push-pull arrangement leads to strong charge separation within the molecule leading to both a strong ground-state dipole moment as well as an increased asymmetric polarization response. This asymmetric polarization response in turn causes the first-order hyperpolarizability. The measured value of the static first-order hyperpolarizability for YLD124 of $\beta_{zzz}(0) = (2200 \pm 1100) \cdot 10^{-30} esu$ is more than an order of magnitude larger compared to lithium niobate.[36]

An electro-optic material consists of many such chromophores arranged in a way that overall acentric order, $\langle \cos^3 \theta \rangle$, is present in the material. A variety of organic push-pull type chromophore systems exist that spontaneously form acentric crystals, however, overall electro-optic activity of these materials remains relatively moderate.[37–41] Conversely, depending on processing conditions, many high-performance electro-optic chromophore systems, like the YLD124 chromophore system shown above, spontaneously form centrosymmetrically ordered crystals or isotropic, randomly ordered film morphologies. In order for these materials to possess non-vanishing acentric order it needs to be induced externally. Acentric order is typically achieved by electric field poling, which involves applying a strong external DC field across the material to apply a torque to chromophores due to their high dipole moment. The material is heated near its glass transition temperature so chromophores are able to rearrange in response to the poling field.

Although the focus in the present work is on electric field poling, the ordering process may be further aided by suitable chemical and physical driving potentials such as ionic and hydrogen-bonding interactions, as well as strong light fields selectively melting unordered regions of the material (laser-assisted poling).[42,43]

Developing suitable ONLO materials can be extremely time-consuming. Synthesis of a trial compound can take many months to years without the guarantee that resulting chromophore properties are favorable. It is therefore necessary to have an optimized chromophore selection process before synthesis is started. Theoretical modeling can guide this process in a variety of ways. For example, quantum mechanical modeling such as density functional theory (DFT) can predict molecular geometries, charge distributions, chromophore dipole moments, and first-order hyperpolarizabilities β.[44–46] Statistical mechanical calculations can then be used to predict macroscopic properties under poling conditions such as the dielectric constant and the EO activity which are proportional to the average, non-centrosymmetric order parameters $\langle\cos\theta\rangle$ and $\langle\cos^3\theta\rangle$, respectively.[27,46–48]

1.2 Sum Rules and Figures of Merit

In order to characterize and improve existing electro-optic chromophore designs it is crucial to have estimates of upper bounds on key figures of merit such as the molecular first-order hyperpolarizability and the electro-optic activity. Based on generalized Thomas-Reiche-Kuhn sum rules, Prof. Mark G. Kuzyk has previously developed an estimate of the maximum, off-resonant molecular first-order hyperpolarizability, β_{max}, that depends on the number of π electrons[1], N, and the wavelength of lowest energy optical transition, λ_{10}:[49]

$$\beta_{max} = \sqrt[4]{3}\left(\frac{e\hbar}{\sqrt{m}}\right)^3 N^{3/2}\frac{\lambda_{10}^{7/2}}{(hc)^{7/2}} = \mathbf{1.789\cdot 10^{-8}\cdot N^{3/2}(\lambda_{10}/nm)^{7/2}\cdot 10^{-30} esu} \quad (1\text{-}4)$$

[1] The chromophore is treated as a harmonic oscillator and the electrons participating in the electro-optic response are assumed to be freely moving along the length of the chromophore.

In conjunction with an experimental value for the first-order hyperpolarizability in the static, long-wavelength limit, $\beta_{zzz}(0)$, this upper limit can be used to define an intrinsic chromophore first-order hyperpolarizability $\beta_{int} = \beta_{zzz}(0)/\beta_{max}$. This intrinsic value can be used as a figure of merit for comparing different nonlinear optical materials with respect to their potential maximum.

His work also provides an estimate of the corresponding size of the quantum system depending on the same parameters as β_{max}:

$$\Delta x = \sqrt{\frac{\hbar^2}{2mhc}}\sqrt{N\lambda_{10}/nm} = \mathbf{5.543\ pm} \cdot \sqrt{\boldsymbol{N\lambda_{10}/nm}} \tag{1-5}$$

For example, for the YLD124 chromophore presented in figure 1.2 the number of delocalized electrons participating in the electro-optic response is taken to be $N = 21$, the experimental lowest energy optical transition occurs at $\lambda_{10} = 786\ nm$, and its measured first-order hyperpolarizability is $\beta_{zzz}(0) = (2200 \pm 1100) \cdot 10^{-30} esu$, yielding the following estimates:

$$\boldsymbol{\Delta x = 7.12\ \text{Å}\ ;\ \beta_{max} = 23{,}400 \cdot 10^{-30} esu\ \Rightarrow \beta_{int} = 9.4\ \pm 4.7\%} \tag{1-6}$$

Table 1.1 compiles these values for the chromophore systems discussed in this work which have published values for the first-order hyperpolarizability.

Table 1.1: Key figures of merit for select individual electro-optic chromophores: β_{max} and β_{int}

Chromophore	$\beta_{zzz}(0)^*$	λ_{10} [nm]	N	Δx	$\beta_{max}{}^*$	β_{int}
YLD124[33]	2200 ± 1100	786	21	7.12	**23,438**	**(9 ± 5) %**
JRD1[33]		780		7.09	**22,818**	**(10 ± 5) %**
CLD-C1[50,51]		750		6.96	**19,891**	**(11 ± 6) %**
C1[50,51]	1100 ± 550	753	23	7.29	**23,120**	**(5 ± 3) %**
DAST[38]	175	471	17	4.85	**2,844**	**6.2 %**

*in units of $10^{-30}\ esu$

The figure of merit defining electro-optic device performance, however, is the electro-optic activity, r_{33}, as defined in equation (1-2). From a device perspective, one wants an extension of Kuzyk's method to provide an upper limit for bulk electro-optic material performance, r_{max}, as opposed to an upper limit for isolated chromophores.

The maximum electro-optic activity, r_{max}, consistent with Kuzyk's limit can be attained from equation (1-2) using the maximum, off-resonant molecular first-order hyperpolarizability, β_{max}, in conjunction with perfect acentric order ($\langle cos^3\,\theta\rangle = 1$):

$$r_{33} = \frac{2g(\omega,\varepsilon)}{n_\omega^4}\beta_{max}\rho_N^{max} \tag{1-7}$$

Note that for the systems discussed in this work the local field factor typically is $\frac{2g(\omega,\varepsilon)}{n_\omega^4} \approx 1$ and is therefore omitted for simplicity from now on. For neat chromophore material the number density, ρ_N^{max}, consistent with Kuzyk's work, can be expressed using the corresponding size of the quantum system from equation (1-5):

$$\rho_N^{max} = \frac{1}{V_{chromophore}} = \frac{1}{\Delta x^3} \tag{1-8}$$

This result is an upper limit to the chromophore number density because it only takes into account the chromophore volume participating in the electro-optic response and it assumes an ideal chromophore packing fraction of 1. The value calculated for YLD124 is $\rho_N^{max}(YLD124) = 27.7 \cdot 10^{20}\ molecules/cc$ which is about five times larger than the experimentally observed number density of $5.4 \cdot 10^{20}\ molecules/cc$.[33]

Combining equations (1-4), (1-5), (1-6), and (1-8) yields an expression for the upper limit of the bulk electro-optic activity:[2]

$$r_{max} = \frac{1}{\varepsilon_0}\frac{\sqrt[4]{3}e^3 2^{3/2}}{(hc)^2}\lambda_{10}^2 = \mathbf{43.818 \cdot 10^{-3} \cdot (\lambda_{10}/nm)^2}\ \frac{\boldsymbol{pm}}{\boldsymbol{V}} \tag{1-9}$$

Interestingly, both the dependence on the number of electrons as well as their mass cancels out, leaving only a dependence on the wavelength of the lowest energy optical transition. In analogy to Kuzyk's intrinsic first-order hyperpolarizability, β_{int}, the upper limit of the electro-optic activity can be used to define an intrinsic electro-optic activity $r_{int} = r_{33}/r_{max}$ using the experimentally measured electro-optic activity, r_{33}. Therefore, r_{int} is a function of quantities that can be measured experimentally, r_{33} and λ_{10}, without the need for additional assumptions about the number of electrons participating in the electro-optic response.

However, electro-optic activity depends on the amount of acentric order. For organic electro-optic materials aligned in an external electric field acentric order is a function of the applied poling field magnitude. In other words, in order to compare electro-optic activities between different experiments to evaluate chromophore performance, even when identical chromophores are used, acentric order needs to be accounted for. Therefore, a slightly modified, effective intrinsic electro-optic activity, r_{eff}, can be defined:

$$r_{eff} = \frac{r_{33}}{r_{max}\langle cos^3\,\theta\rangle} \tag{1-10}$$

Note that in this definition knowledge of the average, bulk acentric order, $\langle cos^3\,\theta\rangle$, is needed which is not easily measured experimentally but can be obtained from statistical mechanics simulations such as those presented in this dissertation.

[2] In order to obtain SI-units an additional $1/\varepsilon_0$ has to be factored in.

Table 1.2 provides a compilation of these bulk figures of merit (r_{max}, r_{int}, and r_{eff}) for the chromophore systems discussed in this work, complimentary to the compilation individual electro-optic chromophore figures of merit found in table 1.1.

Table 1.2: Key figures of merit for select bulk electro-optic materials: r_{max}, r_{int}, and r_{eff}

Chromophore	λ_{10} [a]	r_{33} [b]	r_{max} [b]	r_{int}	$\langle \cos^3 \theta \rangle$	r_{eff}
YLD124[33]	786	200 ± 20	27,071	**(7.4 ± 0.7) ‰**	0.15 ± 0.06	**(5 ± 2) %**
JRD1[33]	780	360 ± 20	26,659	**(13.5 ± 0.8) ‰**	0.22 ± 0.03	**(6 ± 1) %**
CLD-C1[50,51]	750	210 ± 30	24,648	**(8.5 ± 1.2) ‰**	0.15 ± 0.04	**(6 ± 2) %**
C1[50,51]	753	140 ± 35	24,845	**(5.6 ± 1.4) ‰**	0.17 ± 0.04	**(3 ± 1) %**
DAST[38]	471	53 ± 6	9,679	**(5.5 ± 0.7) ‰**	0.83	**(0.7 ± 0.1) %**

[a]in units of nm; [b]in units of $\left[\frac{pm}{V}\right]$

The intrinsic first-order hyperpolarizability, β_{int}, is about 10% for all chromophores utilizing a chromophore core similar to YLD124 (YLD124, JRD1, and CLD-C1) and about 5-6% for both C1 and DAST which is surprising given that they are very different chromophores. The intrinsic electro-optic activity, r_{int}, differs between molecules using the YLD124 chromophore core, with values ranging from about 7-14 ‰ (per thousand). However, similarly to the β_{int} values observed, both C1 and DAST are around the same value, $r_{int} = 6$ ‰, identical within error. One could thus conclude that C1 and DAST should perform similarly. However, clearly this is not the case as C1 has about threefold improved electro-optic activity compared to DAST. The effective intrinsic electro-optic activity, r_{eff}, corrects this behavior. All molecules employing the YLD124 chromophore core show the same value within error of $r_{eff} = (6 \pm 2)$ %, the C1 chromophore as expected from its electro-optic activity and first-order hyperpolarizability yields half, $r_{eff} = (3 \pm 1)$ %. Furthermore, DAST has an about fourfold lower r_{eff} value compared to C1 which may be indicative of an overall low optimization potential for DAST in the bulk material.

Particularly for the YLD124 chromophore core, these results indicate that there is substantial room for improvement in both chromophore design and poling techniques in order to obtain transformatively large electro-optic constants.

1.3 SIMULATION APPROACH

One goal of this work is the *ab-initio* simulation of the chromophore loading parameter, $\rho_N\langle\cos^3\theta\rangle$, for strongly dipolar, condensed high-performing electro-optic chromophore systems. Each individual electro-optic chromophore typically consists of hundreds of atoms (Figure 1.3 shows a poled YLD124 chromophore system) and while small-scale all-atom simulations may be feasible with an abundance of compute time, coarse-graining approaches are needed in order to progress simulations far enough for converged acentric order results, especially given that experimental poling times are measured in tens of seconds.

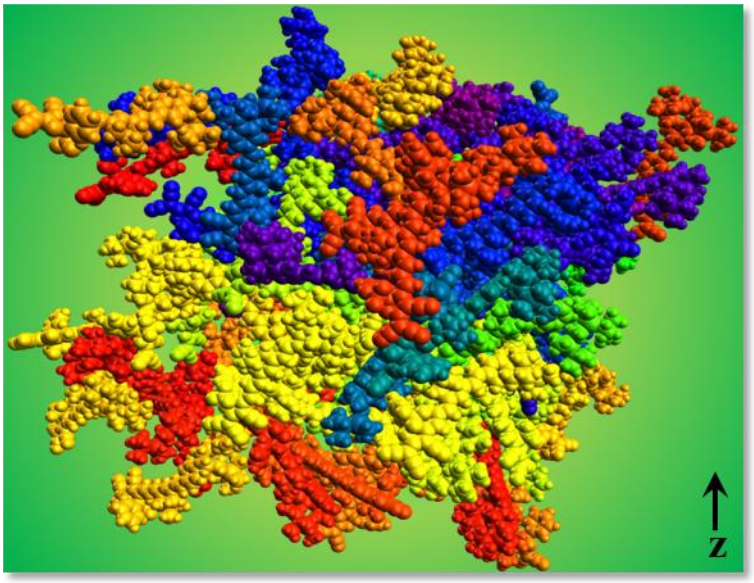

Figure 1.3: Poled YLD124 chromophore system (108 molecules, each consisting of 125 atoms). Lennard-Jones radii were scaled by 50% and each chromophore was assigned a unique color.

On currently available computer workstations, molecular dynamics (MD) simulations typically only allow tens of nanoseconds to be investigated due to the computational expense of solving equations of motion at a reasonable time step. This makes them ideal for the simulation of dynamic processes on these fast time scales. On the other hand, approaches such as Metropolis Monte-Carlo (MC) simulations using a similar number of calculations compared to MD simulations are typically able to cover more configurational phase space at the expense of physical molecule movement. However, system properties averaged over system configurations (MC) are equivalent to those averaged over time (MD) when system energies are at equilibrium (ergodic principle). Therefore, MC simulations are better suited for the simulation of poling induced acentric order.

Ab-initio quantum-mechanical modeling is used to inform all-atom force-fields following an established procedure by Dr. Lewis E. Johnson and Dr. Bruce E. Eichinger.[44,46,52] In general, structure calculations are performed with the hybrid functional B3LYP using the 6-31G(d) basis set in Gaussian 09.[53] The electrostatic potential around the resulting optimized molecule is then used to fit charges at the center of each atom, using so called CHELPG[54] charges. In conjunction with parameters for Lennard-Jones radii and energies of individual atoms – we typically use parameters derived from OPLS-AA[55], but others such as the Merck force field[56] or AMOEBA[57] could be used as well – this approach yields the underlying fully-atomistic model. Its coarse-grained representation consisting of connected ellipsoids is calculated using the so called Level-of-Detail (LoD) method described in chapter 2.

The Monte-Carlo software used throughout this dissertation is written in C++ and developed in-house by myself,[48] based on a previous version[46,58] by Dr. Lewis E. Johnson and Robin Barnes which itself was ported from MATLAB code employed previously. [44,59,60]

It features classical force fields such as pair-wise point charge as well as point dipole interactions, Lennard-Jones interactions with ellipsoid anisotropy handled through an algorithm developed by Perram and Wertheim[61], external electric field interactions, and an Onsager-type self-consistent reaction field.[62] These classic interaction potentials used have been described in detail previously.[44,46,48,58–60]

A major development effort was to extend the previously used MC code in order to gain the ability to simulate complex chromophore systems by supporting connected ellipsoids to form coarse-grained representations of molecules. Bonds connecting ellipsoids are positioned corresponding to the underlying all-atom force field bond locations[3]. Bonded movement constraints can be set up in a coarse-grained way using fixed bond distances, with free bond rotations and/or free bond bending. Additionally, classical bond potentials (stretch, bend, dihedral) can also be assigned. Furthermore, the entire workflow from simulation setup to data analysis is fully scriptable and uses human-readable text files parsed by the software. Further extensions beyond the classical MC method and their application to the simulation of condensed electro-optic materials are described in the following chapters of this dissertation.

[3] For example, if atom A and B are bonded in the all-atom model and atom A now belongs to ellipsoid 1 while atom B is placed in ellipsoid 2 then ellipsoids 1 and 2 are connected with a bond originating at atom A's center location inside ellipsoid 1 and terminating at atom B's center location inside ellipsoid 2.

1.4 DISSERTATION OUTLINE

Chapter 2 describes the development of our coarse-grained force field called the Level-of-Detail (LoD) method. The LoD method enables systematic coarse-graining from an all-atom force-field utilizing ellipsoidal shapes rather than spheres as the fundamental building blocks to represent molecular subunits. Coarse-grained shapes and potential energy parameters are calculated using a systematic rule set with no adjustable parameters. In conjunction with traditional combination rules this allows for a practically unlimited variety of shapes and sizes. Furthermore, example calculations of the binary 1:1 mixture of benzene and hexafluorobenzene and of a polyethylene hydrocarbon chain with 32 repeat units demonstrate the LoD method's ability to accurately represent the underlying all-atom force field behavior.

In chapter 3, a novel method called adiabatic volume adjustment (AVA)[48] is introduced which allows a system to reach equilibrium order after fewer calculations compared to traditional canonical ensemble (NVT) or isothermal, isobaric ensemble (NPT) Monte-Carlo simulations. The AVA method adjusts the simulation volume in a controllable manner while concurrently adjusting the attractive contribution of the Lennard-Jones potential thus improving simulation configuration space sampling and overcoming local energetic barriers. Simulation results are used to verify these claims and a first set of electro-optic chromophore design criteria is derived from simulation results.

Chapter 4 describes the determination of dielectric constants from simulation results which is then applied to a wide variety of molecules. An enhanced reaction field description consistent with the Onsager reaction field is introduced for systems using point charges and point dipoles, as well as for systems with ionic contributions. Simulation results of the organic solvents

acetonitrile, ethylene carbonate, and the first room-temperature ionic liquid, ethyl ammonium nitrate are presented and compared to experimental results. The chapter culminates in simulation results of the chromophore systems YLD124 and JRD1.[14,25–33]

Chapter 5 represents the bulk of the simulation work performed on electro-optic chromophore systems using the tricyanofuran (TCF) acceptor. [63,64] Simulation results on C1 and CLD-C1,[50,51,65] YLD124 and JRD1,[14,25–33] as well as the binary chromophore system PSLD41/YLD124[13,26,28,42,44,66] are presented. All simulated results are within error of the experimental results.

Chapter 6 presents simulation results performed on existing[67,68] small chromophores containing the tricyanopyrroline (TCP) acceptor. An exciting result is the observed chromophore loading is about 50% larger than for the much larger TCF-based chromophores presented in chapter 5.

Chapter 7 serves as a collection of the design criteria discovered throughout this work. Furthermore, the theoretical framework presented in this work is used to develop an additional design criterion from simulations using simplified chromophore LoD representations incorporating up to five ellipsoids.

1.5 REFERENCES FOR CHAPTER 1

[1] Cisco Visual Networking Index: Global Mobile Data Traffic Forecast Update 2014–2019 White Paper http://cisco.com/c/en/us/solutions/collateral/service-provider/visual-networking-index-vni/white_paper_c11-520862.html (accessed Jul 15, 2015).

[2] The Zettabyte Era—Trends and Analysis http://cisco.com/c/en/us/solutions/collateral/service-provider/visual-networking-index-vni/VNI_Hyperconnectivity_WP.html (accessed Jul 15, 2015).

[3] Carter, L.; United Nations Environment Programme; World Conservation Monitoring Centre. *Submarine Cables and the Oceans: Connecting the World.*; UNEP World Conservation Monitoring System ; International Cable Protection Committee: Cambridge; Lymington, 2009.

[4] Alferness, R. C. Guided-Wave Devices for Optical Communication. *IEEE J. Quantum Electron.* **1981**, *17*, 946–959.

[5] Becker, R. A. Multigigahertz Lumped-Element Electrooptic Modulators. *IEEE J. Quantum Electron.* **1985**, *21* (8), 1144–1146.

[6] Jackel, J. L. Mach-Zehnder Integrated Optical Modulator. US4709978 A, December 1, 1987.

[7] Takagi, K. Mach-Zehnder Modulator. US6198854 B1, March 6, 2001.

[8] Wang, Z.; Huang, Y.-K.; Ip, E.; Prucnal, P. R.; Wang, T. Performance Investigation of Polarization-Multiplexed 16-QAM Using All-Optical OFDM Transmission and Digital Coherent Detection. In; OSA, 2011; p OMS5.

[9] Voigt, W. Ueber Das Elektrische Analogon Des Zeemaneffectes. *Ann. Phys.* **1901**, *309* (1), 197–208.

[10] Pockels, F. *Lehrbuch Der Kristalloptik*; Teubner: Leipzig und Berlin, 1906.

[11] Singer, K. D.; Kuzyk, M. G.; Sohn, J. E. Second-Order Nonlinear-Optical Processes in Orientationally Ordered Materials: Relationship between Molecular and Macroscopic Properties. *J. Opt. Soc. Am. B* **1987**, *4* (6), 968–976.

[12] Dalton, L. R.; Steier, W. H.; Robinson, B. H.; Zhang, C.; Ren, A.; Garner, S.; Chen, A.; Londergan, T.; Irwin, L.; Carlson, B.; Fifield, L.; Phelan, G.; Kincaid, C.; Amend, J.; Jen, A. From Molecules to Opto-Chips: Organic Electro-Optic Materials. *J. Mater. Chem.* **1999**, *9* (9), 1905–1920.

[13] Sullivan, P. A.; Rommel, H.; Liao, Y.; Olbricht, B. C.; Akelaitis, A. J. P.; Firestone, K. A.; Kang, J.-W.; Luo, J.; Davies, J. A.; Choi, D. H.; Eichinger, B. E.; Reid, P. J.; Chen, A.; Jen, A. K.-Y.; Robinson, B. H.; Dalton, L. R. Theory-Guided Design and Synthesis of

Multichromophore Dendrimers: An Analysis of the Electro-Optic Effect. *J. Am. Chem. Soc.* **2007**, *129* (24), 7523–7530.

[14] Sullivan, P. A.; Dalton, L. R. Theory-Inspired Development of Organic Electro-Optic Materials. *Acc. Chem. Res.* **2010**, *43* (1), 10–18.

[15] Wooten, E. L.; Kissa, K. M.; Yi-Yan, A.; Murphy, E. J.; Lafaw, D. A.; Hallemeier, P. F.; Maack, D.; Attanasio, D. V.; Fritz, D. J.; McBrien, G. J. A Review of Lithium Niobate Modulators for Fiber-Optic Communications Systems. *Sel. Top. Quantum Electron. IEEE J. Of* **2000**, *6* (1), 69–82.

[16] Jundt, D. H. Temperature-Dependent Sellmeier Equation for the Index of Refraction, n_e, in Congruent Lithium Niobate. *Opt. Lett.* **1997**, *22* (20), 1553–1555.

[17] Freude, W.; Leuthold, J.; Alloatti, L.; Vallaitis, T.; Korn, D.; Palmer, R.; Koos, C.; Brosi, J.; Dumon, P.; Baets, R. 100 Gbit/s Electro-Optic Modulator and 56 Gbit/s Wavelength Converter for DQPSK Data in Silicon-Organic Hybrid (SOH) Technology. In *Photonics Society Summer Topical Meeting Series, 2010 IEEE*; 2010; pp 96–97.

[18] Palmer, R.; Koeber, S.; Elder, D. L.; Woessner, M.; Heni, W.; Korn, D.; Lauermann, M.; Bogaerts, W.; Dalton, L.; Freude, W.; Leuthold, J.; Koos, C. High-Speed, Low Drive-Voltage Silicon-Organic Hybrid Modulator Based on a Binary-Chromophore Electro-Optic Material. *J. Light. Technol.* **2014**, *32* (16), 2726–2734.

[19] Haffner, C.; Heni, W.; Fedoryshyn, Y.; Niegemann, J.; Melikyan, A.; Elder, D. L.; Baeuerle, B.; Salamin, Y.; Josten, A.; Koch, U.; Hoessbacher, C.; Ducry, F.; Juchli, L.; Emboras, A.; Hillerkuss, D.; Kohl, M.; Dalton, L. R.; Hafner, C.; Leuthold, J. All-Plasmonic Mach–Zehnder Modulator Enabling Optical High-Speed Communication at the Microscale. *Nat. Photonics* **2015**, *9* (8), 525–528.

[20] Koos, C.; Leuthold, J.; Freude, W.; Kohl, M.; Dalton, L.; Bogaerts, W.; Giesecke, A. L.; Lauermann, M.; Melikyan, A.; Koeber, S.; Wolf, S.; Weimann, C.; Muehlbrandt, S.; Koehnle, K.; Pfeifle, J.; Palmer, R.; Alloatti, L.; Elder, D.; Wahlbrink, T.; Bolten, J. Silicon-Organic Hybrid (SOH) and Plasmonic-Organic Hybrid (POH) Integration. In; OSA, 2015; p Tu2A.1.

[21] Elder, D. L.; Benight, S. J.; Song, J.; Robinson, B. H.; Dalton, L. R. Matrix-Assisted Poling of Monolithic Bridge-Disubstituted Organic NLO Chromophores. *Chem. Mater.* **2014**, *26* (2), 872–874.

[22] Liu, A.; Jones, R.; Liao, L.; Samara-Rubio, D.; Rubin, D.; Cohen, O.; Nicolaescu, R.; Paniccia, M. A High-Speed Silicon Optical Modulator Based on a Metal–oxide–semiconductor Capacitor. *Nature* **2004**, *427* (6975), 615–618.

[23] Yi, H.; Long, Q.; Tan, W.; Li, L.; Wang, X.; Zhou, Z. Demonstration of Low Power Penalty of Silicon Mach–Zehnder Modulator in Long-Haul Transmission. *Opt. Express* **2012**, *20* (25), 27562.

[24] Cao, L.; Aboketaf, A.; Wang, Z.; Preble, S. Hybrid Amorphous Silicon (a-Si:H)–LiNbO3 Electro-Optic Modulator. *Opt. Commun.* **2014**, *330*, 40–44.

[25] Baehr-Jones, T.; Hochberg, M.; Wang, G.; Lawson, R.; Liao, Y.; Sullivan, P. A.; Dalton, L.; Jen, A.-Y.; Scherer, A. Optical Modulation and Detection in Slotted Silicon Waveguides. *Opt. Express* **2005**, *13* (14), 5216–5226.

[26] Pereverzev, Y. V.; Gunnerson, K. N.; Prezhdo, O. V.; Sullivan, P. A.; Liao, Y.; Olbricht, B. C.; Akelaitis, A. J. P.; Jen, A. K.-Y.; Dalton, L. R. Guest−Host Cooperativity in Organic Materials Greatly Enhances the Nonlinear Optical Response. *J. Phys. Chem. C* **2008**, *112* (11), 4355–4363.

[27] Benight, S. J.; Bale, D. H.; Olbricht, B. C.; Dalton, L. R. Organic Electro-Optics: Understanding Material Structure/function Relationships and Device Fabrication Issues. *J. Mater. Chem.* **2009**, *19* (40), 7466.

[28] Dalton, L. R.; Sullivan, P. A.; Bale, D. H. Electric Field Poled Organic Electro-Optic Materials: State of the Art and Future Prospects. *Chem. Rev.* **2010**, *110* (1), 25–55.

[29] Dalton, L. R.; Benight, S. J.; Johnson, L. E.; Knorr, D. B.; Kosilkin, I.; Eichinger, B. E.; Robinson, B. H.; Jen, A. K.-Y.; Overney, R. M. Systematic Nanoengineering of Soft Matter Organic Electro-Optic Materials. *Chem. Mater.* **2011**, *23* (3), 430–445.

[30] Kim, S.-K.; Pei, Q.; Fetterman, H. R.; Olbright, B. C.; Dalton, L. R. Photoassisted Corona Poled YLD-124/DR1-Co-PMMA Electrooptic Device Using Photoisomerization. *IEEE Photonics Technol. Lett.* **2011**, *23* (13), 845–847.

[31] Dalton, L.; Benight, S. Theory-Guided Design of Organic Electro-Optic Materials and Devices. *Polymers* **2011**, *3* (4), 1325–1351.

[32] Benight, S. J.; Robinson, B. H.; Dalton, L. R.; Meghea, A. Nano-Engineering of Molecular Interactions in Organic Electro-Optic Materials. *Mol. Interact.* **2012**.

[33] Jin, W.; Johnston, P. V.; Elder, D. L.; Tillack, A. F.; Olbricht, B. C.; Song, J.; Reid, P. J.; Xu, R.; Robinson, B. H.; Dalton, L. R. Benzocyclobutene Barrier Layer for Suppressing Conductance in Nonlinear Optical Devices during Electric Field Poling. *Appl. Phys. Lett.* **2014**, *104* (24), 243304.

[34] Liao, Y.; Eichinger, B. E.; Firestone, K. A.; Haller, M.; Luo, J.; Kaminsky, W.; Benedict, J. B.; Reid, P. J.; Jen, A. K.-Y.; Dalton, L. R.; Robinson, B. H. Systematic Study of the Structure−Property Relationship of a Series of Ferrocenyl Nonlinear Optical Chromophores. *J. Am. Chem. Soc.* **2005**, *127* (8), 2758–2766.

[35] Hammond, S. R.; Clot, O.; Firestone, K. A.; Bale, D. H.; Lao, D.; Haller, M.; Phelan, G. D.; Carlson, B.; Jen, A. K.-Y.; Reid, P. J.; Dalton, L. R. Site-Isolated Electro-Optic Chromophores Based on Substituted 2,2′-Bis(3,4-Propylenedioxythiophene) π-Conjugated Bridges. *Chem. Mater.* **2008**, *20* (10), 3425–3434.

[36] Bale, D. H. Nonlinear Optical Materials Characterization Studies Employing Photostability, Hyper-Rayleigh Scattering, and Electric Field Induced Second Harmonic Generation Techniques, University of Washington, 2008.

[37] Pan, F.; Wong, M. S.; Bosshard, C.; Günter, P. Crystal Growth and Characterization of the Organic Salt 4-N, N-Dimethylamino-4′-N-Methyl-Stilbazolium Tosylate (dast). *Adv. Mater.* **1996**, *8* (7), 592–595.

[38] Jazbinsek, M.; Mutter, L.; Gunter, P. Photonic Applications With the Organic Nonlinear Optical Crystal DAST. *IEEE J. Sel. Top. Quantum Electron.* **2008**, *14* (5), 1298–1311.

[39] Kwon, O.-P.; Kwon, S.-J.; Jazbinsek, M.; Brunner, F. D. J.; Seo, J.-I.; Hunziker, C.; Schneider, A.; Yun, H.; Lee, Y.-S.; Günter, P. Organic Phenolic Configurationally Locked Polyene Single Crystals for Electro-Optic and Terahertz Wave Applications. *Adv. Funct. Mater.* **2008**, *18* (20), 3242–3250.

[40] Chemla, D. S. *Nonlinear Optical Properties of Organic Molecules and Crystals*; Elsevier, 2012.

[41] Lee, S.-H.; Kang, B.-J.; Kim, J.-S.; Yoo, B.-W.; Jeong, J.-H.; Lee, K.-H.; Jazbinsek, M.; Kim, J. W.; Yun, H.; Kim, J.; Lee, Y. S.; Rotermund, F.; Kwon, O.-P. New Acentric Core Structure for Organic Electrooptic Crystals Optimal for Efficient Optical-to-THz Conversion. *Adv. Opt. Mater.* **2015**, *3* (6), 756–762.

[42] Olbricht, B. C.; Sullivan, P. A.; Wen, G.-A.; Mistry, A. A.; Davies, J. A.; Ewy, T. R.; Eichinger, B. E.; Robinson, B. H.; Reid, P. J.; Dalton, L. R. Laser-Assisted Poling of Binary Chromophore Materials. *J. Phys. Chem. C* **2008**, *112* (21), 7983–7988.

[43] Dalton, L. R.; Günter, P.; Jazbinsek, M.; Kwon, O.-P.; Sullivan, P. A. *Organic Electro-Optics and Photonics: Molecules, Polymers and Crystals*; Cambridge University Press, 2015.

[44] Sullivan, P. A.; Rommel, H. L.; Takimoto, Y.; Hammond, S. R.; Bale, D. H.; Olbricht, B. C.; Liao, Y.; Rehr, J.; Eichinger, B. E.; Jen, A. K.-Y.; Reid, P. J.; Dalton, L. R.; Robinson, B. H. Modeling the Optical Behavior of Complex Organic Media: From Molecules to Materials. *J. Phys. Chem. B* **2009**, *113* (47), 15581–15588.

[45] Bale, D. H.; Eichinger, B. E.; Liang, W.; Li, X.; Dalton, L. R.; Robinson, B. H.; Reid, P. J. Dielectric Dependence of the First Molecular Hyperpolarizability for Electro-Optic Chromophores. *J. Phys. Chem. B* **2011**, *115* (13), 3505–3513.

[46] Johnson, L. E. Multi-Scale Modeling of Organic Electro-Optic Materials, University of Washington, 2012.

[47] Kim, W.-K.; Hayden, L. M. Fully Atomistic Modeling of an Electric Field Poled Guest-Host Nonlinear Optical Polymer. *J. Chem. Phys.* **1999**, *111* (11), 5212–5222.

[48] Tillack, A. F.; Johnson, L. E.; Rawal, M.; Dalton, L. R.; Robinson, B. H. Modeling Chromophore Order: A Guide For Improving EO Performance. In *Symposium II/JJ/KK* –

Materials, Processes and Devices for Nanophotonics, Nonlinear Optics and Resonant Optics; MRS Online Proceedings Library; 2014; Vol. 1698.

[49] Kuzyk, M. G.; Pérez-Moreno, J.; Shafei, S. Sum Rules and Scaling in Nonlinear Optics. *Phys. Rep.* **2013**, *529* (4), 297–398.

[50] Benight, S. J.; Johnson, L. E.; Barnes, R.; Olbricht, B. C.; Bale, D. H.; Reid, P. J.; Eichinger, B. E.; Dalton, L. R.; Sullivan, P. A.; Robinson, B. H. Reduced Dimensionality in Organic Electro-Optic Materials: Theory and Defined Order. *J. Phys. Chem. B* **2010**, *114* (37), 11949–11956.

[51] Benight, S. Nanoengineering of Soft Matter Interactions in Organic Electro-Optic Materials, University of Washington, 2011.

[52] Bale, D. H.; Eichinger, B. E.; Liang, W.; Li, X.; Dalton, L. R.; Robinson, B. H.; Reid, P. J. Dielectric Dependence of the First Molecular Hyperpolarizability for Electro-Optic Chromophores. *J. Phys. Chem. B* **2011**, *115* (13), 3505–3513.

[53] Frisch, M. J.; Trucks, G. W.; Schlegel, H. B.; Scuseria, G. E.; Robb, M. A.; Cheeseman, J. R.; Scalmani, G.; Barone, V.; Mennucci, B.; Petersson, G. A.; Nakatsuji, H.; Caricato, M.; Li, X.; Hratchian, H. P.; Izmaylov, A. F.; Bloino, J.; Zheng, G.; Sonnenberg, J. L.; Hada, M.; Ehara, M.; Toyota, K.; Fukuda, R.; Hasegawa, J.; Ishida, M.; Nakajima, T.; Honda, Y.; Kitao, O.; Nakai, H.; Vreven, T.; Montgomery Jr., J. A.; Peralta, J. E.; Ogliaro, F.; Bearpark, M. J.; Heyd, J.; Brothers, E. N.; Kudin, K. N.; Staroverov, V. N.; Kobayashi, R.; Normand, J.; Raghavachari, K.; Rendell, A. P.; Burant, J. C.; Iyengar, S. S.; Tomasi, J.; Cossi, M.; Rega, N.; Millam, N. J.; Klene, M.; Knox, J. E.; Cross, J. B.; Bakken, V.; Adamo, C.; Jaramillo, J.; Gomperts, R.; Stratmann, R. E.; Yazyev, O.; Austin, A. J.; Cammi, R.; Pomelli, C.; Ochterski, J. W.; Martin, R. L.; Morokuma, K.; Zakrzewski, V. G.; Voth, G. A.; Salvador, P.; Dannenberg, J. J.; Dapprich, S.; Daniels, A. D.; Farkas, Ö.; Foresman, J. B.; Ortiz, J. V.; Cioslowski, J.; Fox, D. J. *Gaussian 09*; Gaussian, Inc.: Wallingford, CT, USA, 2009.

[54] Breneman, C. M.; Wiberg, K. B. Determining Atom-Centered Monopoles from Molecular Electrostatic Potentials. The Need for High Sampling Density in Formamide Conformational Analysis. *J. Comput. Chem.* **1990**, *11* (3), 361–373.

[55] Jorgensen, W. L.; Maxwell, D. S.; Tirado-Rives, J. Development and Testing of the OPLS All-Atom Force Field on Conformational Energetics and Properties of Organic Liquids. *J. Am. Chem. Soc.* **1996**, *118* (45), 11225–11236.

[56] Halgren, T. A. Merck Molecular Force Field. I. Basis, Form, Scope, Parameterization, and Performance of MMFF94. *J. Comput. Chem.* **1996**, *17* (5-6), 490–519.

[57] Ponder, J. W.; Wu, C.; Ren, P.; Pande, V. S.; Chodera, J. D.; Schnieders, M. J.; Haque, I.; Mobley, D. L.; Lambrecht, D. S.; DiStasio, R. A.; Head-Gordon, M.; Clark, G. N. I.; Johnson, M. E.; Head-Gordon, T. Current Status of the AMOEBA Polarizable Force Field. *J. Phys. Chem. B* **2010**, *114* (8), 2549–2564.

[58] Johnson, L. E.; Barnes, R.; Draxler, T. W.; Eichinger, B. E.; Robinson, B. H. Dielectric Constants of Simple Liquids: Stockmayer and Ellipsoidal Fluids. *J. Phys. Chem. B* **2010**, *114* (25), 8431–8440.

[59] Robinson, B. H.; Dalton, L. R. Monte Carlo Statistical Mechanical Simulations of the Competition of Intermolecular Electrostatic and Poling-Field Interactions in Defining Macroscopic Electro-Optic Activity for Organic Chromophore/Polymer Materials. *J. Phys. Chem. A* **2000**, *104* (20), 4785–4795.

[60] Rommel, H. L.; Robinson, B. H. Orientation of Electro-Optic Chromophores under Poling Conditions: A Spheroidal Model. *J. Phys. Chem. C* **2007**, *111* (50), 18765–18777.

[61] Perram, J. W.; Wertheim, M. S. Statistical Mechanics of Hard Ellipsoids. I. Overlap Algorithm and the Contact Function. *J. Comput. Phys.* **1985**, *58* (3), 409–416.

[62] Onsager, L. Electric Moments of Molecules in Liquids. *J. Am. Chem. Soc.* **1936**, *58* (8), 1486–1493.

[63] Robinson, B. H.; Dalton, L. R.; Harper, A. W.; Ren, A.; Wang, F.; Zhang, C.; Todorova, G.; Lee, M.; Aniszfeld, R.; Garner, S.; Chen, A.; Steier, W. H.; Houbrecht, S.; Persoons, A.; Ledoux, I.; Zyss, J.; Jen, A. K. Y. The Molecular and Supramolecular Engineering of Polymeric Electro-Optic Materials. *Chem. Phys.* **1999**, *245* (1–3), 35–50.

[64] Zhang, C.; Dalton, L. R.; Oh, M.-C.; Zhang, H.; Steier, W. H. Low V_π Electrooptic Modulators from CLD-1: Chromophore Design and Synthesis, Material Processing, and Characterization. *Chem. Mater.* **2001**, *13* (9), 3043–3050.

[65] Olbricht, B. C.; Sullivan, P. A.; Dennis, P. C.; Hurst, J. T.; Johnson, L. E.; Benight, S. J.; Davies, J. A.; Chen, A.; Eichinger, B. E.; Reid, P. J.; Dalton, L. R.; Robinson, B. H. Measuring Order in Contact-Poled Organic Electrooptic Materials with Variable-Angle Polarization-Referenced Absorption Spectroscopy (VAPRAS). *J. Phys. Chem. B* **2011**, *115* (2), 231–241.

[66] Sullivan, P. A. Theory Guided Design and Molecular Engineering of Organic Materials for Enhanced Second-Order Nonlinear Optical Properties, University of Washington, 2006.

[67] Rawal, M. Cross-Conjugated Moieties as Design Motifs for a Class of Novel Electro-Optic Chromophores, University of Washington, 2013.

[68] Rawal, M.; Garrett, K.; Tillack, A. F.; Kaminsky, W.; Jucov, E.; Shelton, D. P.; Timofeeva, T. V.; Eichinger, B. E.; Robinson, B. H.; Dalton, L. R. Cross-Conjugation as a Motif for Organic Non-Linear Optical Molecules. In *Symposium II/JJ/KK – Materials, Processes and Devices for Nanophotonics, Nonlinear Optics and Resonant Optics*; MRS Online Proceedings Library; 2014; Vol. 1698.

2 COARSE-GRAIN FORCE FIELD DEVELOPMENT: LEVEL OF DETAIL (LOD) METHOD

2.1 INTRODUCTION

The search for accurate and systematic coarse-grained (CG) methods is an ongoing challenge in classical chemical simulation methods. A successful approach not only minimizes computational expense but also enables systematic construction from high level force field representations of a wide variety of molecules. Maintaining the accuracy needed to capture complex self-assembly processes and allowing for interactions between complex molecules over a wide range of sizes and shapes is what makes developing CG methods challenging.

Most computational all-atom (AA) force fields represent interactions between neutral atoms by spherically symmetrical potentials such as the Lennard-Jones (LJ) potential. Molecules can be constructed using these neutral atoms as building blocks and taking into account additional potential contributions from partial charges due to bonding. Interaction potentials between molecules are then obtained by summing over pair-wise interactions of constituent atoms. Generally, the resulting fully-atomistic molecular interaction potential sum is not spherically symmetrical anymore and the calculation cost for a pair of molecules scales with the product of the numbers of atoms contained in each interacting molecule.

Many coarse-graining (CG) approaches exist to reduce computational cost by expressing interaction potentials between molecules or molecular moieties with less complex, effective potentials.[1–8] Typically, these approaches consist of a spherically symmetrical, isotropic

potential contributions (i.e. effective Lennard-Jones or Potential-of-Mean-Force) and anisotropic contributions such as charges as well as anisotropic correction terms. For example, all SPC water models[9–12] (and most others) consist of a single Lennard-Jones sphere and charges to represent constituent atom partial charges. The MARTINI force field[4,13,14] uses a similar approach (spherical LJ, charges, anisotropic corrections) for molecular moieties.

The use of spheres as building blocks in CG representations can lead to difficulties when formerly independent shape contributions (i.e. LJ-like) are mixed with electrostatics contributions or are contained in effective correction terms to the system Hamiltonian. Our approach is to keep shape contributions separately from electrostatics contributions and to only allow correction terms with straight-forward physical representations.

Ellipsoids provide an improved representation for anisotropic or planar systems, but require a computationally efficient method for generating a reduced potential. We have used ellipsoids in much of our prior work[15–17] and find they are quite viable as efficient descriptors of molecular subcomponents. Ellipsoids can be computationally efficient, can be systematically generated, and can be added to the pallet of tools available for molecular modelling.

This chapter serves to describe the development of our coarse-grained force field called the Level-of-Detail (LoD) method. The LoD method enables systematic coarse-graining from an all-atom force-field utilizing ellipsoids as the fundamental building blocks to represent molecular subunits.

2.2 ALL-ATOM FORCE FIELD DESCRIPTION

The ultimate goal of the work in this thesis is ab-initio, in-silico prediction of ONLO chromophore behavior in 2nd order electro-optical bulk material which inherently is a multi-method process. Ab initio quantum-mechanical modeling can be used in order to describe individual molecular properties such as the ground state charge distribution and optimal bond distances, as well as the frequency-dependent polarizabilities as well as hyperpolarizabilities. The functionals used and steps performed follow an established procedure by Dr. Lewis E. Johnson and Dr. Bruce E. Eichinger in-house.[18–20]

It is with this goal and background in mind that all our AA force-fields are based upon geometries calculated from density functional theory (DFT) calculations. Briefly, for structure calculations DFT calculations with the hybrid functional B3LYP using a 6-31G(d) basis set in Gaussian 09[21] are employed. The electrostatic potential around the resulting optimized molecule is then used to fit charges at the center of each atom, using so called CHELPG[22] charges.

The thus obtained set of atomic coordinates and charges are employed as the basis for our statistical mechanics calculations in conjunction with parameters for Lennard-Jones radii and energies of individual atoms – we typically use parameters derived from OPLS-AA[23], but others such as the Merck force field[24] or AMOEBA[25] could be used as well.

2.3 LEVEL-OF-DETAIL (LOD) METHOD

We use CG representations composed of connected ellipsoids to give what we call Level of Detail (LoD) representations of functional groups of atoms in our simulations. This is a natural extension to work on single ellipsoids previously reported by our group.[15,16]

Ellipsoids provide a wider pallet of molecular shapes, and can be fit around many different molecular units, such as aromatic rings and long conjugated systems. The general deformability of an ellipsoid allows one to use an LoD with fewer units, and fit the overall geometric shape of the molecule more easily.

The use of ellipsoids is philosophically very similar to the Gay-Berne potential[1] in that both methods lead directly to an anisotropic LJ-like interaction potential that is coarse-grained, but as faithful as possible to the underlying all atom force-field (FF). Although not necessary, in most LoDs each ellipse can freely rotate about the connecting units linking the ellipsoids. Therefore, we typically define unit boundaries between ellipsoids across single bonds.

The LoD method allows for greatly improved calculation runtimes while still being able to describe the underlying system well. To illustrate this point, figure 2.1 shows multiple representations of a CLD-1 type chromophore[26] comparing the fully-atomistic Lennard-Jones potential calculation times for a single chromophore with LoD representation of three ellipsoids down to a single ellipsoid. Tremendous calculation time savings can be realized using the LoD method while also maintaining the accuracy needed to describe complex self-assembly interactions.

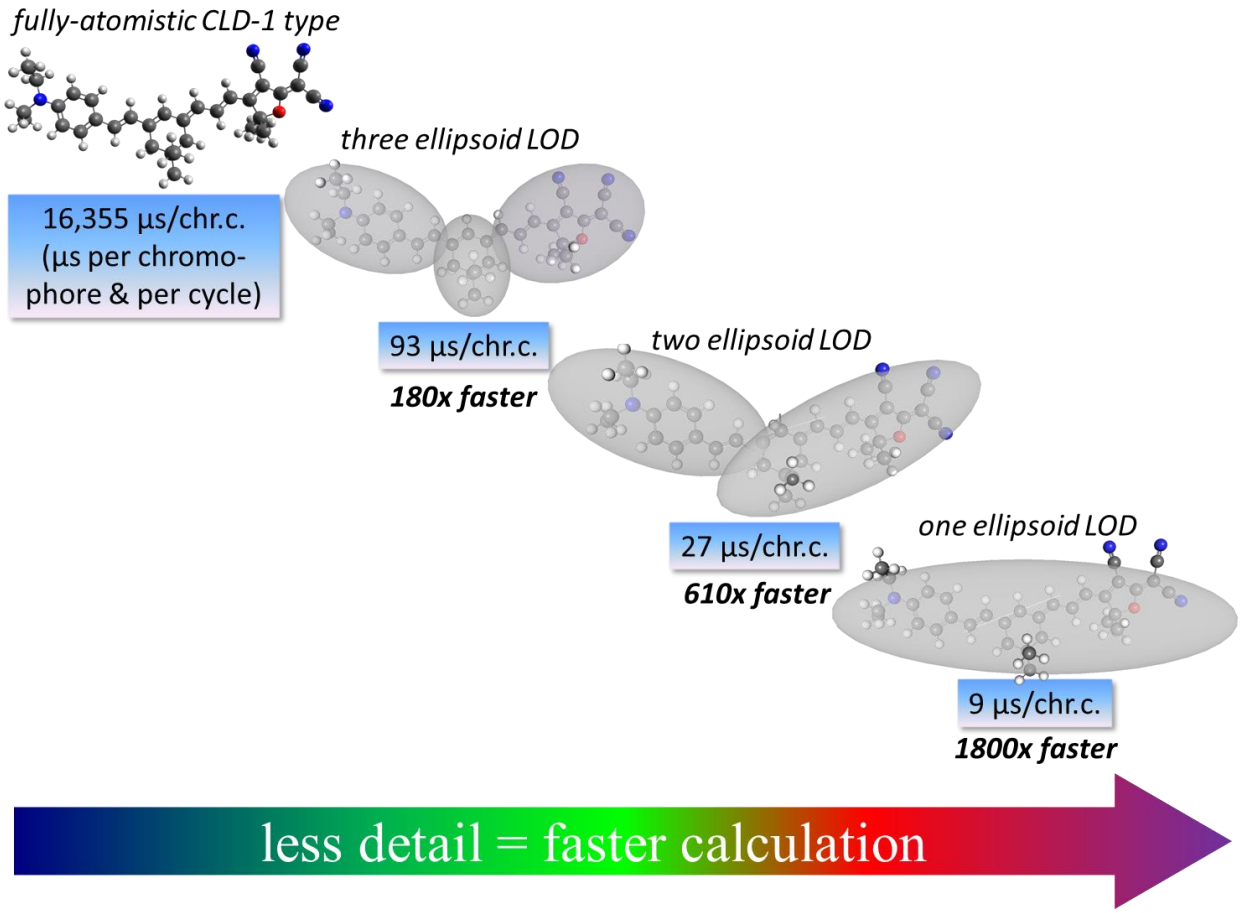

Figure 2.1: Computational speedup of LoD representations of CLD-1 type chromophore (top left) of decreasing complexity; calculation times shown are for Lennard-Jones interactions

2.3.1 PERRAM AND WERTHEIM CONTACT FUNCTION: THE COST OF ELLIPSOIDS

The drawback to using ellipsoids is the additional computational cost compared to spheres. The reason for this additional cost is that for proper ellipsoids with non-degenerate semiaxes the distance of closest contact between two ellipsoids in three-dimensions has not yet been solved analytically and requires the use of an iterative, numerical method.

To get the numerically exact solution to the contact problem, we use a method described by Perram & Wertheim[27] to iteratively obtain the contact function between two (hyper) ellipsoids A and B,

$$F_{AB} = \frac{\vec{R}_{AB}{}^{\dagger} \cdot \vec{R}_{AB}}{\vec{R}_{AB}^{0}{}^{\dagger} \cdot \vec{R}_{AB}^{0}} = \left(\frac{|R_{AB}^{0}|}{|R_{AB}|}\right)^{-2} \tag{2-1}$$

Here, $\vec{R}_{AB}$ is the vector between the centers of two ellipsoids and $\vec{R}_{AB}^{0}$ is the vector between the centers if the two ellipsoids were moved along the line connecting the centers, $\vec{R}_{AB}$, to the point when the ellipsoids just touch. See Appendix A for the computer code (C++ language) of the optimized[1] routine used for the calculation of the inverse contact function.

Based on this simple touch distance ratio, an effective LJ interaction potential between two ellipsoids, as previously employed by our group,[15,16] can then be calculated using the contact function:

$$V_{AB} = 4\varepsilon_{AB} F_{AB}^{-3}(F_{AB}^{-3} - 1) = 4\varepsilon_{AB}\left[\left(\frac{R_{AB}^{0}}{R_{AB}}\right)^{12} - \left(\frac{R_{AB}^{0}}{R_{AB}}\right)^{6}\right] \tag{2-2}$$

[1] ~40% faster compared to our previous iteration of this code, described in Dr. Lewis E. Johnson's dissertation[18]

Here ε_{AB} represents the potential well depth, R_{AB}^{0} and R_{AB} are defined as above which implies that both will depend on the shapes, sizes, and orientations of both ellipsoids.

As it turns out, the calculation of this "simple touch" LJ interaction energy by the method of Perram and Wertheim[27] only takes 2-5 times longer for a pair of ellipsoids versus a pair of spheres, as can be observed in Figure 2.2 for an increasing number of ellipsoids, N, in the simulation box. Simulations were run with periodic boundary conditions, within a simulation volume corresponding to constant ellipsoid number densities, with LJ interactions calculated up to a spherical cutoff set at half the simulation cube's length[2]. The ellipsoids employed in Figure 2.2 cover a wide gamut of eccentricities: almost spherical (CH_3), oblate spheroid (Benzene), and highly eccentric (CLD-1 type chromophore[26]). See Appendix B for ellipsoid parameters.

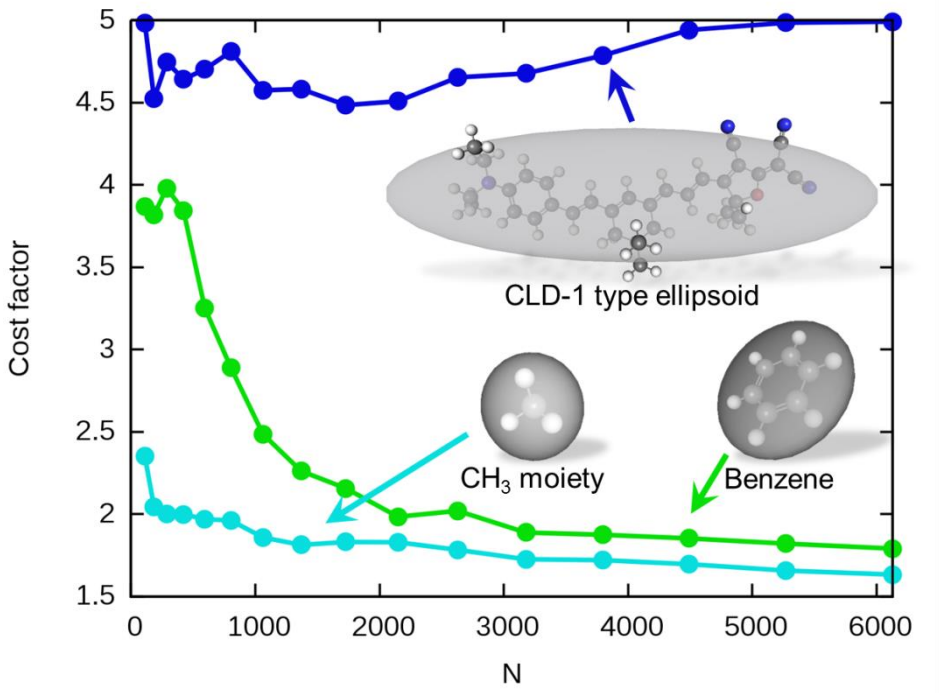

Figure 2.2: Cost factor of LoD ellipsoids representing a CH_3 moiety, Benzene, and a CLD-1 type chromophore relative to the computational cost of LJ interaction between simple spheres

[2] Every ellipsoid will interact with approximately N ellipsoids. This is a worst case scenario as one would typically limit cutoff distances to a certain number of neighboring shells independent of box size.

The shapes of the resultant cost curves as a function of the ellipsoid number give insight into the contact function routine's behavior. The CLD-1 type ellipsoids curve stays at a fixed cost of about five while both CH_3 and Benzene cost functions slowly asymptote towards a value of one (no additional cost). After staying at relatively constant cost initially (up to $N = 422$), the Benzene cost function starts to drop off rapidly.

The reason for this behavior lies in the contact function algorithm's iterative nature in calculating F_{AB} with fixed precision: ***More iterations are needed the larger an ellipsoid pair's eccentricities and the shorter the distance is between them.*** An initially constant cost indicates that the number of iterations stays constant until a precision distance threshold[3] is hit after which the number of iterations starts to drop off, lowering the algorithm's overall cost. While the CH_3 cost curve's distance threshold is already passed before the initial data point, the CLD-1 type's cost is still in the fixed cost range. In both cases, this can be attributed the respective ellipsoid's eccentricities. Thus, these two cost curves represent approximate upper and lower cost limits.

Computational cost of pair-wise interactions at worst scales with the square of the number of entities, N^2. This means that twice or three times the number of entities results in 4 or 9 times the computational cost. Because ellipsoids can encompass a wider range of molecular shapes than spheres more molecular subunits can be grouped into them which can offset the additional cost of ellipsoids compared to sphere based CG approaches. For example, Benzene can be described by one ellipsoid while the popular MARTINI CG force field uses three spheres.[4]

In summary, ellipsoids cost at most five times the computational time compared to spheres. Thus, when an ellipsoid can encompass at least two to three spheres then one is not disadvantaged by the additional computational expense of ellipsoids.

[3] The fraction of interactions with ellipsoids further away increases with increasing numbers of ellipsoids in the box.

2.3.2 IMPROVED ELLIPSOID LENNARD-JONES POTENTIAL

The ellipsoid LJ-type interaction potential using the contact function $F_{AB} = \left(\frac{\sigma_{AB}}{R_{AB}}\right)^{-2}$, with σ_{AB} taking the place of the contact distance R_{AB}^{0} from equation (2-2), is not only a function of the semi-axes of the two ellipsoids, but also depends on the relative orientation of the two ellipsoids and the distance between centers, $R_{AB} = \left|\vec{R}_B - \vec{R}_A\right|$. If the two ellipsoids are both simple spheres with radii a and b, then the contact function gives $\sigma_{AB} = a + b$. Thus the contact function for ellipsoids (and hyper-ellipsoids) is consistent with the LJ potential.

The downside of the LJ-type potential (2-2) is σ_{AB} determines both the ellipsoid boundaries and the LJ potential well width. In conjunction with a constant LJ energy parameter ε_{AB}, this creates the behavior exhibited in Figure 2.3 for long, dipolar prolates (see parameters in Appendix B).

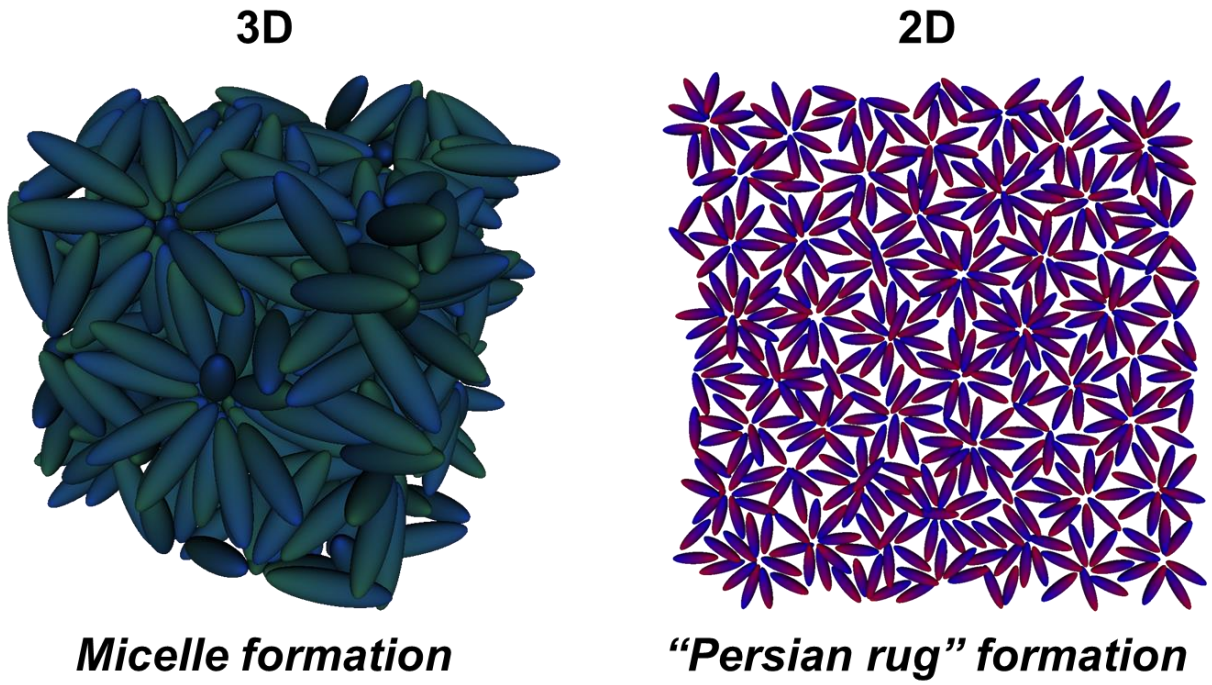

Figure 2.3: Behavior of prolate, "simple touch" ellipsoid LJ potential (2-2) in 3D and 2D system

The reason for the observed micelle formation in three dimensions and the flower petal pattern in two dimensions is that σ_{AB} adjusts to every possible orientation of each pair of ellipsoids with the minimum energy configuration being close to touching but with no energy difference between orientations. For an ensemble of prolate ellipsoids, however, the wider LJ potential well width closer to the long ends of a prolate ellipsoid allows for multiple ellipsoids in the strongly attractive region of the LJ potential. Thus, the energetically favored arrangement for an ensemble of prolates is to maximize the number of long ends in the same space, which is the observed behavior. However, this is not the correct physical behavior for long prolate molecules with no functional groups at either end, as one would expect a more stacked molecular system.

An improvement to the "simple-touch" ellipsoid LJ interaction potential is to hold the potential well width constant. The LJ potential width is determined by its numerator, σ_{AB}, which also determines the zero-crossing of the potential and hence the shape boundaries. In order to allow for a constant potential width with a constant numerator, σ^0, while maintaining the boundaries of the underlying shape, equation (2-2) can be rewritten as:

$$V_{AB} = 4\varepsilon_{AB}\left\{\left(\frac{\sigma^0}{R_{AB}-\delta}\right)^{12} - \left(\frac{\sigma^0}{R_{AB}-\delta}\right)^{6}\right\} \tag{2-3}$$

The utility of the additional parameter δ is to shift the potential such that the original shape boundaries, defined by zero-crossings of equation (2-2), can be retained independent of the choice of σ^0. Equation (2-2) is zero when $\frac{\sigma_{AB}}{R_{AB}(V_{AB}=0)} = 1$, at $R_{AB}(V_{AB}=0) = \sigma_{AB}$. Thus, δ is determined by:

$$1 = \frac{\sigma^0}{R_{AB}(V_{AB}=0)-\delta} = \frac{\sigma^0}{\sigma_{AB}-\delta} \Rightarrow \boldsymbol{\delta = \sigma_{AB} - \sigma^0} \tag{2-4}$$

Combining those two equations leads to a potential which is similar to Gay-Bernes' approach[1]:

$$V_{AB} = 4\varepsilon_{AB}\left\{\left(\frac{\sigma^0}{R_{AB} - \sigma_{AB} + \sigma^0}\right)^{12} - \left(\frac{\sigma^0}{R_{AB} - \sigma_{AB} + \sigma^0}\right)^{6}\right\} \tag{2-5}$$

This GB-type potential, internally called "adjusted width" LJ potential, expressed with the contact function is:

$$V_{AB} = 4\varepsilon_{AB}\left\{\left(\frac{\sigma^0}{R_{AB}\left(1 - \sqrt{1/F_{AB}}\right) + \sigma^0}\right)^{12} - \left(\frac{\sigma^0}{R_{AB}\left(1 - \sqrt{1/F_{AB}}\right) + \sigma^0}\right)^{6}\right\} \tag{2-6}$$

As can be seen in Figure 2.4, this potential, when used on the same prolate ellipsoid system shown in Figure 2.3 but now with a constant LJ potential width of $\sigma^0 = 3$ Å, in three dimensions suppresses the formation of micelles and increases the amount of stacking observable in two dimensions. Adjusting the potential width, however, does not introduce an energetic difference between different orientations of individual ellipsoid pairs. This so called interaction area correction applied to the LJ energy parameter, ε_{AB}, is introduced in section 2.3.5.

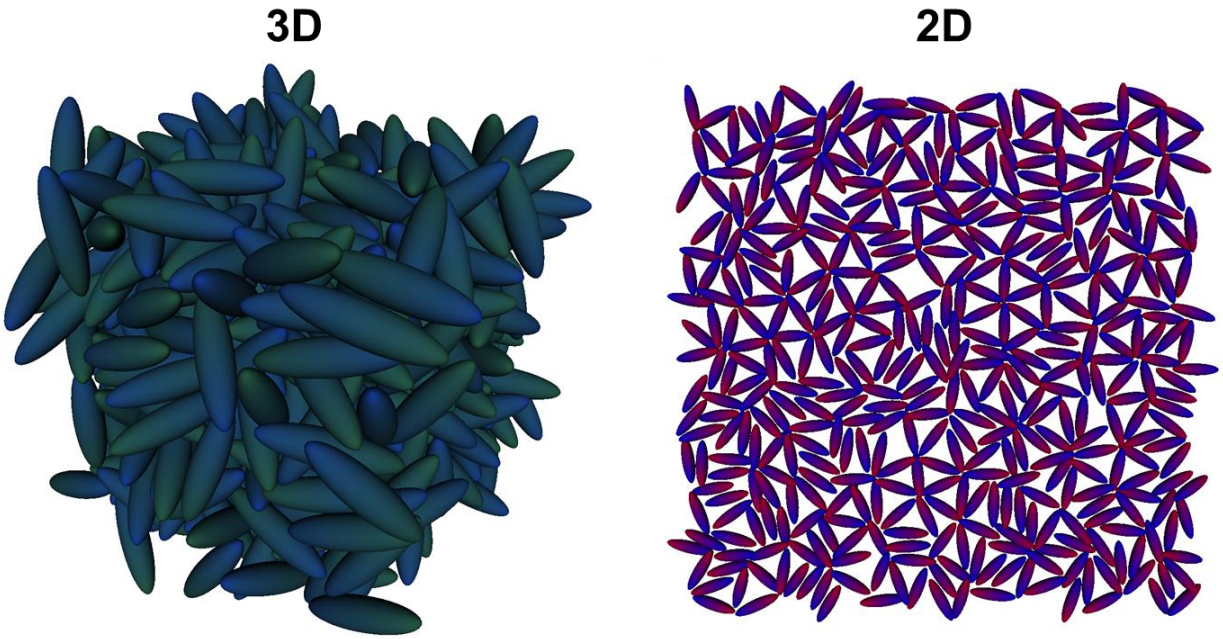

Figure 2.4: Behavior of prolate, "adjusted width" LJ potential (2-6) in 3D and 2D system

Once the shape of the LoD ellipsoid of interest is determined (see next section), the general strategy then is to compare V_{AB}, as defined by the above equation, with that given by the AA force field for the underlying system of atoms. The comparison between the all-atom LJ potential interaction and V_{AB} will be used to determine the best $\sigma^0 and\ \varepsilon_{AB}$ and to determine the extent to which the two potentials agree.[4]

2.3.3 SHAPE DETERMINATION

The reduction to an LoD ellipsoid begins with the overlay of an ellipsoid on a set of atoms within a molecule. This process utilizes the gyration tensor associated with the set of atoms that will be replaced by an ellipsoid. The gyration tensor $S = \frac{3}{N'}\sum_{i=1}^{N'}(\vec{r}_i - \vec{r}_o)(\vec{r}_i - \vec{r}_o)^\dagger$ over an underlying AA system of N' atoms is a real, symmetric tensor. However, it is not translation invariant and hence depends on the ellipsoidal center position, $\vec{r}_o$, which must be calculated from the atom locations from the underlying AA system prior to the determination of S. We found that while a simple average over the atomic locations is a good starting point, we get slightly better LJ potential agreement by using a weighted averaged center position:

$$\vec{r}_o = \frac{\sum \sqrt{\varepsilon_i}\,\vec{r}_i}{\sum \sqrt{\varepsilon_i}} \tag{2-7}$$

using the AA LJ energy parameters as weights. The gyration tensor can be used to construct an approximate ellipsoid (or hyperellipsoid). We begin by finding the three eigenvalues of the gyration tensor:

$$S \cdot \vec{v}_i = \lambda_i^2 \cdot \vec{v}_i \tag{2-8}$$

[4] Note, that an identical approach is used for the "simple touch" form (2-2) where just ε_{AB} needs to be determined.

By construction, S is a real, symmetric matrix and can be diagonalized by an orthogonal rotation. $\vec{v}_i$ is an eigenvector of S, as a column vector, and λ_i^2 is the associated eigenvalue. All eigenvalues of the gyration tensor must be positive, so there is no loss of generality writing the eigenvalue as the square of a positive number. The diagonal matrix, A, of eigenvalues are:

$$A = \begin{bmatrix} \lambda_1^2 & 0 & 0 \\ 0 & \lambda_2^2 & 0 \\ 0 & 0 & \lambda_3^2 \end{bmatrix} \tag{2-9}$$

All three eigenvectors are assumed to be normalized such that $\|\vec{v}_1\| = \|\vec{v}_2\| = \|\vec{v}_3\| = 1$. The gyration tensor can be diagonalized by a proper rotation matrix, $\boldsymbol{R}$. The rotation matrix has the properties that the $\det \boldsymbol{R} = +1$, and that it is an orthogonal rotation, or that its inverse is the transpose. The rotation matrix, $\boldsymbol{R}$, diagonalizes S so that:

$$\boldsymbol{R} \cdot A \cdot \boldsymbol{R^{-1}} = S \tag{2-10}$$

There are three cases to consider for the construction of a proper rotation matrix, $\boldsymbol{R}$. When all eigenvalues are distinct the gyration tensor describes an ellipsoid. R can directly be obtained from the eigenvectors and the requirement that $\det \boldsymbol{R} = +1$ can be achieved by multiplying one individual eigenvector by ± 1. Thus: $\boldsymbol{R} = [\vec{v}_1 \quad \pm\vec{v}_2 \quad \vec{v}_3]$. In the spheroid case, with two degenerate eigenvalues, the rotation matrix is constructed from two linearly independent eigenvectors $\vec{v}_i$ and $\vec{v}_j$ as well as their cross-product $\vec{v}_k = \vec{v}_i \times \vec{v}_j$ as the third linearly independent vector. For example, if $\lambda_1^2 = \lambda_2^2 \neq \lambda_3^2$ the rotation matrix is constructed as

$$\boldsymbol{R} = [\vec{v}_1 \quad \pm(\vec{v}_1 \times \vec{v}_3) \quad \vec{v}_3] \tag{2-11}$$

The sign is used to ensure a proper rotation matrix. When all eigenvalues are identical the rotation matrix is simply the identity matrix because the resulting shape is a sphere. The utility of the gyration tensor is that the elements $\lambda_1,\ \lambda_2, \lambda_3$ are the semi-axes of an ellipsoid ($\{a, b, c\}$), and

the surface of the ellipsoid is defined as: $\left(\frac{x}{\lambda_1}\right)^2 + \left(\frac{y}{\lambda_2}\right)^2 + \left(\frac{z}{\lambda_3}\right)^2 = 1$, where the coordinates, $\vec{\rho}$, apply to the ellipsoid in the diagonal frame centered at the origin: $\vec{\rho}^{\dagger} \cdot A^{-1} \cdot \vec{\rho} = 1$. The rotation matrix can be used to orient the ellipsoid back to its original position $\vec{r}$: $\vec{r} - \vec{r}_o = R \cdot \vec{\rho}$.

Below is a demonstration for the case of benzene of the LoD process, step by step, where the entire molecule is replaced by a single ellipsoid. In this case the symmetry is such that the weighting of the atomic coordinates to find $\vec{r}_o$ make no difference.

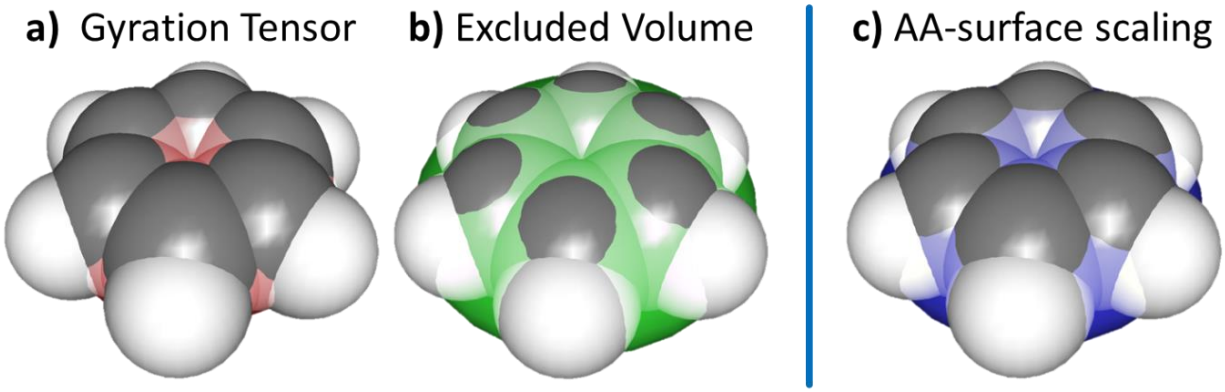

Figure 2.5: Ellipsoid representations of Benzene compared to AA van der Waals (vdW) surface; a) Gyration tensor ellipsoid (2.90x2.90x1.52 Å, red), b) Gyration tensor semi-axes uniformly scaled to match the excluded volume of AA-system (3.43x3.43x1.80 Å, green), and c) individually scaled ellipsoid semi-axes based on AA-system vdW surface (3.33x3.27x1.66 Å, blue) as explained below.

The square roots of the gyration tensor eigenvalues define an ellipsoid with semi-axes $\lambda_1, \lambda_2, \lambda_3$ shown in Figure 2.5a. Note that the gyration tensor has degenerate semi-axes in the x-y plane and thus molecular symmetry may not coincide with the coordinate system. The semi-axes obtained from the gyration tensor are typically too small for a given set of underlying objects and rescaling becomes necessary. We found scaling all semi-axes by the same amount to match the excluded volume of the underlying AA system (Figure 2.5b) typically leads to density-matched results; however, it also tends to lead to Lennard-Jones interaction energies which are too large.

We consider the optimum semi-axes to be those that best describe the underlying AA shape and give similar resulting system pressures for canonical ensembles (NVT) or similar densities for isothermal isobaric ensembles (NPT). Therefore, we suggest an approach which tries to match the ellipsoid surface as closely as possible to the surface of the underlying all-atom system. The approach relies on the gyration tensor rotation matrix $\boldsymbol{R}$ to give the optimum semi-axis directions, with no further modification, and uses the gyration tensor ellipsoid semi-axes as a starting shape. We now rotate the ellipsoid and the AA system to a common frame in which the ellipsoid is diagonal and centered.

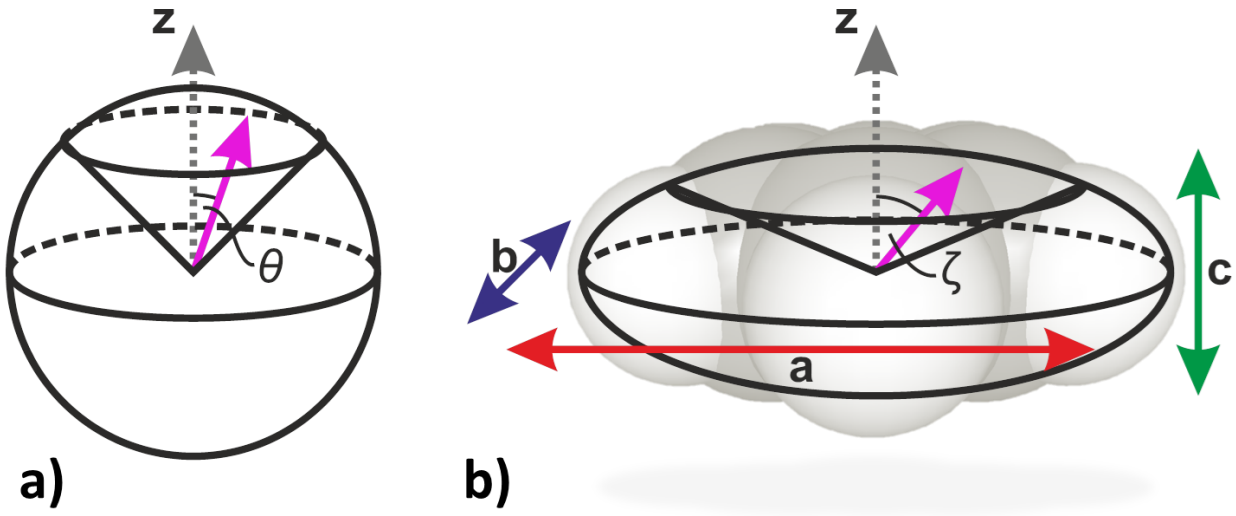

Figure 2.6: a) Sampling over ellipsoid surface through scaling of uniform points within a cone around an axis on a sphere (similar for other axes); **b)** An ellipsoid shown superposed on an AA system, of benzene, showing the semi-axes a, b and c on x, y and z, respectively.

We will modify the semi-axes to go to the same surface as the underlying all atom system. This can only be done exactly for three points; therefore we suggest a best fit that gives agreement in an averaged sense. We begin by selecting a set of points, test point, χ, which gives a reasonably uniform surface coverage, to be places where we would like the spheroid to agree with the underlying AA system. Figure 2.6a shows sampling directions (purple vector) created from

spherical coordinates by sampling linearly in $\cos\theta$ and φ over a conical segment with opening angle 45° pointing along the z axis. We start with the unit vector on a sphere as a function of polar and azimuthal angle:

$$\vec{d}_{cone}(\theta,\varphi) = \begin{pmatrix} \sin\theta\cos\varphi \\ \sin\theta\sin\varphi \\ \cos\theta \end{pmatrix} \text{ with } \begin{matrix} \cos\theta \geq \sqrt{0.5} \\ 0 \leq \varphi < 2\pi \end{matrix} \tag{2-12}$$

The resulting direction vector components are then linearly scaled by a, b, c (denoted by the entry-wise product $\circ$), to take the ellipsoidal shape into account (Figure 2.6b) to spread the sampling points uniformly to the surface of the ellipse:

$$\vec{d}_c = \begin{pmatrix} a \\ b \\ c \end{pmatrix} \circ \vec{d}_{cone} \tag{2-13}$$

The uniform coverage follows from the identity that: $\vec{d}_c^{\,\dagger} \cdot A^{-1} \cdot \vec{d}_c = 1$.

This vector will be within a cone around the z-axis. Rotation of $\vec{d}_{cone}(\theta,\varphi)$ by 90° around the y- and x-axis obtains corresponding direction vectors for the x- and y-axis, respectively:

$$\begin{aligned} \vec{d}_a &= \begin{pmatrix} a \\ b \\ c \end{pmatrix} \circ \left(\begin{bmatrix} 0 & 0 & 1 \\ 0 & 1 & 0 \\ -1 & 0 & 0 \end{bmatrix} \cdot \vec{d}_{cone}(\theta,\varphi) \right) \\ \vec{d}_b &= \begin{pmatrix} a \\ b \\ c \end{pmatrix} \circ \left(\begin{bmatrix} 1 & 0 & 0 \\ 0 & 0 & 1 \\ 0 & -1 & 0 \end{bmatrix} \cdot \vec{d}_{cone}(\theta,\varphi) \right) \end{aligned} \tag{2-14}$$

For a specific direction, using the unit vector in that direction, i.e. $\hat{d}_c = \frac{\vec{d}_c}{\|\vec{d}_c\|}$ (as shown in Figure 2.6b), one can find the outer surface of the AA system at a point as $\vec{a} = \vec{a}(\theta,\varphi) = (x_A, y_A, z_A) = r_a \hat{d}_c$. Finding this point comes by matching the AA LJ potential to the ellipsoid. Therefore, we compute the pair-wise LJ potential between the atoms comprising the ellipsoid and a test sphere of radius r_p. The test sphere is moved radially inward toward the center at fixed angles, θ and φ,

until the AA LJ is zero. To find the distance at which the AA LJ potential is zero a bisection method is used, placing the test sphere at inside ($V_{LJ}^{AA} \geq 0$) and outside locations ($V_{LJ}^{AA} < 0$) along the direction $\hat{d}_c$ until the zero-crossing distance is obtained within a given precision. The distance from the center to the test sphere is r_a and represents the contact point on the outer surface of the entire system. For example, if we were fitting a complicated AA FF to a simple sphere then $r_a = r_p + \sigma_a$ and the surface that would best match a sphere to the AA system would be at point σ_a and the effective radius of the ellipsoid would be σ_a. Additionally, if the size of the test sphere, r_p, were set to zero, then $r_a = \sigma_a$. However, for ellipsoids when $r_p > 0$, the point of contact in general does not lie along the same line out from the center.

As shown in Figure 2.7, the test sphere center positioned at $\vec{r}_{AA}^{o}$ causes the AA LJ potential to be zero. Therefore, one would like the ellipsoid that will replace the AA substructure to also be positioned so that its LJ potential will be zero. At present the distance to the surface of the ellipsoid is r_ε, so the ellipsoid surface is at $\vec{a} = \vec{d}_c = r_\epsilon \hat{d}_c$. Now one can test whether this set of semi-axes actually makes contact with the test sphere anywhere by using the contact function, $F = \left(\frac{|\vec{r}_{AA}^{o}|}{|r_c|}\right)^{-2}$, and r_c is the distance that the two spheres would be apart if they were just touching. The contact point does not need to lie along $\vec{d}_c$. If the contact function is 1, $F = 1$, then there is contact and one does not need to correct where $\vec{a}$ is located. However, in the more general case that the contact function is not one then one should move the position of where $\vec{a}$ is located. The additional distance can be a very complicated function but if the correction is small then the extra distance is on the order of $r_{AA}^{0} - r_c$. Therefore a better placement would be:

$$\vec{a} = \vec{d}_c = (r_\epsilon + r_{AA}^{0} - r_c)\hat{d}_c \tag{2-15}$$

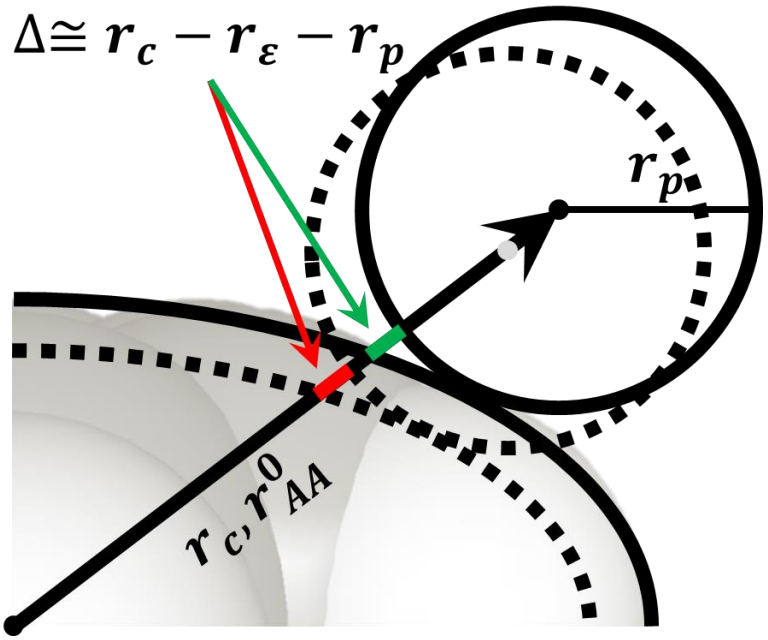

Figure 2.7: Estimate of contact difference Δ shown for best fit ellipsoid shape (solid line) in green and for non-optimum ellipsoid shape with test sphere at contact along same direction (dashed lines) in red; Both the green and red segment are exactly the same length in this figure.

In practice, we have found that the gyration tensor is correct to within 10%. As a practical matter we fixed the test sphere radius to be that of a carbon atom, 1.65 Å.

The next step is to develop a method to improve the agreement of the AA FF LJ crossover points with the overlaid ellipsoid. We outline the iterative method to improve the semiaxes. The ellipsoid semi-axes, originally $a, b, and\ c$ can all be scaled by a factor μ so that the ellipsoid surface will be equal to $A(\theta, \varphi)$, according to the equation of an ellipsoid:

$$\frac{x_A^2}{a^2} + \frac{y_A^2}{b^2} + \frac{z_A^2}{c^2} = \mu^2 \tag{2-16}$$

For each point on the surface, then a value of $\mu = \mu_\chi = \mu(\theta, \varphi)$ can be computed, because the quantities on the left hand side are known. χ represents the set of points sampled within the cone shown in figure 2.6a, and μ represents the uniform inflation factor. However, we now suggest that μ be applied only to the value of c, as that is the semi-axis pointing in the direction of this set

of angles (see Figure 2.6b), clustered around the z axis. Therefore we take a weighted average of μ and find a new value of c, called c', based on the averaged set of μ values:

$$c' = c\frac{\sum(w_\chi \mu_\chi)}{\sum w_\chi} \tag{2-17}$$

The sum is over the set of points, χ, chosen within the cone. After testing several different weighting schemes, we chose to set $w_\chi = \left((0 \quad 0 \quad 1) \cdot \hat{d}_c\right)^2$. The weighting was chosen to make the points that are more along the z axis contribute more toward the average.

The gyration tensor gives a rather good initial set of semiaxes. The modification of both the position for the ellipsoid, $\vec{a}(\theta, \varphi)$, as well as the averaging rule for modifying the semiaxes themselves, require several iteration loops to come to convergence. All points, a for the test sites in the x, y and z, directions are all computed and the corrections are applied only after all of the semiaxes have been completed.

Figure 2.8 depicts the dependence of the ellipsoid semi-axes of Benzene and the average Lennard-Jones potential width w on the size of the test sphere radius, r_p. Both the optimum ellipsoid semi-axes and the average LJ potential width w converge towards a common value. This seemingly unusual behavior can be understood by inspecting the zero-crossing of the interaction potential between a fully atomistic system and a test sphere in the limit of an infinite test sphere radius. The AA LJ potential can be written as:

$$V_{AA,p} = 4\sum_{i=1}^{N}\sqrt{\varepsilon_p \varepsilon_i}\{\mu_i{}^6 - 1\}\ (\mu_i)^6 \text{ where } \mu_i = \frac{w_i + w_p}{R_{ip}} \tag{2-18}$$

Now we consider how to approximate the μ_i when the test sphere size is very large. Imagine that the test sphere is centered on z so that the surface just touches the x-y plane. $\vec{R}_p = -w_p\hat{z}$ and the

positions of the atoms in the AA cluster are at positions r_i, if the test sphere is large compared to the atoms we can approximate $R_{ip} \approx w_p + \hat{z} \cdot \vec{r}_i = w_p + z_i$. Then

$$\mu_i \approx \frac{1 + \frac{w_i}{w_p}}{1 + \frac{\hat{z} \cdot \vec{r}_i}{w_p}_{ip}} \approx 1 + \frac{w_i - z_i}{w_p} \tag{2-19}$$

This gives a simple approximation to the ratio so that when the coordinates of the atom i are negative, then that atom is partially within the test sphere, but the value of μ_i is marginally larger than 1, so that the effect on the LJ potential is really quite small, and can be made arbitrarily small as the test sphere is made larger. This leads to the somewhat counter-intuitive result that there is not much repulsion for atoms that go into a large test sphere. We now evaluate the zero crossing point of the LJ potential, $V_{AA,p} = 0$, for a large test sphere:

$$0 \approx \sum_{i=1}^{N} \sqrt{\varepsilon_p \varepsilon_i} \left\{ \left(1 + \frac{w_i - z_i}{w_p} \right)^6 - 1 \right\} \left(1 + \frac{w_i - z_i}{w_p} \right)^6 \approx 6 \sum_{i=1}^{N} \sqrt{\varepsilon_p \varepsilon_i} \left(\frac{w_i - z_i}{w_p} \right) \tag{2-20}$$

This leads to the simple result that $\sum_{i=1}^{N} w_i \sqrt{\varepsilon_i} = \sum_{i=1}^{N} z_i \sqrt{\varepsilon_i}$. Therefore the point at which the crossing occurs is the weighted average of the positions of the AA system and is equal to the weighted average of the LJ radii:

$$\overline{w} = \frac{\sum_{i=1}^{N} w_i \sqrt{\varepsilon_i}}{\sum_{i=1}^{N} \sqrt{\varepsilon_i}} = \hat{z} \cdot \frac{\sum_{i=1}^{N} \vec{r}_i \sqrt{\varepsilon_i}}{\sum_{i=1}^{N} \sqrt{\varepsilon_i}} \tag{2-21}$$

Thus the weighted-average LJ-sphere size determines the central position of the atoms when VLJ=0, which is a point in the potential equivalent to contact. The weights are the (square roots of the) individual LJ energy parameters. Furthermore, for atoms clustered together, the direction of the test sphere will have no influence on the average sphere size, $\overline{w}$, therefore the direction of

approach does not matter: In short, to a very large test sphere the collection of atoms is equivalent to a single sphere of radius $\bar{w}$.

We can now consider where the minimum in the LJ potential occurs, $\frac{dV_{AA,p}}{dr_o} = 0$. To determine what happens to the minimum point as the size of the test sphere is increased, one needs only to inspect the minimum position on a single sphere, B, of fixed radius w_B. The distance to the center of B from the test sphere edge where the LJ potential minimizes is defined as r_B. After finding the point where the potential minimizes one finds:

$$r_B = \alpha w_p + \sqrt[6]{2} w_B \text{ where } \alpha = \sqrt[6]{2} - 1 = 0.1225 \tag{2-22}$$

For a single sphere, the contact distance is independent of the size of the test sphere. However, the distance at which the potential minimizes from the surface of the test sphere is linearly dependent on the size of the test sphere. This illustrates that to properly find the distance of the particles from the surface of the test sphere in the limit of large test sphere we need to change how the expansion is done. It is necessary to define $z_i = \alpha w_p + \rho_i$, equations (2-18) and (2-19) then yield:

$$\mu_i \approx \frac{1 + \frac{w_i}{w_p}}{(1+\alpha) + \frac{\rho_i}{w_p}_{ip}} = \frac{1}{(1+\alpha)} + \frac{(1+\alpha)w_i - \rho_i}{(1+\alpha)^2 w_p} \tag{2-23}$$

$$\frac{dV_{AA,p}}{dr_o} = 24 \sum_{i=1}^{N} \sqrt{\varepsilon_p \varepsilon_i} \left\{ 2{\mu_i}^6 - 1 \right\} \left(\mu_i \right)^5 \frac{d\mu_i}{dr_o} \text{ where } \frac{d\mu_i}{dr_o} = -\frac{w_i + w_p}{{R_{ip}}^2} \tag{2-24}$$

At the minimum in the LJ potential, this simplifies when using the large sphere limit:

$$0 = \sum_{i=1}^{N} \sqrt{\varepsilon_i} \left\{ 2{\mu_i}^6 - 1 \right\} = 12(1+\alpha) \sum_{i=1}^{N} \sqrt{\varepsilon_i} \left\{ \frac{(1+\alpha)w_i - \rho_i}{(1+\alpha)^2 w_p} \right\} \tag{2-25}$$

$$\sqrt[6]{2}\,\bar{w} = \frac{\sum_{i=1}^{N} \rho_i \sqrt{\varepsilon_i}}{\sum_{i=1}^{N} \sqrt{\varepsilon_i}} = \bar{\rho} \tag{2-26}$$

This is exactly the same result as for the case of a single sphere. Hence, when the test sphere size goes to infinity the set of atoms behave, collectively, as a simple sphere with respect to their properties through the Lennard-Jones potential.

Figure 2.8 shows the calculation results of effective ellipsoid semiaxes dependent on the test sphere radius and verifies the general result: All the semiaxes converge to the same value, which is the weighted mean van der Waals radius, and the set of atoms appears to act similar to a single sphere of that radius as the test sphere becomes much larger than the atomic van der Walls radii.

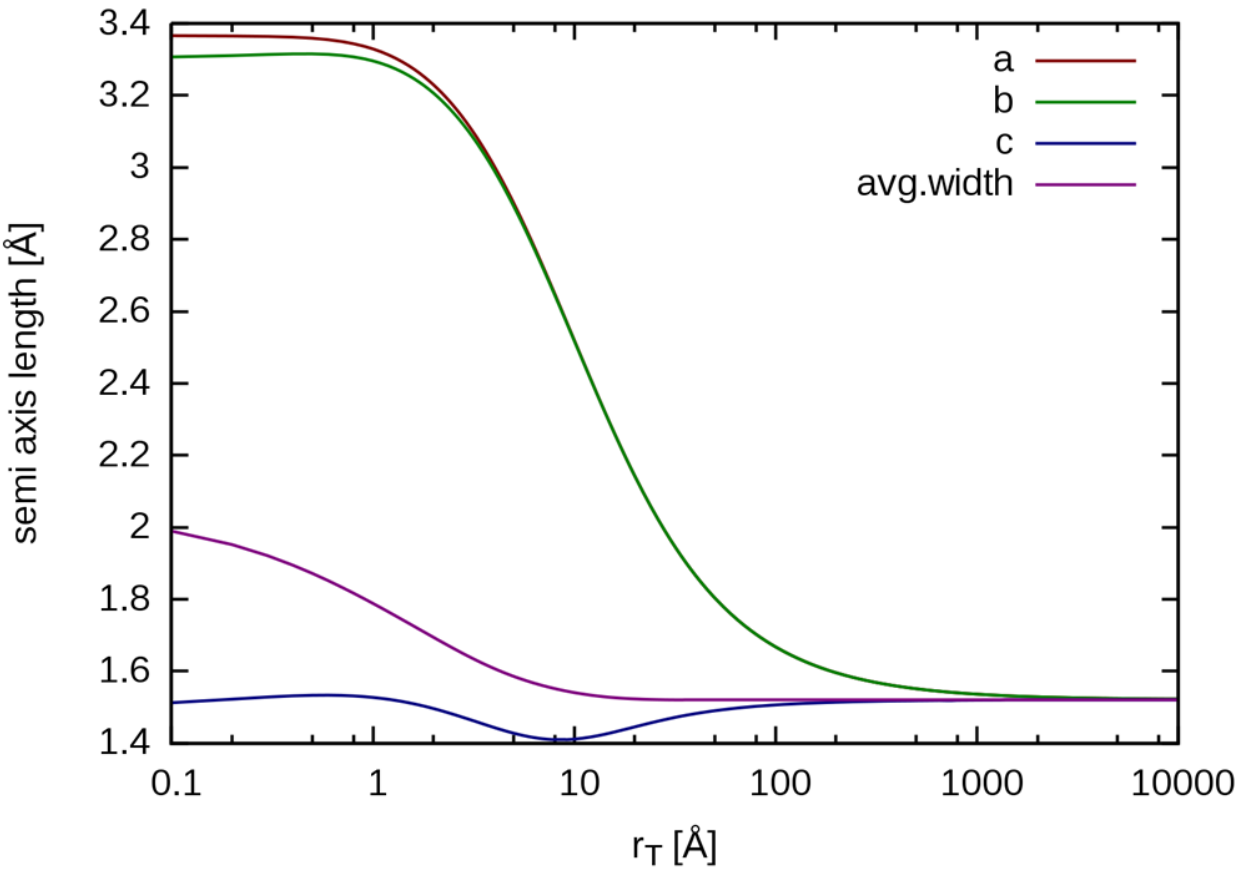

Figure 2.8: Dependence of optimum Benzene semi-axes (a and b are semi-axes in the x-y plane with c perpendicular in the z-direction) and LJ potential width on test sphere radius r_T.

2.3.4 LoD Potential Parameter Determination

In order to determine the best interaction parameters for an individual LoD ellipsoid one could let it interact with all other ellipsoids (including itself) in a given simulation and obtain a set of parameters based on all possible distances and pair orientations in comparison with the underlying fully atomistic potentials. This approach would follow a similar notion compared to other proposed CG approaches.[3,6,28,29] The major downside to such an approach besides computational cost – in essence, running a small scale fully-atomistic simulation to run a large scale coarse-grained simulation – is that resultant parameters will not be transferrable to other systems than the ones for which they were optimized.

For this reason, we chose to let individual LoD ellipsoids interact with a test sphere, p, with a given radius w_p. The parameters of the GB-type LoD are then optimized so that the potential agrees with the potential generated by the underlying AA force field interacting with the same test sphere. In analogy with the full LJ potential (2-23) above we write the LJ potential interaction with a test sphere:

$$V_{A,p} = 4\sqrt{\varepsilon_p \varepsilon_A}\left\{\left(\frac{w_A + w_p}{R_{Ap} - \delta}\right)^{12} - \left(\frac{w_A + w_p}{R_{Ap} - \delta}\right)^{6}\right\} \tag{2-27}$$

Here, ellipsoid A is interacting with a test sphere, p, with LJ energy parameter $\varepsilon_p = 1$, and $\sigma^0 = w_A + w_p$. The value of σ^0 does not affect the point at which $V_{A,p} = 0$. The LJ potential, given by the AA representation of the atoms and the test sphere is given by:

$$V_{FA,p} = \sum_{i=1}^{N} 4\sqrt{\varepsilon_p \varepsilon_i}\left\{\left(\frac{w_i + w_p}{R_{ip}}\right)^{12} - \left(\frac{w_i + w_p}{R_{ip}}\right)^{6}\right\} \tag{2-28}$$

Both potential energies $V_{A,p}$ and $V_{FA,p}$ are functions of the distance between the center of the ellipsoid (which is coincident with the reference point for the set of N atoms), the center of the test sphere, and the orientation of the ellipsoid (and associated N atoms) with respect to the sphere. The sphere size, w_i, of each of the atoms and the LJ energy parameter, ε_i, for each atom are given by the AA force field. We begin by comparing the two potential energies as a function of the orientation of the ellipsoid, Ω, to the sphere. At fixed orientation, two locations on the potential energy surface are of particularly high utility. The first is the crossover point, where $V_{FA,p} = 0$, and the second is the point at which potential energy is minimized. We identify those two unique places as $R_{A,p} = R_1(\Omega)$ and $R_{A,p} = R_2(\Omega)$. We require that $V_{A,p}$ be equal to the AA potential at these two points. Therefore

$$\left(\frac{w_A(\Omega) + w_t}{R_1(\Omega) - \delta}\right)^6 = 1 \quad and \quad \left(\frac{w_A(\Omega) + w_t}{R_2(\Omega) - \delta}\right)^6 = \frac{1}{2} \tag{2-29}$$

$\delta = \delta(\Omega)$ and does not depend on the distance between the centers and is the same at the two positions we are considering. Thus $w_A(\Omega) = \frac{(R_2(\Omega) - R_1(\Omega))}{\left(2^{1/6} - 1\right)} - w_t$. This provides one with a width term that depends on the orientation of the ellipsoid. In general, the width term is not strongly dependent on the orientation, which is one reason why the GB form is a useful approximation. Therefore, a single parameter w_A^o may be obtained as the average over all ellipsoidal orientations:

$$w_A^o = \frac{\int w_A(\Omega) d\Omega}{\int d\Omega} \tag{2-30}$$

This now leaves the energy parameter, $\sqrt{\varepsilon_A}$, to be determined. The optimal energy parameter (as a function of $(\mathrm{R} \text{ and } \Omega)$ is found by setting the two potentials equal $V_{FA,p}(\mathrm{R}, \Omega) = V_{A,p}(\mathrm{R}, \Omega)$:

$$\sqrt{\varepsilon_p \varepsilon_A(\mathrm{R},\Omega)} = \frac{V_{FA,p}}{\nu_{A,p}} \tag{2-31}$$

where

$$\nu_{A,p} = 4\left\{\left(\frac{w_A^o + w_p}{R_{Ap} - \delta}\right)^{12} - \left(\frac{w_A^o + w_p}{R_{Ap} - \delta}\right)^{6}\right\} \tag{2-32}$$

Of the strategies we considered, we chose to obtain an energy parameter as a Boltzmann-weighted average over the entire range of distances (greater than R_1) as the test sphere moves radially from the center of the ellipsoid. The energy parameter depends on the orientation of the ellipsoid, $\varepsilon_A = \varepsilon_A(\Omega)$, but can be reduced to a single value by Boltzmann-averaging over all possible orientations.

$$\sqrt{\varepsilon_p \varepsilon_A^0} = \frac{\int_\Omega \int_{R=R_1(\Omega)}^{R_{max}} e^{-\beta\sqrt{\varepsilon_p \varepsilon_A^0}\,\nu_{A,p}(R,\Omega)} \sqrt{\varepsilon_p \varepsilon_A(\mathrm{R},\Omega)}\,\omega(R)\,dR\,d\Omega}{\int_\Omega \int_{R=R_1(\Omega)}^{R_{max}} e^{-\beta\sqrt{\varepsilon_p \varepsilon_A^0}\,\nu_{A,p}(R,\Omega)}\,\omega(R)\,dR\,d\Omega} \tag{2-33}$$

In this way, both a single optimal effective energy ε_A^0, and single distance w_A^0 are determined by a weighted averaging over all directions. The $\omega(R)$ is a weighting function that subsumes the spherical coordinates, allows for a quadrature or uneven spacing of points on R and improves convergence at large R_{max}. $\omega(R) = 1$ was found to be the best choice after evaluating many weighting functions. Generally, the value of R_{max} is determined based on numerical precision, typically we use values of $R_{max} \approx 14 min\{R_1(\Omega)\}$.

To compute the potential $\nu_{A,p}$ we define δ in a form similar to that for the case where two generalized ellipsoids are interacting:

$$\delta = \left(\sigma_A + \sigma_p\right) - \left(w_A^o + w_p\right) = R_{Ap}\sqrt{1/F_{Ap}} - \left(w_A^o + w_p\right) \tag{2-34}$$

While the size of the test sphere does not affect the value of w_A, the size of the test sphere dramatically changes the energy. The effective energy (see Figure 2.9) from the LoD model needed to match the underlying potential increases with increasing sphere radius, and eventually limits asymptotically to the sum of the individual LJ energies in the AA force field ($\lim_{r\to\infty}\sqrt{\varepsilon_A^o} = \sum_i \sqrt{\varepsilon_i}$). Therefore $\varepsilon_A^o = \varepsilon_A^o(w_p)$.

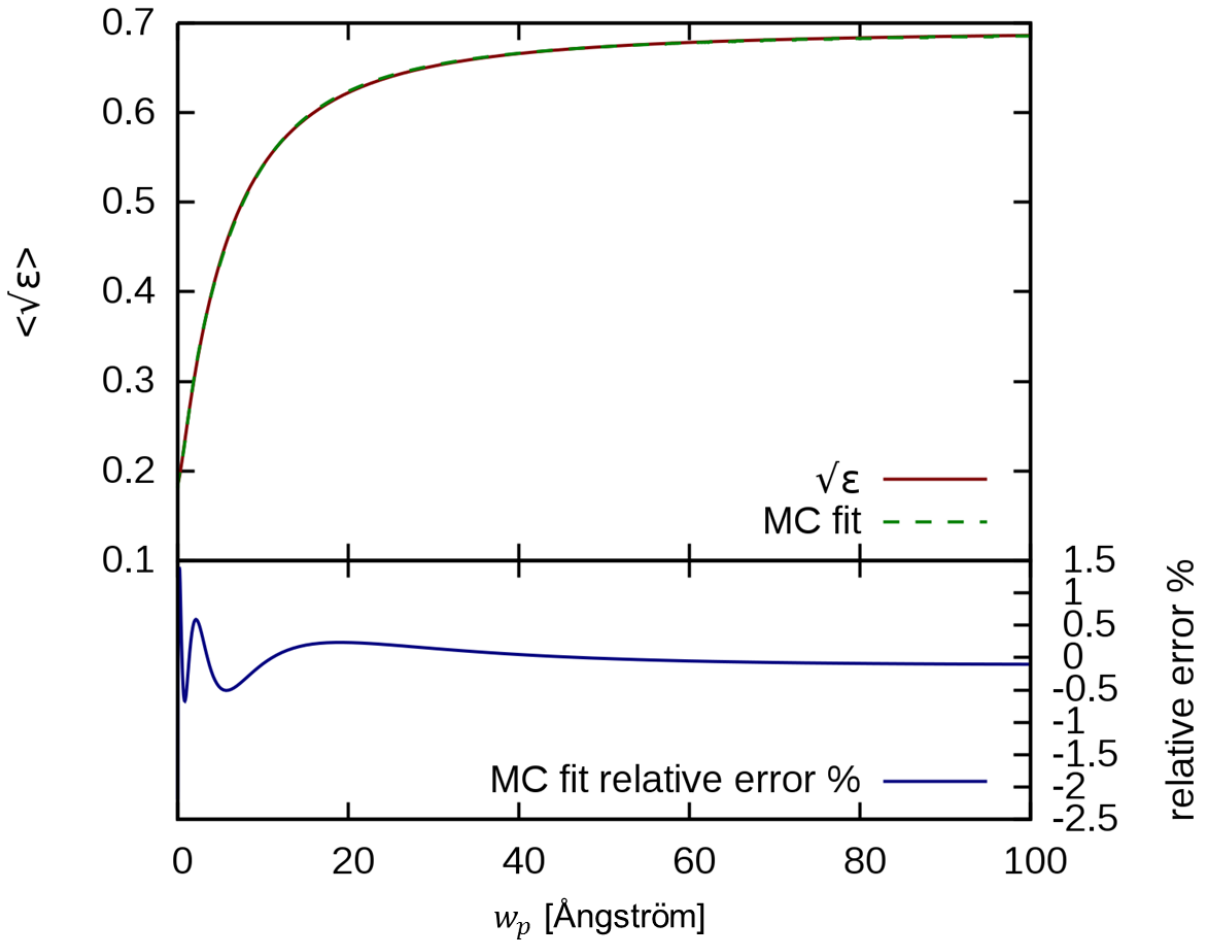

Figure 2.9: Average square root of Lennard-Jones potential well depth as a function of interacting Lennard-Jones sphere of radius w_p

2.3.5 INTERACTION AREA CORRECTION

The best energy parameter, unlike the width parameter, typically is a strong function of the orientation of the ellipsoid with respect to the sphere, because when the ellipsoid presents a large surface to the test sphere, then the interaction energy increases. Therefore we consider how the energy may be scaled by the surface of the ellipsoid that is facing the sphere.

The Lennard-Jones energy between two objects A and B can be understood as the result of two volumes being mutually polarized. Given a fixed interaction depth, this indicates that the energy parameter will scale with the surface areas visible from each object. Normalized and adjusted for the shape difference by a constant factor ν_A, the interaction area factor becomes

$$\eta_{IA}^{A}(B) = \frac{s_A(B)}{\langle s_A \rangle_\Omega} \tag{2-35}$$

Here, $s_A(B)$ describes the surface area on A seen by object B and $\langle s_A \rangle_\Omega$ is the average surface area over all directions. As a computationally efficient approximation to $s_A(B)$ we use the surface area of the ellipse obtained by slicing through the center[30] of ellipsoid A normal to the direction between A and B:

$$s_A(B) = \frac{\pi}{\sqrt{\frac{n_x^2}{b^2c^2} + \frac{n_y^2}{a^2c^2} + \frac{n_z^2}{a^2b^2}}} \tag{2-36}$$

Here, a, b, c are the semi-axes of ellipsoid A and $n_{x,y,z}$ are the components of the unit-vector of the vector between the centers of A and B in the frame of A

$$\hat{n} = R_A^T \frac{(\vec{r}_B - \vec{r}_A)}{\|\vec{r}_B - \vec{r}_A\|} \tag{2-37}$$

R_A^T is the transposed rotation matrix of A.

The orientation dependence of the energy parameters expressed with this so called interaction area factor is

$$\sqrt{\varepsilon_A^s(p)} = \eta_{IA}^A(p)\sqrt{\varepsilon_A^o(w_p)} \tag{2-38}$$

If ellipsoid A is itself a sphere with radius r ($r = a = b = c$), equation (2-32) reduces to the area of a circle with radius r, $s_A(B) = \pi r^2$, independent of the orientation or $\hat{n}$, and hence the interaction area factor is constant, $\eta_{IA}^A(p) = 1$. Figure 2.9 depicts the potential for the AA force field (red dashed line) and the potential for $\nu_{A,p}$ for three different orientations of the Benzene ellipsoid (relative to the test sphere).

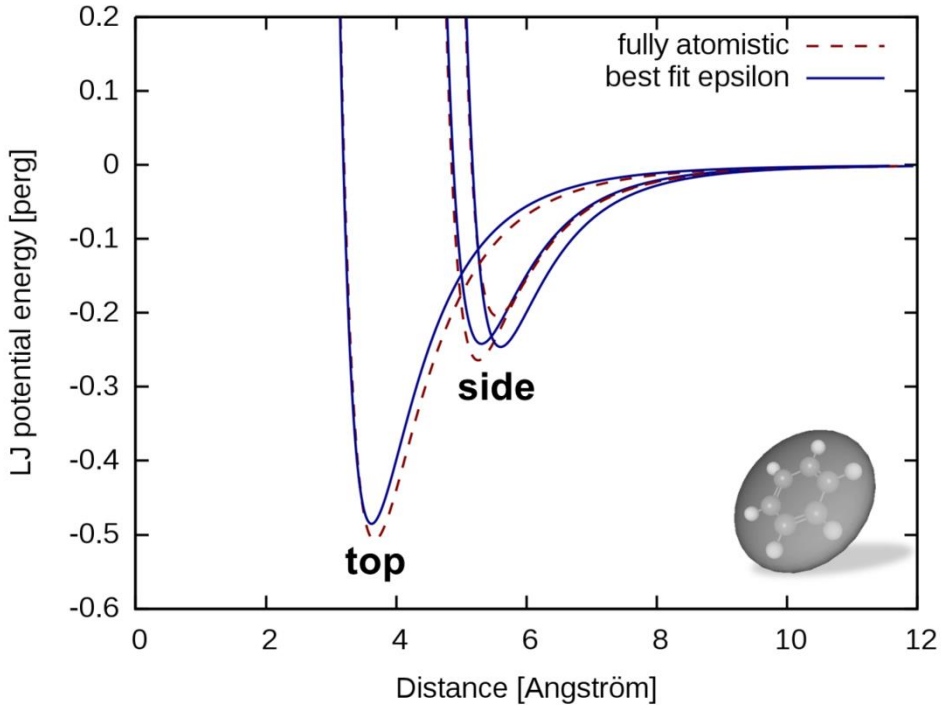

Figure 2.10: Benzene interaction potential of fully-atomistic model (red, dashed) and LoD model (blue, solid) with test sphere of radius matching interaction width $r_p = w_A^0$ of LoD ellipsoid

Once parameters are obtained for a single ellipsoid, they can be applied to the interaction between a pair of ellipsoids, A and B. We continue with the typical combining rules for Lennard-Jones type potentials that the well-depth parameter for the interaction between a pair of ellipsoids of different types is equal to the geometric mean of the well depths of each ellipsoid interacting with an ellipsoid identical to itself, $\varepsilon_{AB} = \sqrt{\varepsilon_A \varepsilon_B}$. Furthermore, we assume that the functional form of σ^o will be the sum of the two individual widths: $\sigma^o = w_A^o + w_B^o$.

Therefore for the two ellipsoids' interaction potential we assume

$$\varepsilon_{AB} = \sqrt{\varepsilon_A^s(B)\varepsilon_A^s(A)} = \eta_{IA}^A(B)\eta_{IA}^B(A)\sqrt{\varepsilon_A^o(w_B^0)\varepsilon_B^o(w_A^0)} \tag{2-39}$$

In this way, each ellipsoid has an energy determined first from interacting with an effective sphere of radius $w_{B,A}^0$ (obtained from the other ellipsoid's interaction width). Then this energy is corrected by the interaction area depending on the orientation of the respective partner ellipse. Notice that if the partners are both spheres all correction factors are unity and the typical combination rule is recovered.

When applied to the long prolate system from Figures 2.3 and 2.4, the interaction area correction (2-39) leads to stacking behavior akin to liquid crystals in both three and two-dimensional systems, as demonstrated in Figure 2.11. This behavior is caused by the approximately four times lower LJ potential energy of side-side interactions compared to end-end interactions.

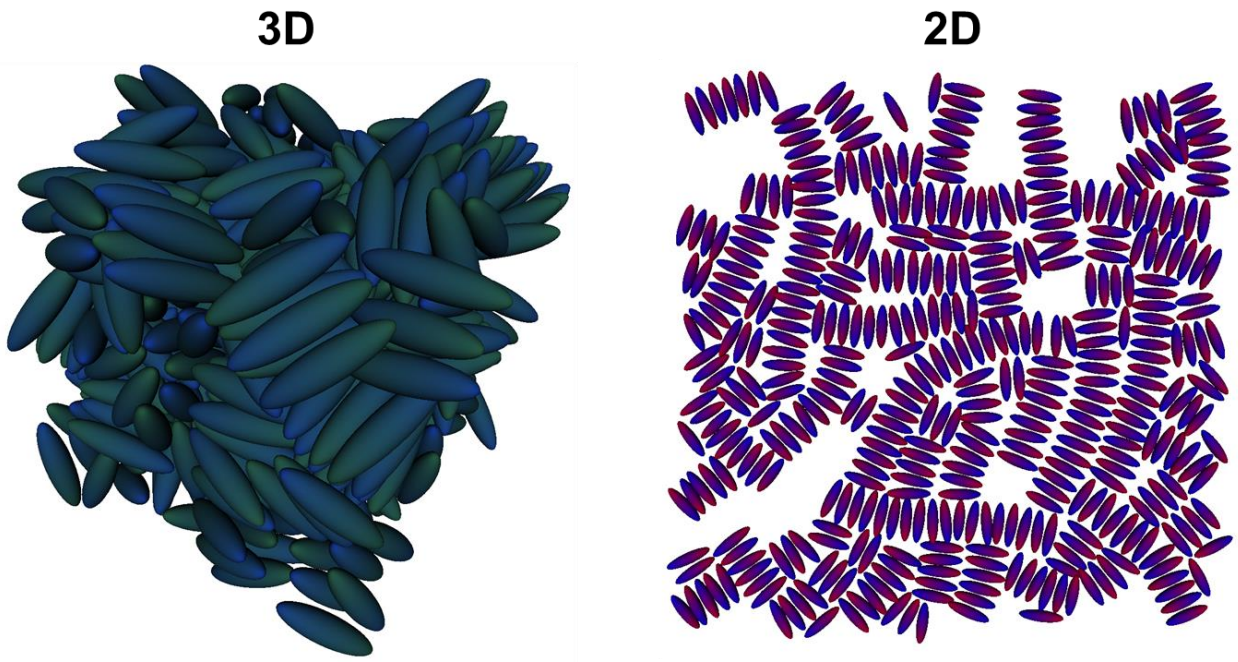

Figure 2.11: Behavior of prolate, "adjusted width" LJ potential (2-6) in 3D and 2D system, using the interaction area correction for the potential well depth ε_{AB} from equation (2-39)

Finally, figure 2.12 shows the top-top and side-side interaction potentials of Benzene with itself using the GB-type full potential from equation (2-6), the width parameter from (2-30), and the energy term of (2-39) compared to the fully-atomistic interaction. Note that the fully-atomistic traces are split in the side-on orientation which is caused by interactions with hydrogens head-on or (as in the ellipsoid shown) with hydrogens of to the side. Due to the semi-axes being averaged over multiple orientations, the LoD model ellipsoid exhibits far less of this splitting with its potential traces located in between the fully-atomistic traces. Overall, the match between the fully-atomistic interaction potential compared to the LoD interaction potential developed from first principles and determined systematically from the AA force field is very good.

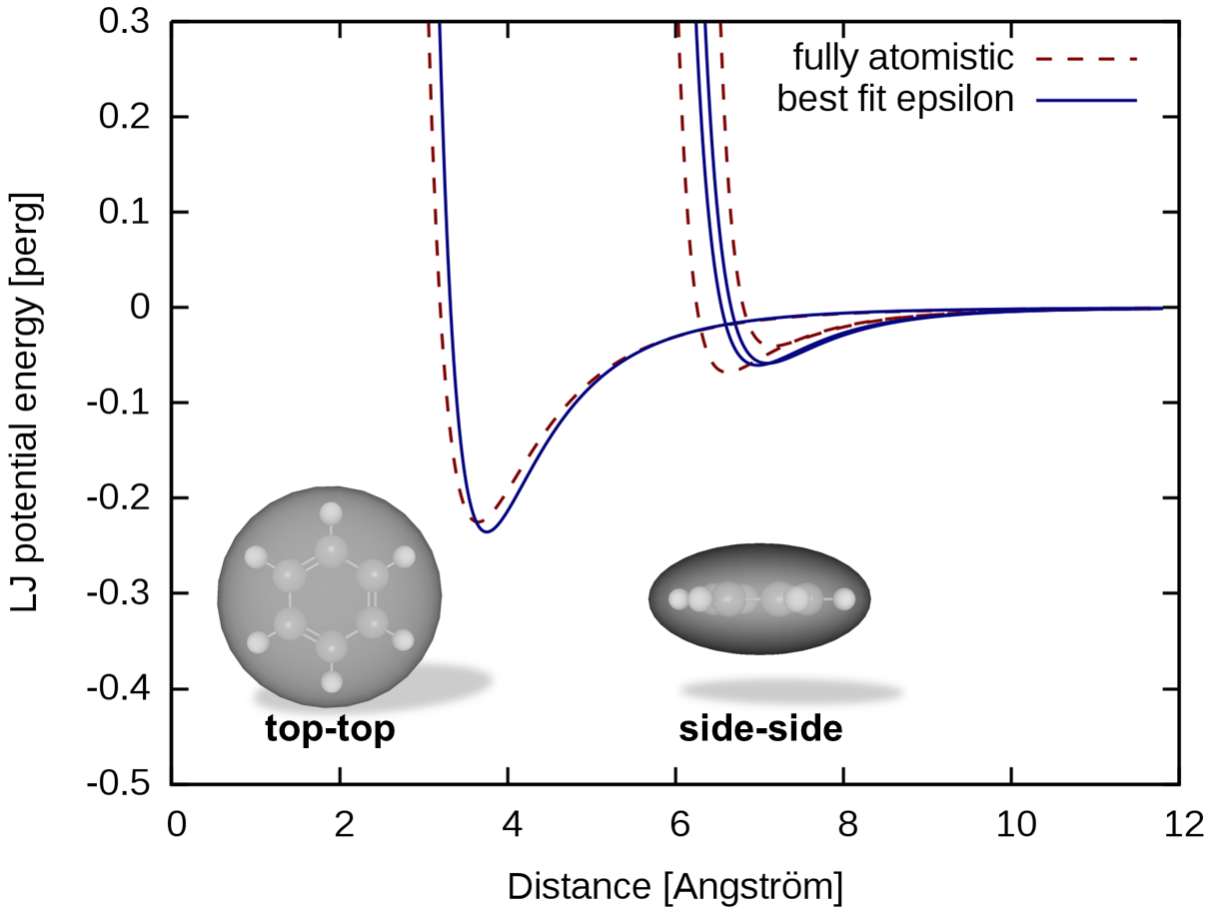

Figure 2.12: Benzene top-top and side-side interaction potential of fully-atomistic model (red, dashed) and LoD model (blue, solid)

In summary, the interaction area correction (2-39) is the final building block to our GB-type "adjusted width" LJ potential (2-6). However, it is also possible to use the interaction area correction with the original "simple touch" LJ potential (2-2) in certain situations with satisfactory results as will be explored in section 2.5. The interaction area correction in conjunction with the entire presented rule set on obtaining an optimal shape, calculating the potential parameters, and determining a pair potential from an underlying AA force field represents the full LoD method's Lennard-Jones potential treatment.

2.4 CHARGE TREATMENT

There are multiple possible treatments for the set of partial charges at the center of the underlying fully-atomistic atoms of an individual LoD ellipsoid. The three methods we typically use are:

1. Keep original partial AA charges, presently at the atomic coordinates, at their locations inside the ellipsoid.
2. Reduction of AA charges using a multipole-expansion approach at the ellipsoid center to a single charge

$$q_{LoD} = \sum_i q_i$$

and a dipole

$$\vec{\mu}_{LoD} = \sum_i (\vec{r}_i - \vec{r}_{LoD}) q_i$$

3. Reduction of AA charges using the multipole expansion from method 2 while also calculating the quadrupole moment tensor

$$\hat{Q}_{LoD} = \sum_k q_k \{3(\vec{r}_i - \vec{r}_{LoD})(\vec{r}_i - \vec{r}_{LoD})^T - (\vec{r}_i - \vec{r}_{LoD})^2 \mathbf{1}\}$$

This quadrupole moment tensor is then used to calculate an equivalent charge distribution of 3-5 charges which are added to the ellipsoid

Those methods can be chosen individually for each LoD ellipsoid in a large molecule. For validation of our LoD method's Lennard-Jones potential, we typically keep the original partial

charges to leave the electrostatics part of the overall interaction potential identical between fully-atomistic and CG simulations.

When simulating large, spread out molecules such as the EO chromophores in Chapters 5 and 6, we generally use method 2, reduction to a single charge and dipole at the ellipsoid center, for improved runtime. However, the added quadrupolar charge distribution from method 3 may be used for certain ellipsoids known to have quadrupolar interactions such as benzene and hexafluorobenzene.

2.5 EXAMPLE CALCULATIONS

The development of the LoD method and its associated set of rules, illustrated with Benzene as an example, were presented in the previous sections. In this section LoD CG simulations using the "simple touch" and "adjusted width" LoD ellipsoid LJ potentials embodied in equations (2-2) and (2-6), respectively, with or without the interaction area correction (2-39) are compared to their fully-atomistic counterparts.

The systems chosen for this comparison are a 1:1 binary mixture of benzene and hexafluorobenzene as well as a fully-flexible hydrocarbon chain of 32 repeat units. These two systems represent a broad cross section of the challenges presented by the simulation of molecular subunits found in ONLO chromophores. Thus, the successful reproduction of those systems' fully-atomistic behavior by their LoD representations can serve as an indication of the overall merit of the LoD method for those much larger ONLO systems.

2.5.1 BENZENE/HEXAFLUOROBENZENE

The binary mixture of benzene and hexafluorobenzene (HBFB) has been studied extensively experimentally as well as theoretically and is seen as a model for π-π interactions.[31–39]

The HBFB system exhibits stacking interactions of benzene to hexafluorobenzene in the solid phase[31,32] and there is experimental evidence of some stacking still present in the liquid phase.[33–35] The stacking of benzene and hexafluorobenzene is attributed to quadrupole-quadrupole interaction as monopolar, dipolar, and octapolar contributions vanish.[40–42] This

makes the HBFB binary system a very interesting benchmark system not only for CG matching of Lennard-Jones interactions but also for electrostatics representations.

Figure 2.13 shows the radial distribution functions of LoD systems consisting of 216 benzene and hexafluorobenzene molecules (108 each) in comparison to the equivalent fully-atomistic system.

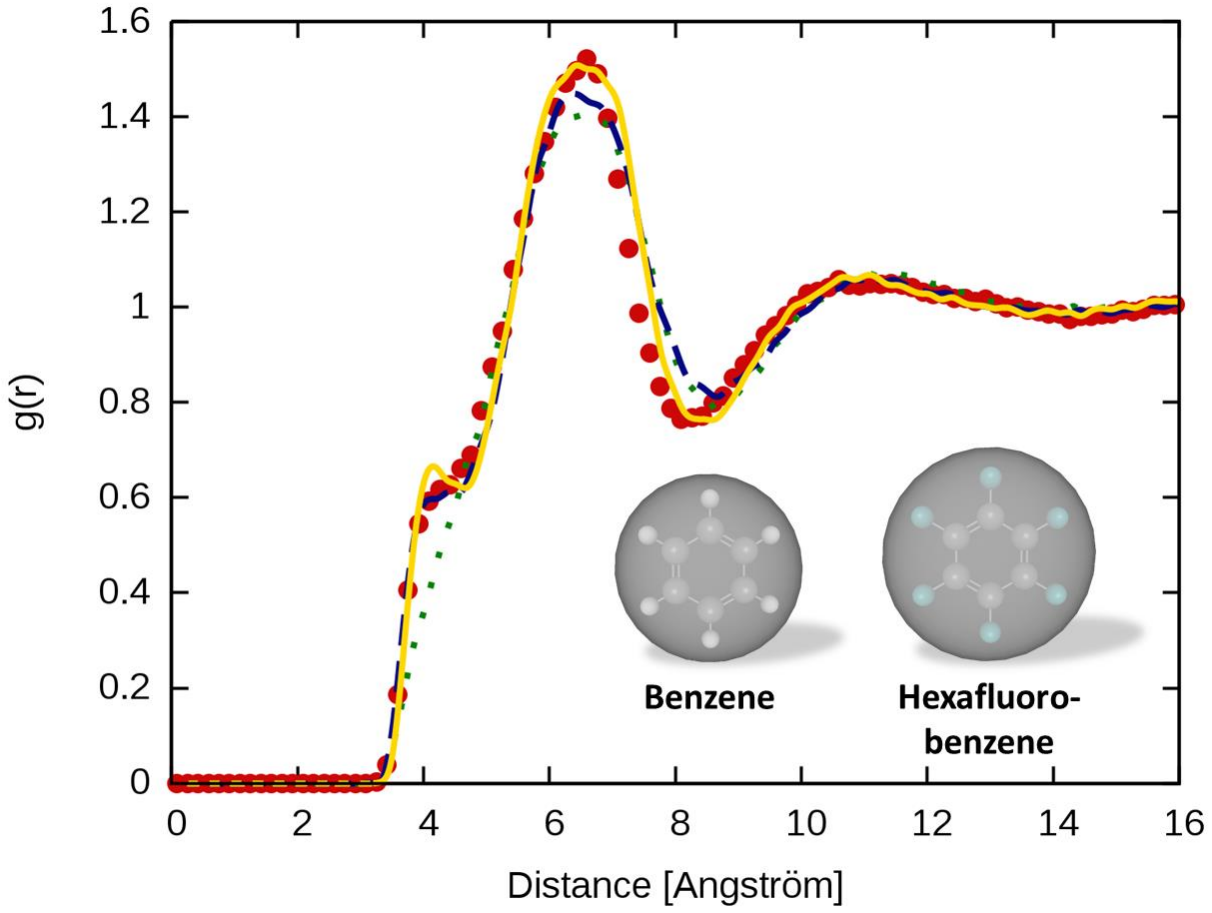

Figure 2.13: Radial distribution function g(r) between benzene and hexafluorobenzene centers for the fully-atomistic simulation (red dots) and LoD simulations with "simple touch" LJ potential (2-2) with constant LJ ε (dotted green), with interaction area correction (2-39) (dashed blue), and with "adjusted width" LJ potential (2-6) and IA correction (2-39) (solid gold)

Calculations were performed with periodic boundary conditions in an isothermal-isobaric (NPT) ensemble at 1 atm pressure and 293 K temperature. The fully-atomistic atom locations and partial charges are based on DFT geometries with CHELPG charges while van der Waals (vdW)

radii and LJ energies are based on OPLS-AA.[23] LoD ellipsoid shapes with a test sphere radius of zero for the shape determination were calculated as outlined previously.[5] All simulations use the same set of charges in order to only focus on Lennard-Jones contributions.

With the interaction area correction (2-39) utilized, both the "simple touch" LJ potential (2-2) and the "adjusted width" LJ potential (2-6) are able to obtain well matching radial distribution functions between the centers of benzene and hexafluorobenzene, with the "adjusted with" potential matching nearly perfectly except for a minor overshoot on the first peak. It is interesting to note that even with no interaction area correction the "simple touch" potential manages to perform well with the exception of the missing first peak.

In terms of the LJ potential, the LoD method does exceptionally well for benzene-like systems. At this point, one could declare victory and move on. However, as mentioned previously the HBFB system should exhibit relatively strong stacking[31–39] which is clearly suppressed in the radial distribution functions shown in Figure 2.13, including the fully-atomistic one.

The reason for this behavior can be found in the location of the partial charges in both molecules. Because of the geometry of benzene-like systems the partial charges are spread out in a plane furthest from the molecule's surface. This sounds fine until one considers their quadrupole moment and its original spatial arrangement in the molecule. The quadrupole moment is caused by π-orbitals oriented perpendicular to the plane of the molecule. Benzene and hexafluorobenzene stack strongly because their resulting quadrupole moments, mimicked by three charges primarily oriented along the z-direction perpendicular to the aromatic plane, are opposing each other. With partial charges arranged in a plane furthest from the molecule's surface the quadrupole moment is too distant and too spread out to cause a strong interaction.

[5] See Appendix B for ellipsoid parameters.

This leads to less overall stacking since in order to have the strongest quadrupolar interaction the molecules need to be aligned perfectly.

In order to improve stacking one can replace the AA partial charges with charges representing the quadrupole moments of both benzene and hexafluorobenzene. A possible arrangement is to place two charges in either direction perpendicular to the molecule's plane with a counter charge at the center. The resulting radial distribution functions are displayed in Figure 2.14.

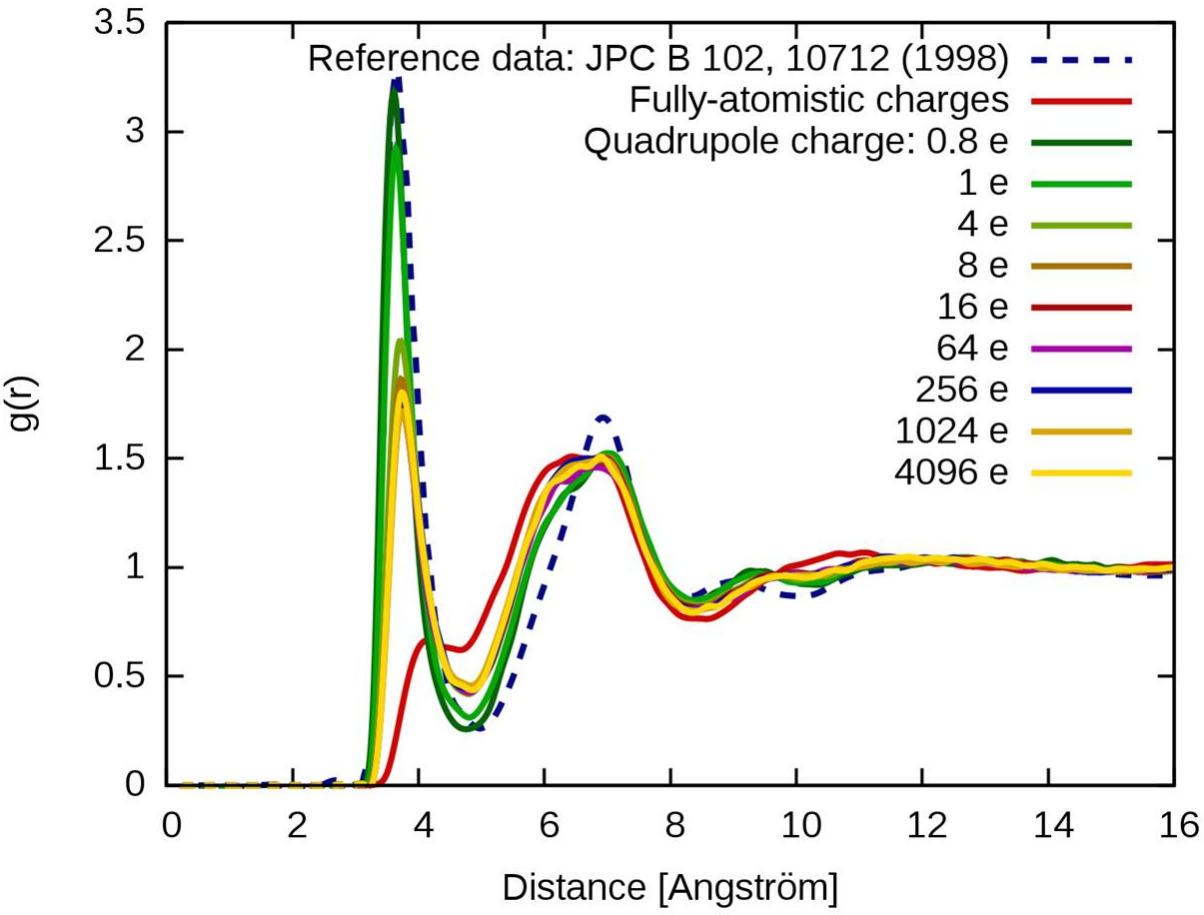

Figure 2.14: Radial distribution function g(r) between benzene and hexafluorobenzene centers for LoD simulations using original partial charges (red) and quadrupole charge expansion with increasingly strong charges moved in closer to the ellipsoid center (see Appendix B) in order to maintain the overall DFT quadrupole moment in the z-direction of $-1.067\ e\text{Å}^2$ for Benzene and $1.541\ e\text{Å}^2$ for Hexafluorobenzene. Reference data reprinted with permission from J. Phys. Chem. B 102 (52), 10712 (1998). Copyright 1998 American Chemical Society.

The magnitude of the charges placed determines their distance from the molecule center to maintain a given quadrupole moment: the smaller the charge the further away from the center it will be placed. The closer a charge gets to the surface of the molecule the stronger its interaction will be with an opposing charge on another molecule, especially because charge-charge interactions drop-off much slower when compared to quadrupolar interactions.

In order to focus purely on electrostatics interactions, the LoD ellipsoid shapes as well as the parameters used in the LoD LJ potential are identical across all simulations run for figure 2.14. In fact, they are identical to the LoD LJ parameters used in figure 2.13 using the "adjusted width" LJ potential (2-6) and the interaction area correction (2-39). Thus the LoD simulation using fully-atomistic charges (red) is identical to the trace shown above in figure 2.13. The other simulated traces use the quadrupole expansion with variable strength charges as outlined above.

It can be observed in figure 2.14 that the smallest charge, 0.8 e, used for the quadrupole expansion on both benzene and hexafluorobenzene which is about 0.6 Å from the surfaces of both benzene and hexafluorobenzene exhibits the strongest stacking interaction (see appendix B for parameters). More importantly, this curve closely matches the radial distribution function between benzene and hexafluorobenzene found in the literature.[35] Moving the quadrupole expansion charges further away from the surface by increasing the charge magnitudes rapidly reduces the stacking peak towards an asymptotic value representing the point quadrupole limit.

The LoD method performs very well at matching the underlying fully-atomistic interactions of benzene-like systems. Changing the electrostatics representation to reflect the quadrupolar nature of benzene and hexafluorobenzene as well as its original spatial arrangement leads to well matched radial distribution functions and stacking behavior as reported in the literature.[35]

2.5.2 *FULLY-FLEXIBLE HYDROCARBON CHAIN*

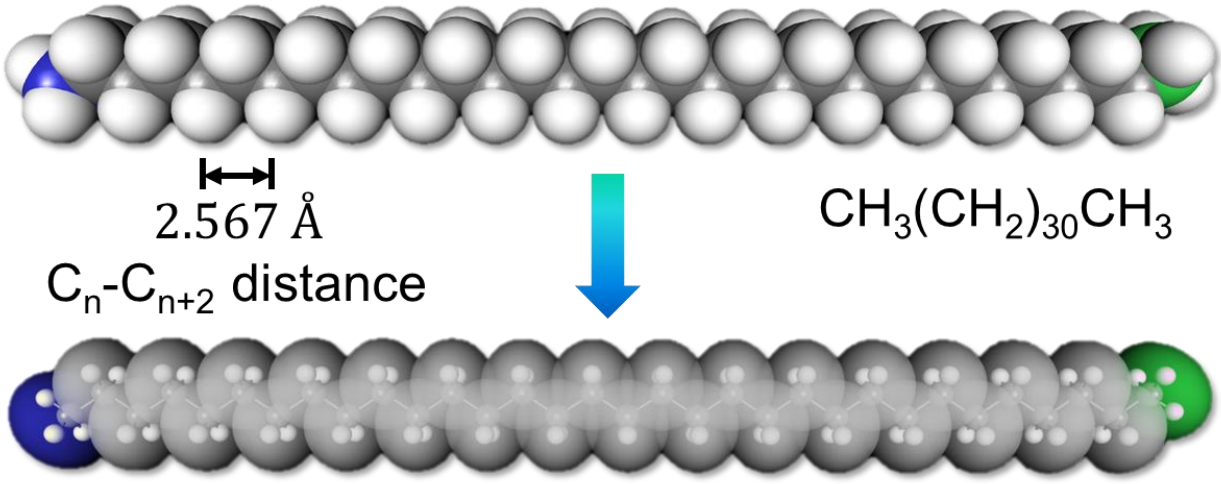

Figure 2.15: Construction of LoD representation from fully-atomistic hydrocarbon chain

In order to study the present LoD Lennard-Jones coarse-graining approach for internal interactions, the end-to-end distance histogram of a saturated alkyl chain with 32 carbons (Figure 2.15) is investigated. Alkyl chains are widely used in ONLO chromophores as linkers and in order to facilitate solubility. Therefore, matching the fully-atomistic chains flexibility (and inflexibility) with a lower detail representation is crucial to successfully simulate ONLO systems.

In the present simulation bond distances and angles between three adjacent carbon centers are held constant as obtained from the DFT geometry (1.534 Å, 113.6°) and only bond rotations are allowed. The theoretical expectation of the average square end-to-end distance for a freely-jointed chain is given by Flory[43] as

$$\langle \vec{R}^2 \rangle = Nl^2 \tag{2-40}$$

Here, $\vec{R}$ is the vector between the end groups, N is the number of monomers, and l is the bond length between monomers. For a freely-jointed hydrocarbon chain similar to the one displayed in

figure 2.16, $N = 32$ and $l = 1.534$ Å, Flory's formula yields an average end-to-end distance of 8.7 Å. Using Flory's random walk approach, in a histogram this would be represented by a symmetric Gaussian distribution.[43] Any hindrances to the movement of such a chain would introduce a skew the distribution towards higher end-to-end distances. A freely-rotating chain is a chain with fixed bond angles but free bond rotations. In order to obtain its theoretical squared end-to-end distance the freely-jointed description (2-40) is multiplied by a characteristic ratio[44]

$$\langle \vec{R}^2 \rangle = C_n N l^2 \text{ with } C_n = \frac{1-\cos\theta}{1+\cos\theta} + \frac{2\cos\theta(1+\cos\theta)^n}{n(1+\cos\theta)^2} \tag{2-41}$$

θ is defined as the bond angle between adjacent monomers. For the present 32 repeat unit alkyl chain with a C-C bond angle of $\theta = 113.6°$ equation (2-41) evaluates to $C_{32} = 2.3$ with a predicted average end-to-end distance of 13.2 Å.

In the present simulations the alkyl chain bond angles are held constant and only bond rotations are allowed. Because of charge interactions and steric limitations (LJ interactions) this is classified as a hindered rotating chain and one would expect the end-to-end distance distribution to be skewed towards longer end-to-end distances compared to the freely-rotating chain.

The LoD model chain is constructed from ellipsoids around the CH_3 end-groups and CH_2 repeat units (Figure 2.15, see Appendix B for model parameters) with partial charges in each ellipsoid kept and placed corresponding to the underlying fully-atomistic model obtained from a DFT calculation. LoD Lennard-Jones and electrostatics interactions are calculated from the second-nearest repeat unit and up. In order to have comparable interaction distances for the fully-atomistic calculation shown as a reference, fourth-nearest atom interactions and up were

calculated.[6] Simulations were run equivalent to an individual alkyl chain, averaged over eight alkyl chains held at fixed locations in the simulation box spaced far apart with cutoff distances set to enforce no interactions between any pair of alkyl chains. In this way, only internal interactions of each alkyl chain contributed to the end-to-end distance histograms shown in Figure 2.16.

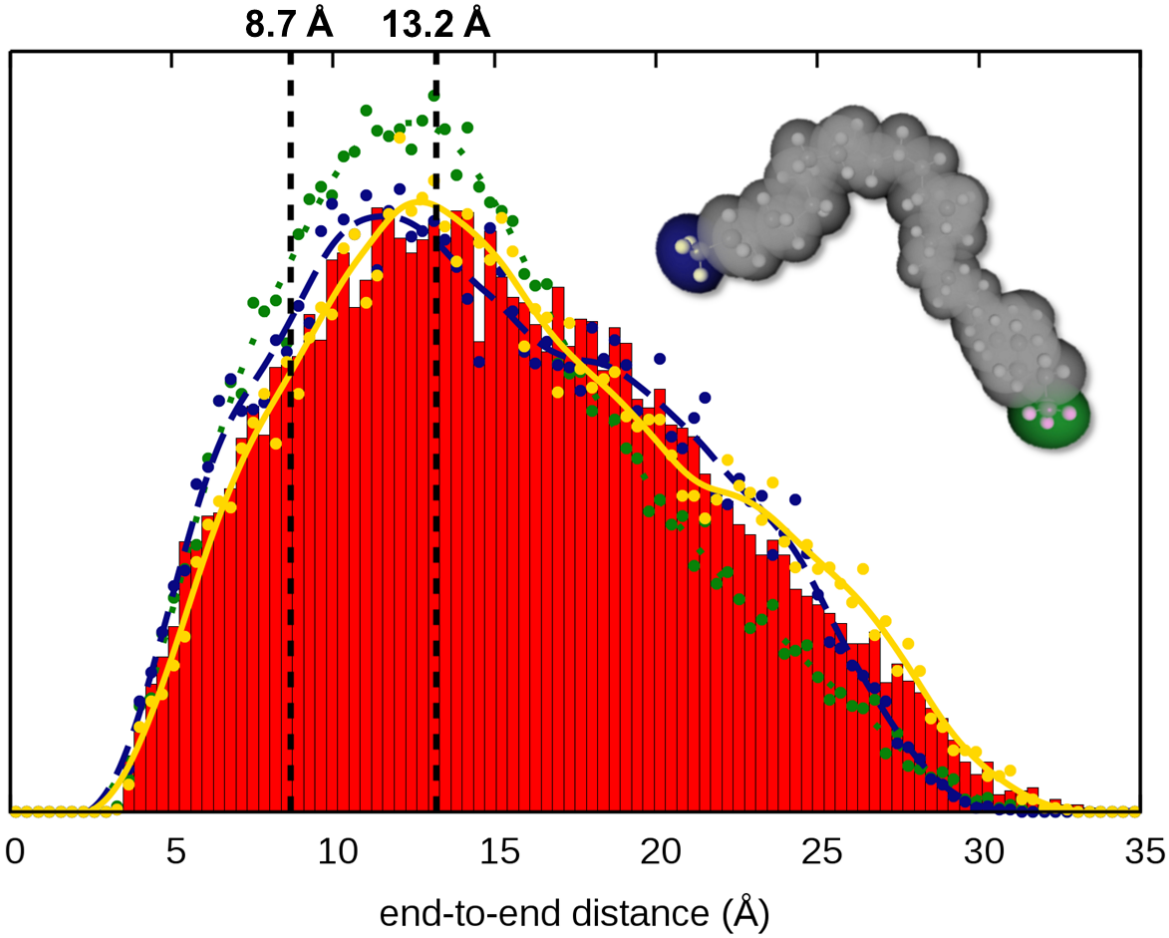

Figure 2.16: End-to-end distance histograms between terminal carbon centers (in blue and green ellipsoids) for fully-atomistic reference (red bars) and LoD simulations with "simple touch" LJ potential (2-2) with constant LJ ε (green dots, dotted line), with interaction area correction (2-39) (blue dots, dashed line), and with "adjusted width" LJ potential (2-6) and IA correction (2-39) (gold dots, solid line); expectation values for the freely-jointed and freely-rotation chain are indicated with vertical, dashed lines

[6] Third nearest atom interactions would correctly include C to H interactions between second nearest repeat units. However, they would also allow H to H interactions between repeat units adjacent to each other, which would not be comparable to LoD simulations with second nearest repeat unit interactions.

Figure 2.16 shows the resulting end-to-end distance histograms for the different expressions of the LoD LJ potential in comparison to the underlying fully-atomistic model as a reference. The expectation values for the freely-jointed (2-40) and freely-rotating (2-41) chain are included as vertical, dashed lines. Both the fully-atomistic and the LoD histogram obtained using the "adjusted-width" LJ potential (2-6) and the interaction area correction (2-39) peak at the expectation value of the corresponding freely-rotating chain and show an exceptionally good overall match. Apart from a small offset in the location of the peak value, when the interaction area correction (2-39) is used the "simple touch" LJ potential (2-2) also displays a good overall match with the fully-atomistic reference. However, with a constant LJ energy as calculated from equation (2-33) the "simple touch" LJ potential (2-2) deviates slightly from the reference giving the appearance of an overall more flexible chain.

Despite providing outstanding accuracy in matching the AA system's behavior, grouping each repeat unit of a hydrocarbon chain into a single LoD ellipsoid is close to the minimum requirement for reducing computation time as outlined in section 2.3.1. In fact, for the calculations depicted in figure 2.14 the LoD representations were "only" a factor of two faster compared to the runtime of the fully-atomistic system. However, the interactions in those simulations were limited to interactions internal to each chain. This means their calculation time scaled linearly with the number of entities, N, in the simulation instead of with the square of N for interactions across an entire simulation volume. Hence, for a bulk simulation with interacting hydrocarbon chains the expected calculation time speedup would be approximately a factor of four.

If calculation times are to be reduced even further, more repeat units of a hydrocarbon chain would need to be grouped into individual LoD ellipsoids. In doing so, care needs to be taken to

still match the underlying fully-atomistic system, particularly for groupings of an even number of repeat units as the original bonds connecting into adjacent ellipsoids would be transoid rather than cisoid for odd numbers. Transoid bond configurations, unlike cisoid configurations, when rotated around bonds, will not exhibit kinks in the resulting chain. In order for groupings of an even number of repeat units with transoid connections between ellipsoids to explore phase space, bond angles need to be artificially flexible.

Figure 2.17 displays the resulting end-to-end distance histograms upon grouping 1, 2, 3, and 4 repeat units of the hydrocarbon chain from figure 2.15 into a single ellipsoid (see Appendix B for model parameters).[7]

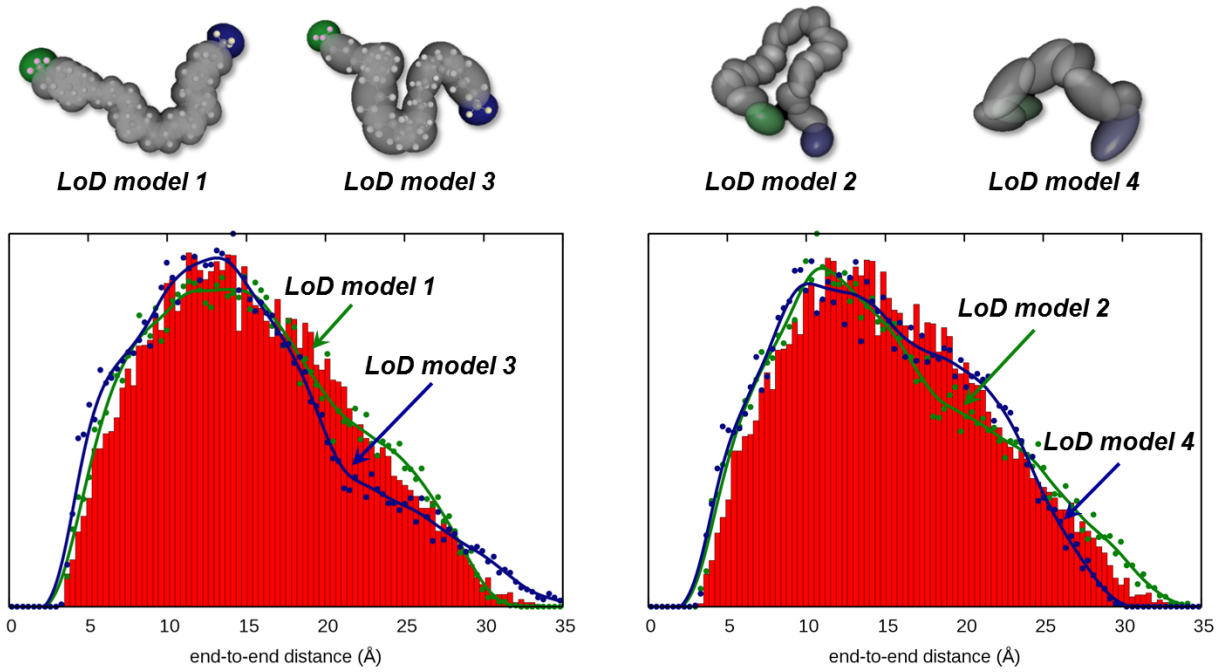

Figure 2.17: End-to-end distance histograms between terminal carbon centers (in blue and green ellipsoids) for fully-atomistic reference (red bars) and LoD simulations grouping 1, 2, 3 and 4 repeat units into a single LoD ellipsoid using the "adjusted width" LJ potential (2-6) and IA correction (2-39)

[7] LoD model 3 groups the terminating CH_3 units into one ellipsoid each and the remaining 30 CH_2 units are grouped three per individual ellipsoid.

For even numbers of repeat units per ellipsoid (LoD models 2 and 4) bonds connecting the ellipsoids are allowed to bend freely. In order to disallow chain overlap through adjacent units folding on themselves and to maintain the modicum of stiffness needed, nearest neighbor interactions are calculated and scaled by 0.1% and 5% for LoD model 2 and 4, respectively. LoD models 1 and 3 use identical rules[8] to the models shown with the solid golden line in figure 2.16 with no additional energy adjustments.

All four LoD models manage to match the underlying fully-atomistic end-to-end distance distribution well. As expected, even groupings of repeat units into ellipsoids needed a minimal amount of adjustment in order to match the fully-atomistic behavior. These adjustment, however, only included allowing bond bending and choosing the nearest neighbor energy fractions. The LoD method potentials and rules remained identical to the ones presented.

The benefit of using ellipsoids in our CG description over spheres, as used for example in the MARTINI force field[4,13,14], is that ellipsoids fill the original space occupied by the underlying system more efficiently. The inherent downside of sphere based CG models is that in order for system interactions to behave physically, all spherical shapes need to be of approximately similar size or void spaces in between connected spheres[9] could easily be filled in with smaller entities. CG representations using ellipsoids, as can be observed with the four LoD models displayed in figure 2.17, have inherently less void space and hence can encompass a larger variety and volume of molecular subunits. Furthermore, because of their better shape correspondence to the underlying moieties, ellipsoid based CG potentials will need less additional adjustments, for example through additional, anisotropic potential terms.

[8] Only bond rotations are allowed, interactions between second nearest neighbors and up are calculated.
[9] An alternative solution to this problem could be to increase the size of the spheres used to fill the void space but this could make those spheres either unnecessarily large or limits the amount of volume encompassed by them.

2.6 CONCLUSIONS

The Level-of-detail (LoD) method, a systematic, bottom up approach to coarse-graining using ellipsoidal shapes rather than spheres has been introduced and developed from first principles. Starting from the fully-atomistic description of a given system, without any additional adjustments, the LoD method is able to match the underlying fully-atomistic behavior of a large variety of systems relevant to ONLO chromophores.

Ellipsoid systems, when using Perram & Wertheim's[27] numerically exact contact function (2-1) for the calculation of the GB-type, ellipsoidal LJ potentials (2-2) and (2-6), cost at most five times the computational time of systems using the same amount of spheres. In other words, LoD representations speed up a simulation when at least two to three atoms are grouped into an individual LoD ellipsoid. This is easily attainable because ellipsoids can fit a larger group of subunits than spheres.

The major contribution of the LoD method is the systematic set of rules to calculate the CG representation shapes and potential parameters as well as its combination rules allowing for a practically unlimited variety of shapes and sizes. Being able to have multiple size regimes in a single CG simulation, to simulate for example a large chromophore being solvated by comparatively small solvent molecules, is an important feature for a wide gamut of applications.

Furthermore, the present work is just the foundation upon which to stand on for future developments such as actually implementing the feature which was the ultimate design goal of the LoD method responsible for its name: Using different levels of detail dependent on interaction distance. This could bring down computational scaling to the "magical" $NlogN$-scaling allowing for large scale system simulations in a fraction of the time that is possible now.

2.7 REFERENCES FOR CHAPTER 2

[1] Gay, J. G.; Berne, B. J. Modification of the Overlap Potential to Mimic a Linear Site–site Potential. *J. Chem. Phys.* **1981**, *74*, 3316.

[2] Allen, M. P.; Tildesley, D. J. *Computer Simulation of Liquids*; Clarendon Press ; Oxford University Press: Oxford [England]; New York, 1989.

[3] Peter, C.; Kremer, K. Multiscale Simulation of Soft Matter Systems – from the Atomistic to the Coarse-Grained Level and Back. *Soft Matter* **2009**, *5* (22), 4357.

[4] Marrink, S. J.; Risselada, H. J.; Yefimov, S.; Tieleman, D. P.; de Vries, A. H. The MARTINI Force Field: Coarse Grained Model for Biomolecular Simulations. *J. Phys. Chem. B* **2007**, *111* (27), 7812–7824.

[5] Izvekov, S.; Voth, G. A. Multiscale Coarse Graining of Liquid-State Systems. *J. Chem. Phys.* **2005**, *123* (13), 134105.

[6] Rudzinski, J. F.; Noid, W. G. The Role of Many-Body Correlations in Determining Potentials for Coarse-Grained Models of Equilibrium Structure. *J. Phys. Chem. B* **2012**, *116* (29), 8621–8635.

[7] Huang, L.; Roux, B. Automated Force Field Parameterization for Nonpolarizable and Polarizable Atomic Models Based on Ab Initio Target Data. *J. Chem. Theory Comput.* **2013**, *9* (8), 3543–3556.

[8] Mladek, B. M.; Fornleitner, J.; Martinez-Veracoechea, F. J.; Dawid, A.; Frenkel, D. Procedure to Construct a Multi-Scale Coarse-Grained Model of DNA-Coated Colloids from Experimental Data. *Soft Matter* **2013**, *9* (30), 7342.

[9] Berendsen, H. J. C.; Postma, J. P. M.; van Gunsteren, W. F.; Hermans, J. Interaction Models for Water in Relation to Protein Hydration. In *Intermolecular Forces*; Pullman, B., Ed.; The Jerusalem Symposia on Quantum Chemistry and Biochemistry; Springer Netherlands, 1981; pp 331–342.

[10] Berendsen, H. J. C.; Grigera, J. R.; Straatsma, T. P. The Missing Term in Effective Pair Potentials. *J. Phys. Chem.* **1987**, *91* (24), 6269–6271.

[11] Grigera, J. R. An Effective Pair Potential for Heavy Water. *J. Chem. Phys.* **2001**, *114* (18), 8064–8067.

[12] Wu, Y.; Tepper, H. L.; Voth, G. A. Flexible Simple Point-Charge Water Model with Improved Liquid-State Properties. *J. Chem. Phys.* **2006**, *124* (2), 024503.

[13] Monticelli, L.; Kandasamy, S. K.; Periole, X.; Larson, R. G.; Tieleman, D. P.; Marrink, S.-J. The MARTINI Coarse-Grained Force Field: Extension to Proteins. *J. Chem. Theory Comput.* **2008**, *4* (5), 819–834.

[14] de Jong, D. H.; Singh, G.; Bennett, W. F. D.; Arnarez, C.; Wassenaar, T. A.; Schäfer, L. V.; Periole, X.; Tieleman, D. P.; Marrink, S. J. Improved Parameters for the Martini Coarse-Grained Protein Force Field. *J. Chem. Theory Comput.* **2013**, *9* (1), 687–697.

[15] Johnson, L. E.; Barnes, R.; Draxler, T. W.; Eichinger, B. E.; Robinson, B. H. Dielectric Constants of Simple Liquids: Stockmayer and Ellipsoidal Fluids. *J. Phys. Chem. B* **2010**, *114* (25), 8431–8440.

[16] Benight, S. J.; Johnson, L. E.; Barnes, R.; Olbricht, B. C.; Bale, D. H.; Reid, P. J.; Eichinger, B. E.; Dalton, L. R.; Sullivan, P. A.; Robinson, B. H. Reduced Dimensionality in Organic Electro-Optic Materials: Theory and Defined Order. *J. Phys. Chem. B* **2010**, *114* (37), 11949–11956.

[17] Tillack, A. F.; Johnson, L. E.; Rawal, M.; Dalton, L. R.; Robinson, B. H. Modeling Chromophore Order: A Guide For Improving EO Performance. In *Symposium II/JJ/KK – Materials, Processes and Devices for Nanophotonics, Nonlinear Optics and Resonant Optics*; MRS Online Proceedings Library; 2014; Vol. 1698.

[18] Johnson, L. E. Multi-Scale Modeling of Organic Electro-Optic Materials, University of Washington, 2012.

[19] Sullivan, P. A.; Rommel, H. L.; Takimoto, Y.; Hammond, S. R.; Bale, D. H.; Olbricht, B. C.; Liao, Y.; Rehr, J.; Eichinger, B. E.; Jen, A. K.-Y.; Reid, P. J.; Dalton, L. R.; Robinson, B. H. Modeling the Optical Behavior of Complex Organic Media: From Molecules to Materials. *J. Phys. Chem. B* **2009**, *113* (47), 15581–15588.

[20] Bale, D. H.; Eichinger, B. E.; Liang, W.; Li, X.; Dalton, L. R.; Robinson, B. H.; Reid, P. J. Dielectric Dependence of the First Molecular Hyperpolarizability for Electro-Optic Chromophores. *J. Phys. Chem. B* **2011**, *115* (13), 3505–3513.

[21] Frisch, M. J.; Trucks, G. W.; Schlegel, H. B.; Scuseria, G. E.; Robb, M. A.; Cheeseman, J. R.; Scalmani, G.; Barone, V.; Mennucci, B.; Petersson, G. A.; Nakatsuji, H.; Caricato, M.; Li, X.; Hratchian, H. P.; Izmaylov, A. F.; Bloino, J.; Zheng, G.; Sonnenberg, J. L.; Hada, M.; Ehara, M.; Toyota, K.; Fukuda, R.; Hasegawa, J.; Ishida, M.; Nakajima, T.; Honda, Y.; Kitao, O.; Nakai, H.; Vreven, T.; Montgomery Jr., J. A.; Peralta, J. E.; Ogliaro, F.; Bearpark, M. J.; Heyd, J.; Brothers, E. N.; Kudin, K. N.; Staroverov, V. N.; Kobayashi, R.; Normand, J.; Raghavachari, K.; Rendell, A. P.; Burant, J. C.; Iyengar, S. S.; Tomasi, J.; Cossi, M.; Rega, N.; Millam, N. J.; Klene, M.; Knox, J. E.; Cross, J. B.; Bakken, V.; Adamo, C.; Jaramillo, J.; Gomperts, R.; Stratmann, R. E.; Yazyev, O.; Austin, A. J.; Cammi, R.; Pomelli, C.; Ochterski, J. W.; Martin, R. L.; Morokuma, K.; Zakrzewski, V. G.; Voth, G. A.; Salvador, P.; Dannenberg, J. J.; Dapprich, S.; Daniels, A. D.; Farkas, Ö.; Foresman, J. B.; Ortiz, J. V.; Cioslowski, J.; Fox, D. J. *Gaussian 09*; Gaussian, Inc.: Wallingford, CT, USA, 2009.

[22] Breneman, C. M.; Wiberg, K. B. Determining Atom-Centered Monopoles from Molecular Electrostatic Potentials. The Need for High Sampling Density in Formamide Conformational Analysis. *J. Comput. Chem.* **1990**, *11* (3), 361–373.

[23] Jorgensen, W. L.; Maxwell, D. S.; Tirado-Rives, J. Development and Testing of the OPLS All-Atom Force Field on Conformational Energetics and Properties of Organic Liquids. *J. Am. Chem. Soc.* **1996**, *118* (45), 11225–11236.

[24] Halgren, T. A. Merck Molecular Force Field. I. Basis, Form, Scope, Parameterization, and Performance of MMFF94. *J. Comput. Chem.* **1996**, *17* (5-6), 490–519.

[25] Ponder, J. W.; Wu, C.; Ren, P.; Pande, V. S.; Chodera, J. D.; Schnieders, M. J.; Haque, I.; Mobley, D. L.; Lambrecht, D. S.; DiStasio, R. A.; Head-Gordon, M.; Clark, G. N. I.; Johnson, M. E.; Head-Gordon, T. Current Status of the AMOEBA Polarizable Force Field. *J. Phys. Chem. B* **2010**, *114* (8), 2549–2564.

[26] Zhang, C.; Dalton, L. R.; Oh, M.-C.; Zhang, H.; Steier, W. H. Low V_π Electrooptic Modulators from CLD-1: Chromophore Design and Synthesis, Material Processing, and Characterization. *Chem. Mater.* **2001**, *13* (9), 3043–3050.

[27] Perram, J. W.; Wertheim, M. S. Statistical Mechanics of Hard Ellipsoids. I. Overlap Algorithm and the Contact Function. *J. Comput. Phys.* **1985**, *58* (3), 409–416.

[28] van Zon, R.; Schofield, J. Constructing Smooth Potentials of Mean Force, Radial Distribution Functions, and Probability Densities from Sampled Data. *J. Chem. Phys.* **2010**, *132* (15), 154110.

[29] Lyubartsev, A.; Mirzoev, A.; Chen, L.; Laaksonen, A. Systematic Coarse-Graining of Molecular Models by the Newton Inversion Method. *Faraday Discuss.* **2010**, *144*, 43.

[30] Klein, P. P. On the Ellipsoid and Plane Intersection Equation. *Appl. Math.* **2012**, *03* (11), 1634–1640.

[31] Patrick, C. R.; Prosser, G. S. A Molecular Complex of Benzene and Hexafluorobenzene. *Nature* **1960**, *187* (4742), 1021–1021.

[32] Overell, J. S. W.; Pawley, G. S. An X-Ray Single-Crystal Study of the Molecular System $C_6F_6.C_6D_6$. *Acta Crystallogr. Sect. B* **1982**, *38* (7), 1966–1972.

[33] Gaw, W. J.; Swinton, F. L. Thermodynamic Properties of Binary Systems Containing Hexafluorobenzene. Part 4.—Excess Gibbs Free Energies of the Three Systems Hexafluorobenzene + Benzene, Touene, and P-Xylene. *Trans. Faraday Soc.* **1968**, *64* (0), 2023–2034.

[34] Bartsch, E.; Bertagnolli, H.; Chieux, P. A Neutron and X-Ray Diffraction Study of the Binary Liquid Aromatic System Benzene-Hexafluorobenzene II. The Mixtures. *Berichte Bunsenges. Für Phys. Chem.* **1986**, *90* (1), 34–46.

[35] Cabaço, M. I.; Danten, Y.; Besnard, M.; Guissani, Y.; Guillot, B. Structural Investigations of Liquid Binary Mixtures: Neutron Diffraction and Molecular Dynamics Studies of Benzene, Hexafluorobenzene, and 1,3,5-Trifluorobenzene. *J. Phys. Chem. B* **1998**, *102* (52), 10712–10723.

[36] Tsuzuki, S.; Uchimaru, T.; Mikami, M. Intermolecular Interaction between Hexafluorobenzene and Benzene: Ab Initio Calculations Including CCSD(T) Level Electron Correlation Correction. *J. Phys. Chem. A* **2006**, *110* (5), 2027–2033.

[37] Gung, B. W.; Amicangelo, J. C. Substituent Effects in $C_6F_6C_6H_5X$ Stacking Interactions. *J. Org. Chem.* **2006**, *71* (25), 9261–9270.

[38] Elola, M. D.; Ladanyi, B. M.; Scodinu, A.; Loughnane, B. J.; Fourkas, J. T. Effects of Molecular Association on Polarizability Relaxation in Liquid Mixtures of Benzene and Hexafluorobenzene. *J. Phys. Chem. B* **2005**, *109* (50), 24085–24099.

[39] Cabaço, M. I.; Danten, Y.; Besnard, M.; Guissani, Y.; Guillot, B. Neutron Diffraction and Molecular Dynamics Study of Liquid Benzene and Its Fluorinated Derivatives as a Function of Temperature. *J. Phys. Chem. B* **1997**, *101* (35), 6977–6987.

[40] Vrbancich, J.; Ritchie, G. L. Quadrupole Moments of Benzene, Hexafluorobenzene and Other Non-Dipolar Aromatic Molecules. *J. Chem. Soc. Faraday Trans. 2 Mol. Chem. Phys.* **1980**, *76*, 648–659.

[41] Hernández-Trujillo, J.; Costas, M.; Vela, A. Quadrupole Interactions in Pure Non-Dipolar Fluorinated or Methylated Benzenes and Their Binary Mixtures. *J. Chem. Soc. Faraday Trans.* **1993**, *89* (14), 2441–2443.

[42] Meyer, E. A.; Castellano, R. K.; Diederich, F. Interactions with Aromatic Rings in Chemical and Biological Recognition. *Angew. Chem. Int. Ed.* **2003**, *42* (11), 1210–1250.

[43] Flory, P. J. *Statistical Mechanics of Chain Molecules*; Interscience Publishers, 1969.

[44] Mark, J. E. *Physical Properties of Polymers Handbook*; Springer Science & Business Media, 2007.

3 ADIABATIC VOLUME ADJUSTMENT (AVA)

3.1 INTRODUCTION

The simulation of non-crystalline condensed matter, such as dendritic and polymeric materials containing ONLO chromophores is extremely challenging. Densities are always around one gram/cc, giving a packing fraction on the order of 70%. Obtaining equilibrium ensembles in such condensed systems is extremely difficult. Using Monte-Carlo (MC) methods at experimental density with a single step-size typically means that individual molecular moves are often rejected unless the move is so small as to be trivial, requiring very long simulations to reach equilibrium.

Accurately simulating the condensed-phase properties of high-density organic materials requires two major tasks: The first, which is discussed in detail in Chapter 2, is to construct simple (but accurate) representations to complex molecules to reduce computational complexity. The second is to develop methods that efficiently extend classical MC-based calculations[1] in the canonical (NVT) and isothermal-isobaric (NPT) ensembles together to obtain correct molecular interactions with maximal control and with efficient (or minimal) number of moves.

In this chapter, a novel method called adiabatic volume adjustment (AVA) is presented which allows a system to reach equilibrium order after fewer calculations compared to traditional NVT or NPT Monte-Carlo.

3.2 MOTIVATION AND METHOD DESCRIPTION

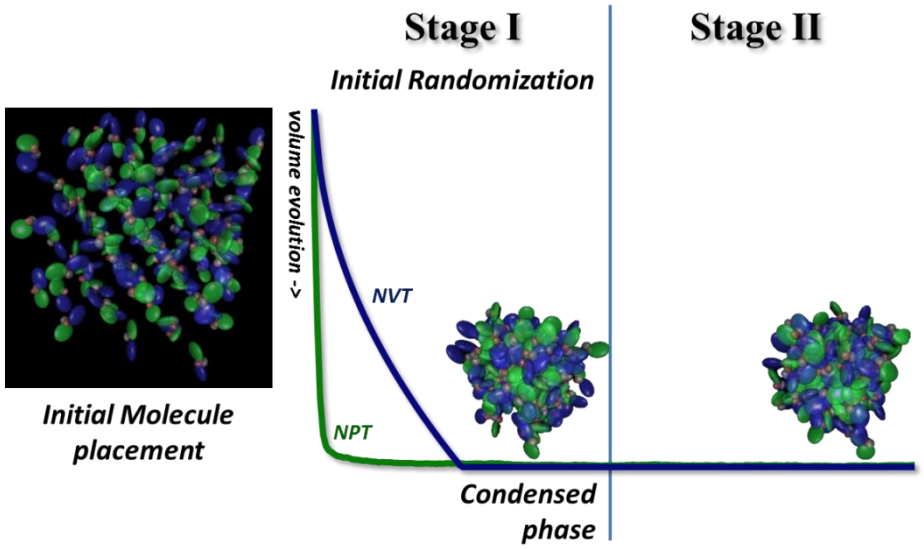

Figure 3.1: Traditional Monte-Carlo simulation stages illustrated using system snapshots along the volume evolution of the simulation system

For the simulation of dense, non-crystalline materials typical Monte-Carlo simulations[1] consist of at least two stages, initial randomization, with only Lennard-Jones potential contributions, followed by system's evolution using the full set of interaction potentials (Figure 3.1). The initial randomization stage is of particular importance to break up the initial placement of molecules and thus start the full system evolution from a truly random, unbiased system state.

During the initial randomization, the volume of canonical (NVT) ensembles is adjusted until the target volume corresponding to the desired system density has been reached. Furthermore, isothermal-isobaric (NPT) ensembles also typically condense during the first stage. When the full set of potential contributions such as electric field interactions and electrostatics are enabled

during the next stage of the simulation the molecular ensemble rearranges until equilibrium configurations are reached.

In a condensed system comprised of large, strongly interacting molecules, however, this rearrangement process toward equilibrium ensembles can require very many simulation cycles and could even potentially get stuck in configurations representing local energetic minima.

Established techniques aimed at improving the configurational space sampled by Monte-Carlo type simulations, such as thermal annealing[2–4], replica exchange sampling,[5–7] and umbrella sampling,[8–10] exist.

Umbrella sampling effectively adds a biasing potential term to the simulation Hamiltonian which can be used to amplify to ordering effects. However, care has to be taken to remove this biasing from system averages obtained at equilibrium. This can be further complicated if the property of interest is directly correlated with the applied bias.

Thermal annealing temporarily sets the simulation temperature to a large value which is subsequently tapered down towards the desired simulation temperature. Higher temperatures effectively allow more “bad” trial moves to be accepted for a limited number of cycles during the second stage of a simulation. Thus, thermal annealing serves to disrupt condensed systems and may even enable a system to overcome local energetic barriers.

However, in systems where equilibrium organizations are driven by small perturbation-like potentials – such as electric field interactions – thermal annealing can potentially drown out those small potential contributions effectively resetting any equilibrium progress already present. Furthermore, for a system stuck in a kinetically trapped configuration, for example due to rapid condensation with only partial potential molecular interactions (such as Lennard-Jones only),

increased simulation temperatures may not be able to overcome the steric hindrances present by large, extended molecule systems. These arguments equally apply to other temperature-based schemes such as replica exchange.

For this reason, the method proposed in this chapter is based on the adjustment of a simulation system's volume rather than temperature. It was developed based on observations made when simulating the ordering under NPT conditions in an external poling field of two ONLO chromophore systems: CLD-C1[11,12] and TCP-Me.[13,14] Some CLD-C1 simulations, instead of condensing rapidly, would expand in the initial randomization phase, then once the full set of simulation potentials was enabled continue to expand and contract again a few times before finally condensing toward an equilibrium volume.

Interestingly, for the systems exhibiting this type of unusual behavior not only was the observed acentric order of these systems about tenfold larger but overall system energies at equilibrium were about 3 kT lower than for the rapidly condensed systems. A less extreme, but similar observation was made for systems in which TCP-Me chromophores, without the extended side-chains and smaller than C1 and CLD-C1 chromophores, could move more easily in a simulation. TCP-Me systems, on the other, sometimes would not condense at all – highlighting the need for more control over the condensation behavior of the simulated system. The resulting novel method, called adiabatic volume adjustment (AVA), adds an additional, transitional stage to the simulation process, as displayed in figure 3.2.

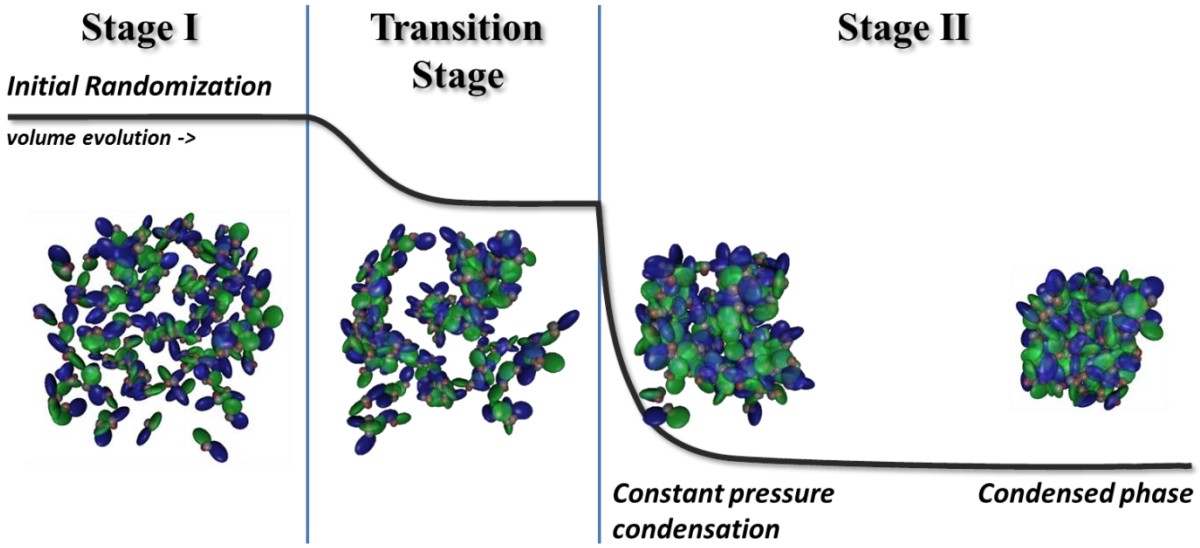

Figure 3.2: AVA method simulation stages illustrated using system snapshots along the volume evolution of the simulation system

With the AVA method, the initial randomization stage of a simulation is locked at the volume occupied during the initial, spread-out molecule placement and the Lennard-Jones potential is made purely repulsive. This is achieved by adding a scale factor λ to the attractive part of the Lennard-Jones potential:

$$V_{AB} = 4\varepsilon_{AB}[f(A,B)^{12} - \lambda f(A,B)^{6}] \tag{3-1}$$

Here, ε_{AB} is the constant or interaction area corrected Lennard-Jones potential energy described in equations (2-33) or (2-39), respectively. The term $f(A,B)$ is defined by comparison with either the "simple touch" or the "adjust-width" LJ potentials (2-2) or (2-6), respectively. This "soft-ellipsoid" type LJ interaction is akin to having an implicit solvent in the simulation volume allowing for full randomization of an ensemble.

The transition stage is introduced in order to slowly modulate the system from the implicit solvent type simulation at the placement volume to the desired simulation type for a given

simulation. This transition typically involves adjusting both the volume and the amount of LJ attraction, represented by λ, and is adiabatic in the quantum mechanical sense that two properties are changed slowly.[1] During the transition stage the calculation of the full set of electrostatics and other potential contributions such as electric field interactions is enabled.

For NVT ensembles, the transition stage leaves the system at the desired volume. For NPT ensembles, on the other hand, one does not have to fully condense the simulation system. Because the transition is mostly done around halfway through the cycles reserved for the transition stage, it could be advantageous to drop the system off at a volume that is slightly larger than the final, condensed volume. This way, the system has more cycles to equilibrate at a larger volume potentially bypassing potential energetic traps.

3.3 Chromophore Order as a Function of Dipole Moment and Number Density of CLD-Based Electro-Optic Chromophores

Monte-Carlo simulations can give insights into design parameters not easily modified in the experimental environment. The dipole moment of a chromophore is one such parameter, as it would require redesigning a chromophore from scratch which can take months to years to accomplish. In a simulation, on the other hand, the chromophore dipole moment can be changed easily at will or even scripted as done for the following examples.

The following calculations illustrate the interplay of chromophore dipole moment and chromophore number density using different LoD representations of a CLD-1 type

[1] In the thermodynamics sense of a rapid system change with no transfer of heat, this adjustment could be classified as at least quasi-adiabatic when one considers that the energy imparted due to compressing the (initially repulsive) system is balanced by the increasingly attractive LJ potential contributions.

chromophore.[15] Calculations were run under NVT conditions with the "soft-ellipsoid" LJ potential (3-1) with $\lambda = 0$, using a constant Lennard-Jones potential energy $\varepsilon_{AB} = 0.243\ perg$ and $f(A,B)$ using the contact function as defined in the "simple touch" LJ potential (2-2). Simulations involved 432 chromophores (see Appendix B for model parameters) run for 240,000 cycles (about one hundred million configurations), the first 40 kcycles were used for initial randomization and the second 40 kcycles for the AVA transition when used. The last 40 kcycles (17.28 million configurations) were used in the calculation of system averages.

Using AVA in this NVT case simply meant applying a slow isothermal compression once electrostatics and poling contributions were enabled, as the Lennard-Jones potential was kept purely repulsive throughout the simulations.

Despite the seeming simplicity of the approach, understanding the simulation results and how one could potentially achieve similar results in real world systems was not only far from trivial, as will be seen in chapter 7, but is also intricately linked to the development of the mathematical framework and rule set of the LoD method as presented in chapter 2.

3.3.1 TEMPERATURE ANNEALING VS. AVA

This section compares two strategies for breaking up a dense system, thermal annealing and isothermal compression as employed using the AVA method for NVT type systems.

Figure 3.3 displays the simulated, average chromophore loading, $N\langle\cos^3\theta\rangle$, under an external poling field of $100\frac{V}{\mu m}$ shown as a function of the dipole moment and number density for a system of 432 CLD-1 type single ellipsoids (see Appendix B for model parameters) averaged over the last 40 kcycles of sixteen individual runs spanning 240 kcycles.

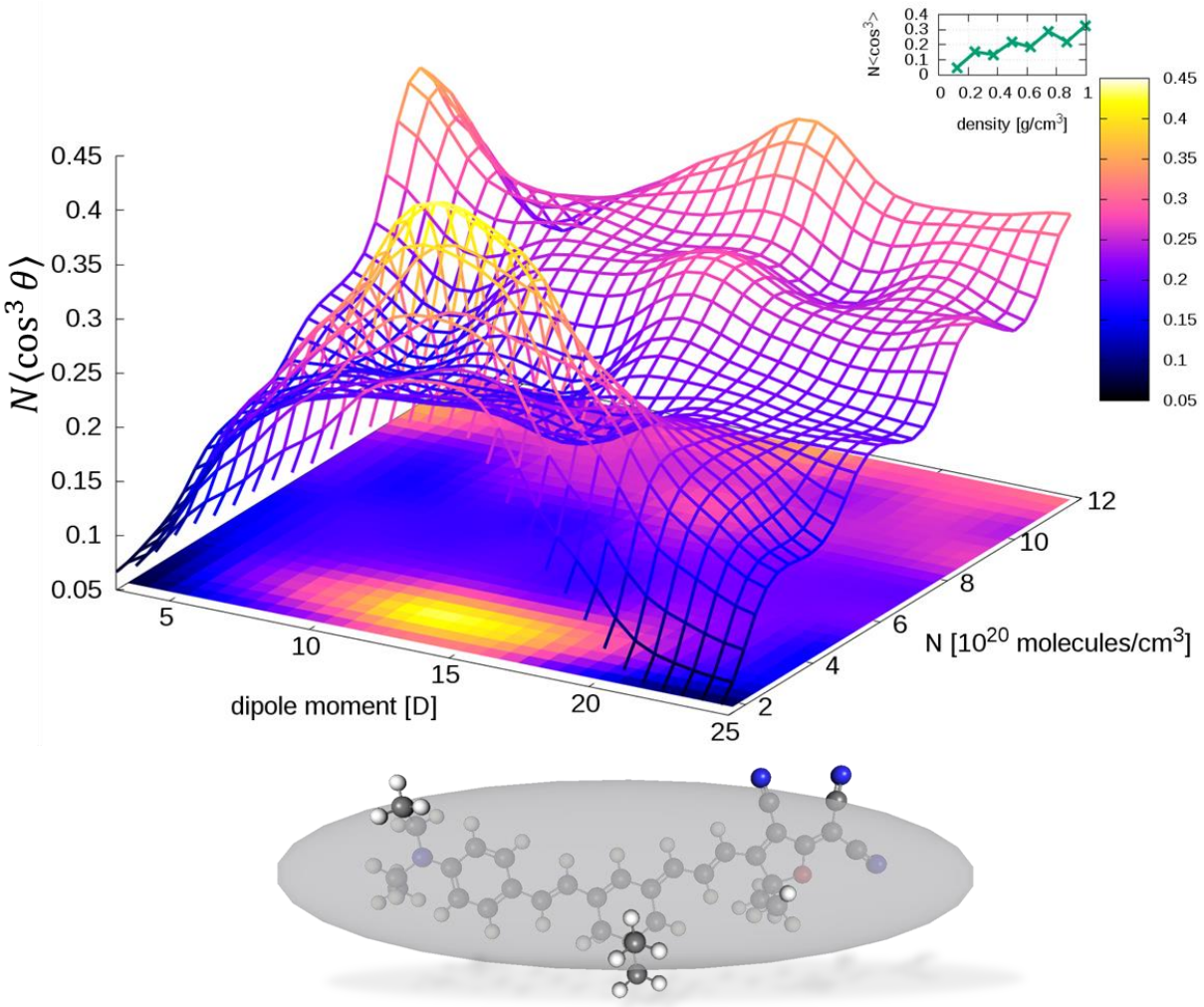

Figure 3.3: Thermally annealed CLD-1 type simulation results with single ellipsoid LoD model, shown is chromophore loading as a function of chromophore dipole moment and number density; Chromophore loading as a function of density is shown in the inset for simulations with a dipole moment of 25 D, corresponding to the experimentally expected dipole moment.

Thermal annealing was used for the first 20 kcycles of the initial randomization synchronously to adjusting the simulation volume from the initial placement volume of $15{,}747\ nm^3$ down to volumes corresponding to multiples of $364\ nm^3$, corresponding to a density of $1\ g/cc$, or a number density of $12 \cdot 10^{20}\ molecules/cc$, and a packing density of 72%.

Overall, there are a number of interesting features observed in the dependence of chromophore loading on the chromophore dipole moment and chromophore number density. Firstly, increased chromophore loading is indicated in the region characterized by dipole moments of $8 - 20\ Debye$ and number densities of $(1.5 - 3) \cdot 10^{20}\ molecules/cc$. This indicates dramatically increased acentric order because of the relatively low number density in this region, leading to the first design criterion for the development of improved EO materials: ***For a given chromophore size and shape, there is an optimal dipole moment that maximizes acentric order.*** Secondly, once the system density is increased close to a level corresponding to neat materials, chromophore loading recovers independently of the chromophore dipole moment and gets close to peak levels observed at lower densities. The inset in figure 3.3 showing linearly increasing chromophore loading as a function of density for the largest dipole moment further corroborates this, leading to another design criterion: ***System number density needs to be maximized as it can outperform an associated drop in acentric order.***

Those first two design criteria are not only supported by the information figure 3.3 provides. Figure 3.4 shows simulation results presented in identical fashion to figure 3.3 but using isothermal compression (AVA method for NVT ensembles). For these simulations, the initial randomization was kept at constant volume for 40 kcycles, and then the system was adjusted to identical values as uses previously using a smooth isothermal compression for 20 kcycles during the transition stage as outlined in figure 3.2.

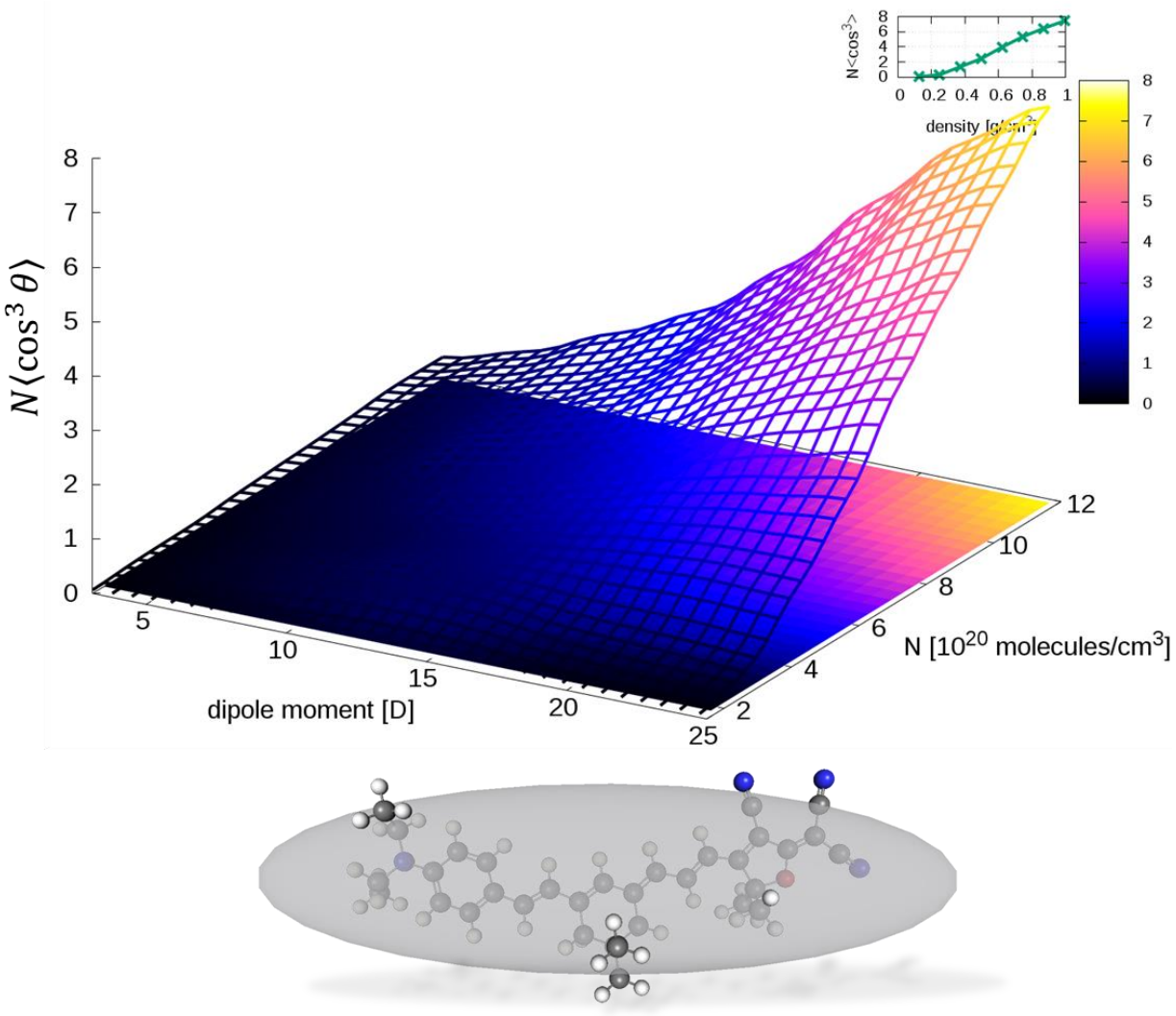

Figure 3.4: AVA method (isothermal compression) CLD-1 type simulation results with single ellipsoid LoD model, shown is chromophore loading as a function of chromophore dipole moment and number density; Chromophore loading as a function of density is shown in the inset for simulations with a dipole moment of 25 D, corresponding to the experimentally expected dipole moment.

A strong increase in chromophore loading can be observed when larger dipole moments and larger number densities are reached. This is attributed directly to a dramatic increase of average acentric order as shown in figure 3.5. Figure 3.5 compares the corresponding average acentric order values of thermally annealed and AVA method (isothermal compression) systems from figures 3.3 and 3.4.

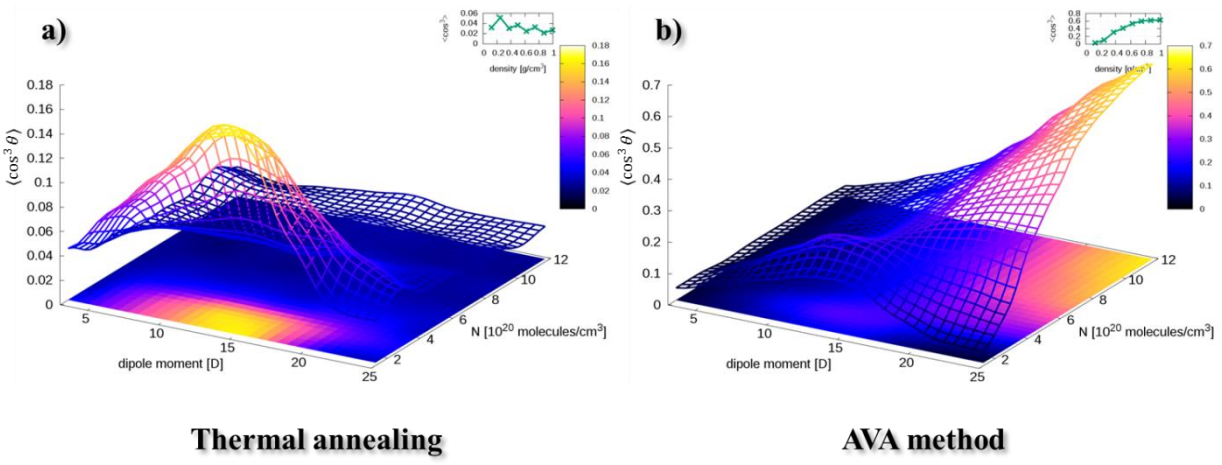

Figure 3.5: Thermally annealed and AVA method (isothermal compression) CLD-1 type simulation results with single ellipsoid LoD model, shown is average acentric order as a function of chromophore dipole moment and number density; Chromophore loading as a function of density is shown in the insets for simulations with a dipole moment of 25 D, corresponding to the experimentally expected dipole moment.

Interestingly, both methods display a similar acentric order peak at medium dipole strength and low number densities and also display very similar behavior at low number densities and dipole strengths. However, the AVA method system using isothermal compression (Figure 3.5b) exhibits strongly increased acentric order, exceeding Langevin order by about a factor of two, at strong dipole moments and high number densities compared to the thermally annealed system. At its highest number density and dipole moment the single-ellipsoid model is able to achieve a chromophore loading of about $8 \cdot 10^{20}\ molecules/cc$.

Which system is more realistic? Based on the energy differences between the mean energies of both methods and their associated confidence intervals at 95% confidence, displayed in figure 3.6, the AVA method (isothermal compression) simulation results are more likely, particularly in regions of strong dipole moments and high number densities with favorable energy differences as large as 45 NkT observed. Because of these strongly favorable energetic differences using the

AVA method it is expected that thermally annealed systems run with more computational cycles will eventually converge with the AVA results as can be seen for the TCP-Me system below. In all other regions, energetic differences well below 3 NkT are within their respective confidence intervals indicating already good overlap between AVA and thermal annealing.

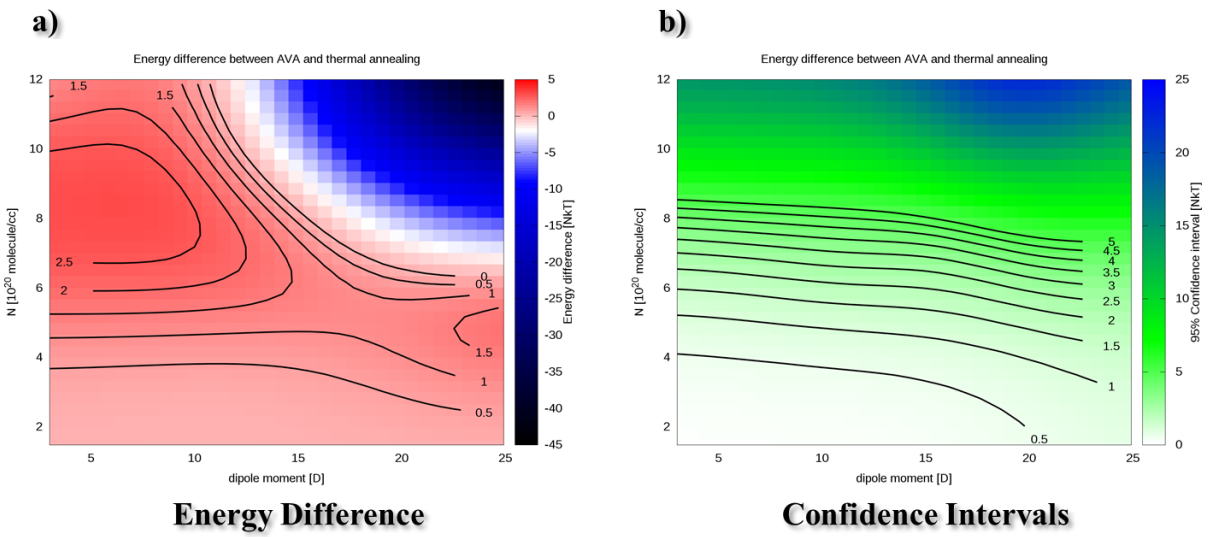

Figure 3.6: a) Energy difference and **b)** associated confidence intervals between simulation results of thermally annealed and AVA method (isothermal compression) CLD-1 type

In summary, volume adjustment not only opens up more configurational space compared to thermal annealing but it also achieves equilibrium results more quickly for dense, strongly dipolar systems as indicated by significantly lower energies at the end of two similar simulation series. Even though the single ellipsoid results were obtained under highly idealized conditions, such as no additional chromophore moieties needed for increased solubility or melting point temperature, it seems entirely possible to achieve "Hyper-Langevin" acentric order. However, these results are not easily transferable to systems with more realistic model representations as will be shown in the next two sections.

3.3.2 TWO-ELLIPSOID MODEL

The single ellipsoid model introduced in the previous chapter was able to achieve acentric order parameters and chromophore loading parameters which, if transferable to real systems, would lead to spectacular improvements of ONLO materials. However, experimental results of the chromophore type the single ellipsoid LoD model is derived from indicate much lower order parameters.

In order to test the dependence on the LoD model this section uses a two-ellipsoid model with otherwise identical simulation settings (repulsive LJ, NVT) using the AVA method as described in the previous section. In these simulations, a single charge and a point dipole corresponding to the underlying charge distribution were placed at each ellipsoid center and then scaled linearly to scale the overall dipole moment of the chromophores.

Figure 3.7 shows simulated chromophore loading results dependent on the overall chromophore dipole moment and system number density using the two-ellipsoid LoD model and the AVA method (isothermal compression).

The two-ellipsoid model maintains half the chromophore loading, $N\langle\cos^3\theta\rangle$, compared to the single ellipsoid LoD model results displayed in figure 3.4. This strong reduction in acentric order can be attributed to two factors: the broken symmetry of the bent, two-ellipsoid arrangement and the intricate orientation of dipole moments within the two ellipsoids. Furthermore, the previously observed peak around $8-20\ Debye$ and number densities of $(1.5-3)\cdot 10^{20}\ molecules/cc$ has shifted to larger values.

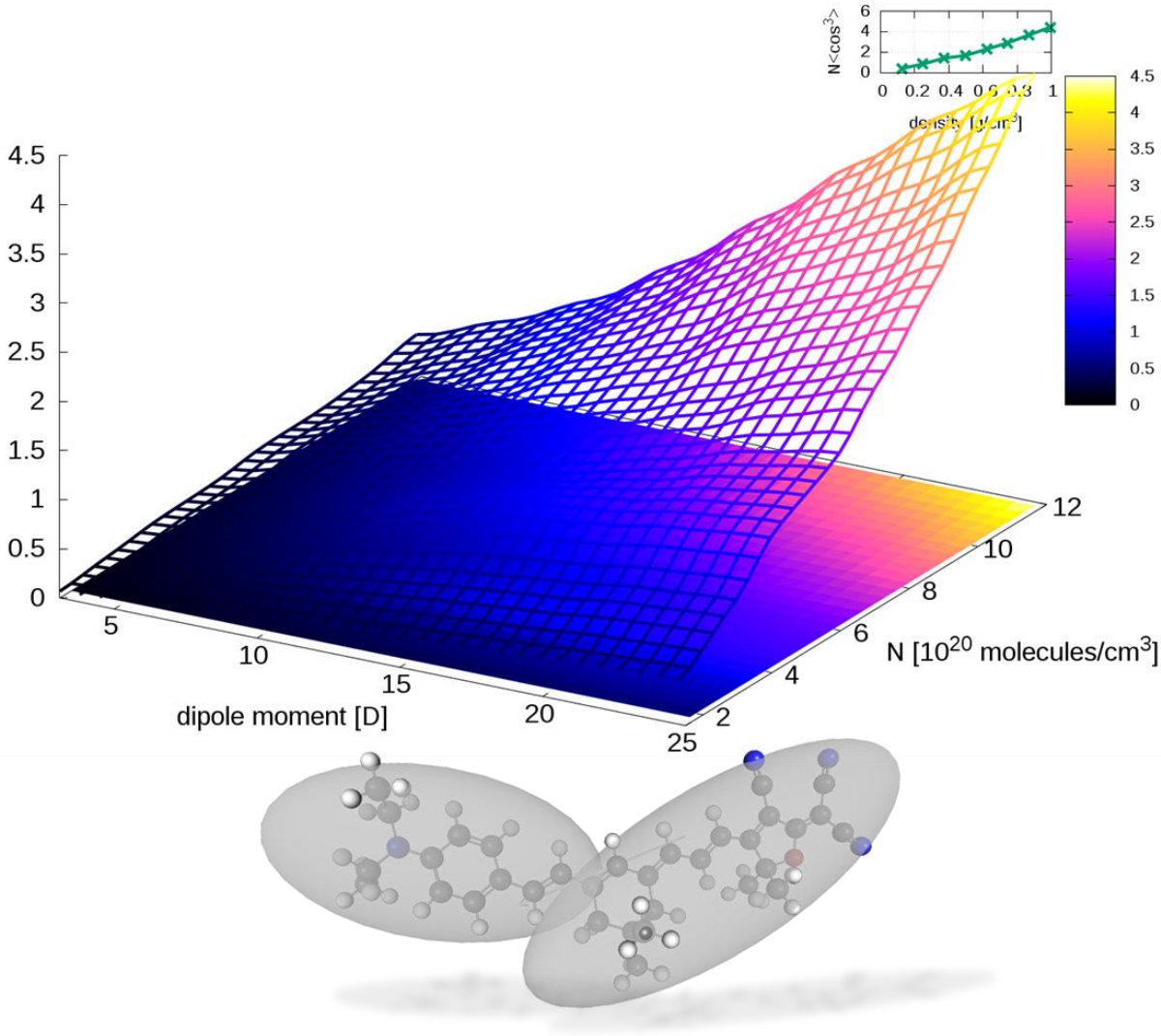

Figure 3.7: AVA method CLD-1 type simulation results with two-ellipsoid LoD model, shown is chromophore loading as a function of chromophore dipole moment and number density; inset shows trace of chromophore loading dependent on density at largest dipole moment, corresponding to the experimentally expected dipole moment

Figure 3.8 display the shifted peak at around $12 - 25\ Debye$ and number densities of $(3 - 5) \cdot 10^{20}\ molecules/cc$. Note that this peak shift, however, can be reversed to the original peak location of the single, dipolar ellipsoid by using a quadrupolar charge distribution inside both ellipsoids. This is another indication of the more complex electrostatics interactions of the dipole moments present in the two-ellipsoid model.

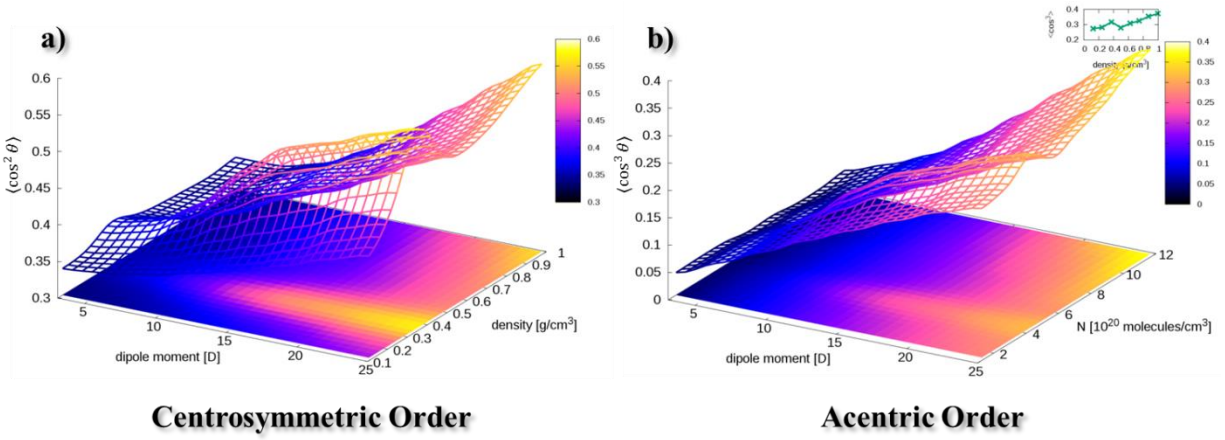

Figure 3.8: AVA method CLD-1 type simulation results with two-ellipsoid LoD model, shown is **a)** average centrosymmetric order and **b)** average acentric order as a function of chromophore dipole moment and number density; inset shows trace of average acentric order at largest dipole moment, corresponding to the experimentally expected dipole moment

Overall, the two-ellipsoid LoD model, while qualitatively providing similar results to the single ellipsoid model, strongly reduced overall acentric order by about a factor of two. Nonetheless, this model still displays acentric order (inset in figure 3.8b) roughly equal to the expected Langevin order and, at higher chromophore number densities, is even able to exceed Langevin order by about 20%. At the highest chromophore number density and a dipole moment corresponding to the experimentally expected dipole the chromophore loading of the two-ellipsoid model maximizes at about $4 \cdot 10^{20}\ molecules/cc$, with or without quadrupolar contributions to the electrostatics interactions.

As noted previously, in addition to the chromophore core, the model system studied here does not feature any additional moieties adding crucial material properties such as solubility or melting point temperature. Thus, the highest number density is about twice that of a realistic chromophore system with these moieties.

With knowledge of the number density of a real system featuring the CLD-1 type chromophore core, the results shown here can already serve as a very good estimator of lower chromophore density systems, such as chromophore systems in a host matrix. Although "fully discovered" in the discussions to chapter 5 and 6 simulation results, this already hints at a third design criterion: ***The chromophore core, particularly its size, shape, and dipole moment, is what fundamentally determines resulting chromophore loading.***

3.3.3 THREE-ELLIPSOID MODEL

This section introduces a three-ellipsoid LoD representation of the CLD-1 type chromophore core to compare against the single and two-ellipsoid systems. The two-ellipsoid LoD model discussed above resulted in acentric order lowered by about a factor of two compared to the single ellipsoid LoD model. However, the two-ellipsoid LoD model represents the underlying chromophore system better than a single ellipsoid whose perfect symmetry and point-dipole charge representation enabled the greatly enhanced chromophore loading results.

Figure 3.9 shows chromophore loading as a function of number density simulated using the three-ellipsoid LoD model of the CLD-1 type chromophore. The trace displayed was calculated using the largest dipole moment, corresponding to the experimentally expected dipole moment, calculated when using the single and two-ellipsoid LoD models as shown in the insets in figures 3.4 and 3.7.

The results closely match those of the two-ellipsoid LoD model. Although a small depression in overall chromophore loading can be observed, the two-ellipsoid and three-ellipsoid models are identical within their respective confidence intervals.

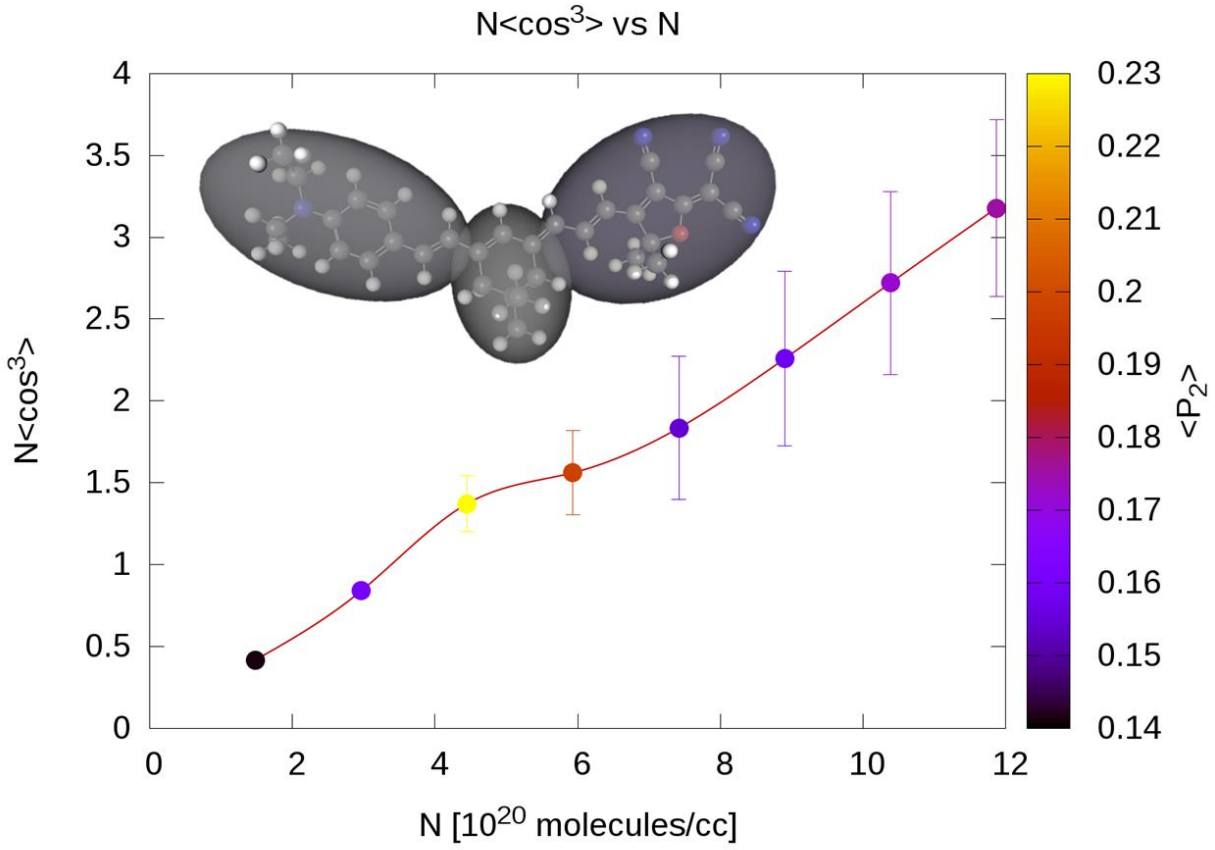

Figure 3.9: AVA method CLD-1 type simulation results with three-ellipsoid LoD model, shown is chromophore loading as a function of number density at experimentally expected dipole moment of about 25 $Debye$; data points are displayed with associated 95% confidence intervals and are color coded corresponding to $\langle P_2 \rangle$ values representing the amount of centrosymmetric order of these systems.

The observed quantitative overlap between the two and three-ellipsoid LoD models within their respective confidence intervals leads to the conclusion that the two-ellipsoid LoD model is the best representation of the CLD-1 type chromophore, as it represents the lowest number of ellipsoid needed to correctly capture the underlying behavior.

3.4 TCP-Me Chromophore Order Convergence

In this section, the average orientation of an ensemble of ONLO chromophores in a poling field, where θ is the angle between the chromophore's dipole moment and the field, is investigated. Figure 3.10 demonstrates that various methods for allowing the molecules to condense give different order parameters.

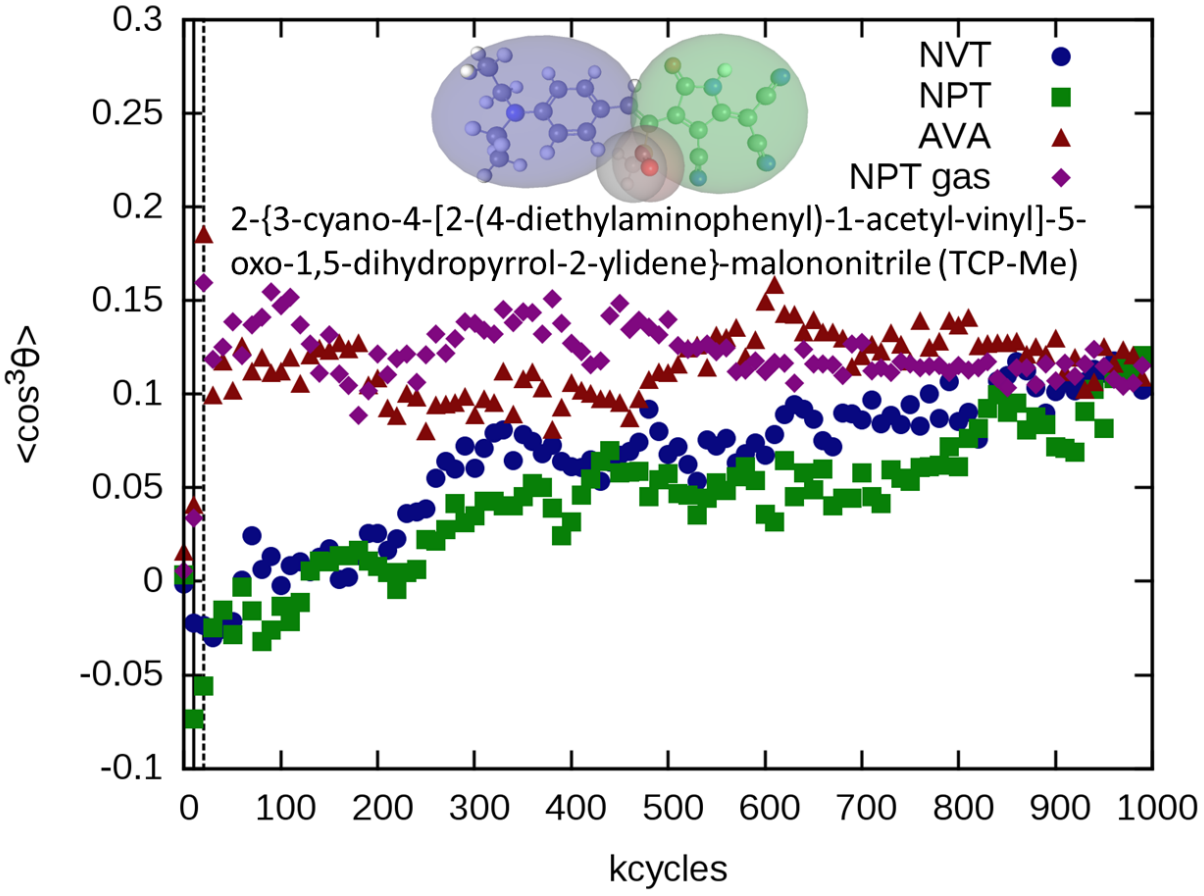

Figure 3.10: TCP-Me acentric order parameter $\langle \cos^3 \theta \rangle$ under a poling field of 100 $V/\mu m$ using four different methods: NVT, NPT (condensed and starting in the gas phase), and the adiabatic volume adjustment (AVA) method. The solid vertical line shows when the calculation is changed from LJ only to include charges and poling field. The dashed line indicates the end of AVA's transition region.

The initial fully-atomistic model was calculated using standard DFT packages with the B3LYP/6-31G(d) functional and CHELPG charges at atom locations in conjunction with OPLS-AA parameters for Lennard-Jones radii and energies of individual atoms. Bond distances are fixed and rotations are only permitted around single bonds.

When simulating poling under an external electric field, an interaction term for each molecule with the resulting internal field $V_{\mu E}(i) = -\overrightarrow{\mu_i} \cdot \vec{E}$ is introduced. While this energy term typically only amounts to about 1% of the total energy of the system it biases the simulation enough to reach overall acentric order (see in Figure 3.10). The calculations simulate the average acentric order of 108 TCP-Me chromophores[13,14] (shown in Figure 3.10) under a poling field of 100 V/μm as a progression of simulation cycles (each corresponding to 187 trial configurations) using NVT (77,964 Å^3 corresponding to the equilibrated NPT density of 0.9 g/cc), NPT (condensed and gas phase randomization states), and a novel variant on mixing NVT and NPT called the adiabatic volume adjustment (AVA) method. For an NPT simulation initial placement of molecules there is a critical separation distances above which the system will go into the gas phase if run with only the LJ potential, used in the initial randomization phase. As observable in figure 3.11, the system will usually condense once electrostatic interactions are enabled.

The number of wasted cycles while the system is in the gas phase can vary greatly. For this reason we use a new method we call adiabatic volume adjustment (AVA), which forces the system to condense under a controlled NVT simulation in which the volume is slowly, and smoothly reduced to a volume that gives a density around one sixth that of the final condensed density (1 gram/cc) while the attractive Lennard-Jones potential part is transitioned from off to fully on concurrently. At that point the simulation is switched to an NPT run, where the pressure is one atmosphere, and the system is allowed to finish condensing.

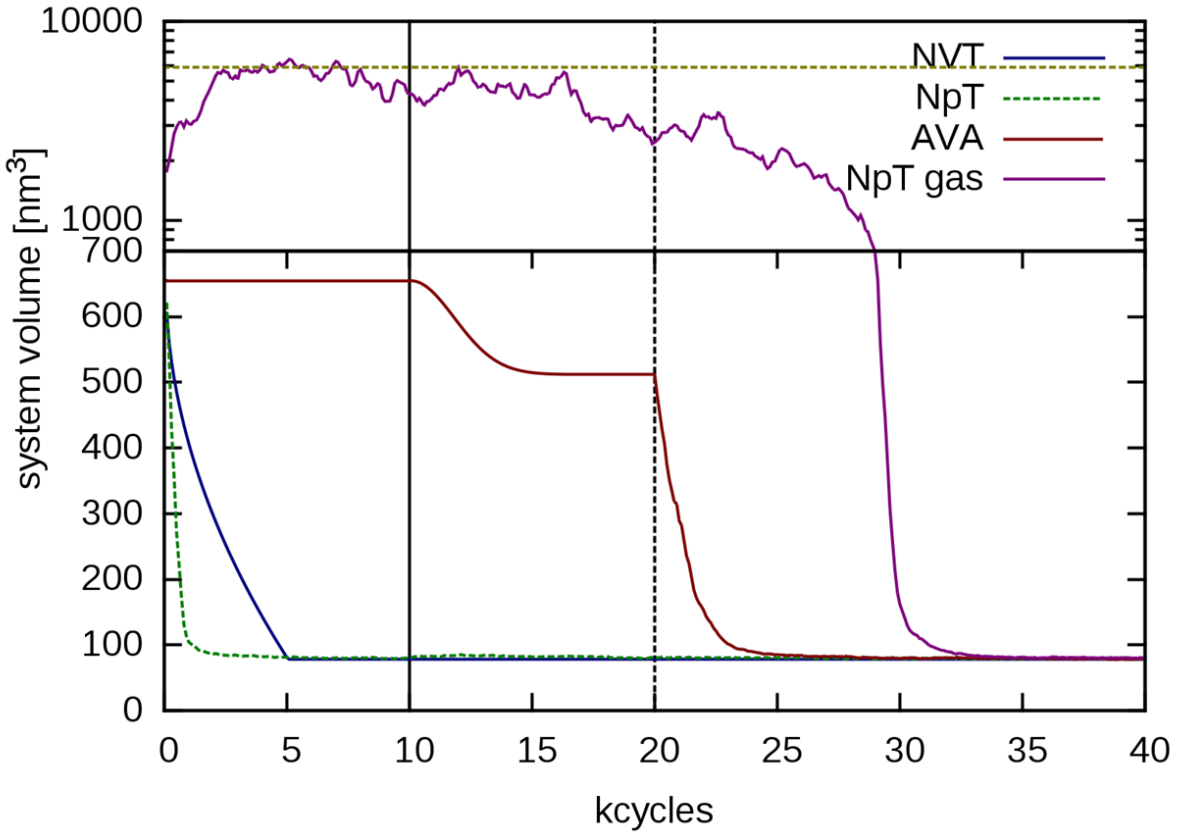

Figure 3.11: TCP-Me volume progression under a poling field of 100 $V/\mu m$ using four different methods: NVT, NPT (condensed and starting in the gas phase), and the adiabatic volume adjustment (AVA) method. The solid vertical line shows when the calculation is changed from LJ only to include charges and poling field. The dashed line indicates the end of AVA's transition region.

One observes (Figure 3.10) that for both NVT and NPT simulations which are condensed during the randomization phase (Lennard-Jones driven) the initial acentric order is fairly low after the total system energy reaches equilibrium around 100 kcycles as can be observed in figure 3.12.

Interestingly, this behavior is not due to unfavorable electrostatic energies compared to runs with larger acentric order but rather because of stronger centrosymmetric ordering (dipole pairing).

Furthermore, after around 1 million cycles both reach the acentric order obtained by the "gas phase" NPT and AVA method for TCP-Me. This indicates that total system energy convergence is **not** a good indication of order convergence.

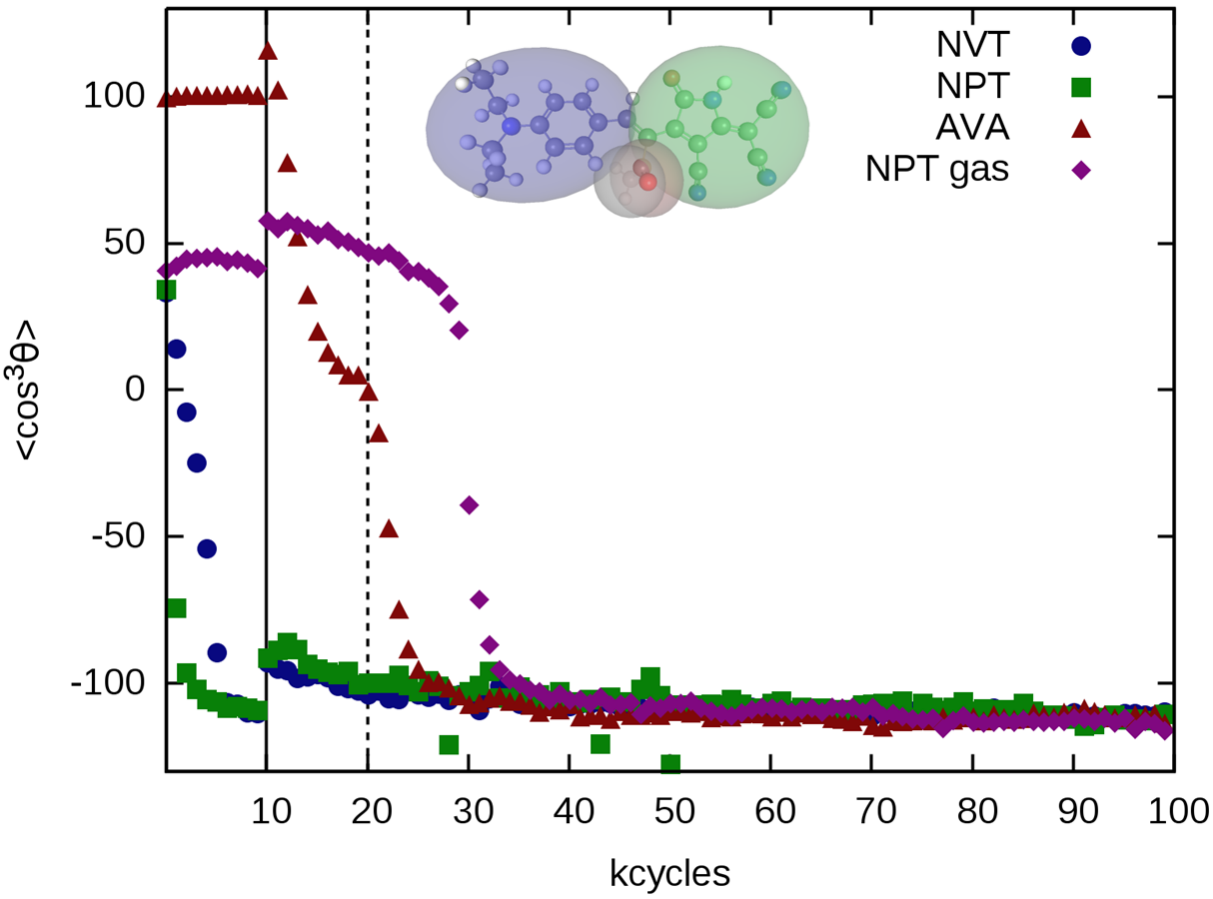

Figure 3.12: TCP-Me simulation energy convergence of the TCP-Me system using four different methods: NVT, NPT (condensed and starting in the gas phase), and the adiabatic volume adjustment (AVA) method. The solid vertical line shows when the calculation is changed from LJ only to include charges and poling field. The dashed line indicates the end of AVA's transition region.

For more complex chromophores, however, we have seen pure NPT simulations getting trapped in lower order configurations even in longer simulations. Use of the AVA method seems to assist in improving simulation convergence by avoiding these local energetic minima.

An interesting feature of simulations using AVA for NPT ensemble simulations are the system configurations exhibited due to the AVA transition stage. Figure 3.13 display a system snapshot of the TCP-Me NPT simulation using AVA as displayed in figure 3.10 and 3.11 taken at the end of the AVA transition at 20 kcycles.

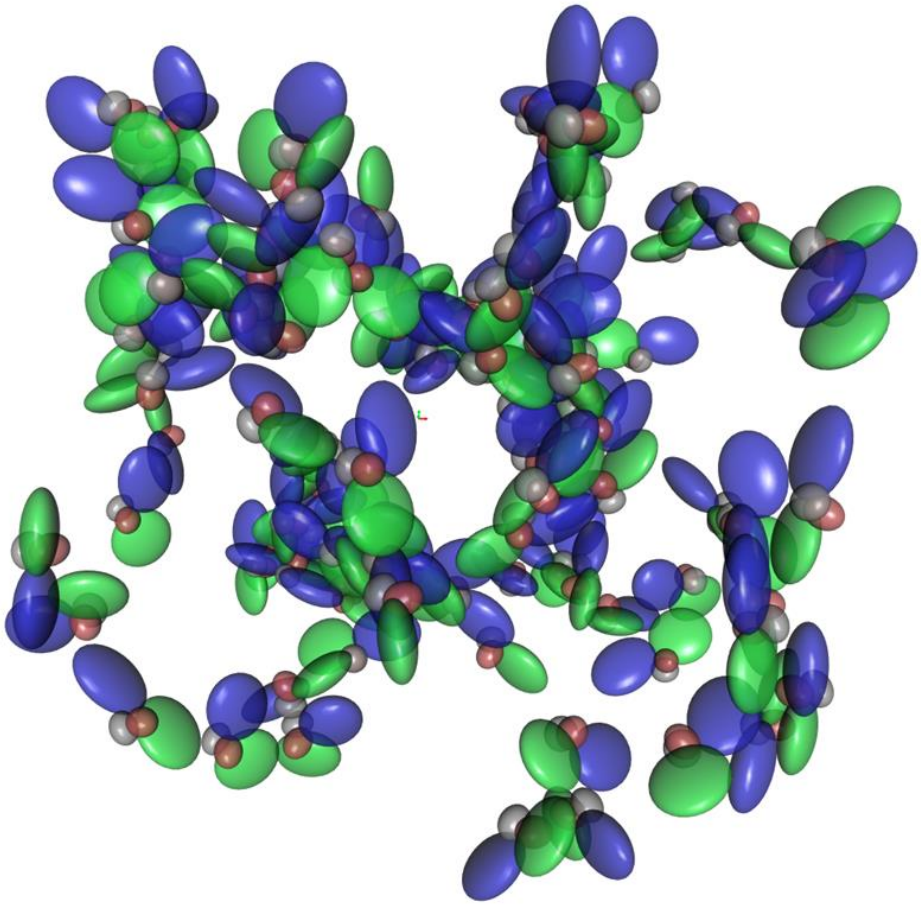

Figure 3.13: Snapshot of TCP-Me NPT simulation at the end of the AVA transition stage

Using AVA, the TCP-Me chromophores are self-assembled into a string-like arrangement akin to the expected arrangement for a plastic material. This string-like arrangement is not observed for the other simulation types displayed in figures 3.10 and 3.11. Particularly not for the "gas phase" NPT simulation which at a comparable volume in its simulation evolution displays partially stacked groups of three to four chromophores only loosely connected. This can be explained by

the much more rapid condensation – with no adjustment period at an intermediate volume – exhibited by the "gas phase" NPT simulation as shown in figure 3.11.

In summary, the type of order simulated in Figure 3.10 shows that the various MC equilibration methods will give similar answers in the very long limit, and that the AVA method converges fastest, making it the method of choice. Furthermore, the added control over the condensation behavior of the simulation system enabled through the AVA method can lead to system behavior akin to the behavior expected of plastic materials. The value of the acentric order parameter obtained for TCP-Me, around 0.13 is quite representative of many such ONLO chromophores. In conjunction with the observed number density of the TCP-Me system this represents a chromophore loading of $1.8 \cdot 10^{20}\ molecules/cc$.

3.5 CONCLUSIONS

The adiabatic volume adjustment (AVA) method is a novel method aimed at improving system convergence by improving simulation configuration space sampling and overcoming local energetic barriers. The AVA method adjusts the simulation volume in a controllable manner while concurrently adjusting the attractive contribution of the Lennard-Jones potential.

For otherwise identical systems, it was shown that volume adjustment not only opens up more configurational space compared to thermal annealing but it also achieves equilibrium results more quickly for dense, strongly dipolar systems as indicated by significantly lower equilibrium energies.

A first set of three ONLO chromophore design criteria, based on simulation results using different CG LoD representations of a CLD-1 type chromophore system, was discovered. Those criteria will be summarized in Chapter 7. Furthermore, it was established that for the simulation of CLD-type chromophores the minimum number of ellipsoid accurately representation the chromophore core behavior is two.

The simulation of a novel chromophore system type using the TCP acceptor, TCP-Me, was conducted with traditional NVT and NPT approaches and compared to results obtained using the AVA method. The AVA method converged fastest, making it the method of choice. It was found that equilibrium energy convergence did not equal order convergence. Furthermore, the added control over the condensation behavior of the simulation system enabled through the AVA method lead to a string-like arrangement akin to the expected arrangement for a plastic material not observable in the simulations using the traditional NVT and NPT approaches.

3.6 ACKNOWLEDGEMENTS

This chapter is partially based upon work supported by the National Science Foundation under Grant Numbers (DMR-1303080, DMR-0905686, and DMR-0120967). Any opinions, findings, and conclusions or recommendations expressed in this material are those of the author(s) and do not necessarily reflect the views of the National Science Foundation. The authors would like to thank Bruce E. Eichinger for the helpful discussion on the project. The authors also acknowledge partial financial support from the Air Force Office of Scientific Research (FA9550-10-1-0558, FA9550-09-1-0682).

3.7 REFERENCES FOR CHAPTER 3

[1] Allen, M. P.; Tildesley, D. J. *Computer Simulation of Liquids*; Clarendon Press ; Oxford University Press: Oxford [England]; New York, 1989.

[2] Kirkpatrick, S.; Gelatt, C. D.; Vecchi, M. P. Optimization by Simulated Annealing. *Science* **1983**, *220* (4598), 671–680.

[3] Kawai, H.; Kikuchi, T.; Okamoto, Y. A Prediction of Tertiary Structures of Peptide by the Monte Carlo Simulated Annealing Method. *Protein Eng.* **1989**, *3* (2), 85–94.

[4] *Numerical Recipes in C: The Art of Scientific Computing*, 2nd ed.; Press, W. H., Ed.; Cambridge University Press: Cambridge ; New York, 1992.

[5] Swendsen, R. H.; Wang, J.-S. Replica Monte Carlo Simulation of Spin-Glasses. *Phys. Rev. Lett.* **1986**, *57* (21), 2607–2609.

[6] Hukushima, K.; Nemoto, K. Exchange Monte Carlo Method and Application to Spin Glass Simulations. *J. Phys. Soc. Jpn.* **1996**, *65* (6), 1604–1608.

[7] Falcioni, M.; Deem, M. W. A Biased Monte Carlo Scheme for Zeolite Structure Solution. *J. Chem. Phys.* **1999**, *110* (3), 1754–1766.

[8] Torrie, G. M.; Valleau, J. P. Nonphysical Sampling Distributions in Monte Carlo Free-Energy Estimation: Umbrella Sampling. *J. Comput. Phys.* **1977**, *23* (2), 187–199.

[9] Kumar, S.; Rosenberg, J. M.; Bouzida, D.; Swendsen, R. H.; Kollman, P. A. THE Weighted Histogram Analysis Method for Free-Energy Calculations on Biomolecules. I. The Method. *J. Comput. Chem.* **1992**, *13* (8), 1011–1021.

[10] Frenkel, D.; Smit, B. *Understanding Molecular Simulation: From Algorithms to Applications*; Academic Press, 2001.

[11] Benight, S. J.; Johnson, L. E.; Barnes, R.; Olbricht, B. C.; Bale, D. H.; Reid, P. J.; Eichinger, B. E.; Dalton, L. R.; Sullivan, P. A.; Robinson, B. H. Reduced Dimensionality in Organic Electro-Optic Materials: Theory and Defined Order. *J. Phys. Chem. B* **2010**, *114* (37), 11949–11956.

[12] Dalton, L. R.; Benight, S. J.; Johnson, L. E.; Knorr, D. B.; Kosilkin, I.; Eichinger, B. E.; Robinson, B. H.; Jen, A. K.-Y.; Overney, R. M. Systematic Nanoengineering of Soft Matter Organic Electro-Optic Materials. *Chem. Mater.* **2011**, *23* (3), 430–445.

[13] Rawal, M. Cross-Conjugated Moieties as Design Motifs for a Class of Novel Electro-Optic Chromophores, University of Washington, 2013.

[14] Rawal, M.; Garrett, K.; Tillack, A. F.; Kaminsky, W.; Jucov, E.; Shelton, D. P.; Timofeeva, T. V.; Eichinger, B. E.; Robinson, B. H.; Dalton, L. R. Cross-Conjugation as a Motif for Organic Non-Linear Optical Molecules. In *Symposium II/JJ/KK – Materials, Processes and Devices for Nanophotonics, Nonlinear Optics and Resonant Optics*; MRS Online Proceedings Library; 2014; Vol. 1698.

[15] Zhang, C.; Dalton, L. R.; Oh, M.-C.; Zhang, H.; Steier, W. H. Low V_π Electrooptic Modulators from CLD-1: Chromophore Design and Synthesis, Material Processing, and Characterization. *Chem. Mater.* **2001**, *13* (9), 3043–3050.

4 DIELECTRIC BEHAVIOR OF SMALL MOLECULES AND COMPLEX CHROMOPHORE SYSTEMS

4.1 INTRODUCTION

Quantitative ab initio computation of a material's dielectric response remains a challenging problem. At present, computer simulations are typically limited to system sizes well below the number of molecules needed to exhibit bulk behavior. Thus, electrostatics interactions can effectively only be of short or medium range and long-range interactions with the bulk of the material have to be modeled.

In general, long-range electrostatic models can be categorized broadly by their use of either Ewald sums[1] or a reaction field[2]. Ewald summation and related lattice methods, because of their computational efficiency and good accuracy compared to direct summation, have found widespread acceptance. However, lattice summation methods can impose artificial periodicity on inherently non-periodic systems.[3–7]

In this chapter, an alternative approach to Ewald sums – the use of a reaction field – is introduced. The reaction field approach is based on Onsager's reaction field[2] in the formulation of Barker and Watts[8] and was previously implemented for dipolar, ellipsoidal systems.[9,10] Its underlying concept of image dipoles in an infinite, continuous dielectric medium is then applied to discrete charge distributions and extended for use with non-neutral reaction spheres. The enhanced reaction field approach can be used with models containing discrete charges as used in the LoD method (see Chapter 2) and with net-neutral systems containing ionic contributions.

4.2 DETERMINATION OF DIELECTRIC CONSTANTS

Maxwell's equations teach us that the behavior of a linear, isotropic material[1] in an external electric field $\vec{E}$ gives rise to an electric displacement field $\vec{D} = \varepsilon\vec{E}$ in cgs-units[2] proportional to the external field by the dielectric constant ε. The displacement field is connected to the materials polarization density $\vec{P}$ and the external field as

$$\vec{D} = \varepsilon\vec{E} = \vec{E} + 4\pi\vec{P} \tag{4-1}$$

In a net-neutral system, the polarization density $\vec{P}$ can be expressed by the average total dipole moment $\langle\vec{M}\rangle$ calculated from point charges q_i at their respective locations $\vec{r}_i$ and dipole moments $\vec{\mu}_j$ and divided by the system volume V:

$$\vec{P} = \frac{\langle\vec{M}\rangle}{V} = \frac{\langle\sum_i q_i\vec{r}_i + \sum_j \vec{\mu}_j\rangle}{V} \tag{4-2}$$

If the external electric field is known the dielectric constant ε can be computed directly upon rearrangement of equations (4-1) and (4-2):

$$\begin{gathered}(\varepsilon - 1)\vec{E} = 4\pi\vec{P} \\ \Rightarrow \varepsilon = \frac{4\pi}{V}\frac{\langle\vec{M}\rangle\cdot\vec{E}}{E^2} + 1 = \frac{4\pi}{V}\frac{\langle M\rangle_E}{E} + 1\end{gathered} \tag{4-3}$$

Here E is the magnitude of the external field and $\langle M\rangle_E = \langle\vec{M}\rangle\cdot\hat{E}$ is the average total dipole moment in the direction of the external field.

[1] In a linear, anisotropic material permittivities are expressed as tensors rather than scalars. Scalar permittivities can be used even for ONLO materials with in general tensorial, non-linear permittivities under the condition that electric field interactions are in the static limit and in one direction only (i.e. an external poling field).

[2] For dielectric constants the cgs-unit system equations are beneficial. SI units introduce an additional complication with the vacuum permittivity ε_0 such that $\varepsilon = \varepsilon_r\varepsilon_0$, with the dielectric constant now ε_r.

Using equation (4-3), the dielectric constant could also be obtained for two slightly different external field strengths E and $E + \delta$:

$$(\varepsilon - 1)\delta = 4\pi(P_{E+\delta} - P_E) = \frac{4\pi}{V}(\langle M\rangle_{E+\delta} - \langle M\rangle_E) \tag{4-4}$$

In order to solve this equation it is necessary to write $\langle M\rangle_E$ as a statistical mechanical average

$$\langle M\rangle_E = \frac{\int e^{-\beta H_0} e^{-\beta V_{ME}} M_E d\Omega}{\int e^{-\beta H_0} e^{-\beta V_{ME}} d\Omega} = \frac{\int P_0 e^{\beta E_0 M_E} M_E d\Omega}{\int P_0 e^{\beta E_0 M_E} d\Omega} \tag{4-5}$$

Here, $P_0 = e^{-\beta H_0}$ with $\beta = \frac{1}{kT}$ is the system probability based on the Hamiltonian with no external field contributions, the interaction energy between the total dipole moment in the direction of the local field, M_E, and the local field is given by $V_{ME} = -E_0 M_E$. For a system embedded in a dielectric continuum with dielectric ε_S the local field $\vec{E}_0$ acting on the system's dipole moments is given by[11]

$$\vec{E}_0 = L_f \vec{E} = \frac{2\varepsilon_S + \varepsilon}{2\varepsilon_S + 1}\vec{E} \tag{4-6}$$

Here, L_f represents the field factor between local and external electric field. A distinction is made between ε_S and ε, the calculated dielectric constant of the simulation system. This allows ε_S to be set to a particular, fixed value in order to bias a simulation. Typically, we apply the self-consistency condition $\varepsilon_S = \varepsilon$ leading the field factor in equation (4-6) to be the Lorentz field factor $L_f = \frac{3\varepsilon}{2\varepsilon+1}$. This approach requires recalculation of ε during a simulation. A series expansion of $e^{\beta(E_0+\delta_0)M_E}$ around $\delta_0 = 0$ truncated after the first two terms yields

$$e^{\beta(E_0+\delta_0)M_E} \approx e^{\beta E_0 M_E}(1 + \beta\delta_0 M_E) \tag{4-7}$$

Note that M_E is shorthand for the total dipole moment in the direction of the external field, independent of the field's magnitude.

Thus, the following statistical average for $\langle M\rangle_{E+\delta}$ is obtained

$$\langle M\rangle_{E+\delta} = \frac{\int P_0 e^{\beta E_0 M_E}(1+\beta\delta_0 M_E)M_E d\Omega}{\int P_0 e^{\beta E_0 M_E}(1+\beta\delta_0 M_E)\, d\Omega} = \frac{\langle M\rangle_E + \beta\delta_0\langle M^2\rangle_E}{1+\beta\delta_0\langle M\rangle_E} \tag{4-8}$$

Combining equations (4-4), (4-5), (4-6), and (4-8) gives the desired solution:

$$\frac{(\varepsilon-1)(2\varepsilon_S+1)}{2\varepsilon_S+\varepsilon}\delta = \frac{4\pi}{V}\beta\delta\frac{\langle M^2\rangle_E - \langle M\rangle_E^2}{1+\beta\delta_0\langle M\rangle_E} \tag{4-9}$$

Note that there is no more dependency on the value of the electric field E.

In the limit of $\delta, \delta_0 \to 0$ but with a finite external field magnitude E equation (4-9) is

$$\frac{(\varepsilon-1)(2\varepsilon_S+1)}{2\varepsilon_S+\varepsilon} = \frac{4\pi}{VkT}(\langle M^2\rangle_E - \langle M\rangle_E^2) \tag{4-10}$$

With no external electric field, $E = 0$, the dipole moment averaging in equations (4-5) and (4-8) is over all three space directions thus an additional normalization factor of $1/3$ is needed

$$\frac{(\varepsilon-1)(2\varepsilon_S+1)}{2\varepsilon_S+\varepsilon} = \frac{4\pi}{3VkT}(\langle M^2\rangle_0 - \langle M\rangle_0^2) \tag{4-11}$$

This result is similar to Kirkwood's[12] and Fröhlich's[13] extension to Onsager's approach.[2] Equation (4-11) has been employed in previous publications.[9,10] Note that for a system not in an external field the average polarization typically vanishes, hence $\langle M\rangle_0 = \langle M\rangle_0^2 = 0$.

The approach leading to equation (4-10) came from Bruce H. Robinson in December 2014 and has not been used previously, however, as the direct calculation method of equation (4-3) was employed instead. This chapter's section on poled (in an external field) and unpoled YLD124 systems will make first use of it.

In order for the values of the dielectric constants obtained from these formulations to be self-consistent with the simulation conditions a mechanism needs to exist to allow for dielectric

effects to influence the long-range interactions of molecules in the simulation. This mechanism is given by the reaction field which models long-range dipolar energy contributions with a dielectric continuum.

4.3 KIRKWOOD-ONSAGER REACTION FIELD APPROACH

Figure 4.1 shows the scenario envisioned by Onsager[2] and Kirkwood.[12] A dipole, $\vec{\mu}_i$, at the center of a spherical cavity of radius R_c embedded in an infinite dielectric continuum directly interacts with all other dipoles $\vec{\mu}_j$ in the cavity ***and*** with the image dipole of the total dipole moment of the cavity located on the boundary between the spherical cavity and the dielectric continuum in a direction perpendicular to $\vec{\mu}_i$.

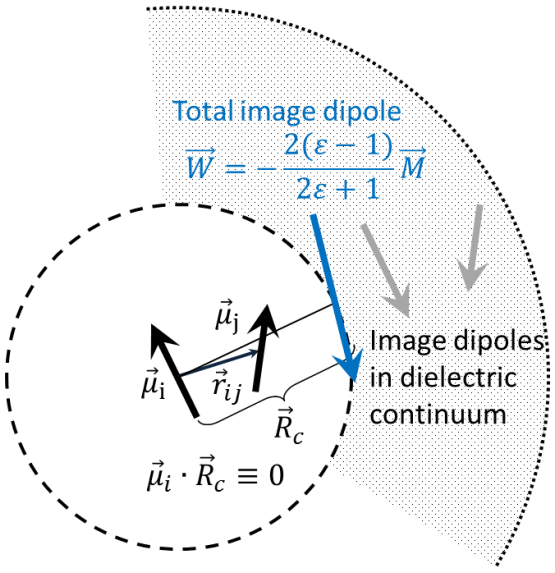

Figure 4.1: Dipole-dipole interaction with reaction field

Based on the interaction of a dipole $\vec{\mu}_i$ with the electric field created by another dipole $\vec{\mu}_j$ separated by a distance $\vec{r}_{ij}$ (following Griffiths[14]), the pairwise dipole-dipole potential energy is given by the expression:

$$V_{ij}^{\mu\mu} = -\vec{\mu}_{\mathrm{i}} \cdot \vec{E}_{\mu_j} = -k\vec{\mu}_{\mathrm{i}} \cdot \frac{3\left(\vec{\mu}_{\mathrm{j}} \cdot \hat{r}_{ij}\right) \cdot \hat{r}_{ij} - \vec{\mu}_{\mathrm{j}}}{r_{ij}^3} \tag{4-12}$$

Here, k is a unit-system dependent proportionality constant, in cgs-units it is one while in SI-units $k = \frac{1}{4\pi\varepsilon_0}$. Note that when either dipole is aligned in such a way that the vector between them is perpendicular to either dipole the interaction energy reduces to $k\vec{\mu}_{\mathrm{i}}\vec{\mu}_{\mathrm{j}}/r_{ij}^3$.

Applied to the situation envisioned by Onsager, the electric field of the cavity, $\vec{E}_c$, created by the total dipole moment $\vec{M}$ inside and at the boundary of the cavity can be calculated as:

$$\vec{E}_c = -k\frac{\vec{M}}{R_c^3} \tag{4-13}$$

The polarization density with the dipolar cavity field diminished by $1/\varepsilon$ at the continuum boundary[3] inside the dielectric continuum can then be calculated using equation (4-3):

$$\vec{P}_c = \frac{1}{4\pi}\frac{\varepsilon - 1}{\varepsilon}\vec{E}_c \tag{4-14}$$

The corresponding electric field, $-\frac{\vec{P}_c V}{r'^3}$, with r' as the distance from the field, then acts back on the cavity. Evaluated at the center of the cavity using equation (4-6), with $r' = R_c$ and using the volume of the cavity, $= \frac{4\pi}{3}R_c^3$, this becomes the electric field interacting with the dipole at the center of the cavity:

$$\vec{E}_{RF} = -\frac{3\varepsilon}{2\varepsilon + 1}\frac{\vec{P}_c V}{R_c^3} = -\frac{3\varepsilon}{2\varepsilon + 1}\frac{1}{4\pi}\frac{\varepsilon - 1}{\varepsilon}\vec{E}_c\frac{4\pi}{3}\frac{R_c^3}{R_c^3} = k\frac{\varepsilon - 1}{2\varepsilon + 1}\frac{\vec{M}}{R_c^3} \tag{4-15}$$

Compared to Onsager's derivation this field seems to be missing a factor of two. Onsager uses the electric potential Φ in the derivation of his results, while the above derivation uses electric

[3] The boundary condition is $\vec{E}_c(cavity) = \varepsilon\vec{E}_c(continuum)$ because the displacements must be equal and the cavity dielectric is taken to be one.

fields. The electric field is defined as the negative gradient of the electric potential, $\vec{E} = -\nabla\Phi$. This means that for the derivation above, once the potential energy is calculated with the $1/r^3$ electric field dependence of dipoles the resulting potential energy is going to be a factor of $1/2$ smaller than expected. With this in mind, in the SI-unit system the interaction potential using the dipolar reaction field is then:

$$V_{RF} = -\frac{1}{4\pi\varepsilon_0}\frac{2(\varepsilon-1)}{2\varepsilon+1}\frac{\vec{\mu}_{\mathrm{i}}\cdot\vec{M}}{R_c^3} \tag{4-16}$$

The method of images is a powerful tool in electrostatics which replicates the same electrostatic boundary conditions and typically allows for an easier representation of the problem at hand, particularly for discrete charge distributions. The reaction field potential energy (4-16) could also be interpreted as the interaction of the center dipole with an image dipole, $\vec{W}$, located on the surface of the cavity in a direction perpendicular to the center dipole as displayed in figure 4.1:

$$\vec{W} = -\frac{2(\varepsilon-1)}{2\varepsilon+1}\vec{M} \Rightarrow V_{\mu W} = k\frac{\vec{\mu}_{\mathrm{i}}\cdot\vec{W}}{R_C^3} = -\frac{1}{4\pi\varepsilon_0}\frac{2(\varepsilon-1)}{2\varepsilon+1}\frac{\vec{\mu}_{\mathrm{i}}\cdot\vec{M}}{R_c^3} \tag{4-17}$$

A similar electrostatic boundary to that found in the reaction sphere cavity embedded in a dielectric is that of an insulated, conducting sphere. Then, the image dipole $\vec{M}'$ and its location $\vec{r}'$ from the center dipole $\vec{\mu}_{\mathrm{i}}$ inside the cavity can be written as:

$$\vec{M}' = -\frac{R_c^3}{r_{ij}^3}\vec{M} \quad \text{located at} \quad \vec{r}' = \frac{R_c^2}{r_{ij}}\hat{r}_{ij} \tag{4-18}$$

Applying Gauss' law[4] to the dipole's equivalent charge distribution (see the next section for more details) one can obtain the apparent image dipole on the surface of the cavity as:

$$\vec{W} = -\frac{R_c^3}{r_{ij}^3}\vec{M} \cdot \frac{R_c^3}{\left(R_c^2/r_{ij}\right)^3} = -\vec{M} \tag{4-19}$$

Comparing equations (4-17) and (4-19) reveals that they are identical apart from the factor:

$$\kappa = \frac{2(\varepsilon - 1)}{2\varepsilon + 1} \tag{4-20}$$

This indicates that there may be a correspondence between the method of images and the reaction sphere cavity embedded in a dielectric. This notion is used in the next section in order to extend the reaction field approach to point charges.

4.4 Reaction Field Extension to Point Charges

The reaction field potential (4-16) introduced in the previous section is so far only valid for dipoles. Most model systems such as fully-atomistic models and LoD ellipsoids, in general make use of discrete point charges. It is thus necessary to extend the reaction field approach to include a comparable treatment for point charges inside the cavity.

The approach is to use the method of images as introduced in the previous section on point charges present inside the cavity. Unlike in the dipolar case, those image charges will typically behave rather complex, forming a line charge, [15–18] due to the dielectric continuum. To get around this problem, image charges are positioned as if the dielectric continuum is merely a uniformly charged insulator and the cavity a conductor, like in the previous example for the

[4] In the dipolar case one could also simply let the center dipole and image dipole interact and obtain the correct reaction field interaction potential.

image dipole. The thus obtained image charges are then moved onto the cavity boundary, using Gauss' law for uniformly charged spheres[5], between the cavity and the dielectric which is where they would physically reside if the cavity were a conductor.

By avoiding the dielectric continuum in this way, the complex line charge inside the dielectric will be collapsed into a single charge on the boundary. By correspondence, the factor representing the dielectric continuum is given in Onsager's dipolar solution. It is not obvious that this approach will lead to similar results when charges, instead of dipoles, are employed. Therefore, the validity of this approach is then tested by comparing the reaction field potential energies using dipoles and equivalent charge distributions.

There are three additional scenarios to the dipole-dipole interactions given in equation (4-16) when extending the dipolar reaction field interaction to encompass both charges and dipoles: 1) charge-charge interactions, 2) dipole-charge interactions, and 3) charge-dipole interactions.

Figure 4.2 displays the first scenario, charge-charge interactions, of a cavity composed of a charge at the center, q_i, and an additional charge, q_j, located at a distance r_{ij} from the center.

[5] This assumes that overall, image charges will be uniformly distributed in the insulating dielectric continuum.

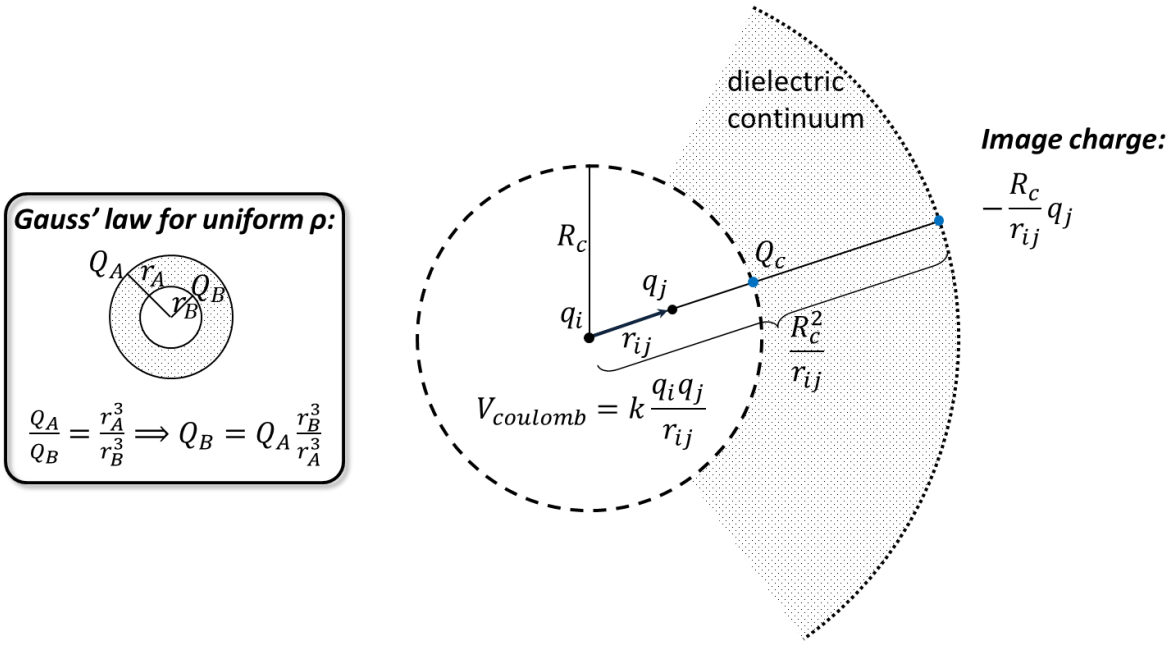

Figure 4.2: Charge-charge interaction with reaction field

The image charge due to the charge q_j has the following magnitude and location:

$$q_j' = -\frac{R_c}{r_{ij}} q_j \quad \text{at} \quad \vec{r}\,' = \frac{R_c^2}{r_{ij}} \hat{r}_{ij} \tag{4-21}$$

Using Gauss' law this turns into a boundary charge at location R_c of:

$$Q_c = -\frac{R_c}{r_{ij}} q_j \frac{R_c^3}{\left(\frac{R_c^2}{r_{ij}}\right)^3} = -q_j \frac{r_{ij}^2}{R_c^2} \tag{4-22}$$

As mentioned previously for Onsager's dipolar case the factor representing the influence of the dielectric continuum involves an additional factor of two which needs to be removed for reaction field interactions involving charges. Furthermore, an additional minus sign is needed for image charge interactions in order to correctly represent the dipolar field behavior (reaction field interaction is negative with dipolar charges pointed in the same direction). The reaction field

interaction potential then is obtained by multiplying the image charge interaction with a factor of $-{}^{1}/_{2}$ compared:

$$V_{RF}^{qq} = -\frac{1}{2}V_{image}^{qq} = \frac{1}{4\pi\varepsilon_0 n^2}\frac{\varepsilon_{RF}-n^2}{2\varepsilon_{RF}+n^2}q_i q_j \frac{r_{ij}^2}{R_c^3} \tag{4-23}$$

The total interaction potential of two charges in the cavity is then:

$$V_{ij}^{qq} = \frac{q_i q_j}{4\pi\varepsilon_0 n^2}\left(\frac{1}{r_{ij}} + \frac{\varepsilon_{RF}-n^2}{2\varepsilon_{RF}+n^2}\frac{r_{ij}^2}{R_c^3}\right) \tag{4-24}$$

The next scenario, dipole-charge interaction, with a dipole $\vec{\mu}_i$ at the center and a charge q_j located at a distance r_{ij} from the center is illustrated in figure 4.3.

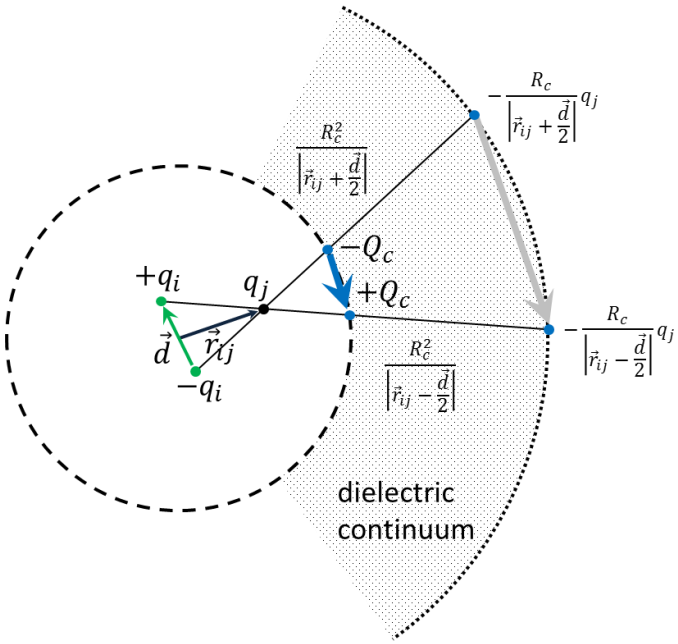

Figure 4.3: Dipole-charge image charge energy derivation

In order to derive the reaction field potential the dipole is first represented by two charges of magnitude q_i with opposite signs separated by an infinitesimally small distance $\vec{d}$.

This will create two image charges due to q_j with the following magnitudes and locations:

$$q_j' = -\frac{R_c}{\left|\vec{r}_{ij} \pm \frac{\vec{d}}{2}\right|} q_j \quad \text{at} \quad \vec{r}\,' = \frac{R_c^2}{\left|\vec{r}_{ij} \pm \frac{\vec{d}}{2}\right|} \hat{r}_{ij} \tag{4-25}$$

Using Gauss' law this turns into boundary charges at location R_c of:

$$\mp Q_C = -\frac{R_c}{\left|\vec{r}_{ij} \pm \frac{\vec{d}}{2}\right|} q_j \frac{R_c^3}{\left(\frac{R_c^2}{\left|\vec{r}_{ij} \pm \frac{\vec{d}}{2}\right|}\right)^3} = -q_j \frac{\left|\vec{r}_{ij} \pm \frac{\vec{d}}{2}\right|^2}{R_c^2} \tag{4-26}$$

This leads to the following reaction field potential:

$$V_{image}^{\mu q} = k\kappa \frac{q_i q_j}{R_c^3}\left(\left|\vec{r}_{ij} + \frac{\vec{d}}{2}\right|^2 - \left|\vec{r}_{ij} - \frac{\vec{d}}{2}\right|^2\right) = k\kappa \frac{2q_i q_j \vec{r}_{ij} \cdot \vec{d}}{R_c^3} = k\kappa \frac{2q_j \vec{r}_{ij} \cdot \vec{\mu}_i}{R_c^3}$$
$$\Rightarrow V_{RF}^{\mu q} = -\frac{1}{2} V_{image}^{\mu q} = -\frac{1}{4\pi\varepsilon_0 n^2} \frac{2(\varepsilon_{RF} - n^2)}{2\varepsilon_{RF} + n^2} \frac{q_j \vec{r}_{ij} \cdot \vec{\mu}_i}{R_c^3} \tag{4-27}$$

Note that the reaction field potential between a dipole $\vec{\mu}$ at the center of the cavity and a charge q_j does not depend on $\vec{d}$, however, for this to be valid $\vec{d}$ needs to infinitesimally small, representing the dipole limit.

The full interaction potential between a between a dipole $\vec{\mu}_i$ at the center of the cavity and a charge q_j then becomes:

$$V_{ij}^{\mu q} = \frac{q_j \vec{r}_{ij} \cdot \vec{\mu}_i}{4\pi\varepsilon_0 n^2}\left(\frac{1}{r_{ij}^3} - \frac{2(\varepsilon_{RF} - n^2)}{2\varepsilon_{RF} + n^2} \frac{1}{R_c^3}\right) \tag{4-28}$$

When the dipole $\vec{\mu}_i$ is pointing in the direction $\vec{r}_{ij}$ the potential will be positive (repulsive) for a positive charge q_j and attractive if the charge is negative. This is the correct behavior as the physical dipole points from its negative to its positive end, thus when pointing towards a charge its positive charge is facing this charge.

The last scenario, charge-dipole interaction, with a charge q_i at the center and a dipole $\vec{\mu}_\mathrm{j}$ located at a distance r_{ij} from the center is illustrated in figure 4.4.

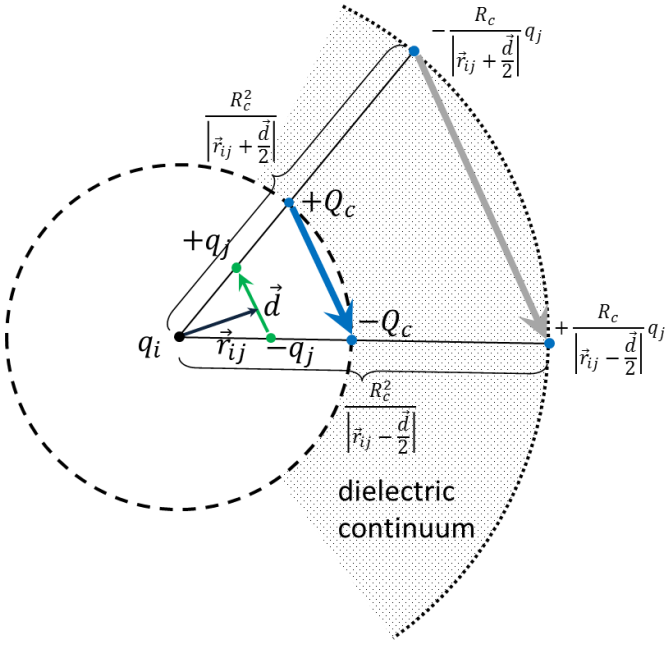

Figure 4.4: Charge-dipole image charge energy derivation

This situation is so similar to the previous scenario that both equations (4-25) and (4-26) correctly describe the image charges and their locations. The only difference to the previous interaction potentials (4-27) and (4-28) is the sign of the interaction. Unlike before, when the dipole $\vec{\mu}_\mathrm{j}$ is pointing in the direction $\vec{r}_{ij}$ its negative end is facing the charge at the center. Thus, the interaction potentials need to be negative when q_i is positive.

The reaction field potential then is:

$$V_{RF}^{q\mu} = \frac{1}{4\pi\varepsilon_0 n^2}\frac{2(\varepsilon_{RF} - n^2)}{2\varepsilon_{RF} + n^2}\frac{q_i\vec{r}_{ij}\cdot\vec{\mu}_j}{R_c^3} \tag{4-29}$$

The full interaction potential between a charge q_i at the center and a dipole $\vec{\mu}_\mathrm{j}$ at location $\vec{r}_{ij}$ inside the cavity fulfilling this requirement is:

$$V_{ij}^{q\mu} = -\frac{q_i\vec{r}_{ij}\cdot\vec{\mu}_j}{4\pi\varepsilon_0 n^2}\left(\frac{1}{r_{ij}^3} - \frac{2(\varepsilon_{RF} - n^2)}{2\varepsilon_{RF} + n^2}\frac{1}{R_c^3}\right) \tag{4-30}$$

This fully describes the enhanced reaction field potential using charges and dipoles with the three additional scenarios: 1) charge-charge with equation (4-23), 2) dipole-charge with equation (4-27), and 3) charge-dipole with equation (4-29).

The test the validity of the enhanced reaction field using charges and dipoles compared to Onsager's dipole-dipole reaction field potential (4-16) three scenarios for two dipoles inside the reaction sphere cavity are calculated as shown in figure 4.5.

a)

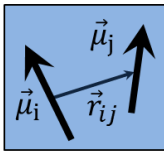

$$V_{RF} \propto -2\vec{\mu}_i(\vec{\mu}_i + \vec{\mu}_j) - 2\vec{\mu}_j(\vec{\mu}_i + \vec{\mu}_j) = -\mathbf{2}\{\boldsymbol{\mu_i^2} + \boldsymbol{\mu_j^2} + \mathbf{2}\vec{\boldsymbol{\mu}}_i\vec{\boldsymbol{\mu}}_j\}$$

b)

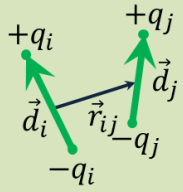

$$\begin{aligned}
V_{RF} &\propto 2q_iq_j\left(-\vec{\imath} + \vec{r}_{ij} + \vec{\jmath}\right)^2 - 2q_iq_j\left(-\vec{\imath} + \vec{r}_{ij} - \vec{\jmath}\right)^2 - 2q_iq_j\left(\vec{\imath} + \vec{r}_{ij} + \vec{\jmath}\right)^2 \\
&\quad + 2q_iq_j\left(\vec{\imath} + \vec{r}_{ij} - \vec{\jmath}\right)^2 - 2q_i^2d_i^2 - 2q_j^2d_j^2 \\
&= 2q_iq_j\{\cancel{r_{ij}^2} + (-\vec{\imath} + \vec{\jmath})^2 + 2\cancel{\vec{r}_{ij}(-\vec{\imath} + \vec{\jmath})} - \cancel{r_{ij}^2} - (-\vec{\imath} - \vec{\jmath})^2 - 2\cancel{\vec{r}_{ij}(-\vec{\imath} - \vec{\jmath})} \\
&\quad - \cancel{r_{ij}^2} - (\vec{\imath} + \vec{\jmath})^2 - 2\cancel{\vec{r}_{ij}(\vec{\imath} + \vec{\jmath})} + \cancel{r_{ij}^2} + (\vec{\imath} - \vec{\jmath})^2 + 2\cancel{\vec{r}_{ij}(\vec{\imath} - \vec{\jmath})}\} \\
&\quad - 2\mu_i^2 - 2\mu_j^2 \\
&= -2q_iq_j\{2(\vec{\imath} + \vec{\jmath})^2 - 2(\vec{\imath} - \vec{\jmath})^2\} - 2\mu_i^2 - 2\mu_j^2 \\
&= -2\{\mu_i^2 + \mu_j^2 + q_iq_j(4\vec{\imath}\cdot\vec{\jmath} - 2(-2\vec{\imath}\cdot\vec{\jmath}))\} = -2\{\mu_i^2 + \mu_j^2 + 2q_iq_j\vec{d}_i\vec{d}_j\} \\
&= -\mathbf{2}\{\boldsymbol{\mu_i^2} + \boldsymbol{\mu_j^2} + \mathbf{2}\vec{\boldsymbol{\mu}}_i\vec{\boldsymbol{\mu}}_j\}
\end{aligned}$$

c)

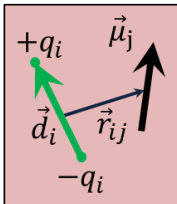

$$\begin{aligned}
V_{RF} &\propto 2q_i\left(-\vec{\imath} + \cancel{\vec{r}_{ij}}\right)\vec{\mu}_j - 2q_i\left(\vec{\imath} + \cancel{\vec{r}_{ij}}\right)\vec{\mu}_j - 2\mu_j^2 - 2q_i^2d_i^2 - 2q_i\left(-\cancel{\vec{r}_{ij}} + \vec{\imath}\right)\vec{\mu}_j \\
&\quad + 2q_i\left(-\cancel{\vec{r}_{ij}} - \vec{\imath}\right)\vec{\mu}_j \\
&= -2\mu_i^2 - 2\mu_j^2 + 2q_i\vec{\mu}_j(-4\vec{\imath}) = -2\{\mu_i^2 + \mu_j^2 + 2q_i\vec{\mu}_j\vec{d}_i\} \\
&= -\mathbf{2}\{\boldsymbol{\mu_i^2} + \boldsymbol{\mu_j^2} + \mathbf{2}\vec{\boldsymbol{\mu}}_i\vec{\boldsymbol{\mu}}_j\}
\end{aligned}$$

Proportionality constant in all cases is: $\frac{k\kappa}{2R_c^3}$

$\vec{\imath} = \frac{\vec{d}_i}{2}; \vec{\jmath} = \frac{\vec{d}_j}{2}$

Figure 4.5: Validity calculations for overall reaction field energies in the dipole limit including self-interactions; note that the factor of two in b) is due to return paths having the same values, e.g. for the path from $+q_i$ to $+q_j$ and back, $\left(-\vec{\imath} + \vec{r}_{ij} + \vec{\jmath}\right)^2 = \left(-\vec{\jmath} - \vec{r}_{ij} + \vec{\imath}\right)^2$

The reference calculation corresponding to the Onsager reaction field approach using just dipoles is given in figure 4.5a). Figure 4.5b) depicts the same two dipoles expressed with charges using the charge-charge reaction field potential (4-23). Because the reaction field contributions of both dipoles at the center of their respective reaction spheres are considered, the scenario depicted in figure 4.5c) employs both the dipole-charge reaction field potential (4-27) as well as the charge-dipole reaction field potential (4-29).

All approaches deliver identical results, even when dipoles are explicitly expressed by point charges separated by a non-infinitesimal distance. This at first sounds surprising, as an infinitesimal distance was necessary for the derivation of the dipole-charge and charge-dipole reaction field contributions. On the other hand, the average electric field of a charge distribution within a sphere of radius R_c is given by:

$$\vec{E} = -\frac{1}{4\pi\varepsilon_0}\frac{\vec{M}}{R_C^3} \tag{4-31}$$

With $\vec{M}$ defined as in equation (4-2), encompassing both charges and dipole moments. Therefore, the reaction field of a sphere should be identical whether dipolar contributions within are expressed as point dipoles or as discrete charges. The enhanced reaction field using discrete charges and/or dipoles leads to identical results compared with Onsager's reaction field approach using dipoles as is mandated by the laws of electrostatics thus validating our approach.

The use of point charges allows for an additional complication: the charge distribution inside the reaction sphere is not always guaranteed neutral, with a potential left-over charge σ

$$\sigma = q_i + \sum_j q_j \tag{4-32}$$

A non-neutral reaction sphere would not only affect the calculation of the reaction field as the reaction sphere also serves as the cut-off for electrostatic interactions in the simulation. Therefore, a treatment for both the reaction field as well as for the electrostatic interaction is necessary.

For net-neutral molecules a solution to enforce neutrality is to always include whole molecules into the spherical cutoff. For ionic systems, on the other hand, one could potentially find a corresponding counter ion and include it explicitly in the reaction sphere. This approach of

finding the counter ion, however, would not only be computationally expensive but the counter ion may not even be in close proximity, more than one may be needed, and in case more than one exists it could be ambiguous which counter ion to choose.

Our solution for net-neutral simulation systems, because the whole simulation volume is neutral and hence counter charges to the residual charge σ of the reaction sphere do exist outside the sphere, is to include them implicitly by placing the counter charge, $-\sigma$, at the reaction sphere boundary. Since this effectively spreads the counter charge over the entire reaction sphere surface it will not have an effect on dipoles at the center and only needs to be applied to a charge at the center of the reaction field:

$$V_{i\sigma} = -\frac{q_i \sigma}{4\pi\varepsilon_0 n^2}\left(\frac{1}{R_c} + \frac{\varepsilon_{RF} - n^2}{2\varepsilon_{RF} + n^2}\frac{R_c^2}{R_c^3}\right) = -\frac{q_i\left(q_i + \sum_j q_j\right)}{4\pi\varepsilon_0 n^2}\frac{1}{R_c}\left(1 + \frac{\varepsilon_{RF} - n^2}{2\varepsilon_{RF} + n^2}\right) \qquad (4\text{-}33)$$

In summary, a reaction field potential has been developed including both dipoles and discrete charges. This enhanced reaction field potential maintains the potential energies of Onsager's reaction field when corresponding dipolar systems are described by discrete charges. Furthermore, a treatment has been proposed for the case of non-neutral reaction spheres caused by ionic fluctuations in a simulation system.

4.5 Case Studies Of Small Organic Molecules

In this section, the enhanced reaction field introduced in the previous section is used in the simulation of the dielectric liquids, acetonitrile and ethylene carbonate, whose experimental properties can be found in table 4.1. Both systems have very large reduced dipole densities,[9,10,19] $y = \frac{4\pi\rho_N\mu^2}{9kT}$, and large dielectric constants. Furthermore, their dipole densities are comparable to electro-optic materials and are therefore good model systems. In addition, the ionic liquid ethyl ammonium nitrate is simulated from first principles and its dielectric constant is obtained using equation (4-11).

Table 4.1: List of experimental properties of some organic solvents sorted by increasing dielectric constant (underlined values are extrapolated) compiled from the CRC Handbook of Chemistry and Physics[20]

Solvent	$T\ [K]$	$\mu\ [D]$	$\rho\ [g/cc]$	$MW\ [g/mol]$	$y = \frac{4\pi\rho_N\mu^2}{9kT}$	dielectric
Chlorobenzene	293	1.69	1.1058	112.557	0.58	5.69
Tetrahydrofuran (THF)	298	1.75	0.8833	72.106	0.77	<u>7.43</u>
1,2-Dichlorobenzene (ODCB)	293	2.50	1.3059	147.002	1.15	10.12
Isopropanol (IPA)	298	1.58	0.7809	60.095	0.66	<u>19.29</u>
Acetone	293	2.88	0.7845	58.079	2.33	21.01
Ethanol	293	1.69	0.7893	46.068	1.02	25.30
Methanol	293	1.70	0.7914	32.042	1.48	33.00
Acetonitrile (MeCN)	293	3.93	0.7857	41.052	6.14	36.64
Dimethylformamide (DMF)	298	3.82	0.9445	73.094	3.85	<u>37.25</u>
Dimethyl sulfoxide (DMSO)	298	3.96	1.1010	78.133	4.52	<u>46.84</u>
Water	298	1.85	0.9970	18.015	3.87	<u>78.41</u>
Ethylene Carbonate	313	[4.9]	1.3214	88.062	7.01	89.78

4.5.1 ACETONITRILE

Acetonitrile simulations have been used as one of the main benchmarks of our Monte-Carlo code. The main reasons for this are acetonitrile's comparable dipole-density to ONLO chromophores, the small number of atoms which allows fully-atomistic calculations in a reasonable timeframe, the body of simulation work done by our and other groups[9,10,21,22], and readily available experimental data[20] (see compilation in table 4.1).

The figure of merit for acetonitrile simulations is the bulk dielectric constant ε. The dielectric constant is a good simulation benchmark for long-range electrostatics interactions. In order for a simulation to obtain a value close to the experimental dielectric constant of $\varepsilon = 36.64$ long-range electrostatics interactions and the bulk dielectric behavior have to be modeled well. Hence, this is a good test of the overall energy landscape, especially with respect to Lennard-Jones and electrostatics interactions.

Previous work[9,10] has shown that an ellipsoidal representation of acetonitrile with a center dipole can achieve the experimental dielectric constant. These results were obtain using Onsager's reaction field[2,8] as defined in equation (4-16) to model long-range electrostatic interactions. The calculation of the dielectric constant followed Kirkwood-Fröhlich's approach[12,13] found in equation (4-11). These results were an important milestone in establishing the usefulness of the ellipsoidal shape, particularly in comparison to a spherical shape with a dipolar center, the so called Stockmayer fluid[23–26], as it exhibited ferroelectric behavior thus overestimating acetonitrile's dielectric constant by almost a factor of three. Those earlier simulations, predating the development of the LoD coarse-graining method presented in chapter 2, used manually

optimized ellipsoid parameters and LJ energies.[9,10] In the present work, the focus is on approximating all-atom force field behavior as closely as possible.

Despite its tremendous success at obtaining the experimental dielectric constant, the single ellipsoid model with a point dipole at its center used in the previous work[9,10] may not represent the underlying fully-atomistic model. To illustrate this point, table 4.2 shows simulation results of 512 acetonitrile molecules in the isothermal-isobaric (NPT) ensemble under 1 atm pressure at 298 K using the enhanced reaction field approach for the OPLS-AA force-field description[27] of acetonitrile (with an overall dipole moment of $\mu = 4.13\ D$) compared to coarse-grained representation using a single ellipsoid – as in the previous work – and a two-ellipsoid LoD representation. While the OPLS-AA acetonitrile description uses partial charges at atomic centers, the LoD CG representations used dipoles and left-over charges at the ellipsoid centers (see Appendix B for model parameters). LoD Lennard-Jones interactions used the "adjusted-width" potential and the interaction area correction from equations (2-6) and (2-39), respectively. Note that while the previous model was hand-optimized, the LoD models used here have been obtained systematically from the OPLS-AA force-field as described in chapter 2.

Table 4.2: Acetonitrile results average from 8 simulations using the NPT ensemble under 1 atm at 298 K with reaction field long range model; fully-atomistic force-field run is OPLS-AA in comparison to coarse-grained, single ellipsoid and two-ellipsoid LoD representations with "adjusted-width" LJ LoD potential and interaction area correction using equations (2-6) and (2-39), respectively. (See Appendix B for model parameters) Note that $\frac{6}{2}k_B$ was added to the heat capacities of the CG LoD results in order to account for internal degrees of freedom.

Model	Density $[g/cc]$	$c_P\ [J/mol-K]$	Dielectric
OPLS-AA with RF	0.737 ± 0.001	99 ± 9	19 ± 3
Single ellipsoid LoD	0.832 ± 0.001	93 ± 6	38 ± 8
Two-ellipsoid LoD	0.687 ± 0.001	94 ± 5	18 ± 2

The dielectric constant of the OPLS-AA acetonitrile system with the enhanced reaction field for charge-charge interactions using equation (4-24) is 19 ± 3. This value is identical within error bars to the previously reported dielectric constant 20.3 ± 0.7 of OPLS-AA acetonitrile by Dr. Lewis Johnson obtained with molecular dynamics simulations using Ewald summation in Tinker 5.1[10] thus further validating the enhanced reaction field approach.

The single ellipsoid LoD system is able to get incredibly close to the experimental dielectric constant. However, this value is actually twice as large as the predicted dielectric constant of the underlying AA model. This indicates that the single ellipsoid model is not a good description of the underlying AA force-field, an observation similar to the one made for the CLD-1 type LoD model discussed in chapter 3. The two-ellipsoid LoD system, on the other hand, is able to reproduce the dielectric constant of the underlying AA force-field.

Within their respective error bars, all OPLS-AA based models are able to match the experimental heat capacity[20] of $91.5 \frac{J}{mol\ K}$. Note that for CG representations $\frac{6}{2} k_B$ were added to the respective heat capacities in order to account for the missing internal degrees of freedom. Furthermore, densities between LoD representations and the OPLS-AA force field were off by $+12.8\%$ for the single ellipsoid and -6.8% for the two-ellipsoid model. These density discrepancies can be readily fixed by scaling the LoD LJ energy, a feature likely included in a future iteration of the LoD approach.

The OPLS-AA force-field does not yield a dielectric constant close to the experimental value, likely because the overall dipole moment of the OPLS-AA molecule does not include polarization effects of other acetonitrile molecules in its vicinity. Therefore, a new set of fully-atomistic model parameters for atom locations and partial charges were obtained in collaboration

with Dr. Lewis Johnson from a DFT calculation using Gaussian 09D[28] at the CCSD/aug-cc-pVTZ level of theory with the PCM solvation model in acetonitrile as a solvent utilizing CHELPG charges at atom centers. Lennard-Jones parameters for atom radii and LJ energies were kept identical to the OPLS-AA force field.[27]

Simulations were run in the isothermal-isobaric (NPT) ensemble with 512 molecules under $1\ atm$ external pressure with a temperature range between $300 - 400\ K$. Molecular geometries as well as partial charges remained fixed throughout simulations and no intra-molecular energies were calculated. Inter-molecular electrostatic interactions between partial charges were calculated within a cutoff radius of 19 Å using the enhanced reaction field approach described by the interaction potential in equation (4-24). Lennard-Jones interactions were calculated up to a center-center distance of 16.4 Å, based on the single precision distance limit with the given model parameters.

The resulting temperature dependence of density, heat capacity, dielectric constant, and enthalpy are displayed in figure 4.6 for the fully-atomistic simulation. A phase transition can be observed at $365\ K$ which is $10\ K$ higher than the experimental value of $355\ K$.

Figure 4.6a) shows both the temperature dependence of system density (red dots and solid line) and heat capacity (green dots with blue dashed line) of the new fully-atomistic model. Compared to the experimental density of acetonitrile, $0.786\ \frac{g}{cc}$ at $293\ K$, this new fully-atomistic model has a lower density of $0.66\ \pm 0.02\ \frac{g}{cc}$. The simulated heat capacities of $(92 \pm 36)\ \frac{J}{mol\ K}$ (liquid) and $(38 \pm 13)\ \frac{J}{mol\ K}$ (gas) extrapolated to $298\ K$ using a linear fit to the data before and after the phase transition compare well to the experimental heat capacities[20] for the liquid and gas phase at $298\ K$ of $91.5\ \frac{J}{mol\ K}$ and $52.2\ \frac{J}{mol\ K}$, respectively.

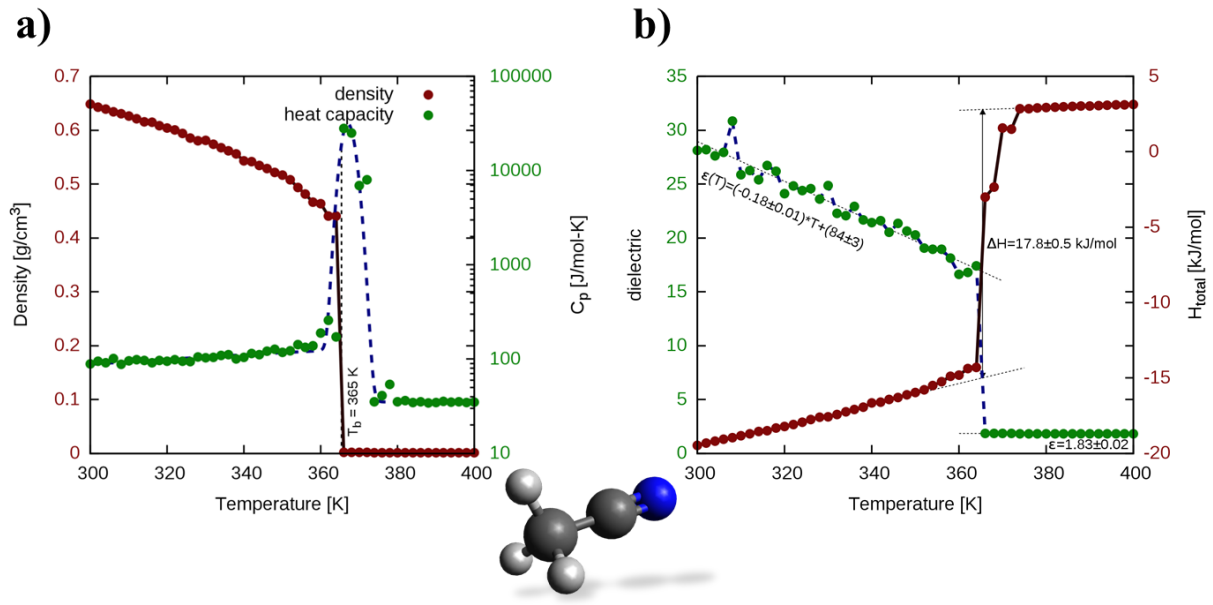

Figure 4.6: Fully-atomistic acetonitrile simulation results using ab-initio DFT atomic geometries and charges and OPLSAA Lennard-Jones parameters. (See Appendix B for model parameters) The data shown is the simulated temperature dependence of **a)** density (red dots and solid line) and heat capacity (green dots with blue dashed line), as well as **b)** dielectric constant (green dots with dashed fit lines and system enthalpy (red dots and solid line) Note that $\frac{6}{2}k_B$ was added to heat capacities in order to account for internal degrees of freedom.

Figure 4.6b) displays the temperature dependence of the simulated dielectric constant (green dots with blue dashed line) and enthalpy (red dots and solid line) of the new fully-atomistic model. The dielectric constant extrapolated to $293\ K$ (dashed black fit line) is 30 ± 4. While this value is lower than the experimental dielectric constant of 36.64 it is much improved compared to the OPLS-AA value of 19 ± 3 and is close to the value of the dielectric constant obtained using the model of Pounds and Madden.[22] The simulated enthalpy of vaporization at the boiling point is $17.8 \pm 0.5 \frac{kJ}{mol}$ which is about 40% below the experimental value of $29.75 \frac{kJ}{mol}$. Note that the enthalpy has a slightly positive value in the gas phase. Enthalpy is defined as the sum of the internal energy with the product of pressure and volume of a system, $H = U + PV$. The observed

behavior is thus due to the PV term, as the internal energy in the gas phase with no intramolecular energy contributions approaches zero.[6]

While there are a variety of empirical approaches to calculate the boiling point of a molecular system[30–33] little insight into the molecular behavior is gained this way. Molecular simulations, on the other hand, provide insight but so far for acetonitrile-like systems were only undertaken with rather complex force fields involving multi-body interactions and also did not directly observe the phase transition.[34–36] The *ab-initio, in silico* determination of the boiling point of a liquid under constant pressure conditions is a challenging simulation target not only because of the sensitivity to intermolecular potential energies but also due to the boiling point's strong dependence on molecular shape and size. Therefore, the reduction of a fully-atomistic model to a coarse-grained representation with simplified interaction potentials and model shapes will necessarily introduce a shift in the observed boiling point compared to the underlying fully-atomistic model. Nonetheless, that makes it a very sensitive benchmark for how well a particular coarse-grained representation reproduces the molecular interactions of its underlying AA system.

Figure 4.7 shows simulation results of the single ellipsoid LoD model using the "simple touch" LJ LoD potential from equation (2-2) run with the constant, best-fit LJ ε obtained from equation (2-33). Simulations were performed under identical conditions compared to the fully-atomistic results exhibited in figure 4.6 with 512 acetonitrile LoD representations placed in the isothermal-isobaric (NPT) ensemble with 1 atm external pressure. Atomic partial charges of the underlying AA model were reduced to a corresponding point dipole of 4.74 D at the ellipsoid center.

[6] In fact, the simulated enthalpy value for the new fully-atomistic system at 400 K is $3.121 \pm 0.003 \frac{kJ}{mol}$ with an intermolecular energy contribution of $-0.153 \pm 0.001 \frac{kJ}{mol}$ and a simulated value of $PV = 3.274 \pm 0.003 \frac{kJ}{mol}$, which is within 2% of the value obtained from the ideal gas law, $3.326 \frac{kJ}{mol}$. Another way of interpreting those numbers is to calculate the fraction the system in the gas phase behaves like an ideal gas, the resulting number at 400 K for these numbers is 94%, very close to the experimental value of the fugacity for acetonitrile at 100 °C.[29]

Displayed in figure 4.7a) is the temperature dependence of equilibrium simulation densities and heat capacities while figure 4.7b) shows dielectric constants and enthalpies. No phase transition is observed.

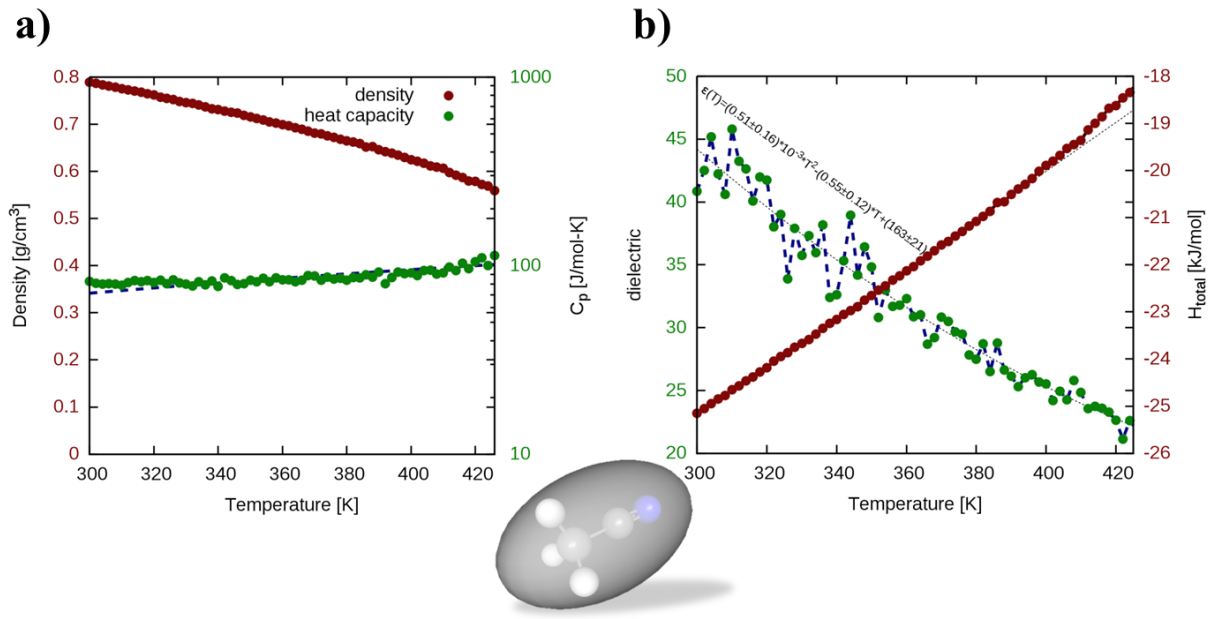

Figure 4.7: Single ellipsoid acetonitrile LoD simulation results with LoD parameters obtained systematically from the aforementioned fully-atomistic model run with the "simple touch" LJ LoD potential from equation (2-2) with best-fit LJ ε obtained using equation (2-33). (See Appendix B for model parameters)
The data shown is the simulated temperature dependence of **a)** density (red dots and solid line) and heat capacity (green dots with blue dashed line), as well as **b)** dielectric constant (green dots with dashed fit lines and system enthalpy (red dots and solid line) Note that $\frac{6}{2}k_B$ was added to heat capacities in order to account for internal degrees of freedom.

As observed previously for OPLS-AA acetonitrile, the single ellipsoid LoD model does not describe the underlying AA system particularly well. For a given temperature, with the exception of the heat capacity, all system properties are larger in magnitude compared to the fully-atomistic model; equilibrium densities and system enthalpies by about 20%, dielectric constants by approximately 45%. Based on equation (4-11) the increased dielectric constant is produced by stronger fluctuations of the total dipole moment. This can be caused by the increased shape

symmetry of the single ellipsoid LoD model lowering steric hindrances and allowing for more movement. The increase in densities and enthalpy magnitudes can be attributed to the shape of the ellipsoid as well as to the width of the Lennard-Jones potential's attractive region. In order to best fit the entire underlying AA model, the single ellipsoid's shape is elongated to match the stronger LJ potential contribution of the C-C-N backbone. This leaves some of the volume originally occupied by the underlying hydrogen atoms unaccounted for in the single ellipsoid which in turns leads to tighter than original molecule packing, increasing the overall density and interaction energies. As outlined in chapter 2, the "simple touch" LJ potential width from equation (2-2) depends on the contact distance between two ellipsoids and their particular relative orientations. Typically, for larger ellipsoids the average LJ interaction width is larger than observed in the AA system leading to increased condensation pressure, in other words larger densities and interaction energy magnitudes, in the simulation.

The LoD Lennard-Jones potential can be improved upon as outlined in chapter 2. Figure 4.8 shows simulation results using an identical ellipsoid shape with the same point dipolar as used for the results displayed in figure 4.7 but with the "adjusted-width" LJ LoD potential from equation (2-6) with the interaction area correction using equation (2-39) (see Appendix B for model parameters). Displayed in figure 4.8a) is the temperature dependence of equilibrium simulation densities and heat capacities while figure 4.8b) shows dielectric constants and enthalpies.

The change of LJ LoD interaction potential to the Gay-Berne like "adjusted width" potential with interaction area correction leads to an observed phase transition in the simulated temperature region at a boiling temperature of $407\ K$. This value is about $40\ K$ (~11.5%) larger than the boiling temperature observed for the underlying fully-atomistic system in figure 4.6.

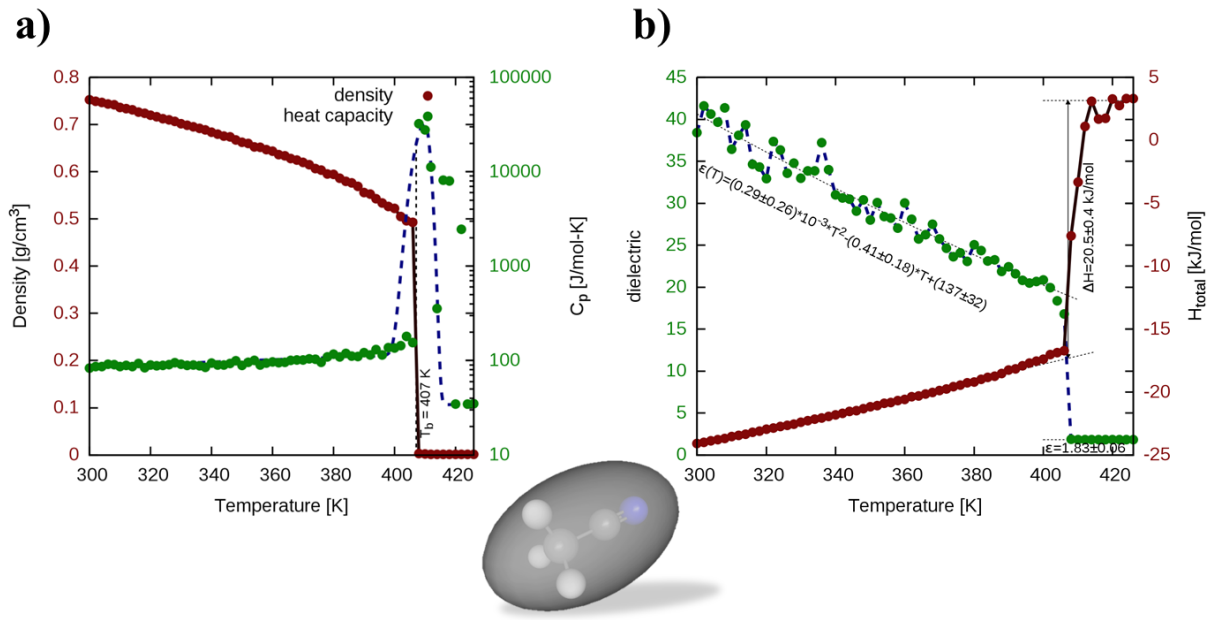

Figure 4.8: Single ellipsoid acetonitrile LoD simulation results with LoD parameters obtained systematically from the aforementioned fully-atomistic model run with the "adjusted-width" LJ LoD potential and interaction area correction using equations (2-6) and (2-39), respectively. (See Appendix B for model parameters)
The data shown is the simulated temperature dependence of **a)** density (red dots and solid line) and heat capacity (green dots with blue dashed line), as well as **b)** dielectric constant (green dots with dashed fit lines and system enthalpy (red dots and solid line) Note that $\frac{6}{2}k_B$ was added to heat capacities in order to account for internal degrees of freedom.

Similarly to the "simple touch" single ellipsoid LoD model in figure 4.7, equilibrium densities, enthalpies, and dielectric constants are still larger in magnitude compared to the fully-atomistic model, although with an overall smaller deviation from the fully-atomistic values. The aforementioned reasons for those increases, the more symmetrical shape, point dipole, and smaller ellipsoid volume compared to the all-atom model still apply.

The observed, simulated enthalpy of vaporization at the boiling point is $20.5 \pm 0.4 \frac{kJ}{mol}$ which is $2.7 \frac{kJ}{mol}$ larger than the corresponding value of the underlying AA system. This increase is due to a corresponding rise in electrostatic interactions due to closer interaction distances indicating that

the ellipsoid shape in conjunction with underestimating the volume of the single ellipsoid LoD model may be responsible for the mismatch with the AA system.

The acetonitrile center-center radial distribution functions, $g(r)$, of the single ellipsoid LoD model calculations at $300\ K$ shown in figure 4.9 further supports this hypothesis. In comparison to the fully-atomistic distribution both single ellipsoid LoD models exhibit narrower peak widths and a more pronounced nearest-neighbor interaction peak.

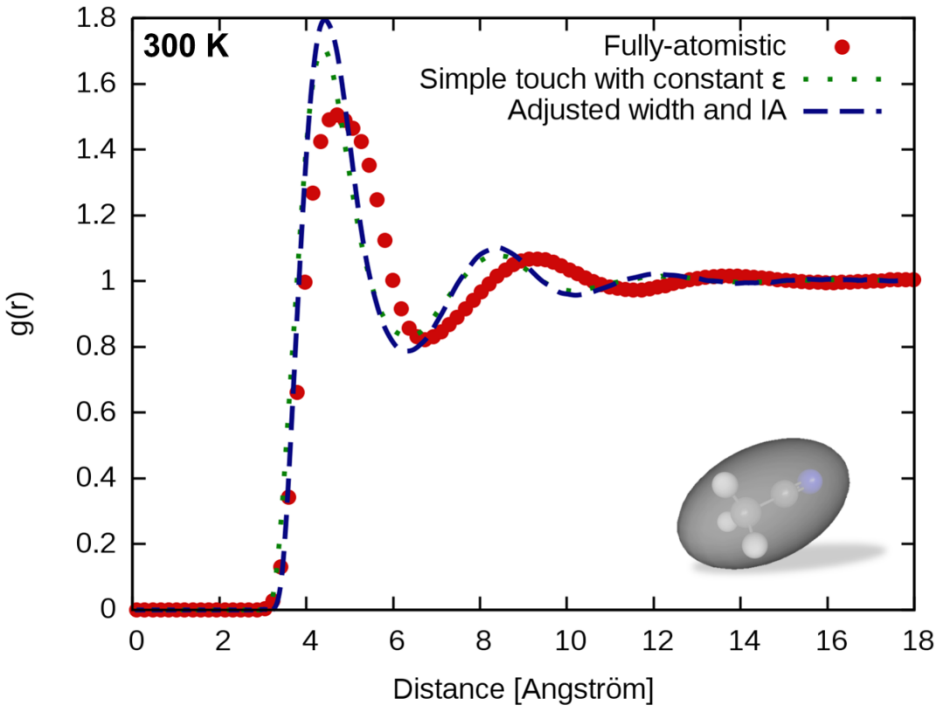

Figure 4.9: Acetonitrile center-center radial distribution function comparison between AA model and single ellipsoid LoD simulation results at $300\ K$ run with the "simple touch" LJ LoD potential with constant, best-fit LJ ε (green, dotted line) and the "adjusted-width" LJ LoD potential with the interaction area correction (blue, dashed line).

The peak widths could potentially be matched manually while maintaining peak heights by isotropically scaling the ellipsoid volume and adjusting the LJ potential energy. Note, however, that the presented results could also indicate the limitations of the ellipsoid shape at describing

the underlying shape. An ellipsoid trying to best encompass a linear, cylindrical molecule growing in length but with similar diameter will get stretched thinner and thinner at its ends thus resulting in a larger volume fraction of such a linear molecule not encompassed by the ellipsoid. A potential, future fix to this problem could be the use of hyperellipsoids as hinted at in chapter 2. The current solution is to break up the linear molecule into more than one ellipsoid.

Figure 4.10 displays simulation results for the two-ellipsoid LoD model based on the fully-atomistic model using identical simulation conditions to the aforementioned simulations. AA model partial charges were reduced to a corresponding point charge and point dipole at each ellipsoid center.

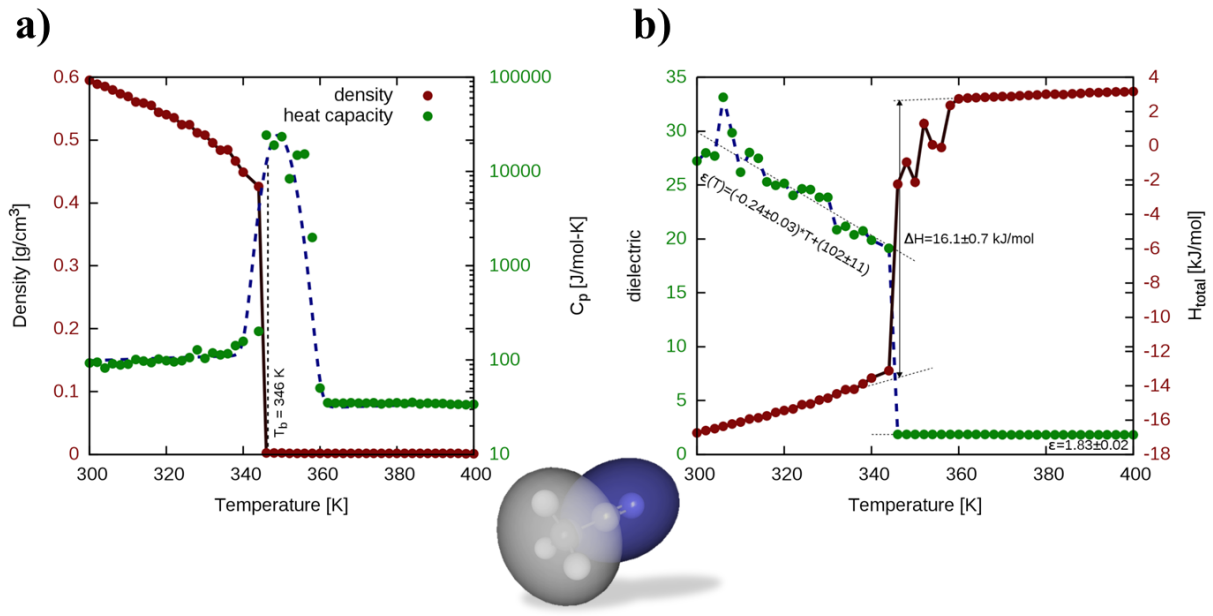

Figure 4.10: Two-ellipsoid acetonitrile LoD simulation results with LoD parameters obtained systematically from the underlying fully-atomistic model run with the "simple touch" LJ LoD potential from equation (2-2) with best-fit LJ ε obtained using equation (2-33). (See Appendix B for model parameters)
The data shown is the simulated temperature dependence of **a)** density (red dots and solid line) and heat capacity (green dots with blue dashed line), as well as **b)** dielectric constant (green dots with dashed fit lines and system enthalpy (red dots and solid line) Note that $\frac{6}{2}k_B$ was added to heat capacities in order to account for internal degrees of freedom.

Figure 4.10a) shows the temperature dependence of equilibrium simulation densities and heat capacities while figure 4.10b) shows dielectric constants and enthalpies. A phase transition can be observed at 346 K, about 20 K (~5.5%) below the value observed for the underlying AA system displayed in figure 4.6. Despite the relative simplicity of this model using the "simple touch" LJ LoD potential almost all properties displayed are within about 8% of the corresponding fully-atomistic values.

Figure 4.11 displays comparatively good results for the two-ellipsoid LoD model using the "adjusted width" LJ LoD potential with the interaction area correction using equations (2-6) and (2-39), respectively.

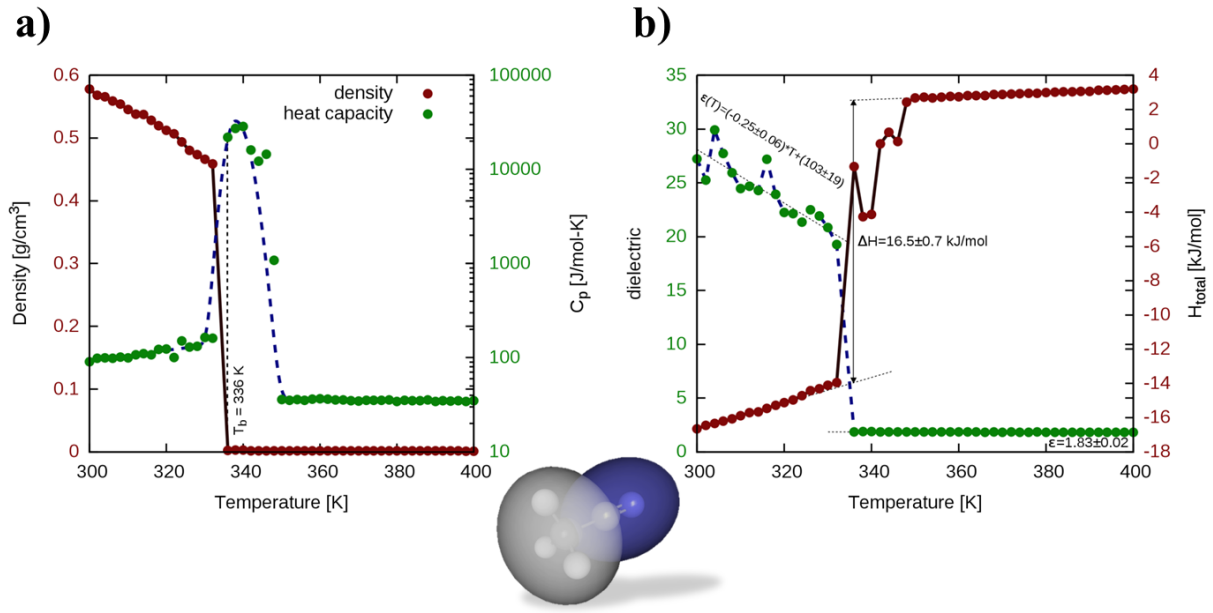

Figure 4.11: Two-ellipsoid acetonitrile LoD simulation results with LoD parameters obtained systematically from the underlying fully-atomistic model run with the "adjusted-width" LJ LoD potential and interaction area correction using equations (2-6) and (2-39), respectively. (See Appendix B for model parameters)
The data shown is the simulated temperature dependence of **a)** density (red dots and solid line) and heat capacity (green dots with blue dashed line), as well as **b)** dielectric constant (green dots with dashed fit lines and system enthalpy (red dots and solid line) Note that $\frac{6}{2}k_B$ was added to heat capacities in order to account for internal degrees of freedom.

The phase transition happens at a lower boiling point of 336 K and the density is lowered slightly, however, the dielectric constants and the system enthalpies are now overlapping with the fully-atomistic values.

A look at the radial distribution functions at 300 K, exhibited in figure 4.12, confirms both two-ellipsoid LoD models to be a close match to the underlying fully-atomistic potential. The reason for the correspondence between both two-ellipsoid models is that the ellipsoid semi axes of either ellipsoid are close to the optimum width of the LJ LoD potential. Therefore, in this particular case the "simple touch" LJ LoD potential behaves identical to the "adjusted width" LJ LoD potential.

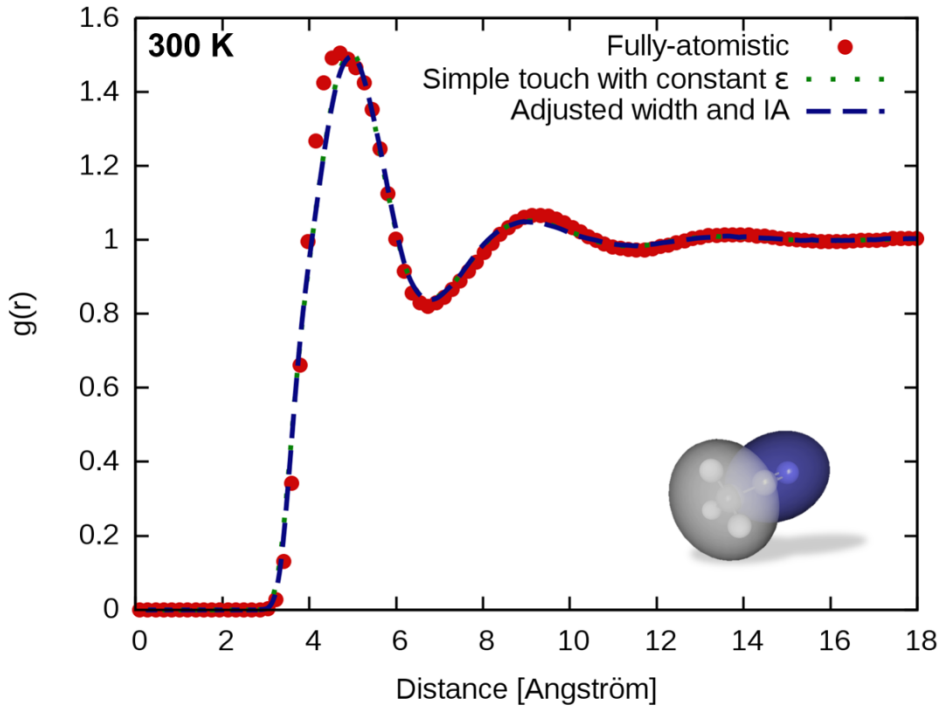

Figure 4.12: Acetonitrile center-center radial distribution function comparison between AA model and two-ellipsoid LoD simulation results at 300 K run with the "simple touch" LJ LoD potential with constant, best-fit LJ ε (green, dotted line) and the "adjusted-width" LJ LoD potential with the interaction area correction (blue, dashed line).

In summary, simulations of the dielectric behavior of acetonitrile were used as a benchmark to investigate the LoD approach outlined in chapter 2. Two fully-atomistic force field descriptions, OPLS-AA and an OPLS-AA based model on using atomic geometries and charges of a coupled-cluster DFT calculation, were utilized. Single and two-ellipsoid LoD representations of these AA models were calculated using the rule set presented in chapter 2 and run under similar simulations conditions compared to the AA simulations. Similarly to the findings in chapter 3, the single ellipsoid LoD model did not match the fully-atomistic results closely while the two-ellipsoid representation closely matched the all-atom description. Furthermore, for the DFT-based AA model simulations over a wide temperature range were performed and phase transitions within $20\ K$ (6%) of the experimental value were observed for the AA system as well as for the two-ellipsoid LoD representation.

4.5.2 ETHYLENE CARBONATE

Ethylene carbonate is an important, organic solvent which has the largest known dielectric constant and dipole density (see table 4.1) of any organic liquid. Its high relative permittivity and strongly polar nature make it suitable for the dissolution of ionic species in electrolyte solutions such as those used in lithium ion batteries. The large dipole density of ethylene carbonate also makes it a good reference system to test the LoD coarse-graining approach in the strong dipolar limit important to the ONLO community.

The fully-atomistic model was obtained using the Gaussian 09D[28] package with the B3LYP/6-311+G(d,p) functional, PCM solvent model (dielectric constant of 90.5, n^2=2.0164), and CHELPG charges at atom locations in conjunction with OPLS-AA parameters for Lennard-Jones radii and energies of individual atoms. Dielectric constant results of earlier LoD model simulations using the "simple touch" LJ LoD potential have previously been reported to be able to match the experimental dielectric constant[37] of 90.5 at 40 $°C$ within the error bar.[38]

In this section, the current rule set of the LoD approach as presented in chapter 2 is used to obtain and perform LoD model simulation. The new results are then compared to the underlying fully-atomistic simulation results under identical simulation conditions. Simulations were run with the "simple touch" LJ LoD potential from equation (2-2) with best-fit LJ ε obtained using equation (2-33) and additionally with the interaction area correction from equation (2-39). Furthermore, our currently best CG approach using the "adjusted width" LJ LoD potential from equation (2-6) with the interaction area correction from equation (2-39) was employed. Partial atomic charges at atomic locations were utilized throughout all simulations – including the LoD CG simulations – in order to focus on the LJ LoD potential descriptions. Two rigid LoD representations were used:

a single ellipsoid model encompassing the entire molecule and a two-ellipsoid model with an ellipsoid containing the OCOO carbonate subunit and one for the CH_2-CH_2 ethylene subunit. All ellipsoids were calculated following the description given in chapter 2.3.3 using a test sphere radius $r_T = 1.545$ Å. Simulations were run with 432 molecules using the NPT ensemble under 1 atm at 40 $°C$.

The simulation results are summarized in table 4.3 with color-coded rows corresponding to the line colors presented in figures 4.13 and 4.14. The red row contains the fully-atomistic results, green rows represent results obtained using the "simple touch" LJ LoD potential with a constant LJ ε, blue rows were run with the "simple touch" LJ LoD potential with the interaction area correction, and golden rows are using the "adjusted width" LJ LoD potential with interaction area correction.

Table 4.3: Ethylene carbonate results average from 8 simulations with associated standard deviations using the NPT ensemble under 1 atm at 40 $°C$ with the models as described in the text (see Appendix B for model details). Note that $\frac{12}{2}k_B$ was added to heat capacities in order to account for internal degrees of freedom. Row colors correspond to the line colors used in figures 4.13 and 4.14.

Model	Density $[g/cc]$	c_P $[J/mol-K]$	Dielectric
AA model	**1.265 ± 0.001**	**123 ± 7**	**91 ± 35**
Single ellipsoid LoD	1.265 ± 0.001	109 ± 4	83 ± 13
Interaction Area (IA)	1.266 ± 0.001	109 ± 2	98 ± 11
"Adjusted width" and IA	**1.274 ± 0.001**	**115 ± 3**	**103 ± 32**
Two-ellipsoid LoD	1.253 ± 0.001	112 ± 7	124 ± 38
Interaction Area (IA)	1.254 ± 0.001	111 ± 3	119 ± 43
"Adjusted width" and IA	**1.212 ± 0.001**	**119 ± 5**	**89 ± 33**

The properties determined from the fully-atomistic simulation are very close to the experimental values of $1.321\,\frac{g}{cc}$ for the density,[20] $134\,\frac{J}{mol\,K}$ for the heat capacity,[39] and 90 for the dielectric constant.[20] The deviations of the AA model from these values are 4.2%, 8.2%, and 1.1%, for density, heat capacity, and dielectric constant, respectively. Given that the AA model was derived from an ab-initio DFT calculation using simple, atomic LJ parameters from the OPLS-AA force field, these are rather reasonable results.

The observed, average LoD ellipsoid (single and two-ellipsoid) simulation densities are within less about 1% of the fully-atomistic average except for the two-ellipsoid LoD model using the "adjusted-width" LJ LoD potential with the interaction area correction which is off by about 4%. Furthermore, observed deviations of the LoD model from the AA model of average heat capacities are within 11% and dielectric constants are within their respective error bars of about 30%.

Based on the tabulated data both LoD models represent the underlying fully-atomistic model well. Sometimes the single ellipsoid model is closer on average (density, dielectric constant for "simple touch" LJ LoD potentials) to the fully-atomistic values; sometimes the two-ellipsoid model excels (heat capacity, dielectric constant for "adjusted width" LJ LoD potential). Overall, no clear best LoD representation emerges.

Figure 4.13 displays radial distribution functions between the carbonate carbon centers for the single ellipsoid LoD representation using the different LoD LJ potentials mentioned above. The single ellipsoid LoD model using any of the three LJ LoD potential descriptions does not capture the intricate details found on the first peaks in the corresponding fully-atomistic data.

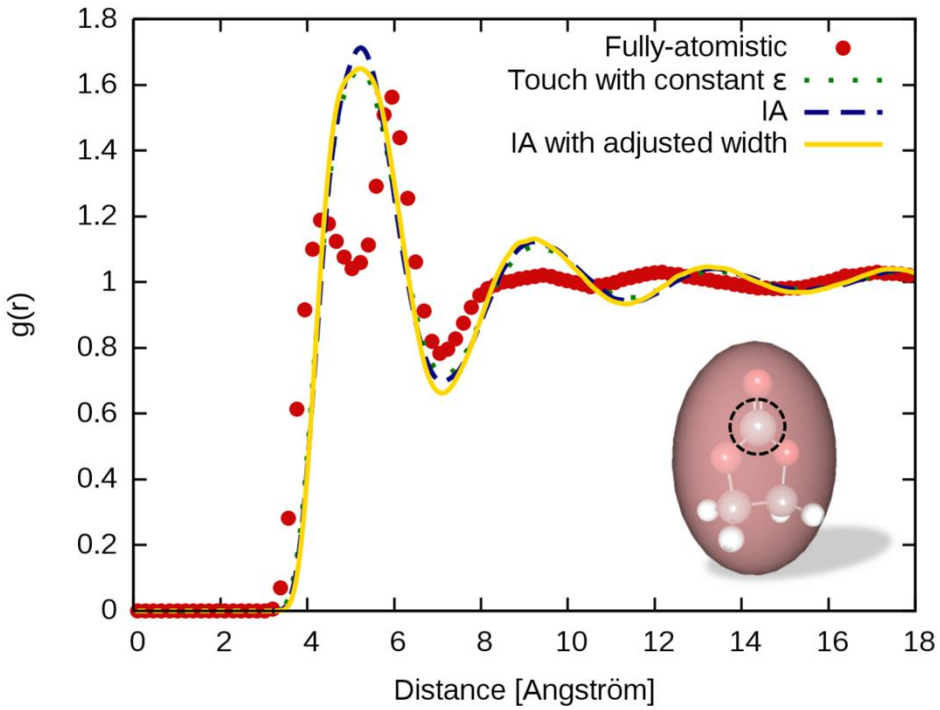

Figure 4.13: Carbonate carbon (highlighted by dashed black circle) center-center radial distribution function comparison between AA model (red dots) and single ellipsoid LoD simulation results with the "simple touch" LJ LoD potential with constant, best-fit LJ ε (green, dotted line), "simple touch" LJ LoD potential with interaction area correction (blue, dashed line), and the "adjusted-width" LJ LoD potential with the interaction area correction (gold, solid line).

Peak heights of the radial distribution function between carbonate center-center locations are typically overshot by the single ellipsoid model and secondary peaks are slightly shifted compared to the AA model. The split first peak observed in the AA model's radial distribution function, representing close-range molecular interactions, turns into a large, slightly narrower peak in the single ellipsoid LoD representation.

In contrast to the single ellipsoid model, figure 4.14 displays the corresponding plots for the two-ellipsoid model. The match between the two-ellipsoid LoD and the fully-atomistic radial distribution function between carbonate carbon center-center distances is outstanding,

particularly for the “adjusted width” LJ LoD potential with the interaction area correction using equations (2-6) and (2-39), respectively.

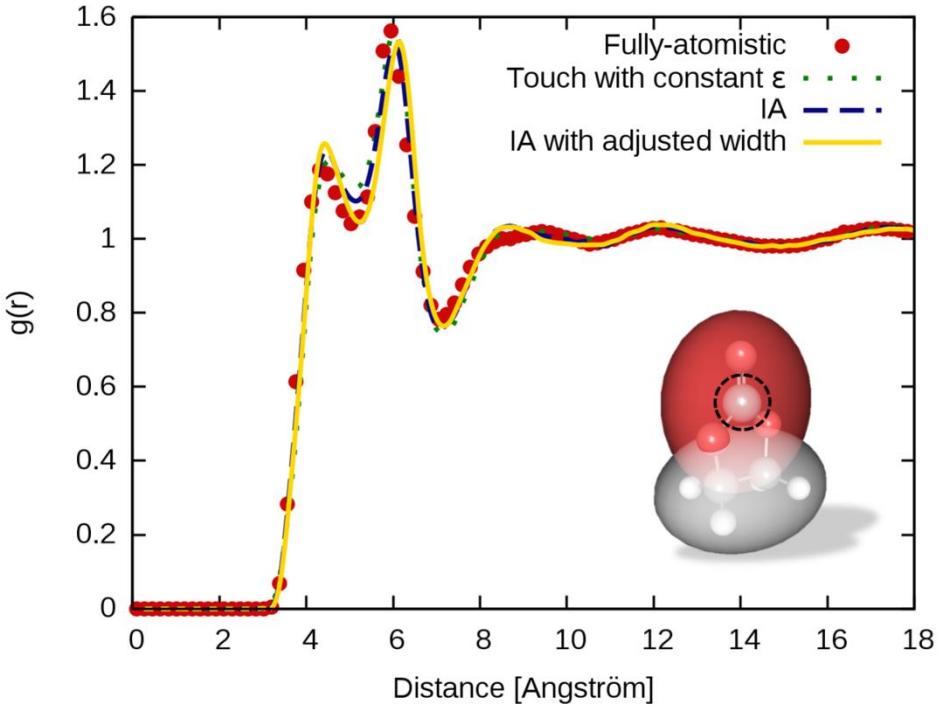

Figure 4.14: Carbonate carbon (highlighted by dashed black circle) center-center radial distribution function comparison between AA model (red dots) and two-ellipsoid LoD simulation results with the “simple touch” LJ LoD potential with constant, best-fit LJ ε (green, dotted line), “simple touch” LJ LoD potential with interaction area correction (blue, dashed line), and the “adjusted-width” LJ LoD potential with the interaction area correction (gold, solid line).

In summary, the ab-initio all-atom model for ethylene carbonate is able to provide a good match between simulation results and experimental values, particularly with respect to the dielectric constant emphasizing the benefits of using the enhanced reaction field approach. Furthermore, single and two-ellipsoid LoD representations are able to match the fully-atomistic simulation results well. However, only the two-ellipsoid LoD model was able the match the fully-atomistic molecular behavior, as evidenced by the radial distribution function between carbonate carbon centers.

4.5.3 *ETHYL AMMONIUM NITRATE*

Ethyl ammonium nitrate was the first room temperature ionic liquid, which was synthesized in 1914 by Paul Walden.[40] It is included here to demonstrate the enhanced reaction field's ability to be employed in systems with ionic contributions.

The fully-atomistic model was obtained using the Gaussian 09D[28] package with the B3LYP/6-31G(d) functional in vacuum and CHELPG charges at atom locations in conjunction with OPLS-AA parameters for Lennard-Jones radii and energies of individual atoms. Simulations were run with 108 ethyl ammonium and 108 nitrate moieties in an NPT ensemble under 1 atm pressure at 298 K using a two-ellipsoid LoD model for ethyl ammonium and a single ellipsoid for nitrate (see Appendix B for model parameters) with the enhanced reaction field model using the neutralized reaction sphere. The "adjusted width" LJ LoD potential from equation (2-6) was used in conjunction with the interaction area correction from equation (2-39).

Simulation results using point charges and point dipoles at ellipsoid centers as well as fully-atomistic partial charges at their original atomic locations inside the LoD ellipsoids are presented in table 4.4.

Table 4.4: Ethyl ammonium nitrate results averages from 8 simulations using the NPT ensemble under 1 atm at 298 K with reaction field long range model using two-ellipsoid LoD model with "adjusted-width" LJ LoD potential and interaction area correction using equations (2-6) and (2-39), respectively. (See Appendix B for model parameters) Note that $\frac{6}{2}k_B$ was added to the heat capacities of the CG LoD results in order to account for internal degrees of freedom.

Model	Density $[g/cc]$	c_P $[J/mol-K]$	Dielectric from $var(M)$	Dielectric from g_K
Point Charge and Point Dipole at Ellipsoid Center	1.110 ± 0.002	75 ± 11	790 ± 138	23 ± 4
AA partial charges	1.107 ± 0.003	147 ± 8	767 ± 134	24 ± 7

Two approaches to estimate the dielectric constant have been used. The first approach is the use of the simulated system's total dipole moment fluctuation, the variance $var(M)$, as presented in equation (4-11). This approach leads to a dielectric constant that is very large, indicating charge transport – as one would expect from an ionic system – is taking place. In order to compensate for these contributions present in the total dipole moments of ionic systems, a second approach using the Kirkwood correlation factor is employed. The Kirkwood correlation factor can be calculated as:[9,10,12,13,41]

$$g_K = 1 + z\langle \cos\gamma \rangle \tag{4-34}$$

Here, γ is the angle between a pair of dipoles and z is the number of neighboring pairs. In this case the Kirkwood-Fröhlich equation[9,10,12,13,41] can be used to calculate the dielectric constant:

$$\frac{(\varepsilon - n^2)(2\varepsilon + n^2)}{3\varepsilon} = \frac{4\pi\rho_N\mu^2}{3kT} g_K \tag{4-35}$$

Here, n^2 is the high-frequency dielectric used to attenuate electrostatics interactions, ρ_N is the number density, and μ is the average molecular dipole moment. In the case of the ethyl ammonium nitrate ionic system, the only permanent dipole is that of the ethyl ammonium ion with a dipole of $\mu = 3.97\ D$. For simulations using AA partial charges a correlation over all ethyl ammonium ions in the system gives $\langle \cos\gamma \rangle = -0.0022 \pm 0.0022$. Each ethyl ammonium ion has $z = 107$ partners to interact with in the simulation box, giving a Kirkwood correlation factor of 0.765 ± 0.002 which in conjunction with the number density of the whole system, $123 \cdot 10^{20} molecule/cc$, and the dipole moment of ethyl ammonium leads to the dielectric constant presented in table 4.2. The dielectric constants thus calculated with the Kirkwood correlation factor g_K from equation (4-34) are very close to the experimental value[42] of 26.3 ± 0.5.

The simulation densities are about 8% below the experimental value[40] of $1.21\,\frac{g}{cc}$. This is likely due to using OPLS-AA derived LJ parameters as seen in previous sections.

Interestingly, the choice of charge distribution for the LoD representation of ethyl ammonium nitrate led to marked differences in the molecule behavior in terms of resulting heat capacities which are different by a factor of about two. The heat capacity obtained using the AA partial charges is closest to the experimental value of $206\,\frac{J}{mol\,K}$.[43]

Figure 4.15 shows the spatial distribution function using point charges and point dipoles at ellipsoid centers between the centers of ethyl ammonium and nitrate nitrogens when calculated from either side. The surface coloration shown represents positional probabilities of finding the opposing nitrogen ranging from fully transparent dark red, over blue to fully opaque bright green colors.

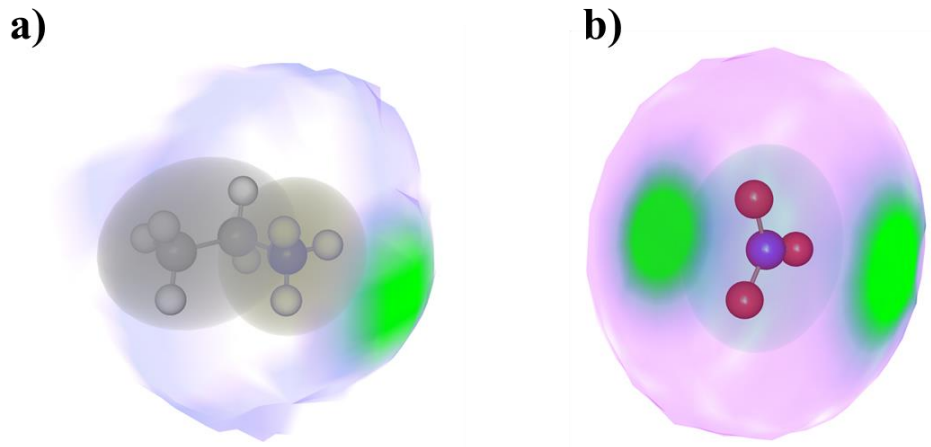

Figure 4.15: Spatial distribution function using point charges and point dipoles at ellipsoid centers between **a)** ethyl ammonium nitrogen and nitrate nitrogen centers, and **b)** nitrate nitrogen and ethyl ammonium nitrogen centers; Surface colors represent positional probabilities of finding the opposing nitrogen ranging from dark red, fully transparent over blue to bright green, fully opaque colors. Note that for clarity only probabilities larger than 10% of the probability distribution peak maximum over all directions are plotted.

With partial charges reduced to a single point charge and point dipole at ellipsoid centers the most likely interaction between the ethyl ammonium ion and the nitrate counterion is in a direction perpendicular to the planes spanned by the hydrogens on the ammonium group and the oxygens on the nitrate.

This behavior is not representative of experimental data. Experimental interaction sites are located around individual ammonium hydrogens and nitrate oxygens.[44] However, when fully-atomistic partial charges are used the experimental interaction behavior can be observed as displayed in figure 4.16. Therefore, in ionic systems with strongly localized ionic charges a simple multipole expansion needs to be avoided.

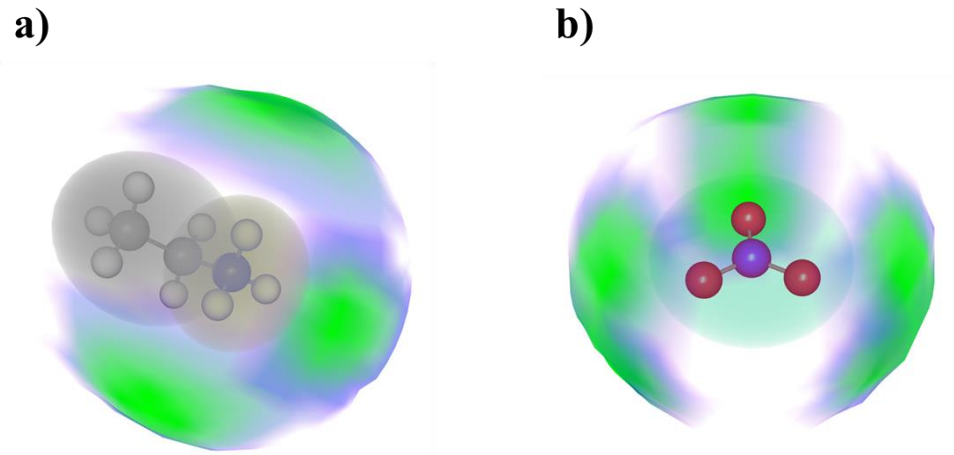

Figure 4.16: Spatial distribution function using fully-atomistic partial charges at original atom centers between **a)** ethyl ammonium nitrogen and nitrate nitrogen centers, and **b)** nitrate nitrogen and ethyl ammonium nitrogen centers; Surface colors represent positional probabilities of finding the opposing nitrogen ranging from dark red, fully transparent over blue to bright green, fully opaque colors. Note that for clarity only probabilities larger than 10% of the probability distribution peak maximum over all directions are plotted.

4.6 DIELECTRIC BEHAVIOR OF POLED AND UNPOLED SYSTEMS OF YLD124

The YLD124 chromophore is one of the workhorse organic non-linear optical chromophores with extensively published results wherein YLD124 is typically embedded in a host system.[45–53] Only very recently has it been used as a neat material.[54]

In this section, results of neat YLD124 systems simulated with and without an external poling field are presented. Fully-atomistic models of both enantiomers of YLD124[7] were obtained using the Gaussian 09D[28] package with the B3LYP/6-31G(d) functional in vacuum and CHELPG charges at atom locations in conjunction with OPLS-AA parameters for Lennard-Jones radii and energies of individual atoms. Simulations consist of a total of 108 chromophores, 54 of each enantiomer, represented by 19 ellipsoids per chromophore. Intra-molecular interaction energies were calculated from second-nearest neighbors and up, in accordance to settings used for the hydrocarbon chain simulations displayed in figure 2.16. Ellipsoids are connected at the bond locations determined by the AA model and only bond rotations are allowed, similarly to the hydrocarbon chain simulations. Partial charges of the underlying AA atom subset inside each ellipsoid were reduced to a point charge and a point dipole at the ellipsoid center. Simulations were run in the NPT ensemble under 1 atm pressure with electrostatics interactions attenuated by $n^2 = 1.7^2$ based on the experimental refractive index. The AVA method[38] (see chapter 3) was utilized throughout.

Note that ellipsoid parameters and LJ energies were obtained using an earlier set of LoD rules (i.e. prior to chapter 2) with volumes typically within 10% of the current rule set and constant LJ

[7] The CF_3-phenyl moieties can be placed on either side of the TCF-acceptor.

energies typically within a factor of two (see Appendix B for model parameters). Equilibrium densities of the presented simulations are within 10% of a simulation with the current ruleset.

When an independent chromophore is placed in an electric field with free rotations in three dimensions its first three average order moments with respect to the electric field are given by the following Langevin order parameters:[10,55,56]

$$\begin{aligned} \langle \cos\theta \rangle_{3D} &= \coth f - f^{-1} \\ \langle \cos^2\theta \rangle_{3D} &= 1 + 2f^{-2} - 2f^{-1}\coth f \\ \langle \cos^3\theta \rangle_{3D} &= \coth f - 3f^{-1} + 6f^{-2}\coth f - 6f^{-3} \end{aligned} \tag{4-36}$$

Here, θ is the angle between the chromophore dipole μ and the electric field E_0, $f = \frac{\mu E_0}{kT}$ is the characteristic parameter at a given temperature T.

In an ensemble of interacting chromophores the relations of equation (4-36) typically overestimate the actually achieved order parameters. In analogy to Kirkwood's introduction of the Kirkwood correlation factor g_K to the calculation of the dielectric constant in equation (4-35) describing effective dipole alignment the Kirkwood correlation factor is introduced to give an effective Kirkwood-Langevin parameter:

$$f_{eff} = \frac{\mu E_0}{kT} g_K = \frac{3\varepsilon}{2\varepsilon + 1} \frac{\mu E}{kT} g_K \tag{4-37}$$

Figure 4.17 displays simulation results depicting the temperature dependence of the average cosine of the angle between the overall, fixed chromophore core dipole (blue center ellipsoids) and the external electric poling field of magnitude $E = 100 \frac{V}{\mu m}$. Langevin order for $\langle \cos\theta \rangle_{3D}$ using equation (4-36) is displayed. Additionally, a single parameter fit to the effective Kirkwood-Langevin order $\langle \cos\theta \rangle$ using the parameter f_{eff} from equation (4-37) yielding $g_K = 0.44 \pm 0.01$

is shown matching the simulated order well over the temperature range. Furthermore, the same value of g_K obtained from the fit to $\langle \cos\theta \rangle$ also matches the order parameters $\langle \cos^2\theta \rangle$ and $\langle \cos^3\theta \rangle$ across the entire temperature range.

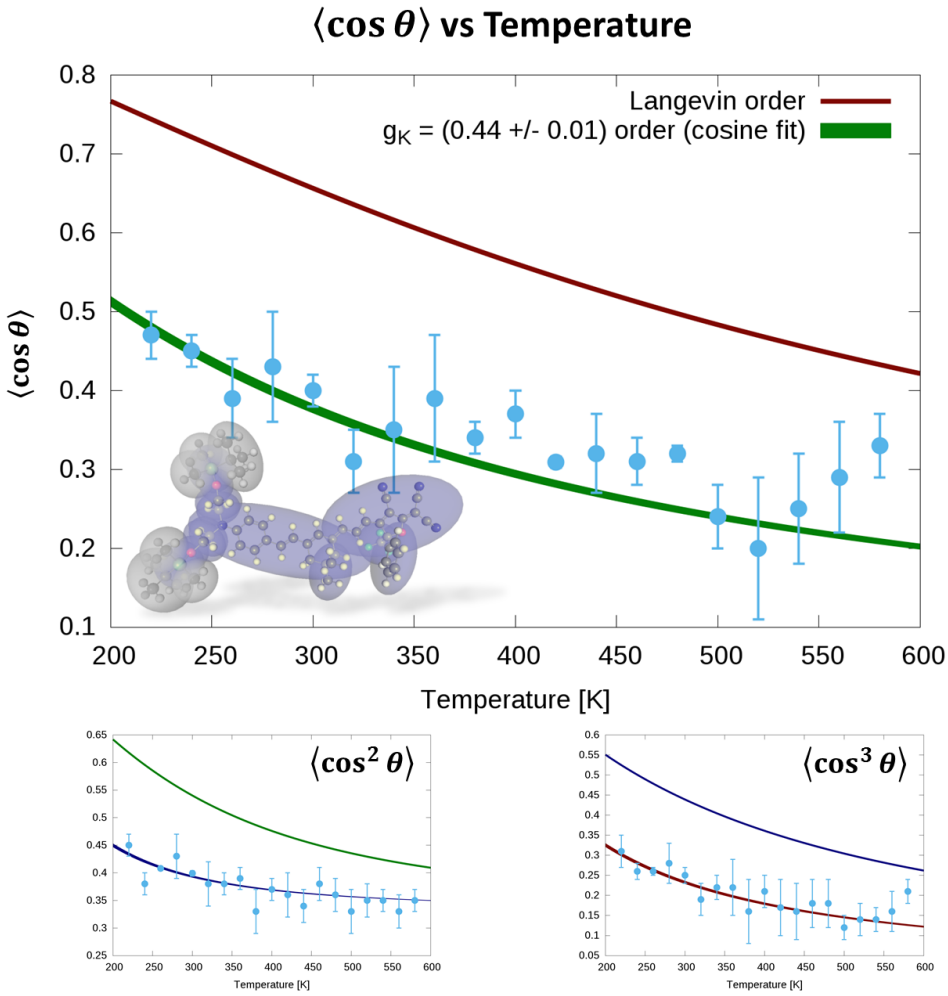

Figure 4.17: Simulated temperature dependence of the average cosine of the angle between overall chromophore dipole moment and external poling field for poled YLD124 systems each containing 108 chromophores; Also shown are traces corresponding Langevin order and to the effective Langevin order scaled by the Kirkwood correlation factor g_K fit to the average cosine order for average $\langle \cos\theta \rangle$, $\langle \cos^2\theta \rangle$, and $\langle \cos^3\theta \rangle$ order parameters.

With the Kirkwood correlation factor determined a calculation of the dielectric constant using the Kirkwood-Fröhlich equation (4-35) can be undertaken. Figure 4.18 shows the results of the thus

obtained dielectric constants over the entire temperature range (green filled curve) matching the simulation dielectric constants (red dots with solid line) calculated using the direct calculation approach from equation (4-3). Also displayed are dielectric constants calculated from the total dipole moment fluctuation using equations (4-10) for poled and (4-11) for unpoled systems.

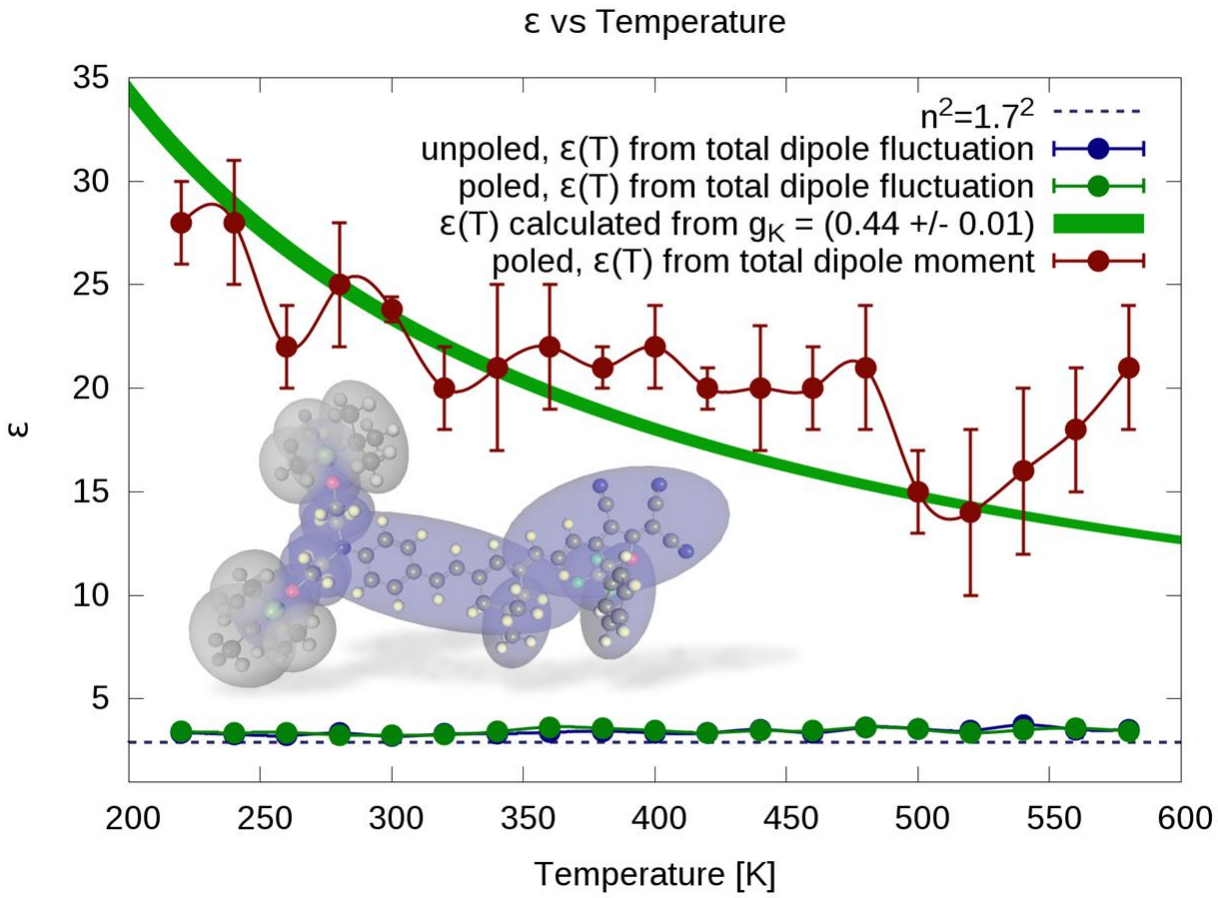

Figure 4.18: Simulated temperature dependence of the dielectric constant of unpoled and poled YLD124 systems each containing 108 chromophores; for the poled system dielectric constants a trace corresponding to the dielectric constant obtained using the Kirkwood-Fröhlich equation using the Kirkwood correlation factor g_K fit in figure 4.17

The dielectric constants obtained using the fluctuation approach (blue and green dots with solid lines) show identical values within their respective error bars slightly above $n^2 = 2.89$ (dashed line). These relatively low dielectric constants correspond to a system that in the simulation

environment cannot move easily, a feature of many dense system simulations. In order for the dipole fluctuations to reach realistic levels, unpoled simulations would have to be run unpractically long (see TCP-Me system order equilibration in chapter 3). Fortunately, for poled systems simulated using AVA, equilibrium order can be achieved more rapidly and the dielectric constants thus obtained can be used.

This notion can be further investigated when, instead of varying temperature, the electric field strength is varied. Figure 4.19 shows simulation results of the dielectric constant at a constant temperature of $400\ K$ but with varying electric field strengths.

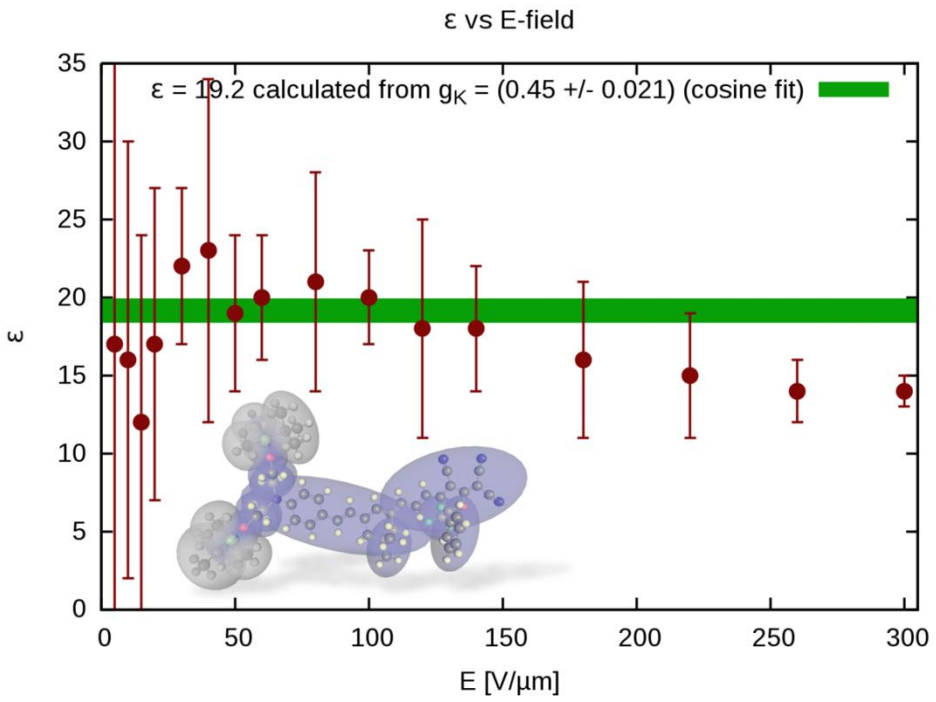

Figure 4.19: Simulated electric field dependence of the dielectric constant of a poled YLD124 system containing 108 chromophores; Also shown is a filled curve corresponding the dielectric constant calculated from g_K obtained from a fit to the average cosine order to the effective Langevin order

Simulations were conducted using traditional NPT ensembles from the first cycle as well as using AVA for the first 40 kcycles dropping the system off at a density of about $0.4\,\frac{g}{cc}$. The displayed averages are Boltzmann-weighted averages using the overall system energy difference between simulations referenced to the first simulation, $e^{-\Delta U_{0i}/kT}$, with $\Delta U_{0i} = U_i - U_0$, in order to avoid numerical problems with large exponents. As previously observed for simulations using AVA, overall system energies were lower compared to traditional NPT simulations.

The dielectric constants calculated directly from the overall dipole moment (red dots with error bars) match the dielectric constant calculated using the Kirkwood-Fröhlich equation (4-35) within the respective error bars up to a field strength of $220\,\frac{V}{\mu m}$ after which the directly calculated dielectric constants drop off somewhat.

The average dielectric constant in conjunction with an estimate of the first-order hyperpolarizability, $\beta_{zzz}(-\omega, 0, \omega)$, and some additional, experimentally available parameters is all that is needed to calculate the electro-optic activity of a chromophore system:[10,49]

$$r_{33} = \frac{2g(\omega,\varepsilon)}{n_\omega^4}\beta_{zzz}(-\omega,0,\omega)\rho_N\langle\cos^3\theta\rangle \text{ with } g(\omega,\varepsilon) = \frac{\varepsilon(n_0^2+2)}{2\varepsilon+n_0^2}\left(\frac{n_\omega^2+2}{3}\right)^2 \qquad (4\text{-}38)$$

Here, ω is the frequency of light passed through a device, n_ω is the refractive index at that operating frequency, ε is the static dielectric constant, and n_0 is the extrapolated zero-frequency refractive index.

For the given CLD-type chromophore systems measured at $1310\ nm$ one can combine the measured parameters and perform unit conversions in order to arrive at the more easily used approximate formula for r_{33}:

$$r_{33}\left[\frac{pm}{V}\right] = 42\,\frac{\beta_{zzz}(-\omega,0,\omega)}{1000\cdot 10^{-30}\ esu}\,\frac{\rho_N\langle\cos^3\theta\rangle}{10^{20}\,\frac{molecules}{cc}} \tag{4-39}$$

The simulations provide values for the chromophore loading, $\rho_N\langle\cos^3\theta\rangle$, in conjunction with an estimate of $\beta_{zzz} = 8100\cdot 10^{-30}\ esu$ the resulting electro-optic activity r_{33} is displayed in figure 4.20. Additionally, traces of the electro-optic activity using Langevin order $\langle\cos^3\theta\rangle_{3D}$ from equation (4-36) and with the effective Langevin order using the Kirkwood-Langevin parameter from equation (4-37) with g_K obtained from a fit to the average cosine order.

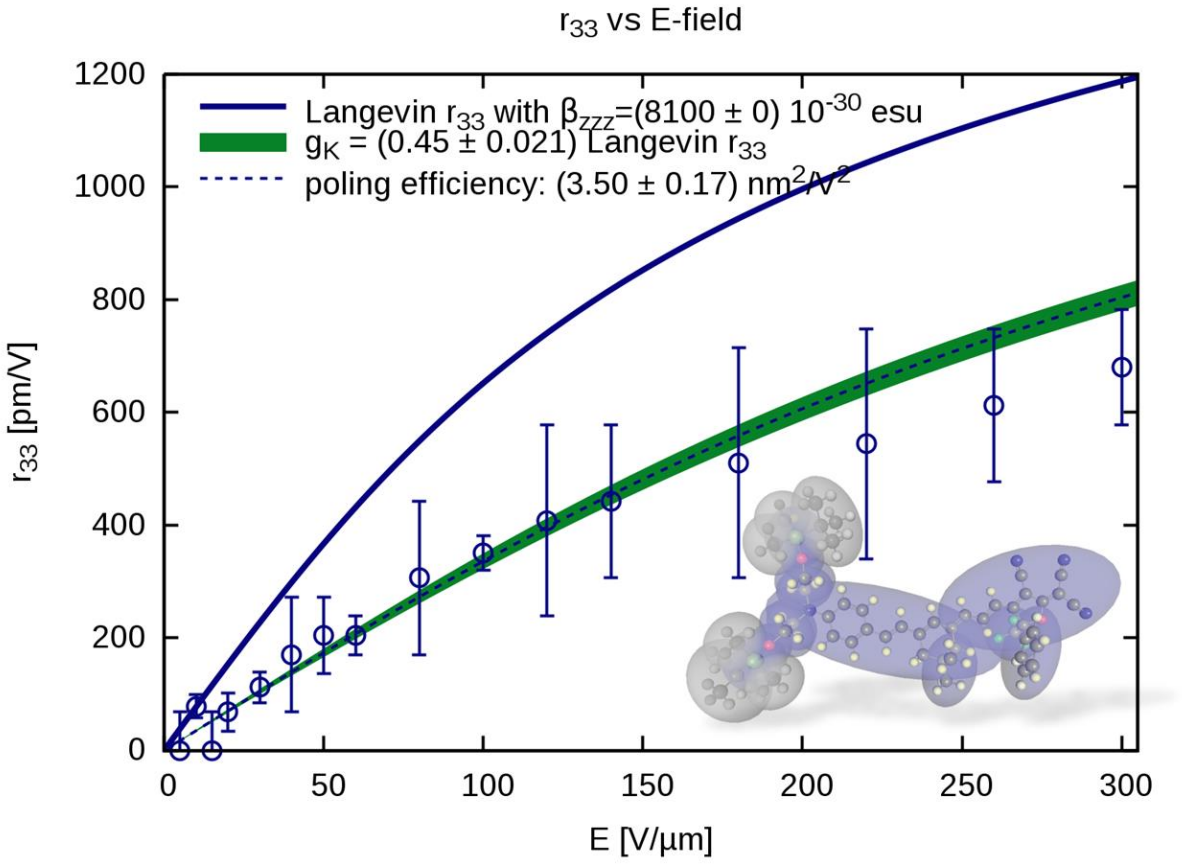

Figure 4.20: Simulated electric field dependence of the electro-optic activity, r_{33}, of a poled YLD124 system containing 108 chromophores; also shown are traces corresponding to r_{33} under Langevin order and under Langevin order scaled by the Kirkwood correlation factor g_K

The simulated poling efficiency of $3.5 \pm 0.2 \frac{nm^2}{V^2}$ is much larger than the experimentally obtained poling efficiency of $1.9 \pm 0.2 \frac{nm^2}{V^2}$.[54] The difference could be explained either by too large of an estimate for β_{zzz} or by simulation order that is much higher than the experimentally observed order. An estimate for the first-order hyperpolarizability matching the experimental value while maintaining the simulated chromophore loading would be $\beta_{zzz} = 4400 \cdot 10^{-30}\ esu$. Without any other information this number does not sound unreasonable.

However, experimental data exists of a similar chromophore, JRD1, which has been modified slightly from YLD124 by substituting diphenyl moieties for the dimethyl moieties on the YLD124's donor attachment.[54] This substitution, from a tert-Butyldimethylsilyl (TBDMS) ether to a tert-Butyldiphenylsilyl (TBDPS) ether, is not coupled into the electro-optically active region of the chromophore and therefore is not expected to change the molecular first-order hyperpolarizability.

The experimentally observed poling efficiency of JRD1[54] is 3.4 ± 0.2, in conjunction with the simulated chromophore loading fit using the effective Kirkwood-Langevin g_K, it can be used to arrive at an estimate of $\beta_{zzz} = (8500 \pm 700) \cdot 10^{-30}\ esu$ as depicted in figure 4.21.

This estimated value of the first-order hyperpolarizability, combining theoretical results with experimental observation, indicates that the observed performance of YLD124 is caused by lower chromophore loading. Together with the theoretical observation that equilibrium acentric order and chromophore loading of both YLD124 and JRD1 are identical within their respective error bars, this leads to the conclusion that YLD124 is kinetically trapped in comparison to JRD1.

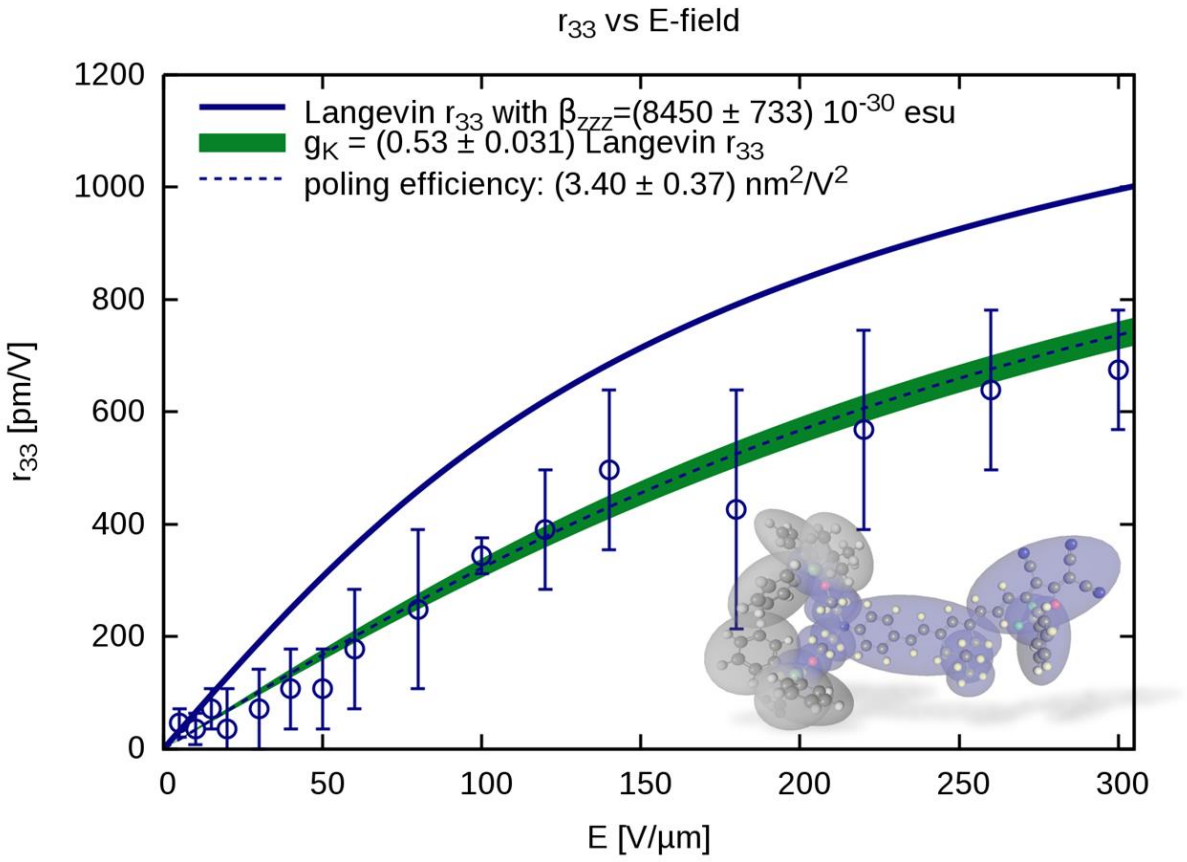

Figure 4.21: Simulated electric field dependence of the electro-optic activity, r_{33}, of a poled JRD1 system containing 108 chromophores; also shown are traces corresponding to r_{33} under Langevin order and under Langevin order scaled by the Kirkwood correlation factor g_K

4.7 CONCLUSIONS

In conclusion, equations for the determination of dielectric constants from simulation results were derived and were applied to a wide variety of molecules. Additionally, an enhanced reaction field description consistent with the Onsager reaction field was introduced that allows the usage of both point charges and point dipoles, and their interaction, as well as being stable for use in net-neutral systems with ionic molecules.

As a first test case, simulations of the dielectric behavior of acetonitrile were used as a benchmark to investigate the LoD approach outlined in chapter 2. Two fully-atomistic force field descriptions, OPLS-AA and an OPLS-AA based model using atomic geometries and charges of a coupled-cluster calculation, were utilized. In both cases, the fully-atomistic behavior was matched by the two-ellipsoid LoD model, a result similar to the observations made in chapter 3 for a CLD-type system. Furthermore, for the CCSD-based AA model simulations over a wide temperature range were performed and phase transitions within $20\ K$ (6%) of the experimental value were observed for the AA system as well as for the two-ellipsoid LoD representation.

Simulation results of ethylene carbonate revealed an even more impressive correspondence of the two-ellipsoid LoD model with fully-atomistic behavior. The experimental dielectric constant of ethylene carbonate was successfully matched by theory with the current LoD rule set by both single and two-ellipsoid LoD models.

Ethyl ammonium nitrate, believed to be the first reported room-temperature ionic liquid, was used to demonstrate the ability to simulate ionic systems. Fully-atomistic charges were needed for the system to behave similar to experimental observations. The experimental dielectric constant of ethyl ammonium nitrate could be matched within the error bar by using the

Kirkwood-Fröhlich equation in conjunction with a determination of the Kirkwood correlation factor g_K from correlations in the simulated trajectories.

Finally, the dielectric behavior of two related, complex ONLO chromophore systems, YLD124 and JRD1, was studied. In conjunction with an effective Langevin order parameter the Kirkwood correlation factor g_K was obtained and used in the description of overall electro-optic activity of those chromophores. By combining theoretical results and experimental observations it could be concluded that YLD124 is kinetically trapped in comparison to JRD1.

4.8 REFERENCES FOR CHAPTER 4

[1] Ewald, P. P. Die Berechnung Optischer Und Elektrostatischer Gitterpotentiale. *Ann. Phys.* **1921**, *369* (3), 253–287.

[2] Onsager, L. Electric Moments of Molecules in Liquids. *J. Am. Chem. Soc.* **1936**, *58* (8), 1486–1493.

[3] Smith, P. E.; Pettitt, B. M. Ewald Artifacts in Liquid State Molecular Dynamics Simulations. *J. Chem. Phys.* **1996**, *105* (10), 4289–4293.

[4] Hünenberger, P. H.; McCammon, J. A. Effect of Artificial Periodicity in Simulations of Biomolecules under Ewald Boundary Conditions: A Continuum Electrostatics Study. *Biophys. Chem.* **1999**, *78* (1–2), 69–88.

[5] Weber, W.; Hünenberger, P. H.; McCammon, J. A. Molecular Dynamics Simulations of a Polyalanine Octapeptide under Ewald Boundary Conditions: Influence of Artificial Periodicity on Peptide Conformation. *J. Phys. Chem. B* **2000**, *104* (15), 3668–3675.

[6] Tobias, D. J. Electrostatics Calculations: Recent Methodological Advances and Applications to Membranes. *Curr. Opin. Struct. Biol.* **2001**, *11* (2), 253–261.

[7] Fukuda, I.; Nakamura, H. Non-Ewald Methods: Theory and Applications to Molecular Systems. *Biophys. Rev.* **2012**, *4* (3), 161–170.

[8] Barker, J. A.; Watts, R. O. Monte Carlo Studies of the Dielectric Properties of Water-like Models. *Mol. Phys.* **1973**, *26* (3), 789–792.

[9] Johnson, L. E.; Barnes, R.; Draxler, T. W.; Eichinger, B. E.; Robinson, B. H. Dielectric Constants of Simple Liquids: Stockmayer and Ellipsoidal Fluids. *J. Phys. Chem. B* **2010**, *114* (25), 8431–8440.

[10] Johnson, L. E. Multi-Scale Modeling of Organic Electro-Optic Materials, University of Washington, 2012.

[11] Neumann, M. Dipole Moment Fluctuation Formulas in Computer Simulations of Polar Systems. *Mol. Phys.* **1983**, *50* (4), 841–858.

[12] Kirkwood, J. G. The Dielectric Polarization of Polar Liquids. *J. Chem. Phys.* **1939**, *7* (10), 911–919.

[13] Fröhlich, H. *Theory of Dielectrics: Dielectric Constant and Dielectric Loss*; Clarendon Press, 1958.

[14] Griffiths, D. J. *Introduction to Electrodynamics*, 4 edition.; Addison-Wesley: Boston, 2012.

[15] Neumann, C. *Hydrodynamische untersuchungen: nebst einem Anhange über die Probleme der Elektrostatik und der magnetischen Induction*; B.G. Teubner, 1883.

[16] Cai, W.; Deng, S.; Jacobs, D. Extending the Fast Multipole Method to Charges inside or Outside a Dielectric Sphere. *J. Comput. Phys.* **2007**, *223* (2), 846–864.

[17] Lin, Y.; Baumketner, A.; Deng, S.; Xu, Z.; Jacobs, D.; Cai, W. An Image-Based Reaction Field Method for Electrostatic Interactions in Molecular Dynamics Simulations of Aqueous Solutions. *J. Chem. Phys.* **2009**, *131* (15), 154103.

[18] Lin, Y.; Baumketner, A.; Song, W.; Deng, S.; Jacobs, D.; Cai, W. Ionic Solvation Studied by Image-Charge Reaction Field Method. *J. Chem. Phys.* **2011**, *134* (4), 044105.

[19] Allen, M. P.; Tildesley, D. J. *Computer Simulation of Liquids*; Clarendon Press ; Oxford University Press: Oxford [England]; New York, 1989.

[20] *CRC Handbook of Chemistry and Physics, 96th Edition*; CRC Press, 2014.

[21] Edwards, D. M. F.; Madden, P. A.; McDonald, I. R. A Computer Simulation Study of the Dielectric Properties of a Model of Methyl Cyanide: I. The Rigid Dipole Case. *Mol. Phys.* **1984**, *51* (5), 1141–1161.

[22] Pounds, M. A.; Madden, P. A. Are Dipolar Liquids Ferroelectric? Simulation Studies. *J. Chem. Phys.* **2007**, *126* (10), 104506.

[23] Stockmayer, W. H. Second Virial Coefficients of Polar Gases. *J. Chem. Phys.* **1941**, *9* (5), 398–402.

[24] Goldman, S. Determination of Static Dielectric Constant-Temperature-Density Surfaces of a Stockmayer Fluid by Perturbation Theory. *Mol. Phys.* **1990**, *71* (3), 491–507.

[25] Bartke, J.; Hentschke, R. Dielectric Properties and the Ferroelectric Transition of the Stockmayer-Fluid via Computer Simulation. *Mol. Phys.* **2006**, *104* (19), 3057–3068.

[26] Bartke, J.; Hentschke, R. Phase Behavior of the Stockmayer Fluid via Molecular Dynamics Simulation. *Phys. Rev. E* **2007**, *75* (6).

[27] Jorgensen, W. L.; Maxwell, D. S.; Tirado-Rives, J. Development and Testing of the OPLS All-Atom Force Field on Conformational Energetics and Properties of Organic Liquids. *J. Am. Chem. Soc.* **1996**, *118* (45), 11225–11236.

[28] Frisch, M. J.; Trucks, G. W.; Schlegel, H. B.; Scuseria, G. E.; Robb, M. A.; Cheeseman, J. R.; Scalmani, G.; Barone, V.; Mennucci, B.; Petersson, G. A.; Nakatsuji, H.; Caricato, M.; Li, X.; Hratchian, H. P.; Izmaylov, A. F.; Bloino, J.; Zheng, G.; Sonnenberg, J. L.; Hada, M.; Ehara, M.; Toyota, K.; Fukuda, R.; Hasegawa, J.; Ishida, M.; Nakajima, T.; Honda, Y.; Kitao, O.; Nakai, H.; Vreven, T.; Montgomery Jr., J. A.; Peralta, J. E.; Ogliaro, F.; Bearpark, M. J.; Heyd, J.; Brothers, E. N.; Kudin, K. N.; Staroverov, V. N.; Kobayashi, R.; Normand, J.; Raghavachari, K.; Rendell, A. P.; Burant, J. C.; Iyengar, S. S.; Tomasi, J.; Cossi, M.; Rega, N.; Millam, N. J.; Klene, M.; Knox, J. E.; Cross, J. B.; Bakken, V.; Adamo, C.; Jaramillo, J.; Gomperts, R.; Stratmann, R. E.; Yazyev, O.; Austin, A. J.; Cammi, R.; Pomelli, C.; Ochterski, J. W.; Martin, R. L.; Morokuma, K.; Zakrzewski, V. G.; Voth, G. A.; Salvador, P.; Dannenberg, J. J.; Dapprich, S.; Daniels, A. D.; Farkas, Ö.; Foresman, J. B.; Ortiz, J. V.; Cioslowski, J.; Fox, D. J. *Gaussian 09*; Gaussian, Inc.: Wallingford, CT, USA, 2009.

[29] Tassios, D. *Applied Chemical Engineering Thermodynamics*; Springer, 2013.

[30] JOBACK, K. G.; REID, R. C. Estimation of Pure-Component Properties from Group-Contributions. *Chem. Eng. Commun.* **1987**, *57* (1-6), 233–243.

[31] Stein, S. E.; Brown, R. L. Estimation of Normal Boiling Points from Group Contributions. *J. Chem. Inf. Comput. Sci.* **1994**, *34* (3), 581–587.

[32] Dearden, J. C. Quantitative Structure-Property Relationships for Prediction of Boiling Point, Vapor Pressure, and Melting Point. *Environ. Toxicol. Chem.* **2003**, *22* (8), 1696–1709.

[33] Rebelo, L. P. N.; Canongia Lopes, J. N.; Esperança, J. M. S. S.; Filipe, E. On the Critical Temperature, Normal Boiling Point, and Vapor Pressure of Ionic Liquids. *J. Phys. Chem. B* **2005**, *109* (13), 6040–6043.

[34] Bukowski, R.; Szalewicz, K.; Chabalowski, C. F. Ab Initio Interaction Potentials for Simulations of Dimethylnitramine Solutions in Supercritical Carbon Dioxide with Cosolvents. *J. Phys. Chem. A* **1999**, *103* (36), 7322–7340.

[35] Sum, A. K.; Sandler, S. I.; Bukowski, R.; Szalewicz, K. Prediction of the Phase Behavior of Acetonitrile and Methanol with Ab Initio Pair Potentials. I. Pure Components. *J. Chem. Phys.* **2002**, *116* (17), 7627–7636.

[36] Sum, A. K.; Sandler, S. I.; Bukowski, R.; Szalewicz, K. Prediction of the Phase Behavior of Acetonitrile and Methanol with Ab Initio Pair Potentials. II. The Mixture. *J. Chem. Phys.* **2002**, *116* (17), 7637–7644.

[37] Chernyak, Y. Dielectric Constant, Dipole Moment, and Solubility Parameters of Some Cyclic Acid Esters. *J. Chem. Eng. Data* **2006**, *51* (2), 416–418.

[38] Tillack, A. F.; Johnson, L. E.; Rawal, M.; Dalton, L. R.; Robinson, B. H. Modeling Chromophore Order: A Guide For Improving EO Performance. In *Symposium II/JJ/KK – Materials, Processes and Devices for Nanophotonics, Nonlinear Optics and Resonant Optics*; MRS Online Proceedings Library; 2014; Vol. 1698.

[39] Peppel, W. J. Preparation and Properties of the Alkylene Carbonates. *Ind. Eng. Chem.* **1958**, *50* (5), 767–770.

[40] Walden, P. Ueber Die Molekulargrösse Und Elektrische Leitfähigkeit Einiger Geschmolzenen Salze. *Извуатстія Императорской Академіи Наукъ VI Серія* **1914**, *8* (6), 405–422.

[41] Schurr, J. M. Dielectric Relaxation and Depolarized Dynamic Light Scattering of a Generalized Debye Model Fluid. *Mol. Phys.* **1980**, *40* (5), 1025–1051.

[42] Weingärtner, H.; Knocks, A.; Schrader, W.; Kaatze, U. Dielectric Spectroscopy of the Room Temperature Molten Salt Ethylammonium Nitrate. *J. Phys. Chem. A* **2001**, *105* (38), 8646–8650.

[43] Allen, M.; Evans, D. F.; Lumry, R. Thermodynamic Properties of the Ethylammonium Nitrate + Water System: Partial Molar Volumes, Heat Capacities, and Expansivities. *J. Solut. Chem.* **1985**, *14* (8), 549–560.

[44] Umebayashi, Y.; Chung, W.-L.; Mitsugi, T.; Fukuda, S.; Takeuchi, M.; Fujii, K.; Takamuku, T.; Kanzaki, R.; Ishiguro, S. Liquid Structure and the Ion-Ion Interactions of Ethylammonium Nitrate Ionic Liquid Studied by Large Angle X-Ray Scattering and Molecular Dynamics Simulations. *J. Comput. Chem. Jpn.* **2008**, *7* (4), 125–134.

[45] Baehr-Jones, T.; Hochberg, M.; Wang, G.; Lawson, R.; Liao, Y.; Sullivan, P. A.; Dalton, L.; Jen, A.-Y.; Scherer, A. Optical Modulation and Detection in Slotted Silicon Waveguides. *Opt. Express* **2005**, *13* (14), 5216–5226.

[46] Pereverzev, Y. V.; Gunnerson, K. N.; Prezhdo, O. V.; Sullivan, P. A.; Liao, Y.; Olbricht, B. C.; Akelaitis, A. J. P.; Jen, A. K.-Y.; Dalton, L. R. Guest−Host Cooperativity in Organic Materials Greatly Enhances the Nonlinear Optical Response. *J. Phys. Chem. C* **2008**, *112* (11), 4355–4363.

[47] Benight, S. J.; Bale, D. H.; Olbricht, B. C.; Dalton, L. R. Organic Electro-Optics: Understanding Material Structure/function Relationships and Device Fabrication Issues. *J. Mater. Chem.* **2009**, *19* (40), 7466.

[48] Dalton, L. R.; Sullivan, P. A.; Bale, D. H. Electric Field Poled Organic Electro-Optic Materials: State of the Art and Future Prospects. *Chem. Rev.* **2010**, *110* (1), 25–55.

[49] Sullivan, P. A.; Dalton, L. R. Theory-Inspired Development of Organic Electro-Optic Materials. *Acc. Chem. Res.* **2010**, *43* (1), 10–18.

[50] Dalton, L. R.; Benight, S. J.; Johnson, L. E.; Knorr, D. B.; Kosilkin, I.; Eichinger, B. E.; Robinson, B. H.; Jen, A. K.-Y.; Overney, R. M. Systematic Nanoengineering of Soft Matter Organic Electro-Optic Materials. *Chem. Mater.* **2011**, *23* (3), 430–445.

[51] Kim, S.-K.; Pei, Q.; Fetterman, H. R.; Olbright, B. C.; Dalton, L. R. Photoassisted Corona Poled YLD-124/DR1-Co-PMMA Electrooptic Device Using Photoisomerization. *IEEE Photonics Technol. Lett.* **2011**, *23* (13), 845–847.

[52] Dalton, L.; Benight, S. Theory-Guided Design of Organic Electro-Optic Materials and Devices. *Polymers* **2011**, *3* (4), 1325–1351.

[53] Benight, S. J.; Robinson, B. H.; Dalton, L. R.; Meghea, A. Nano-Engineering of Molecular Interactions in Organic Electro-Optic Materials. *Mol. Interact.* **2012**.

[54] Jin, W.; Johnston, P. V.; Elder, D. L.; Tillack, A. F.; Olbricht, B. C.; Song, J.; Reid, P. J.; Xu, R.; Robinson, B. H.; Dalton, L. R. Benzocyclobutene Barrier Layer for Suppressing Conductance in Nonlinear Optical Devices during Electric Field Poling. *Appl. Phys. Lett.* **2014**, *104* (24), 243304.

[55] Robinson, B. H.; Dalton, L. R. Monte Carlo Statistical Mechanical Simulations of the Competition of Intermolecular Electrostatic and Poling-Field Interactions in Defining Macroscopic Electro-Optic Activity for Organic Chromophore/Polymer Materials. *J. Phys. Chem. A* **2000**, *104* (20), 4785–4795.

[56] Benight, S. J.; Johnson, L. E.; Barnes, R.; Olbricht, B. C.; Bale, D. H.; Reid, P. J.; Eichinger, B. E.; Dalton, L. R.; Sullivan, P. A.; Robinson, B. H. Reduced Dimensionality in Organic Electro-Optic Materials: Theory and Defined Order. *J. Phys. Chem. B* **2010**, *114* (37), 11949–11956.

5 Simulation Results of TCF-based Electro-Optic Chromophore Systems

5.1 Introduction

This chapter represents the bulk of the simulation work performed on electro-optic chromophore systems using the tricyanofuran (TCF) acceptor. The TCF acceptor[1,2] and its related, stronger analogues, TCF-CF_3[3] and TCF-CF_3-Phenyl,[4,5] have been used in a variety of organic non-linear optical chromophores with large electro-optic activities able to achieve device drive voltages below $V_\pi < 1\ V$.[6–12]

5.2 Methodology

Fully-atomistic model geometries were obtained using the Gaussian 09D[13] package with the B3LYP/6-31G(d) functional in vacuum based on the methodology developed by Dr. Lewis Johnson.[14] Additionally, CHELPG charges at atom locations calculated using Gaussian 09D[13] in conjunction with OPLS-AA parameters for Lennard-Jones radii and energies of individual atoms were utilized.

Intra-molecular interaction energies were calculated from second-nearest neighbors and up, in accordance to settings used for the hydrocarbon chain simulations displayed in figure 2.16. LoD ellipsoids were connected at the bond locations determined by the AA model and only bond

rotations are allowed, similarly to the aforementioned hydrocarbon chain simulations. Partial charges of the underlying AA atom subset inside each ellipsoid were reduced to a point charge and a point dipole at the ellipsoid center. Simulations were run in the NPT ensemble with electrostatics interactions attenuated by $n^2 = 1.7^2$, representing the typical experimental refractive index of these chromophore systems, the reaction field approach presented in chapter 4 was used throughout. Furthermore, all simulation results presented in this chapter were simulated with an external poling field of $100\,\frac{V}{\mu m}$.

The present results represent hundreds of individual simulation runs performed over a time period during which the final rule set of the LoD approach was still emerging. Particularly, the best fit Lennard-Jones potential energy values and their associated combination rules were not yet fully developed. For this reason, all simulations were performed with a constant value of the Lennard-Jones energy, ε_{LoD}, calculated for each LoD ellipsoid from the underlying subset of atoms in a simplified way based on the far-range limit of the LJ energy.

When the interaction distance r_T is much larger than the average ellipsoid size $\langle\sigma_{LoD}\rangle$, the LJ energy asymptotes towards the following upper limit:

$$\varepsilon_{far} \stackrel{\text{def}}{=} \lim_{r_T \gg \langle\sigma_{LoD}\rangle} \varepsilon_{LoD}(r_T) = \left(\sum_{i=1}^{N} \sqrt{\varepsilon_i}\right)^2 \geq \sum_{i=1}^{N} \varepsilon_i \qquad (5\text{-}1)$$

Here, ε_i are the LJ potential energies of the underlying subset of N atoms. In chapter 2 it was shown that ε_{far} is an upper limit to $\varepsilon_{LoD}(r_T)$ (figure 2.9). The right-hand term of the inequality in equation (5-1) fulfills this requirement and could therefore be used to estimate ε_{LoD}:

$$\sqrt{\varepsilon_{far}} \geq \sqrt{N}\sqrt{\frac{1}{N}\sum_{i=1}^{N}\left(\sqrt{\varepsilon_i}\right)^2} = \sqrt{\varepsilon_{LoD}} \tag{5-2}$$

This result can be interpreted as the root sum of squares (RSS) of the individual atomic LJ energy contributions, $\sqrt{\varepsilon_i}$, using the standard LJ energy combination rule $\varepsilon_{iT} = \sqrt{\varepsilon_i \varepsilon_T}$.

A downside to the RSS approach in equation (5-2) is that it gives equal weight to each atom. At closer range, physical LJ interactions are predominantly with atoms close to the surface and inner atoms do not contribute significantly to the overall interaction energy.[1] This can be reflected by adding weights to the RSS approach which are larger the closer an underlying atom's surface is to the ellipsoid surface:

$$\sqrt{\varepsilon_{LoD}} = \sqrt{N}\sqrt{\frac{1}{N}\frac{\sum_{i=1}^{N} w_i \varepsilon_i}{\sum_{i=1}^{N} w_i}} \quad \text{with} \quad w_i = \frac{\|\vec{r}_i - \vec{r}_{LoD}\| + \frac{\sigma_i}{2}}{r_{LoD}^{Surface}(\vec{r}_i - \vec{r}_{LoD})} \tag{5-3}$$

Here, $(\vec{r}_i - \vec{r}_{LoD})$ is the vector from the LoD ellipsoid center to the i-th underlying atom center, $\frac{\sigma_i}{2}$ is the radius of the i-th underlying atom, and the function $r_{LoD}^{Surface}(\vec{r})$ is the distance from the LoD ellipsoid center to its surface in the direction of $\vec{r}$. The choice of weights satisfies the condition described above but better, more accurate weights may exist.[2]

Amazingly, however, the approach in equation (5-3) is able to yield values of the ellipsoidal Lennard-Jones energy parameter ε_{LoD} which are of similar magnitude (typically within a factor of two) than the more sophisticated approach of finding the best-fit value presented in chapter 2. More importantly, this approach was able to yield LJ energy which can now be classified as good enough compared to the final rule set – during the time period some of the simulations presented

[1] This notion is the basis of the GB-like "adjusted width" LJ LoD potential.
[2] For example, the best-fit LJ energy values could be used to determine them.

in this chapter were conducted it was the only available, reliable method for the estimation of LJ energy parameters for ellipsoids representing large collections of atoms.

5.3 C1 AND CLD-C1

The attachment of pendant groups containing benzoyl coumarins to electro-optic chromophores of the FTC and CLD-type has led to about a two- to threefold improvement in the macroscopic electro-optic activity.[15,16] Coumarin-containing polymers observe liquid crystalline stacking behavior with a stacking direction typically perpendicular to the direction of the light field.[17–21]

Experimental data suggests that poled films of C1 (FTC-based) and CLD-C1 (CLD-based) exhibit centrosymmetric chromophore order in the direction of an applied poling field with coumarin alignment perpendicular to the chromophore order.[15,16,22] Reported experimental poling efficiencies for C1 systems are $1.24\,\frac{nm^2}{V^2}$ on ITO and $1.92\,\frac{nm^2}{V^2}$ on TiO_2-coated ITO while CLD-C1 has a reported poling efficiency of $2.52\,\frac{nm^2}{V^2}$ on TiO_2-coated ITO, while no errors were reported for C1 systems, substantial errors of at least 25% were reported for values of CLD-C1.[15,16]

Simulations of both C1 and CLD-C1 systems were conducted with 108 chromophores per simulation in an NPT ensemble at $400\ K$ under a pressure of $1\ atm$ for simulations using AVA and $0.1\ atm$ for older simulations using traditional NPT[3]. The reaction field approach presented in chapter 4 was used and electrostatics interaction were attenuated by $n^2 = 1.7^2$. Fully-atomistic details were obtained using a DFT calculation as outlined in the methodology section.

[3] The slightly lower pressure slowed the condensation behavior and can be seen as a pre-cursor to AVA.

Figure 5.1 displays the LoD representations used for both molecules. Underlying atomic partial charges were reduced to a single charge and a point dipole at each ellipsoid center.

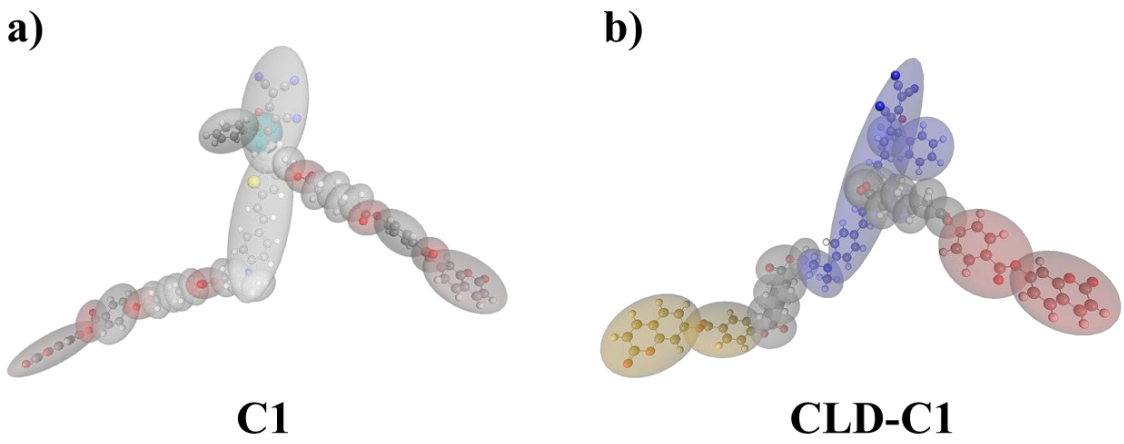

Figure 5.1: LoD representation used for **a)** C1 using 26 ellipsoids, and **b)** CLD-C1 using 24 ellipsoids

Note that the model used for C1 uses two more ellipsoids than the CLD-C1 LoD representation. It was later verified with small-scale CLD-C1 simulations (not included here) that the LoD representation with 24 ellipsoids produced identical results to the slightly more intricate representation using 26 ellipsoids. Since then, of course, the results presented in chapter 3 have shown that for the unprotected CLD-type chromophore core, with no pendant groups attached, the two-ellipsoid LoD representation is more accurate.

Table 5.1 gives an overview of basic simulation results for C1 and CLD-C1. Multiple simulation results of CLD-C1 are presented using the same LoD model but with slightly different prescriptions during the initial stages of the simulations. Most notable, a precursor to the AVA method (chapter 3) using a LJ potential for molecule-internal energy calculations similarly to equation (3-1) slowly ramping up the attractive part until about 80% of the final density was reached. An overall results row (light green) for CLD-C1 was calculated based on a Boltzmann-

weighted average using the overall system energies. Note that no correction based on the internal degrees of freedom was performed for heat capacities.

Table 5.1: C1 and CLD-C1 basic simulation results collection (density, heat capacity, and dielectric constant) sampled over last 40 kcycles of 240 kcycles of simulations. (See Appendix B for model parameters) Note that no correction for internal degrees of freedom for heat capacity results was performed.

Model	# sims	Density $[g/cc]$	H_{total} $[kJ/mol]$	c_P $[J/mol-K]$	Dielectric
C1[a,b]	17	0.98 ± 0.01	-160 ± 2	147 ± 27	16 ± 2
CLD-C1[a]	9	0.95 ± 0.01	-122 ± 7	223 ± 53	11 ± 5
CLD-C1[a,b]	13	0.95 ± 0.01	-118 ± 3	172 ± 58	11 ± 2
CLD-C1[c]	12	0.95 ± 0.01	-121 ± 3	176 ± 56	12 ± 1
CLD-C1[overall]	34	0.95 ± 0.01	-121 ± 4	187 ± 55	12 ± 2

[a]NPT at 0.1 atm, [b]repulsive internal LJ interactions during first 10 kcycles, [c]AVA for first 40 kcycles, NPT at 1 atm

Simulated densities are a little bit larger than expected from more recent simulations, particularly those of YLD124 and JRD1 systems presented in the next section which consistently yield densities of around 0.8 $\frac{g}{cc}$. This behavior, while certainly not unphysical, may be caused by a slight overestimation of the ellipsoid Lennard-Jones energies that have been calculated using equation (5-3). Interestingly, both the simulated system enthalpy magnitude and the value of the dielectric constant are increased by about 33% in C1 compared to CLD-C1 while the heat capacity of C1 is predicted to be lower by about 21%. Based on small-scale CLD-C1 simulations using a similarly partitioned model, the additional two ellipsoids used in the C1 model are responsible for the shift in energy. The differences in heat capacity and dielectric constant cannot be attributed to this effect, however, because the heat capacity decreases (stronger energy

fluctuations would increase it) and the dielectric constant increases instead of staying constant as C1's slightly lower dipole moment of about $22\ D$ compared to about $24\ D$ for CLD-C1 is compensated by the difference in number density. The increase in dielectric constant thus could be indicative of higher acentric order.

Table 5.2 lists average order parameters for C1 and CLD-C1 based on the angle, θ, of the fixed chromophore core dipole moment with the external electric field. Furthermore, estimates of C1 and CLD-C1 poling efficiencies using equation (4-39) with estimated first-order hyperpolarizabilities of $\beta_{zzz}^{1310\ nm}(C1) = 4050 \cdot 10^{-30} esu$ and $\beta_{zzz}^{1310\ nm}(CLD - C1) = 8100 \cdot 10^{-30} esu$ are included for comparison with experimental results. Note that errors on estimated poling efficiencies do not include error contributions from first-order hyperpolarizabilities.

Table 5.2: C1 and CLD-C1 average order related simulation results ($\langle P_2(\theta)\rangle$, $\langle\cos^3\theta\rangle$, $\rho_N\langle\cos^3\theta\rangle$ of 17 C1 and 34 CLD-C1 simulations, and estimated poling efficiency) sampled over last 40 kcycles of 240 kcycles of simulations.

Model	Chromophore $\langle P_2\rangle$	Coumarin $\langle P_2\rangle$	$\langle\cos^3\theta\rangle$	$\rho_N\langle\cos^3\theta\rangle$[d]	est. poling efficieny[e]
C1[a,b]	0.03 ± 0.05	0.01 ± 0.05	0.17 ± 0.04	0.75 ± 0.17	1.3 ± 0.3
CLD-C1[overall]	0.04 ± 0.05	-0.01 ± 0.05	0.15 ± 0.04	0.60 ± 0.17	2.0 ± 0.6

[a]NPT at 0.1 atm, [b]repulsive internal LJ interactions during first 10 kcycles, [c]AVA for first 40 kcycles, NPT at 1 atm, [d]in units of $10^{20}\ molecules/cc$, [e]in units of nm^2/V^2

Within error bars C1 and CLD-C1 exhibit identical theoretically predicted order parameters and chromophore loading. This is consistent with expectations since from a CG simulation perspective CLD-C1 and C1 are very similar with respect to their molecular shape and dipole distribution. What distinguishes both chromophores are their inherent first-order

hyperpolarizabilities. The estimated poling efficiency for CLD-C1 of $(2.0 \pm 0.7)\frac{nm^2}{V^2}$ is close to the experimental value[16] of $2.52\frac{nm^2}{V^2}$, especially when the experimentally observed error in the data of about 25% ($\pm 0.6\frac{nm^2}{V^2}$) is considered. The estimated theoretical poling efficiency for C1 of $(1.3 \pm 0.3)\frac{nm^2}{V^2}$ corresponds very well to reported data of C1 on ITO of $1.24\frac{nm^2}{V^2}$ but seems too low compared to the value on TiO_2-coated ITO of $1.92\frac{nm^2}{V^2}$.[15,16] However, if one were to assume an experimental error similar to that reported for CLD-C1 of 25% for the C1 results than the experimental results on ITO and TiO_2-coated ITO would exhibit overlapping error bars with each other and with the theoretical value. This seems consistent with results from a study using chromophores very similar to those used here, YLD124 and JRD1 on TiO_2-coated ITO, that did not observe improved poling results due to TiO_2 but exhibited similar errors.[23]

An important feature of the experimental reports on C1 and CLD-C1 is the centrosymmetric order parameter $\langle P_2(\theta)\rangle = \frac{1}{2}(3\langle\cos^2\theta\rangle - 1)$. The reported experimental values for C1 centrosymmetric order are $\langle P_2\rangle = 0.24$ for the chromophore core and $\langle P_2\rangle = -0.19$ for the coumarins.[16] Comparative data on CLD-C1 seems to be slightly inconclusive with reported values for the chromophore of $\langle P_2\rangle = 0.12, 0.29$ and opposite behavior for the coumarins of $\langle P_2\rangle = +0.08$.[16]

Theoretical data does not indicate a significant centrosymmetric order in the poling direction for chromophore cores or perpendicular to it for the coumarins when averaged over the entire data set (see table 5.2). For some hand-selected trajectories, however, when investigated using a Q-tensor analysis[24–27] to determine the direction of maximum centrosymmetric order, data sets can

be identified which exhibit increased centrosymmetric order for both the chromophore core and the coumarins.

Figure 5.2 shows the result of the Q-tensor data analysis of select trajectories for both C1 and CLD-C1. Shown is a unit sphere on which the order directors of the chromophore core (red dots) and of the coumarins (green dots) are placed. The centrosymmetric order parameter in each of these order directors is displayed as well. The $\langle P_2 \rangle$ values of 0.21 ± 0.02 and 0.12 ± 0.02 of the chromophore core centrosymmetric order of C1 and CLD-C1, respectively, compare well with the individual results observed in the experiment.

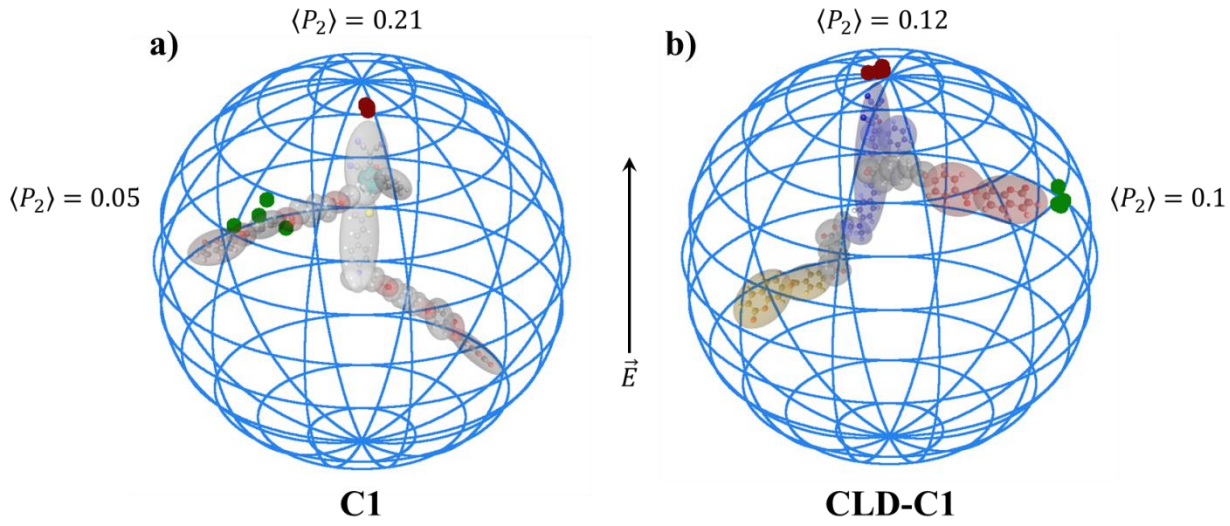

Figure 5.2: Major centrosymmetric order directions determined using a Q-tensor analysis of a select trajectory for **a)** C1, and **b)** CLD-C1 ; Red dots represent order directions for the chromophore core, green dots for coumarins. $\langle P_2 \rangle$ values for each director are provided for the particular analyses shown.

The directors of coumarin centrosymmetric order are rotated about $35° - 70°$ away from the chromophore order director with $\langle P_2 \rangle$ values between 0.05 ± 0.02 and 0.1 ± 0.02 corresponding to a predominantly perpendicular alignment with respect to the chromophore. This is consistent with the experimental observation.

Table 5.3 summarizes values obtained from the Q-tensor analysis averaged over the entire data set. Averages of $\langle P_2 \rangle = 0.06 \pm 0.12$ for the C1 chromophore core, $\langle P_2 \rangle = 0.07 \pm 0.10$ for the CLD-C1 chromophore, and $\langle P_2 \rangle = -0.01 \pm 0.10$ for both the C1 and the CLD-C1 set of coumarins were obtained. Within respective error bars, this data overlaps with the data presented in table 5.2 and also partially with experimental data, particularly with data reported for CLD-C1.

Table 5.3: Average Q-tensor centrosymmetric order results for chromophore core, overall coumarin order, and individual coumarins of 17 C1 and 34 CLD-C1 simulations over last 40 kcycles of 240 kcycles of simulations.

Model	Chromophore $\langle P_2 \rangle$	Donor Coumarin $\langle P_2 \rangle$	Bridge Coumarin $\langle P_2 \rangle$	Overall Coumarin $\langle P_2 \rangle$
C1[a,b]	0.06 ± 0.12	0.04 ± 0.13	0.03 ± 0.13	-0.01 ± 0.10
CLD-C1[overall]	0.07 ± 0.10	-0.05 ± 0.13	0.05 ± 0.12	-0.01 ± 0.10

[a]NPT at 0.1 atm, [b]repulsive internal LJ interactions during first 10 kcycles, [c]AVA for first 40 kcycles, NPT at 1 atm

In summary, C1 and CLD-C1 simulations were performed and average system properties determined. Estimations of overall poling efficiency, based on simulated acentric order and number density for C1 and CLD-C1, were consistent with experimental results of C1 on ITO and CLD-C1 on TiO_2-coated ITO. Furthermore, a Q-tensor analysis spanning the entire data set was undertaken. For the entire data set, resulting $\langle P_2 \rangle$ values only partially matched experimental values. However, for selected trajectories out of the entire data set, chromophore and coumarin centrosymmetric order parameters fully consistent with experimental values could be found. This observed strong variance in the centrosymmetric behavior, particularly for the coumarin moieties, may explain a similar fluctuation seen in experimental data points.

Overall, theoretical results match experimental acentric order well but seem to underestimate centrosymmetric order, especially for the coumarin moieties. The present work on C1 and CLD-

C1 used an earlier iteration of the now complete LoD rule set. In addition to using the current LoD approach, future work on C1 and CLD-C1 will focus on improving interactions between coumarins as the driving force for enhanced centrosymmetric order based on the approach used in chapter 2.5.1 successfully modeling the π-stacking interactions of benzene and hexafluorobenzene.

5.4 YLD124 AND JRD1

It is a wide-spread approach to embed electro-optic chromophores in a polymer host such as poly(methyl methacrylate) (PMMA) or amorphous polycarbonate (APC).[28–30] There are multiple benefits to such a strategy including material processability, EO chromophore protection from mechanical, chemical, as well as optical stresses, and possible adjustability of the composite material's glass transition temperature. Furthermore, for non-film forming chromophores this guest-host type architecture may be the only available route to a functioning EO material.

The downside of the guest-host approach, however, is a lowered EO chromophore number density compared to a neat material only consisting of EO chromophores. A diminished chromophore number density directly leads to a diminished electro-optic activity. A possible solution to this problem is to replace the electro-optically inactive polymer host with an electro-optic material. One such resulting binary chromophore system, based on the chromophores PSLD41 with YLD124, is presented in the next section. Another strategy is to avoid the host polymer altogether. The addition of interacting side-chains to the EO chromophore such as the coumarin-containing pendant groups of C1 and CLD-C1 discussed in the previous section is one such strategy.[15,16]

In this section, the EO chromophores YLD124 and JRD1[23] are investigated as neat materials using the simulation approach outlined in the methodology section and in chapter 4.6.

Figure 5.3 displays the LoD representations used for both molecules. Underlying atomic partial charges were reduced to a single charge and a point dipole at each ellipsoid center. Furthermore, an additional quadrupolar expansion at each ellipsoid center was investigated as well. Simulations consisted of a total of 108 chromophores, 54 of each enantiomer.

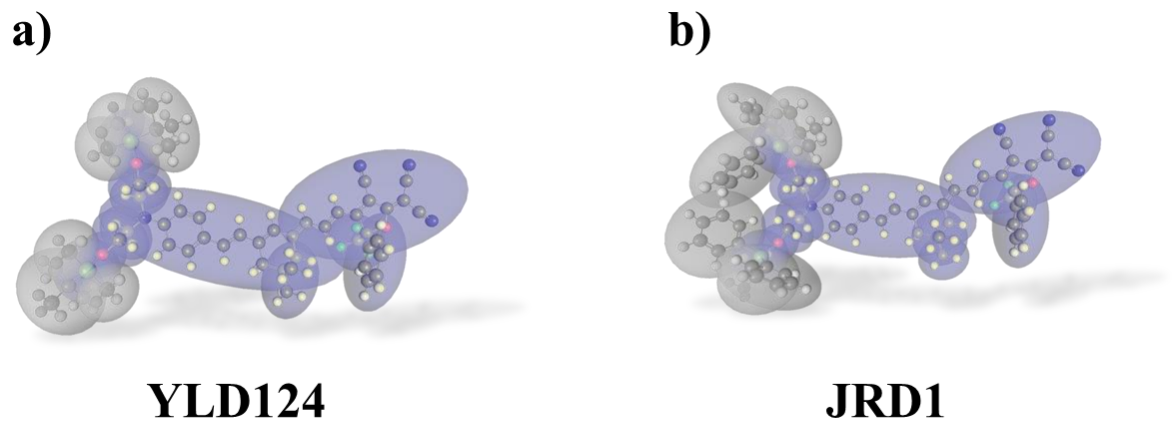

Figure 5.3: LoD representation used for **a)** YLD124 using 19 ellipsoids, and **b)** JRD1 using 20 ellipsoids

Table 5.4 gives an overview of the obtained simulation results. No significant centrosymmetric order was observed and it was thus omitted from this table. The results in table 5.4 are divided by row color into two simulation approaches: traditional NPT (light orange) and AVA simulations (light green). Overall values Boltzmann-averaged over NPT and AVA simulations (light blue rows) for dipolar systems using Boltzmann-weighted averages based on the overall simulation energies are included as well.[4]

[4] Quadrupolar averages mirror dipolar averages but are excluded here due to the JRD1 simulations' slow system convergence.

Table 5.4: YLD124 and JRD1 simulation results collection (density, heat capacity, dielectric constant, acentric order, and chromophore loading) sampled over last 40 kcycles of 240 kcycles of simulations. (See Appendix B for model parameters) Light orange colored rows represent traditional NPT simulations, light green colored rows used AVA for first 40 kcycles, and light blue colored rows show overall average quantities based on Boltzmann-weighted averaging. Note that no correction for internal degrees of freedom for heat capacity results was performed.

Model	#	Density[c]	c_P[d]	Dielectric	$\langle\cos^3\theta\rangle$	$\rho_N\langle\cos^3\theta\rangle$[e]
YLD124[a]	6	0.82 ± 0.01	105 ± 23	6 ± 1	0.04 ± 0.02	0.23 ± 0.13
YLD124[a,b]	5	0.80 ± 0.01	156 ± 41	9 ± 2	0.06 ± 0.02	0.31 ± 0.10
JRD1[a]	10	0.83 ± 0.01	127 ± 29	14 ± 4	0.14 ± 0.05	0.63 ± 0.24
JRD1[a,b]	8	0.79 ± 0.01	>5000[f]	12 ± 3	0.13 ± 0.05	0.53 ± 0.19
YLD124[c]	8	0.79 ± 0.06	141 ± 77	19 ± 2	0.17 ± 0.01	0.93 ± 0.08
YLD124[b,c]	5	0.71 ± 0.03	126 ± 33	20 ± 2	0.21 ± 0.03	1.04 ± 0.14
JRD1[c]	8	0.81 ± 0.02	115 ± 26	18 ± 2	0.22 ± 0.03	0.95 ± 0.11
JRD1[b,c]	4	0.78 ± 0.02	>5000[f]	20 ± 4	0.25 ± 0.04	1.04 ± 0.19
YLD124[overall]	14	0.79 ± 0.03	135 ± 66	17 ± 6	0.15 ± 0.06	0.83 ± 0.33
JRD1[overall]	18	0.82 ± 0.02	121 ± 27	16 ± 4	0.18 ± 0.06	0.79 ± 0.25

[a]NPT at 0.1 atm, [b]uses quadrupole expansion at ellipsoid centers, [c]AVA for first 40 kcycles, NPT at 0.1 atm, [c]in units of $\frac{g}{cc}$, [d]in units of $\frac{J}{mol\,K}$, [e]in units of 10^{20} $molecules/cc$, [f]slowly condensing system still in transition

In traditional NPT simulations rapid condensation was observed for YLD124 systems partially explaining lower observed order compared to more slowly condensing JRD1 NPT simulation systems. Interestingly, resulting order related properties (dielectric constant, acentric order, and chromophore loading) are within error bars for YLD124 and JRD1 simulations when AVA was employed for the first 40 kcycles of the simulations.

Furthermore, AVA simulations were more energetically favorable for YLD124 simulations than for their JRD1 counterparts leading the overall averages to be identical for both chromophores. Based on these simulation results one would expect both chromophores to perform about

identical, a similar conclusion to the results presented in chapter 4.6. More importantly, one would expect electro-optic performance to increase by at least 33% compared to the CLD-C1 results obtained earlier.

An extensive experimental study of neat YLD124 and JRD1 has been performed which yielded experimental poling efficiencies of $(1.9 \pm 0.2)\ nm^2/V^2$ for YLD124 and $(3.4 \pm 0.2)\ nm^2/V^2$ for JRD1.[23] This corresponds to experimental chromophore loading values[5] of 0.56 ± 0.06 for YLD124 and 1.00 ± 0.06 for JRD1, using equation (4-39) with an estimated first-order hyperpolarizability $\beta_{zzz}^{1310\ nm} = 8100$ at a poling field of $100\frac{V}{\mu m}$. The experimental value for JRD1 matches the chromophore loading simulated for JRD1 within the error for both AVA and Boltzmann-averaged quantities. However, the experimentally observed chromophore loading of YLD124 is only within the lower error bar of its simulated, Boltzmann-averaged value and not at all close to the AVA simulated quantity.

In other words, YLD124 in the experiment seems to exhibit similar behavior to the simulated behavior in traditional NPT simulations, trapped in its ability to respond to the external poling field. Because system energies are more favorable for the more ordered states calculated in the AVA simulations this indicates YLD124 may be kinetically limited in the experiment possibly due to the initial arrangement upon film formation.

The conclusion from comparing theory and experiment suggests several experimental test: the use of a slightly different solvent for YLD124 or to mix YLD124 with small amounts of a solubilizing agent to increase chromophore mobility.

[5] In units of $10^{20}\ molecules/cc$.

In summary, simulations conducted on YLD124 and JRD1 system match well with the slightly newer theoretical results present in chapter 4.6 investigating acentric order as a function of temperature and poling field strength. JRD1 simulation results using AVA and Boltzmann-averaged results over all simulations performed align well with experimental observations. By combining theoretical results with experimental observation for YLD124 it can be concluded that YLD124 is likely kinetically trapped.

5.5 THE BINARY CHROMOPHORE SYSTEM PSLD41/YLD124

The binary mixture of YLD124 with the multichromophore dendrimer PSLD41, consisting of three connected FTC-type chromophores, features experimental electro-optic activities larger than the sum of its constituents by themselves.[11,12,31–34]

Simulation results using the PSLD41 chromophore have been undertaken previously.[12,34] The present theoretical investigation of the PSLD41/YLD124 binary system represents the largest-scale LoD simulations undertaken thus far with system sizes of up to 4384 ellipsoids. The PSLD41 molecule consists of 431 atoms, a system too large to be optimized in a single DFT calculation with current memory and time-constraints. Therefore, the molecule was broken up into three identical building blocks which were optimized separately using the method outlined earlier and then assembled in the simulation setup.

For this purpose, an algorithm was developed allowing the assembly of LoD fragments into a larger so called "super group". This process involves stitching subunits together across original bonds. For example, if one wanted to stitch together two methanes, CH_4, across the C-H bonds on both molecules, first both bonds are aligned with bonds facing each other ($H_3CH \cdots HCH_3$), then both hydrogens are removed and their partial charges are added to the carbons taking their place ($H_3C \cdots CH_3$), and finally the two carbons are linked with the distance determined by the following relation:

$$l_{C_1-C_2} = \frac{V(C_1)}{V(C_1)+V(H_1)} l_{C_1-H_1} + \frac{V(C_2)}{V(C_2)+V(H_2)} l_{C_2-H_2} \tag{5-4}$$

Here, l_{A-B} is the interatomic distance between A and B and $V(C)$ is the volume of element C. The interaction energy of the linked entity (H_3C-CH_3) is then minimized by rotating around the newly created bond.

The individual PSLD41 subunits used to assemble PSLD41 are shown in figure 5.4 along with their respective linkage sites. Each of the units shown was obtained using a DFT calculation as outlined in the methodology section.

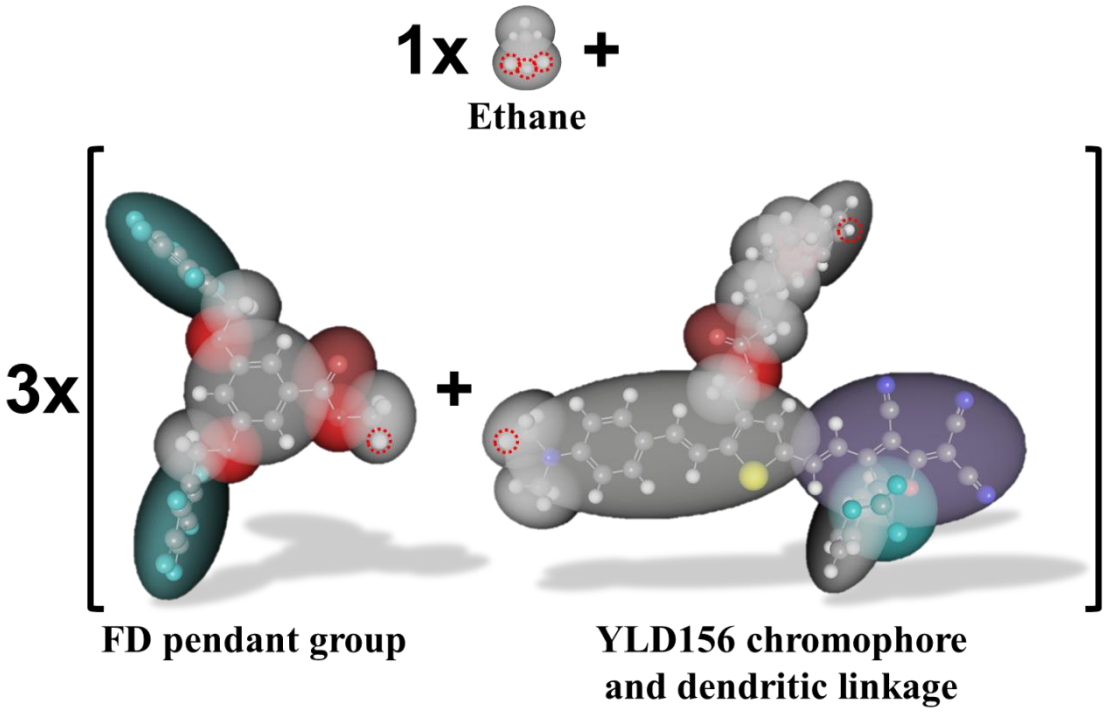

Figure 5.4: Subunits used to assemble PSLD41 in their LoD representation with linkage sites highlighted by dotted red circles

Figure 5.5 displays the resulting LoD representations of PSLD41with the core chromophore part highlighted in blue. Additionally to the PSLD41 model the LoD representation of YLD124 is shown similar to figure 5.3a). See Appendix B for model parameters.

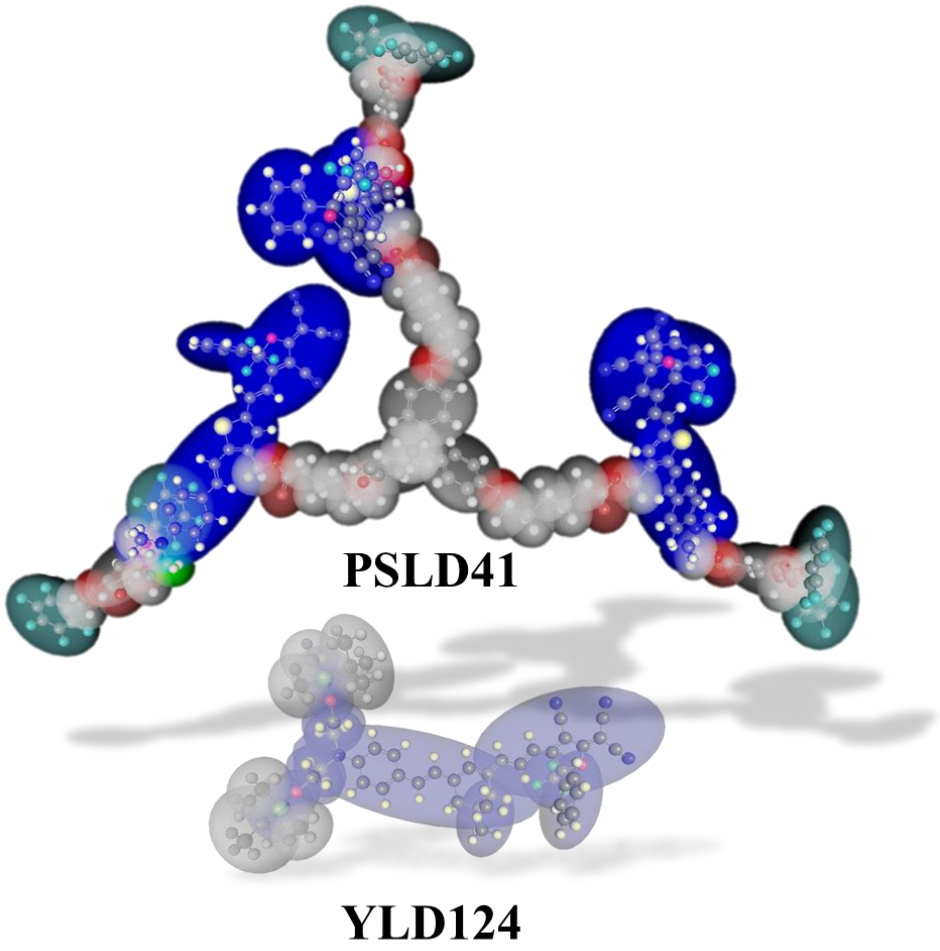

Figure 5.5: LoD representation of PSLD41 using 80 ellipsoids with LoD model of YLD124 using 19 ellipsoids (also shown in figure 5.3a))

Simulations with an external poling field of $100\frac{V}{\mu m}$ were performed in the NPT ensemble under $1\ atm$ at $400\ K$ using AVA for the first 40 kcycles of 240 kcycles. The reaction field approach presented in chapter 4 was used and electrostatic interactions were attenuated by $n^2 = 1.7^2$. Each simulation contained 32 PSLD41 chromophores and a given number of YLD124 chromophores (16, 32, 36, 40, 44, 48, 52, 56, 76, and 96, leading to number densities between 0.5 and $2.5 \cdot 10^{20}\ molecules/cc$). For each YLD124 number density eight simulations were run and results were Boltzmann-averaged using the individual simulation energies.

Figure 5.6 displays estimated electro-optic activity values from the set of simulation results of the PSLD41/YLD124 binary chromophore system as a function of the resulting YLD124 number density based on the overall simulation densities. Poling efficiency estimates used equation (4-39) with estimated first-order hyperpolarizabilities of $\beta_{zzz}^{1310\,nm}(FTC) = 4050$ and $\beta_{zzz}^{1310\,nm}(YLD124) = 8100$. Note that simulation densities were on average 0.8 $\frac{g}{cc}$, or about 20% lower than the value of 1 $\frac{g}{cc}$ typically assumed in experimental publications.

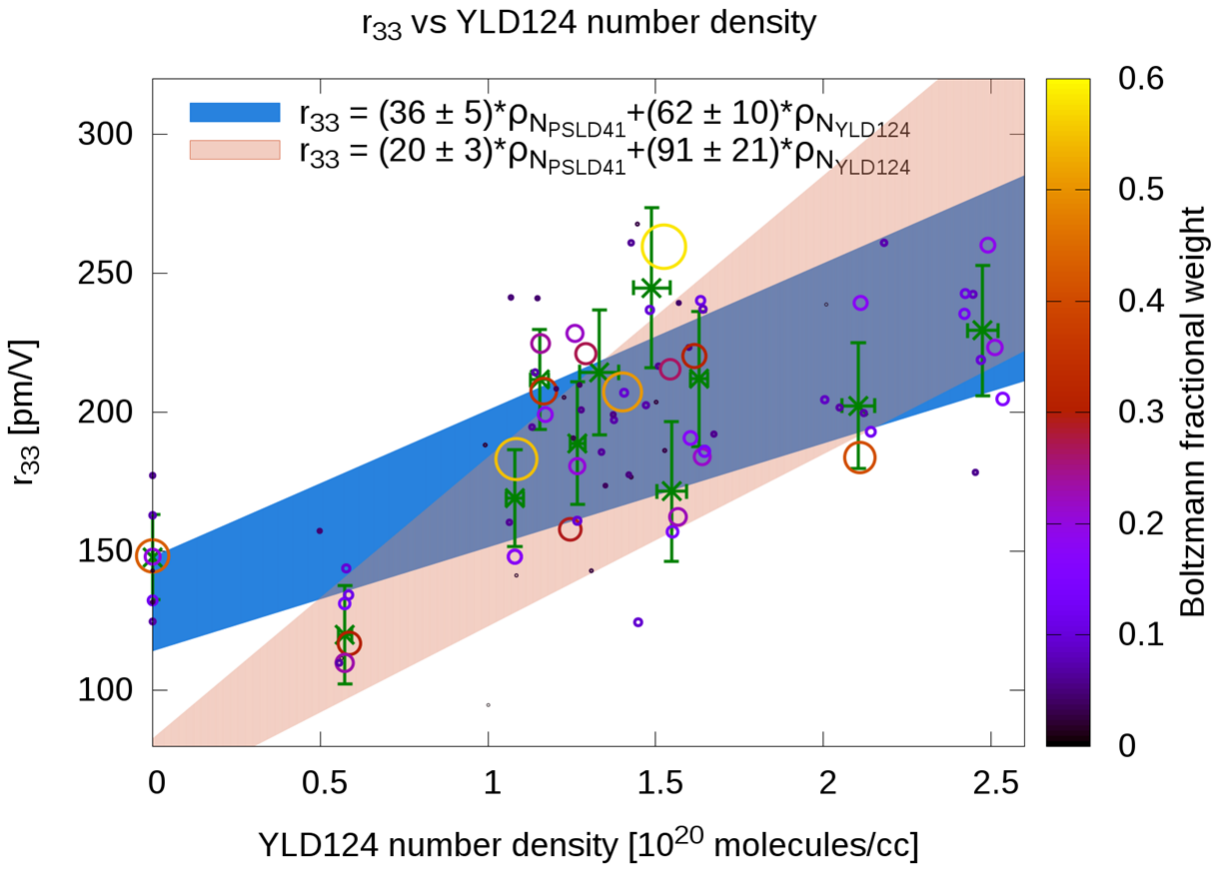

Figure 5.6: Estimated electro-optic activity r_{33} from simulation results of binary chromophore system PSLD41/YLD124; Also shown are fit curves representing a fit to PSLD41 and YLD124 contributions (blue curve) and holding the PSLD41 contribution fixed at the experimental value while fitting the YLD124 contribution (red curve).

The blue fit curve displayed in figure 5.6 was obtained by individually fitting the electro-optic contributions of PSLD41 and YLD124. The red curve fixes the PSLD41 contribution to the experimental value and fits only the resulting YLD124 contribution. Estimated PSLD41 electro-optic contributions as well as YLD124 contributions were fit as a function of their respective number densities. Figure 5.7 displays this fitting process. Note that instead of r_{33} the corresponding poling efficiencies $\frac{r_{33}}{E}$ are displayed using $E = 100\frac{V}{\mu m}$.

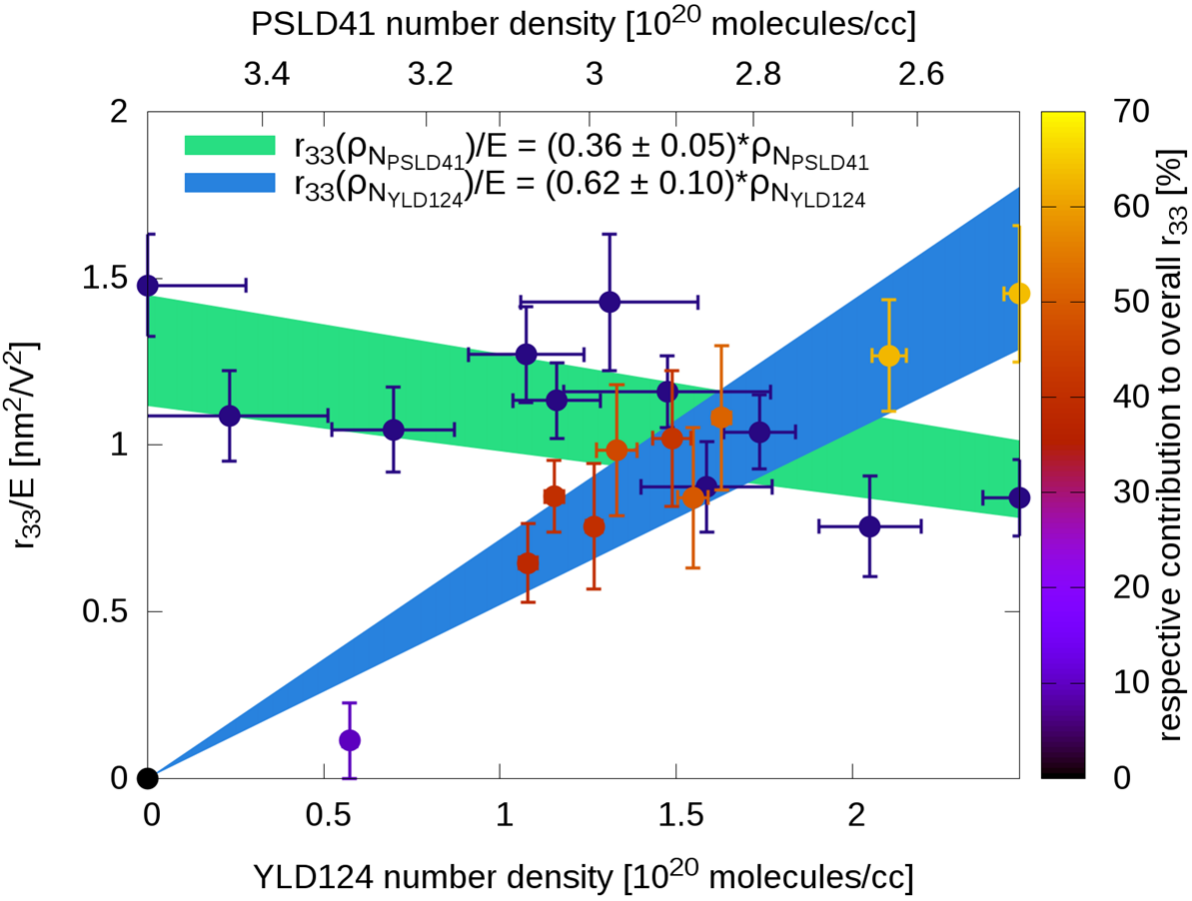

Figure 5.7: Estimated poling efficiencies and fits to individual contributions of PSLD41 and YLD124; Note that an additional data point for neat PSLD41 is added obtained from the averages of 8 similar simulations.

The poling efficiency per number density of PSLD41 in the simulated binary system[6] of $(0.36 \pm 0.05) \cdot \rho_N$ is about 80% larger than the reported experimental value[31,32] of $(0.199 \pm 0.030) \cdot \rho_N$ of free PSLD41 which was used in the experimental determination of the YLD124 contribution with a reported value[7] of $(1.378 \pm 0.207) \cdot \rho_N$.[31] The estimated, simulated contribution due to YLD124 of $(0.62 \pm 0.10) \cdot \rho_N$ is not close to the of the experimental YLD124 contribution. However, when one assumes the experimentally determined value for the PSLD41 contribution of $(0.199 \pm 0.030) \cdot \rho_N$, the resulting fit value $(0.91 \pm 0.21) \cdot \rho_N$ of the YLD124 contribution is within experimental error bars of 15%. Furthermore, the estimated simulated poling efficiency at an YLD124 number density of $1.71 \cdot 10^{20}\ molecules/cc$, corresponding to an experimental weight percentage of 25%, is $(2.1 \pm 0.4)\ nm^2/V^2$, independent of which fit is used. Within error bars, this value matches the experimental value of $(2.85 \pm 0.43)\ nm^2/V^2$.[31,32]

The electro-optic contribution of PSLD41 in the binary chromophore system may have been underestimated so far. The added data point shown in figure 5.7 for neat PSLD41, simulated without YLD124, demonstrates an about 40% larger poling efficiency of $(1.5 \pm 0.2)\ nm^2/V^2$ compared to the experimental value of $(1.04 \pm 0.16)\ nm^2/V^2$. This observation potentially indicates the first-order hyperpolarizability of PSLD41 is lowered in neat material compared to the binary material. The estimated YLD124 contribution to the poling efficiency of $(0.62 \pm 0.10) \cdot \rho_N$ at a number density of $1.71 \cdot 10^{20}\ molecules/cc$ leads to a poling efficiency of $(1.06 \pm 0.17)\ nm^2/V^2$, consistent with the experimentally observed poling efficiency of YLD124 in APC of[35] $(1.27 \pm 0.08)\ nm^2/V^2$ further indicating that the role PSLD41 has been underestimated thus far.

---

[6] All reported poling efficiency per number density value are in units of $\frac{nm^2/V^2}{10^{20}\ molecules/cc}$.

[7] As a service to the reader: The values can be found in table 4.5.2 of Phil Sullivan's thesis.[31] At 25% YLD124 loading by weight, corresponding to a number density of 1.71 $10^{20}\ molecules/cc$ assuming a density of $1\ g/cc$, these values give a poling efficiency of 2.93 nm^2/V^2, close to the experimental value of 2.85 nm^2/V^2.[32]

In summary, simulations of the binary chromophore system of PSLD41 and YLD124 were conducted. The estimated poling efficiency corresponding to 25% YLD124 by weight of $(2.1 \pm 0.4)\ nm^2/V^2$ is consistent with the experimentally observed value of $(2.85 \pm 0.43)\ nm^2/V^2$.[31,32] However, unlike postulated in the experimental analysis YLD124 was not observed to exceed Langevin-order. Instead, based on theoretical results it seems that the role of PSLD41 so far has been underestimated, likely due to suppressed first-order hyperpolarizability of PSLD41 in neat material compared to the binary chromophore system.

5.6 CONCLUSIONS

In this chapter, simulation results performed with electro-optic chromophores containing the TCF-acceptor were presented. Theoretical results in general matched or overlapped within the error bar with experimental results.

C1 displayed slightly improved chromophore loading compared to CLD-C1, however, overall results were similar within their respective error bars. While the simulated poling efficiency of CLD-C1 was matching experimental results within both theoretical and experimental error, the estimated poling efficiency of C1 was slightly lower compared to experimental results with error bars only slightly overlapping. No significant centrosymmetric order could be found in the poling direction. However, Q-tensor derived centrosymmetric order parameters slightly off from the poling direction for individual simulations were close to experimentally observed values for both chromophore cores as well as pendant-group coumarins. However, average centrosymmetric order over all performed simulations was only found for the chromophore cores of C1 and CLD-C1 but not for the coumarins. Future work thus will focus on improving coumarin interactions

using the current LoD rule set in conjunction with the approach used in chapter 2.5.1 successfully modeling the π-stacking interactions of benzene and hexafluorobenzene.

Neat YLD124 and JRD1 chromophore systems have been investigated. JRD1 simulation results using AVA and Boltzmann-averaged results over all simulations performed align well with experimental observations. Furthermore, simulation results predict YLD124 to yield similar chromophore loading to JRD1, an observation not shared by experimental reality.[23] By combining theoretical results with experimental observation for YLD124 it can be concluded that YLD124 is likely kinetically trapped.

Simulations of the binary chromophore system of the multichromophore dendrimer PSLD41 and the YLD124 chromophore were conducted. Within error bars simulations predicted comparable poling efficiencies compared to experimental values. Unlike experimental results, however, which concluded a more than two-fold increase in YLD124 acentric order by subtracting free PSLD41 poling results, theoretical results indicate that the role of PSLD41 in the binary chromophore system was likely underestimated. This suggests suppressed first-order hyperpolarizability of PSLD41 in neat material compared to the binary chromophore system.

Overall, all simulated TCF-acceptor containing chromophores exhibited chromophore loading values of around $\rho_N\langle\cos^3\theta\rangle = (0.8 \pm 0.3) \cdot 10^{20}\ molecules/cc$ upon poling in an external field of $100\,\frac{V}{\mu m}$, leading to estimated poling efficiencies of $(1.4 \pm 0.5)\ nm^2/V^2$ for YLD156-type chromophores and $(2.7 \pm 1.0)\ nm^2/V^2$ for YLD124-type chromophores. These values were obtained over a wide range of different chromophores and are relatively independent of chromophore attachments leading to an additional design criterion: ***The chromophore core determines observed chromophore loading.***

5.7 REFERENCES FOR CHAPTER 5

[1] Robinson, B. H.; Dalton, L. R.; Harper, A. W.; Ren, A.; Wang, F.; Zhang, C.; Todorova, G.; Lee, M.; Aniszfeld, R.; Garner, S.; Chen, A.; Steier, W. H.; Houbrecht, S.; Persoons, A.; Ledoux, I.; Zyss, J.; Jen, A. K. Y. The Molecular and Supramolecular Engineering of Polymeric Electro-Optic Materials. *Chem. Phys.* **1999**, *245* (1–3), 35–50.

[2] Zhang, C.; Dalton, L. R.; Oh, M.-C.; Zhang, H.; Steier, W. H. Low V_π Electrooptic Modulators from CLD-1: Chromophore Design and Synthesis, Material Processing, and Characterization. *Chem. Mater.* **2001**, *13* (9), 3043–3050.

[3] Liu, S.; Haller, M. A.; Ma, H.; Dalton, L. R.; Jang, S.-H.; Jen, A. K.-Y. Focused Microwave-Assisted Synthesis of 2,5-Dihydrofuran Derivatives as Electron Acceptors for Highly Efficient Nonlinear Optical Chromophores. *Adv. Mater.* **2003**, *15* (7-8), 603–607.

[4] Liao, Y.; Eichinger, B. E.; Firestone, K. A.; Haller, M.; Luo, J.; Kaminsky, W.; Benedict, J. B.; Reid, P. J.; Jen, A. K.-Y.; Dalton, L. R.; Robinson, B. H. Systematic Study of the Structure−Property Relationship of a Series of Ferrocenyl Nonlinear Optical Chromophores. *J. Am. Chem. Soc.* **2005**, *127* (8), 2758–2766.

[5] Hammond, S. R.; Clot, O.; Firestone, K. A.; Bale, D. H.; Lao, D.; Haller, M.; Phelan, G. D.; Carlson, B.; Jen, A. K.-Y.; Reid, P. J.; Dalton, L. R. Site-Isolated Electro-Optic Chromophores Based on Substituted 2,2′-Bis(3,4-Propylenedioxythiophene) π-Conjugated Bridges. *Chem. Mater.* **2008**, *20* (10), 3425–3434.

[6] Shi, Y. Low (Sub-1-Volt) Halfwave Voltage Polymeric Electro-Optic Modulators Achieved by Controlling Chromophore Shape. *Science* **2000**, *288* (5463), 119–122.

[7] Baehr-Jones, T.; Hochberg, M.; Wang, G.; Lawson, R.; Liao, Y.; Sullivan, P. A.; Dalton, L.; Jen, A.-Y.; Scherer, A. Optical Modulation and Detection in Slotted Silicon Waveguides. *Opt. Express* **2005**, *13* (14), 5216–5226.

[8] Dalton, L.; Robinson, B.; Jen, A.; Ried, P.; Eichinger, B.; Sullivan, P.; Akelaitis, A.; Bale, D.; Haller, M.; Luo, J.; Liu, S.; Liao, Y.; Firestone, K.; Bhatambrekar, N.; Bhattacharjee, S.; Sinness, J.; Hammond, S.; Buker, N.; Snoeberger, R.; Lingwood, M.; Rommel, H.; Amend, J.; Jang, S.-H.; Chen, A.; Steier, W. Electro-Optic Coefficients of 500 pm/V and beyond for Organic Materials. In *Proceedings of SPIE*; Eich, M., Ed.; 2005; pp 593502–593502.

[9] Dalton, L. Photonic Integration Improves on Current Technologies. *SPIE Newsroom* **2007**.

[10] Dalton, L. R.; Olbricht, B. C.; Sullivan, P. A. Advances in Organic Materials for Optical Modulation. In *Microwave Photonics, 2007 IEEE International Topical Meeting on*; 2007; pp 1–4.

[11] Dalton, L. R.; Sullivan, P. A.; Bale, D. H. Electric Field Poled Organic Electro-Optic Materials: State of the Art and Future Prospects. *Chem. Rev.* **2010**, *110* (1), 25–55.

[12] Sullivan, P. A.; Rommel, H.; Liao, Y.; Olbricht, B. C.; Akelaitis, A. J. P.; Firestone, K. A.; Kang, J.-W.; Luo, J.; Davies, J. A.; Choi, D. H.; Eichinger, B. E.; Reid, P. J.; Chen, A.; Jen, A. K.-Y.; Robinson, B. H.; Dalton, L. R. Theory-Guided Design and Synthesis of Multichromophore Dendrimers: An Analysis of the Electro-Optic Effect. *J. Am. Chem. Soc.* **2007**, *129* (24), 7523–7530.

[13] Frisch, M. J.; Trucks, G. W.; Schlegel, H. B.; Scuseria, G. E.; Robb, M. A.; Cheeseman, J. R.; Scalmani, G.; Barone, V.; Mennucci, B.; Petersson, G. A.; Nakatsuji, H.; Caricato, M.; Li, X.; Hratchian, H. P.; Izmaylov, A. F.; Bloino, J.; Zheng, G.; Sonnenberg, J. L.; Hada, M.; Ehara, M.; Toyota, K.; Fukuda, R.; Hasegawa, J.; Ishida, M.; Nakajima, T.; Honda, Y.; Kitao, O.; Nakai, H.; Vreven, T.; Montgomery Jr., J. A.; Peralta, J. E.; Ogliaro, F.; Bearpark, M. J.; Heyd, J.; Brothers, E. N.; Kudin, K. N.; Staroverov, V. N.; Kobayashi, R.; Normand, J.; Raghavachari, K.; Rendell, A. P.; Burant, J. C.; Iyengar, S. S.; Tomasi, J.; Cossi, M.; Rega, N.; Millam, N. J.; Klene, M.; Knox, J. E.; Cross, J. B.; Bakken, V.; Adamo, C.; Jaramillo, J.; Gomperts, R.; Stratmann, R. E.; Yazyev, O.; Austin, A. J.; Cammi, R.; Pomelli, C.; Ochterski, J. W.; Martin, R. L.; Morokuma, K.; Zakrzewski, V. G.; Voth, G. A.; Salvador, P.; Dannenberg, J. J.; Dapprich, S.; Daniels, A. D.; Farkas, Ö.; Foresman, J. B.; Ortiz, J. V.; Cioslowski, J.; Fox, D. J. *Gaussian 09*; Gaussian, Inc.: Wallingford, CT, USA, 2009.

[14] Johnson, L. E. Multi-Scale Modeling of Organic Electro-Optic Materials, University of Washington, 2012.

[15] Benight, S. J.; Johnson, L. E.; Barnes, R.; Olbricht, B. C.; Bale, D. H.; Reid, P. J.; Eichinger, B. E.; Dalton, L. R.; Sullivan, P. A.; Robinson, B. H. Reduced Dimensionality in Organic Electro-Optic Materials: Theory and Defined Order. *J. Phys. Chem. B* **2010**, *114* (37), 11949–11956.

[16] Benight, S. Nanoengineering of Soft Matter Interactions in Organic Electro-Optic Materials, University of Washington, 2011.

[17] Anet, R. The Photodimers of Coumarin and Related Compounds. *Can. J. Chem.* **1962**, *40* (7), 1249–1257.

[18] Hammond, G. S.; Stout, C. A.; Lamola, A. A. Mechanisms of Photochemical Reactions in Solution. XXV. The Photodimerization of Coumarin. *J. Am. Chem. Soc.* **1964**, *86* (15), 3103–3106.

[19] Hoffman, R.; Wells, P.; Morrison, H. Organic Photochemistry. XII. Further Studies on the Mechanism of Coumarin Photodimerization. Observation of an Unusual "Heavy Atom" Effect. *J Org Chem* **1971**, *36* (1), 102.

[20] Tian, Y.; Kong, X.; Nagase, Y.; Iyoda, T. Photocrosslinkable Liquid-Crystalline Block Copolymers with Coumarin Units Synthesized with Atom Transfer Radical Polymerization. *J. Polym. Sci. Part Polym. Chem.* **2003**, *41* (14), 2197–2206.

[21] Kim, C.; Trajkovska, A.; Wallace, J. U.; Chen, S. H. New Insight into Photoalignment of Liquid Crystals on Coumarin-Containing Polymer Films. *Macromolecules* **2006**, *39* (11), 3817–3823.

[22] Olbricht, B. C.; Sullivan, P. A.; Dennis, P. C.; Hurst, J. T.; Johnson, L. E.; Benight, S. J.; Davies, J. A.; Chen, A.; Eichinger, B. E.; Reid, P. J.; Dalton, L. R.; Robinson, B. H. Measuring Order in Contact-Poled Organic Electrooptic Materials with Variable-Angle Polarization-Referenced Absorption Spectroscopy (VAPRAS). *J. Phys. Chem. B* **2011**, *115* (2), 231–241.

[23] Jin, W.; Johnston, P. V.; Elder, D. L.; Tillack, A. F.; Olbricht, B. C.; Song, J.; Reid, P. J.; Xu, R.; Robinson, B. H.; Dalton, L. R. Benzocyclobutene Barrier Layer for Suppressing Conductance in Nonlinear Optical Devices during Electric Field Poling. *Appl. Phys. Lett.* **2014**, *104* (24), 243304.

[24] Low, R. J. Measuring Order and Biaxiality. *Eur. J. Phys.* **2002**, *23* (2), 111.

[25] Mottram, N. J.; Newton, C. Introduction to Q-Tensor Theory. *Univ. Strathclyde Dep. Math. Res. Rep.* **2004**, *2004*, 10.

[26] *Visualization and Processing of Tensor Fields*; Laidlaw, D., Weickert, J., Eds.; Farin, G., Hege, H.-C., Hoffman, D., Johnson, C. R., Polthier, K., Rumpf, M., Series Eds.; Mathematics and Visualization; Springer Berlin Heidelberg: Berlin, Heidelberg, 2009.

[27] Majumdar, A.; Zarnescu, A. Landau-De Gennes Theory of Nematic Liquid Crystals: The Oseen-Frank Limit and beyond. *Arch. Ration. Mech. Anal.* **2010**, *196* (1), 227–280.

[28] Lee, K.-S. *Polymers for Photonics Applications I*; Springer, 2003.

[29] Taylor, R. E.; Jr, R. R. B.; Eades, W. D. Polymer Guest-Host Systems and Polymer Electro-Optic Waveguide Systems. US6978069 B1, December 20, 2005.

[30] Allen, N. S. *Photochemistry and Photophysics of Polymeric Materials*; John Wiley & Sons, 2010.

[31] Sullivan, P. A. Theory Guided Design and Molecular Engineering of Organic Materials for Enhanced Second-Order Nonlinear Optical Properties, University of Washington, 2006.

[32] Pereverzev, Y. V.; Gunnerson, K. N.; Prezhdo, O. V.; Sullivan, P. A.; Liao, Y.; Olbricht, B. C.; Akelaitis, A. J. P.; Jen, A. K.-Y.; Dalton, L. R. Guest−Host Cooperativity in Organic Materials Greatly Enhances the Nonlinear Optical Response. *J. Phys. Chem. C* **2008**, *112* (11), 4355–4363.

[33] Olbricht, B. C.; Sullivan, P. A.; Wen, G.-A.; Mistry, A. A.; Davies, J. A.; Ewy, T. R.; Eichinger, B. E.; Robinson, B. H.; Reid, P. J.; Dalton, L. R. Laser-Assisted Poling of Binary Chromophore Materials. *J. Phys. Chem. C* **2008**, *112* (21), 7983–7988.

[34] Sullivan, P. A.; Rommel, H. L.; Takimoto, Y.; Hammond, S. R.; Bale, D. H.; Olbricht, B. C.; Liao, Y.; Rehr, J.; Eichinger, B. E.; Jen, A. K.-Y.; Reid, P. J.; Dalton, L. R.; Robinson, B. H. Modeling the Optical Behavior of Complex Organic Media: From Molecules to Materials. *J. Phys. Chem. B* **2009**, *113* (47), 15581–15588.

[35] Elder, D. L.; Benight, S. J.; Song, J.; Robinson, B. H.; Dalton, L. R. Matrix-Assisted Poling of Monolithic Bridge-Disubstituted Organic NLO Chromophores. *Chem. Mater.* **2014**, *26* (2), 872–874.

6 SIMULATION RESULTS OF TCP-BASED ELECTRO-OPTIC CHROMOPHORE SYSTEMS

6.1 INTRODUCTION

This chapter presents simulations performed on electro-optic chromophore systems using the tricyanopyrroline (TCP) acceptor. The TCP acceptor[1–4] has first been developed by Carboni[1] at DuPont and found extensive use in dyes for synthetic fabric coloration[5,6] and in thermal transfer printing[7,8] before being suggested for use in electro-optic chromophores with an expected about two-fold increase in acceptor strength compared to the TCF-acceptor.[3,4,9–11] The simulated chromophores presented here were synthesized and discussed previously[10–12] and one of its representatives, TCP-Me was already introduced in chapter 3.

6.2 METHODOLOGY

The methodology used in this chapter is identical to chapter 5 and just reprinted here for convenience. Fully-atomistic model geometries were obtained using the Gaussian 09D[13] package with the B3LYP/6-31G(d) functional in vacuum based on the methodology developed by Dr. Lewis Johnson.[14] Additionally, CHELPG charges at atom locations calculated using Gaussian 09D[13] in conjunction with OPLS-AA parameters for Lennard-Jones radii and energies of individual atoms were utilized.

Intra-molecular interaction energies were calculated from second-nearest neighbors and up, in accordance to settings used for the hydrocarbon chain simulations displayed in figure 2.16. LoD

ellipsoids were connected at the bond locations determined by the AA model and only bond rotations are allowed, similarly to the aforementioned hydrocarbon chain simulations. Partial charges of the underlying AA atom subset inside each ellipsoid were reduced to a point charge and a point dipole at the ellipsoid center. Unless otherwise noted, simulations were run using AVA as presented in chapter 3 in the NPT ensemble with electrostatics interactions attenuated by $n^2 = 1.7^2$, representing the typical experimentally observed refractive index. The reaction field approach presented in chapter 4 was used throughout. Furthermore, all simulation results presented in this chapter were simulated with an external poling field of $100\,\frac{V}{\mu m}$.

6.3 TCP-1 AND TCP-ME

The synthesis of TCP-1 was first reported by Jang et al. in 2006[3]. It was later revisited by Dr. Meghana Rawal as the basis for the synthesis and experimental analysis of other, short TCP-1 based chromophores with attached cross-conjugated moieties to limit the formation of strong dipole-dipole aggregates.[10,11]

Figure 6.1 displays the LoD models used in this study for both TCP-1 and TCP-Me, with both rotational isomers for the TCP-Me model A and a slightly more detailed LoD representation of TCP-Me in model B. All-atom models were obtained using the method described in the methodology section. All simulations except when otherwise noted were run using AVA with a total of 108 chromophores in the NPT ensemble under $0.1\ atm$ at $400\ K$ and utilized the "simple touch" LJ LoD potential from equation (2-2) with a constant LJ energy calculated using the approximation presented in equation (5-3).

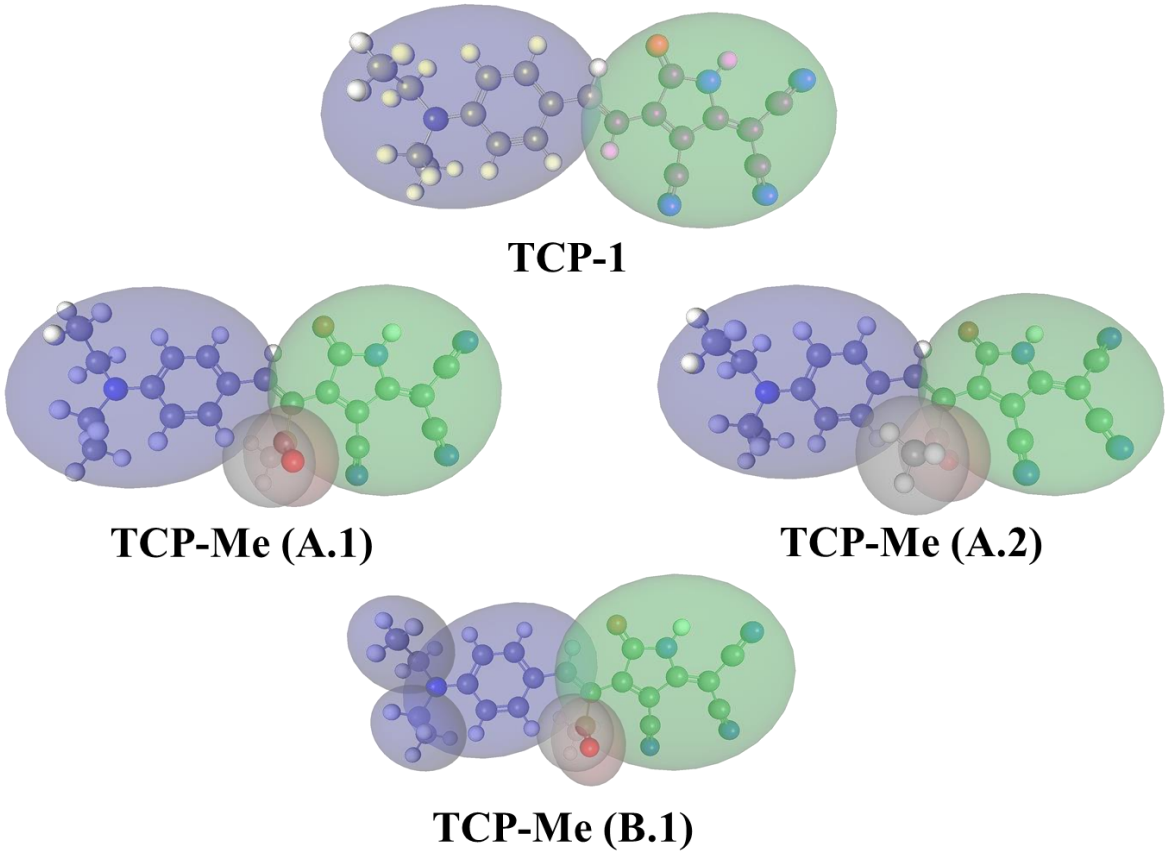

Figure 6.1: LoD representations of TCP-1 and TCP-Me chromophores with both rotational isomers of TCP-Me for model A, and slightly more detailed representation for TCP-Me model B

Table 6.1 summarizes the simulation results. Rows are colored by the simulation type with light orange colored rows representing traditional NPT simulations, light green colored rows the use of AVA for the first 40 kcycles, and light blue colored rows AVA simulations with a quadrupolar expansion at ellipsoid centers. As reported previously on many occasions throughout chapters 3-5 simulations using AVA during the initial stages of the simulation result in overall more favorable system energies. The current simulations on TCP-1 and TCP-Me systems are no exception. When AVA was used, system energies were more favorable by 0.3 kJ/mol and 1.5 kJ/mol for TCP-1 and TCP-Me, respectively. While these energetic changes may seem small, they lead to dramatic order differences. An in-depth study of AVA on TCP-Me systems can be found in chapter 3.[12]

Table 6.1: TCP-1 and TCP-Me simulation results collection (density, system enthalpy, heat capacity, dielectric constant, centrosymmetric order, acentric order, and chromophore loading) sampled over last 40 kcycles of 240 kcycles of simulations with error in the last digit in parentheses. (See Appendix B for model parameters) Light orange colored rows represent traditional NPT simulations, light green colored rows the use of AVA for the first 40 kcycles, and light blue colored rows AVA simulations with a quadrupolar expansion at ellipsoid centers. Note that no correction for internal degrees of freedom for heat capacity results was performed.

Model	#	Density[c]	H_{total}[d]	c_P[e]	Dielectric	$\langle\cos^2\theta\rangle$	$\langle\cos^3\theta\rangle$	$\rho_N\langle\cos^3\theta\rangle$[f]
TCP-1[a]	24	0.837(3)	-80.9(5)	55(8)	16(4)	0.35(3)	0.09(3)	1.3 ± 0.4
TCP-1[b]	32	0.834(4)	-81.2(5)	57(12)	22(4)	0.35(2)	0.13(3)	1.9 ± 0.4
TCP-1[b,c]	32	0.859(5)	-99.0(7)	43(7)	18(4)	0.35(3)	0.10(3)	1.5 ± 0.4
TCP-Me (A.1)[a]	24	0.892(4)	-62.8(6)	49(5)	12(5)	0.34(3)	0.06(3)	0.8 ± 0.3
TCP-Me (A.1)[b]	24	0.891(4)	-64.3(6)	50(9)	19(3)	0.34(3)	0.10(2)	1.5 ± 0.3
TCP-Me (A.2)[b]	24	0.885(3)	-75.5(7)	50(6)	23(5)	0.35(3)	0.13(4)	1.8 ± 0.5
TCP-Me (B.1)[b]	24	0.961(4)	-56.0(7)	61(7)	23(4)	0.35(2)	0.12(3)	1.8 ± 0.4
TCP-Me (A.1)[b,c]	20	0.905(5)	-71.5(7)	47(9)	21(3)	0.34(3)	0.11(3)	1.6 ± 0.3
TCP-Me (A.2)[b,c]	20	0.896(5)	-83.1(9)	44(7)	22(5)	0.36(3)	0.12(4)	1.7 ± 0.5

[a]NPT at 0.1 atm, [b]AVA for first 40 kcycles, NPT at 0.1 atm, [c]quadrupole expansion at ellipsoid centers, [c]in units of $\frac{g}{cc}$, [d]in units of $\frac{kJ}{mol}$, [e]in units of $\frac{J}{mol\ K}$, [f]in units of $10^{20}\ molecules/cc$

No significant centrosymmetric order was observed for either system. However, the overall average acentric order was found to be $\langle\cos^3\theta\rangle = (0.12 \pm 0.03)$ for both TCP-1 and TCP-Me systems. Despite this relatively moderate acentric order, comparable to CLD-C1 systems, the overall average chromophore loading is $\rho_N\langle\cos^3\theta\rangle = (1.6 \pm 0.4) \cdot 10^{20}\ molecules/cc$ for both TCP-1 and TCP-Me due to very large number densities of these smaller chromophores. This underscores their possible utility. Despite their smaller size, similar small TCP-acceptor based chromophores with an improved donor are predicted to exhibit first-order hyperpolarizabilities comparable to larger TCF-based chromophore analogues such as YLD156 or even YLD124.

Interestingly, using a quadrupolar charge distribution in TCP-1 simulations lowered chromophore loading significantly while no such effect was observed for the TCP-Me chromophore. This is likely due to the added protection the cross-conjugated moiety in TCP-Me provides in comparison the planar geometry of TCP-1.

A significant energetic difference can be observed in the simulated system enthalpies between the two rotational isomers of TCP-Me, with the TCP-Me (A.2) isomer featuring about 11 kJ/mol lower system energies compared to the TCP-Me (A.1) isomer. Furthermore, only one rotational isomer corresponding to the TCP-Me (A.2) isomer was observed in the experimental crystal structure.[10]

The resulting energy landscape of a potential energy scan of the of the cross-conjugated methyl-ketone moiety around the donor-side vinyl-ketone dihedral angle is displayed in figure 6.2.

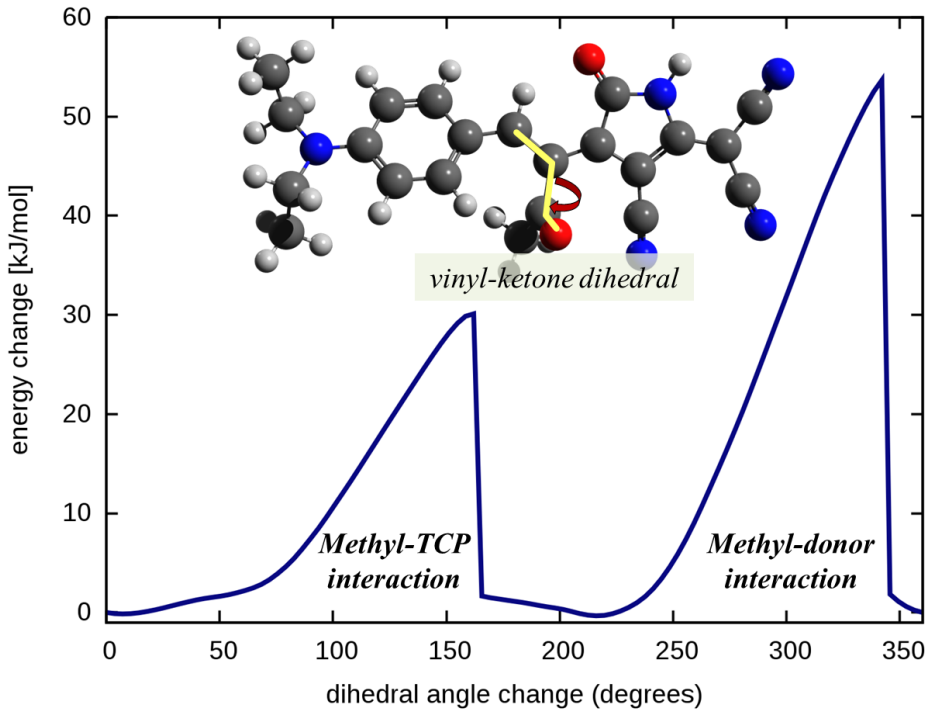

Figure 6.2: TCP-Me energy landscape upon clockwise rotation of the cross-conjugated methyl-ketone moiety around the donor-side vinyl-ketone dihedral angle

Calculations were performed with Gaussian 09C[13] using the B3LYP/6-31G(d) potential in vacuum, similar to how simulation geometries were obtained.. Two peaks representing interactions of the methyl subunit with the TCP-acceptor and the donor-side phenyl ring with energetic barriers of $28\ kJ/mol$ and $54\ kJ/mol$, respectively, can be observed. The observed energy barrier for the Methyl-TCP interaction of $28\ kJ/mol$ is comparable to the energetic difference between the eclipsed and the anti conformations in butane.[15] In conjunction with the strongly favorable energy of the condensed TCP-Me (A.2) system, it can thus be concluded that in a condensed system of TCP-Me rotation of the methyl-ketone is likely to occur and that the TCP-Me (A.2) rotational isomer is more likely to be found. This is the experimental observation.

Furthermore, TCP-Me simulation results using a slightly more detailed LoD description of the donor region with the TCP-Me (B.1) model yielded comparable order parameters to the TCP-Me (A.1) model. TCP-Me (B.1) simulations featured a slightly increased density and heat capacity due to the additional degrees of freedom as well as slightly lowered system energies due to different LJ energy parameters.

6.4 TCP-PH, TCP-PHF, AND TCP-PHF$_5$

Addition of phenyl moieties instead of a methyl moiety to the cross-conjugated vinyl-ketone leads the chromophore TCP-Ph. Substitution of phenyl hydrogen atoms with fluorine lead to TCP-PhF and TCP-PhF$_5$. Both TCP-Ph and TCP-PhF have been synthesized and tested experimentally.[10,11]

Figure 6.3 displays the LoD representations used in the simulation of these chromophores, with TCP-Ph, TCP-PhF, and TCP-PhF$_5$ chromophore representation for both rotational isomers.

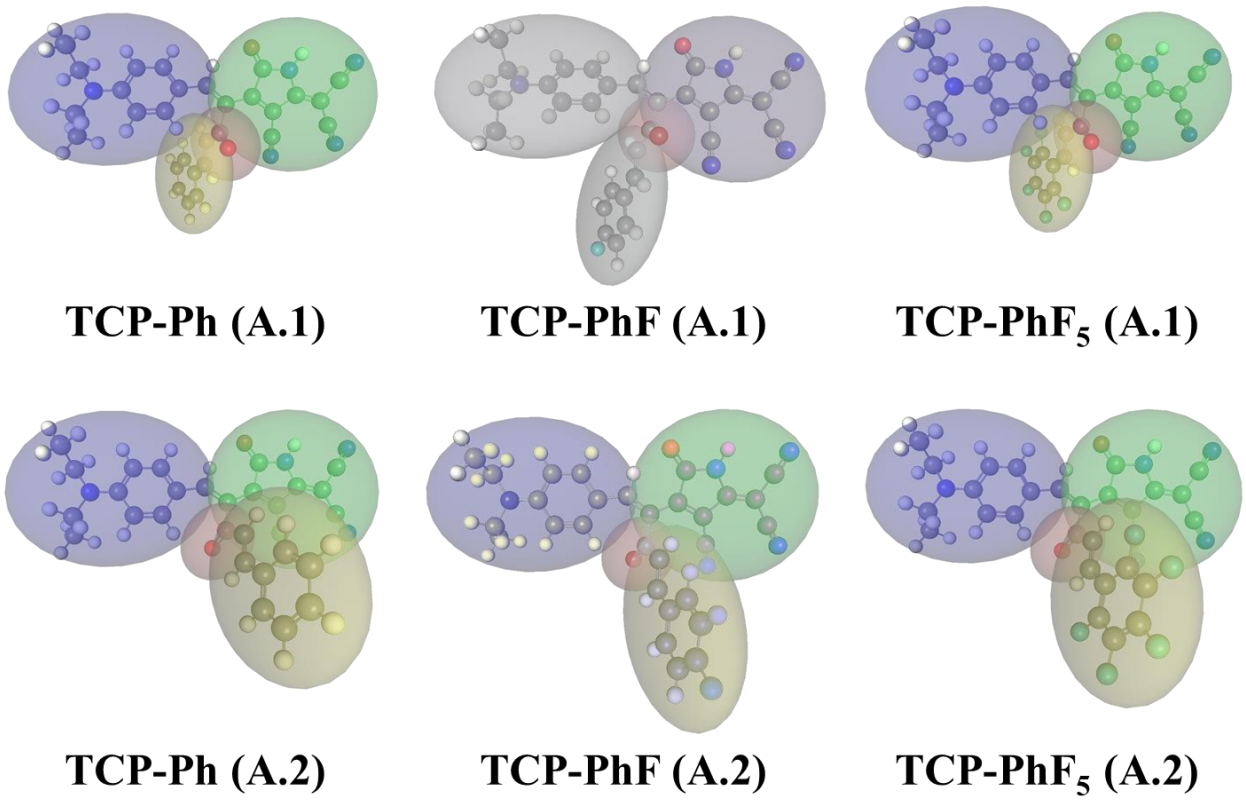

Figure 6.3: LoD representations of TCP-Ph, TCP-PhF, and TCP-PhF$_5$ chromophores with both rotational isomers

Table 6.2: TCP-Ph, TCP-PhF, TCP-PhF_5, and a 1:1 (m/m) mixture of TCP-PhF:TCP-PhF_5 simulation results averages of 24 simulations (density, system enthalpy, heat capacity, dielectric constant, centrosymmetric order, acentric order, and chromophore loading) sampled over last 40 kcycles of 240 kcycles of simulations with error in the last digit in parentheses. (See Appendix B for model parameters) Light orange colored rows represent traditional NPT simulations, light green colored rows the use of AVA for the first 40 kcycles, and light blue colored rows AVA simulations with a quadrupolar expansion at ellipsoid centers. Note that no correction for internal degrees of freedom for heat capacity results was performed.

Model	Density[c]	H_{total}[d]	c_P[e]	Dielectric	$\langle\cos^2\theta\rangle$	$\langle\cos^3\theta\rangle$	$\rho_N\langle\cos^3\theta\rangle$[f]
TCP-Ph (A.1)[a]	0.861(4)	-81.0(7)	63(9)	9(4)	0.34(3)	0.05(3)	0.5 ± 0.3
TCP-Ph (A.1)[b]	0.861(3)	-83.3(7)	57(7)	20(3)	0.36(2)	0.15(3)	1.6 ± 0.3
TCP-Ph (A.2)[b]	0.862(3)	-102(1)	62(10)	22(4)	0.35(2)	0.14(3)	1.5 ± 0.4
TCP-Ph (A.1)[b,c]	0.868(4)	-87.2(9)	54(7)	20(4)	0.36(4)	0.13(4)	1.5 ± 0.4
TCP-Ph (A.2)[b,c]	0.871(4)	-109(1)	55(7)	21(5)	0.35(3)	0.13(4)	1.5 ± 0.4
TCP-PhF (A.1)[b]	0.881(3)	-85.9(7)	58(7)	18(4)	0.35(2)	0.13(4)	1.4 ± 0.4
TCP-PhF (A.2)[b]	0.882(4)	-104(1)	60(11)	20(4)	0.36(3)	0.14(3)	1.5 ± 0.3
TCP-PhF (A.1)[b,c]	0.889(5)	-90.1(8)	59(16)	20(5)	0.34(2)	0.13(4)	1.5 ± 0.4
TCP-PhF (A.2)[b,c]	0.892(4)	-112(1)	55(10)	18(4)	0.35(2)	0.11(3)	1.2 ± 0.4
TCP-PhF_5 (A.1)[b]	0.982(4)	-91.2(6)	52(6)	19(4)	0.36(3)	0.14(4)	1.5 ± 0.4
TCP-PhF_5 (A.2)[b]	0.982(5)	-112(1)	64(15)	21(3)	0.35(3)	0.15(3)	1.5 ± 0.3
TCP-PhF_5 (A.1)[b,c]	0.986(4)	-94.1(9)	51(5)	17(3)	0.36(3)	0.13(4)	1.3 ± 0.4
TCP-PhF_5 (A.2)[b,c]	0.988(5)	-118(1)	55(9)	19(3)	0.35(3)	0.13(2)	1.4 ± 0.2
TCP-Ph+ TCP-PhF_5 (A.1+A.2)[b]	0.921(4)	-96.7(6)	56(7)	19(5)	0.34(5)	0.12(6)	1.3 ± 0.6
TCP-Ph+ TCP-PhF_5 (A.1+A.2)[b,c]	0.932(5)	-101(1)	53(7)	19(4)	0.36(4)	0.13(5)	1.4 ± 0.5

[a]NPT at 0.1 atm, [b]AVA for first 40 kcycles, NPT at 0.1 atm, [c]quadrupole expansion at ellipsoid centers, [c]in units of $\frac{g}{cc}$, [d]in units of $\frac{kJ}{mol}$, [e]in units of $\frac{J}{mol\ K}$, [f]in units of $10^{20}\ molecules/cc$

Table 6.2 summarizes simulation results. Rows are colored by the simulation type with light orange colored rows representing traditional NPT simulations, light green colored rows the use of AVA for the first 40 kcycles, and light blue colored rows AVA simulations with a quadrupolar expansion at ellipsoid centers. Simulations using AVA for the first 40 kcycles resulted in systems with an average energy lowered by 2.3 kJ/mol. These results show that, yet again, the AVA method leads to the energetically favored state. A three-fold improvement of acentric order could be observed between AVA and traditional NPT simulation results.

No significant centrosymmetric order was observed, however, slightly increased acentric order compared to the TCP-1 and TCP-Me systems could be observed for the present chromophores.

The average overall acentric order for TCP-Ph, TCP-PhF, TCP-PhF_5 was found to be $\langle \cos^3 \theta \rangle = (0.13 \pm 0.04)$ with an average overall chromophore loading of $\rho_N \langle \cos^3 \theta \rangle = (1.4 \pm 0.4) \cdot 10^{20}\ molecules/cc$.

As observed for TCP-Me simulations there is a difference in system energies when the A.2 rotational isomer is used instead of the A.1 rotational isomer. Energy differences of 19 kJ/mol, 18 kJ/mol, and 21 kJ/mol were found for TCP-Ph, TCP-PhF, and TCP-PhF_5 systems, respectively.

Figure 6.4 shows a potential energy scan obtained with Gaussian 09C[13] using the B3LYP/6-31G(d) potential in vacuum of the of the cross-conjugated phenylethene-ketone moiety in TCP-Ph around the donor-side vinyl-ketone dihedral angle, similar to the investigation of the rotational energy landscape for TCP-Me displayed in figure 6.2.

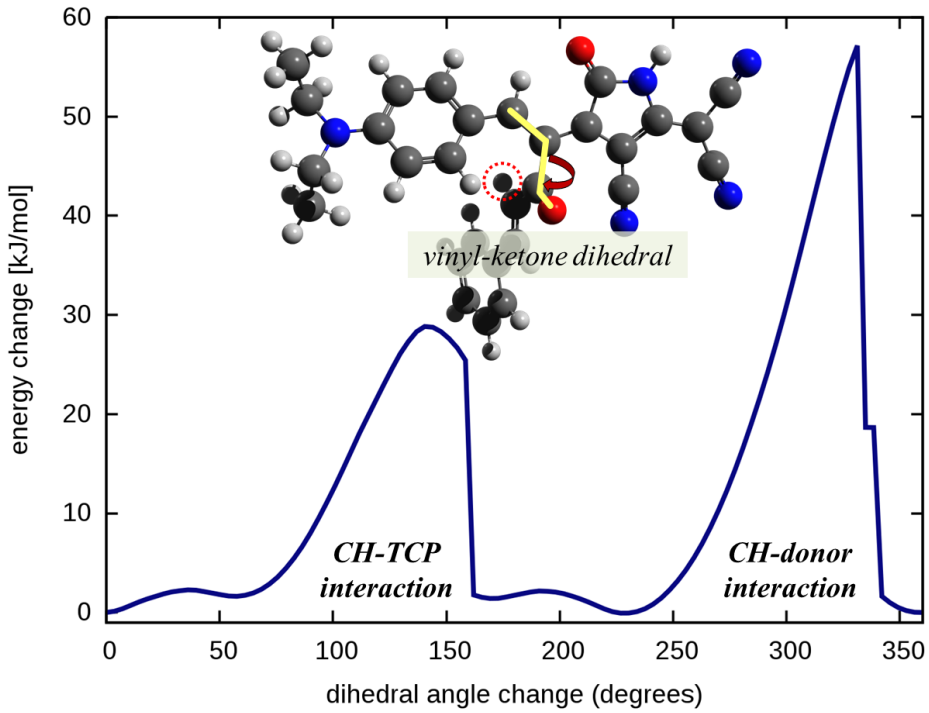

Figure 6.4: TCP-Ph energy landscape upon clockwise rotation of the cross-conjugated phenylethene-ketone moiety around the donor-side vinyl-ketone dihedral angle

The rotation around the donor-side vinyl-ketone dihedral is hindered by the hydrogen atom at the end of the phenylethene subunit (red dotted circle in figure 6.4). This scenario is similar to the rotational hindrance observed for TCP-Me in figure 6.2. Therefore, one would expect similar rotational energy barriers between TCP-Ph and TCP-Me which is the observed behavior.

With even larger energy differences between rotamers, one would expect to observe predominantly the TCP-Ph (A.2) species in a condensed film. Interestingly, this was not observed in the experimental crystal structure of TCP-Ph which featured both rotation isomers.[10] A potential explanation of this observation could be that in the CG LoD simulations the twist angle between diethylamino donor and the TCP acceptor was held fixed at the theoretically predicted values of 27.3° and 27.6° for TCP-Me (A.1) and (A.2), respectively, as well as 31.0° and 4.4° for the TCP-Ph (A.1) and (A.2) rotational isomers.

For TCP-Me the experimentally observed twist angle in the crystal structure[10] was about 23° with only the (A.2) rotamer present, close to the theoretically predicted value used in the simulations. For TCP-Ph, on the other hand, the experimentally observed twist angle in the crystal structure[10] was about 16° for both rotational isomers, very different from the value used in the presented simulations. The change of twist angle between donor and TCP-acceptor units can potentially equalize the energetic differences found between TCP-Ph (A.1) and (A.2) rotational isomers thus leading to the experimentally observed presence of both rotational isomers.

In order to represent this behavior in future simulation work, a torsion potential between donor and TCP-acceptor ellipsoids could be included, calculated using quantum-mechanical potential energy scans similar to the ones used for figures 6.2 and 6.4. In order to improve simulation behavior for TCP-Ph/TCP-PhF5 mixtures, additional work should focus on applying the π-stacking interactions observed between benzene and hexafluorobenzene in chapter 2.5.1, as currently no stacking interactions between phenyl and pentafluorophenyl moieties could be observed.

6.5 CONCLUSIONS

Simulations on existing[10,11] small chromophores containing the TCP-acceptor were conducted. The observed chromophore loading was about 50% larger than for the much larger TCF-based chromophores presented in chapter 5. Overall average chromophore loading for this new class of chromophores is expected to be $\rho_N\langle\cos^3\theta\rangle = (1.5 \pm 0.4) \cdot 10^{20}\ molecules/cc$ obtained from averaging over all present simulation results. This is an exciting result because currently developed small TCP-acceptor chromophore systems are predicted to have similar first-order hyperpolarizabilities comparable to larger TCF-based chromophores (studied in chapter 5) such as YLD124.

This work in conjunction with the benzene/hexafluorobenzene work from chapter 2.5.1 and the current LoD rule set lays the foundation for future work on these systems. The use of quantum-mechanical potential energy scans such as the ones presented in figures 6.2 and 6.4 may lead to improved accuracy in the prediction of these chromophore systems. Their relatively small size compared to traditional chromophores presents another advantage to the simulation of these systems as far fewer units can be used to properly describe them. This can directly lead to large-scale simulations providing even better theoretical predictions.

6.6 REFERENCES FOR CHAPTER 6

[1] Carboni, R. A. 5-Cyanomethylene-2-Oxo-3-Pyrrolines. US3013013 A, December 12, 1961.

[2] Matumoto, H.; Imai, H.; Tada, S. Pyrroline Derivative. US4845235 A, July 4, 1989.

[3] Jang, S.-H.; Luo, J.; Tucker, N. M.; Leclercq, A.; Zojer, E.; Haller, M. A.; Kim, T.-D.; Kang, J.-W.; Firestone, K.; Bale, D.; Lao, D.; Benedict, J. B.; Cohen, D.; Kaminsky, W.; Kahr, B.; Brédas, J.-L.; Reid, P.; Dalton, L. R.; Jen, A. K.-Y. Pyrroline Chromophores for Electro-Optics. *Chem. Mater.* **2006**, *18* (13), 2982–2988.

[4] Jen, K.-Y.; Jang, S.-H.; Kahr, B. Pyrroline Chromophores. US7307173 B1, December 11, 2007.

[5] Cavanagh, D.; James, M. R.; Meyrick, B. H.; Wight, P. Blue to Green Disperse Dyes for Synthetic Fiber Material. US5865857 A, February 2, 1999.

[6] Brierley, D.; Bullock, J. F.; Leaver, A. Disperse Dye Mixtures. EP1121393 B1, September 4, 2002.

[7] Shuttleworth, L.; McManus, M. J. In Situ Dye Generation for Thermal Transfer Printing. US5011811 A, April 30, 1991.

[8] Shuttleworth, L.; Weber, H. Acylated Dicyanovinylpyrroline Dye-Donor Element for Thermal Dye Transfer. US5166128 A, November 24, 1992.

[9] Leclercq, A.; Zojer, E.; Jang, S.-H.; Barlow, S.; Geskin, V.; Jen, A. K.-Y.; Marder, S. R.; Brédas, J. L. Quantum-Chemical Investigation of Second-Order Nonlinear Optical Chromophores: Comparison of Strong Nitrile-Based Acceptor End Groups and Role of Auxiliary Donors and Acceptors. *J. Chem. Phys.* **2006**, *124* (4), 044510.

[10] Rawal, M. Cross-Conjugated Moieties as Design Motifs for a Class of Novel Electro-Optic Chromophores, University of Washington, 2013.

[11] Rawal, M.; Garrett, K.; Tillack, A. F.; Kaminsky, W.; Jucov, E.; Shelton, D. P.; Timofeeva, T. V.; Eichinger, B. E.; Robinson, B. H.; Dalton, L. R. Cross-Conjugation as a Motif for Organic Non-Linear Optical Molecules. In *Symposium II/JJ/KK – Materials, Processes and Devices for Nanophotonics, Nonlinear Optics and Resonant Optics*; MRS Online Proceedings Library; 2014; Vol. 1698.

[12] Tillack, A. F.; Johnson, L. E.; Rawal, M.; Dalton, L. R.; Robinson, B. H. Modeling Chromophore Order: A Guide For Improving EO Performance. In *Symposium II/JJ/KK – Materials, Processes and Devices for Nanophotonics, Nonlinear Optics and Resonant Optics*; MRS Online Proceedings Library; 2014; Vol. 1698.

[13] Frisch, M. J.; Trucks, G. W.; Schlegel, H. B.; Scuseria, G. E.; Robb, M. A.; Cheeseman, J. R.; Scalmani, G.; Barone, V.; Mennucci, B.; Petersson, G. A.; Nakatsuji, H.; Caricato, M.; Li, X.; Hratchian, H. P.; Izmaylov, A. F.; Bloino, J.; Zheng, G.; Sonnenberg, J. L.; Hada, M.; Ehara, M.; Toyota, K.; Fukuda, R.; Hasegawa, J.; Ishida, M.; Nakajima, T.; Honda, Y.; Kitao, O.; Nakai, H.; Vreven, T.; Montgomery Jr., J. A.; Peralta, J. E.; Ogliaro, F.; Bearpark, M. J.; Heyd, J.; Brothers, E. N.; Kudin, K. N.; Staroverov, V. N.; Kobayashi, R.; Normand, J.; Raghavachari, K.; Rendell, A. P.; Burant, J. C.; Iyengar, S. S.; Tomasi, J.; Cossi, M.; Rega, N.; Millam, N. J.; Klene, M.; Knox, J. E.; Cross, J. B.; Bakken, V.; Adamo, C.; Jaramillo, J.; Gomperts, R.; Stratmann, R. E.; Yazyev, O.; Austin, A. J.; Cammi, R.; Pomelli, C.; Ochterski, J. W.; Martin, R. L.; Morokuma, K.; Zakrzewski, V. G.; Voth, G. A.; Salvador, P.; Dannenberg, J. J.; Dapprich, S.; Daniels, A. D.; Farkas, Ö.; Foresman, J. B.; Ortiz, J. V.; Cioslowski, J.; Fox, D. J. *Gaussian 09*; Gaussian, Inc.: Wallingford, CT, USA, 2009.

[14] Johnson, L. E. Multi-Scale Modeling of Organic Electro-Optic Materials, University of Washington, 2012.

[15] Carey, F. A.; Sundberg, R. J. *Advanced Organic Chemistry: Part A: Structure and Mechanisms*; Springer Science & Business Media, 2007.

7 ELECTRO-OPTIC CHROMOPHORE DESIGN CRITERIA

7.1 INTRODUCTION

This chapter serves as a collection of the electro-optic chromophore design criteria discovered thus far. Furthermore, the theoretical framework presented in this work is used to develop an additional design criterion from simulations using simplified chromophore LoD representations incorporating up to five ellipsoids.

7.2 CHROMOPHORE PROTECTION

A recurring motif in the electro-optic chromophore community is the protection of chromophore cores in order to avoid centrosymmetric packing due to strong dipole-dipole interactions.[1–11] For this purpose, a common idea is to add bulky substituent groups along the conjugated backbone of the electro-optic chromophore. The beneficial effect of such added bulk can be verified with a simple statistical mechanics simulation.

The chromophore core is modeled as an ellipsoid (semi axes: 1.8 Å x 3.8 Å x 12.8 Å with a dipole moment along the ellipsoid major axis of 24 D, representative of the CLD-1 type chromophore core. The protection group added is an oblate spheroid with no electrostatic content centered at the chromophore ellipsoid with a fixed semi axis of 4.8 Å in the direction of the ellipsoid major axis and an adjustable radius perpendicular to it. Lennard-Jones interactions were modeled using the "adjusted-width" LJ LoD potential in equation (2-6) with interaction area

correction from equation (2-39). The chromophore core ellipsoid LJ energy used in equation (2-39) was $0.285\ perg$ while the protecting group LJ energy was $0.1\ perg$. Both ellipsoids used a width parameter for the "adjusted width" LJ potential of $\sigma_0 = 2$ Å. The values chosen are similar to LoD method parameters for the CLD-1 chromophore and tert-butyl protecting group when expressed as single ellipsoids. All simulations, after the initial 80 kcycles using AVA, were conducted in the isothermal, isobaric (NPT) ensemble under $1\ atm$ at $420\ K$ with an external poling field of $100\frac{V}{\mu m}$.

Figure 7.1 displays the simulation results of this endeavor. Simulated chromophore loading as well as acentric order is predicted to rise with increasing protecting group radius after the protecting group radius is large enough (>2 Å) to encompass the center chromophore spheroid. A maximum chromophore loading of about $\rho_N\langle\cos^3\theta\rangle = (1.04 \pm 0.07) \cdot 10^{20}\ molecules/cc$ with a corresponding acentric order of $\langle\cos^3\theta\rangle = (0.31 \pm 0.02)$ is reached.

Note that observed order and chromophore loading are seemingly much lower compared to the results presented in chapter 3 using a similar ellipsoidal chromophore representation. These differences are due to the use of the isothermal, isobaric (NPT) ensemble here, as opposed to the canonical (NVT) ensemble with a purely repulsive LJ potential, acting as an intrinsic protection to avoid close dipole-dipole interactions, for the calculations presented in chapter 3.

Resulting number densities in this chapter are more comparable to experimentally expected values of around $5.0 \cdot 10^{20}\ chromophores/cc$.[12] This value is about 2.5 times smaller than the largest number density investigated in the study in chapter 3 which also featured strongly enhanced acentric order. In order to obtain comparable number densities (and order) in the NPT ensemble unrealistically large external pressures would have to be employed.

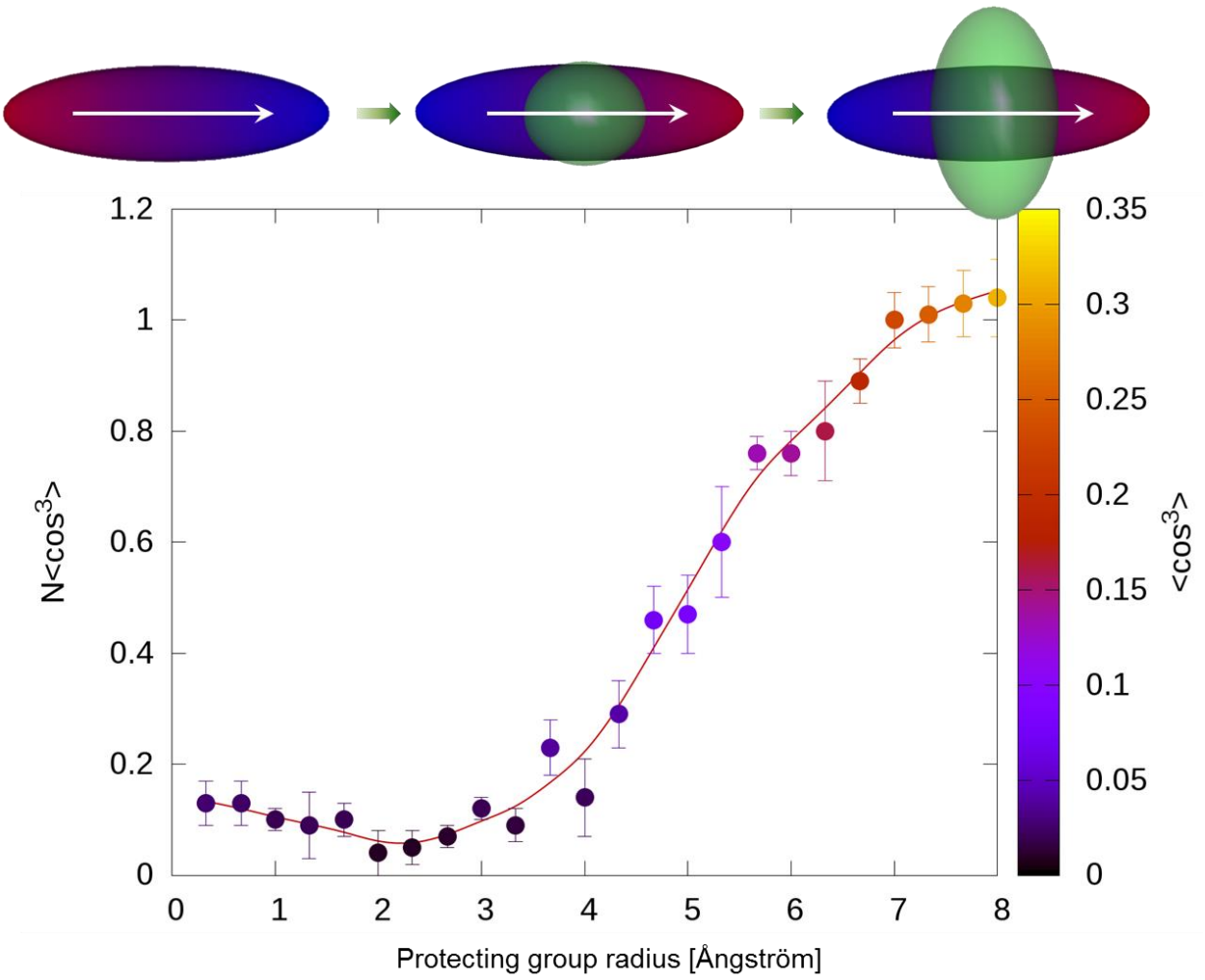

Figure 7.1: Chromophore loading averages as a function of protecting group radius (green center spheroid) for protected single ellipsoid. Dot coloration corresponds to the average acentric order $\langle \cos^3 \theta \rangle$.

Furthermore, the observed acentric order for the NVT calculations of chapter 3 at a comparable number density of $4.5 \cdot 10^{20}\ chromophores/cc$, $\langle \cos^3 \theta \rangle_{NVT} = (0.30 \pm 0.04)$, is similar to the observed maximum acentric order in figure 7.1. This indicates that the notion of dipole protection works both implicitly, with a repulsive LJ potential as demonstrated in chapter 3 as well as explicitly with a protective group as shown here.

Figure 7.2 shows the simulated average centrosymmetric order parameter $\langle P_2 \rangle$ as a function of the average acentric order $\langle \cos^3 \theta \rangle$ to further investigate the ordering behavior of this system.

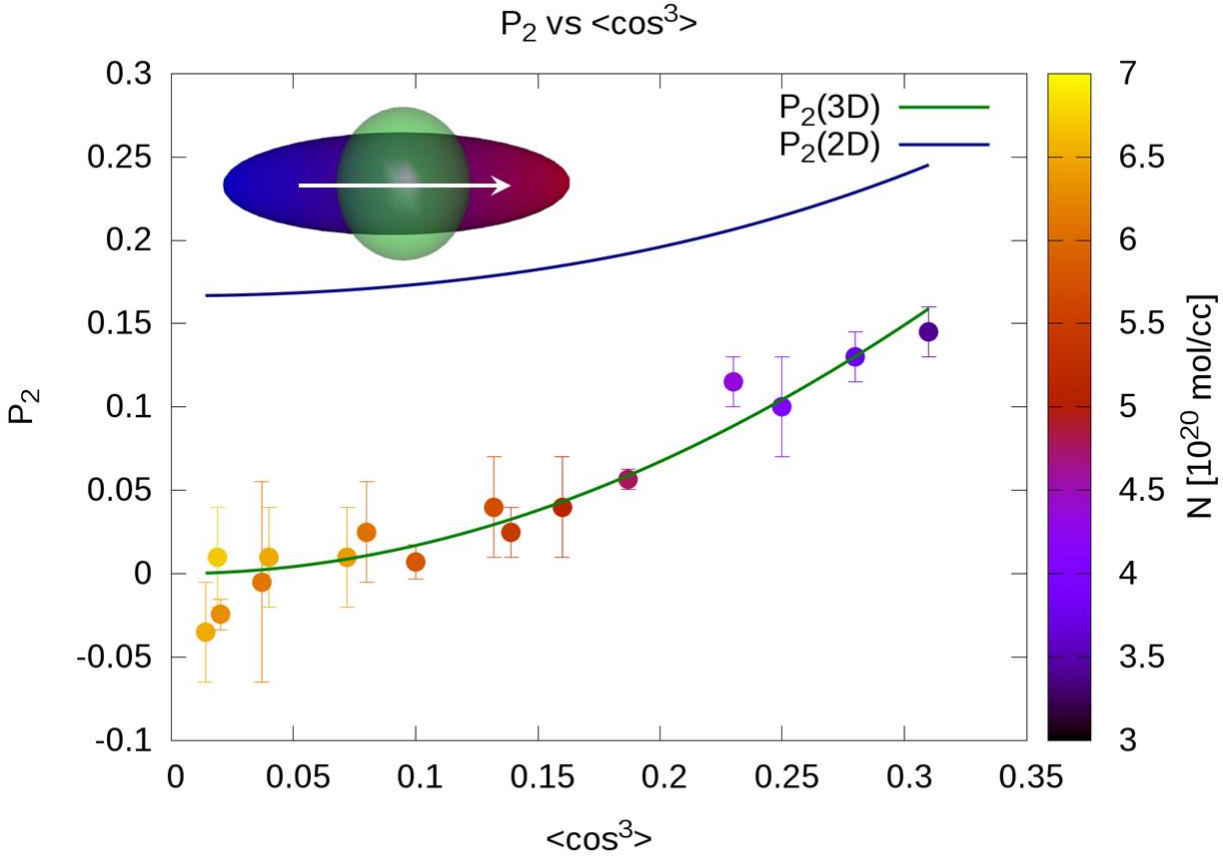

Figure 7.2: Average centrosymmetric order parameter $\langle P_2 \rangle$ as a function of average acentric order $\langle \cos^3 \theta \rangle$ for protected single ellipsoid. Theoretically predicted $\langle P_2(\cos^3 \theta) \rangle$ traces are shown for the two-dimensional (blue line) and three-dimensional (green line) cases of dipole orientational space

In addition to the presented simulation results, theoretically predicted $\langle P_2(\cos^3 \theta) \rangle$ traces obtained using Langevin theory for two-dimensional (blue line) and three-dimensional (green line) dipole order orientational spaces are included.[13] The simulated data corresponds well with the 3D case indicating that dipole rotations were allowed in all three dimension in the simulated systems.

Overall, the presented simulation data supports the hypothesis of using a bulky protecting group to maximize chromophore loading in an electro-optic material. Furthermore, because the Lennard-Jones interaction potential used in the simulations shown is as realistic as possible using the single ellipsoidal CG LoD approach, better correspondence with experimental results of a similar chromophore may be observed. On the other hand, electrostatic interactions due to strong overall dipole moments predominantly drive the interactions of these chromophores. As was observed in the results in chapter 3, the single point dipole at the center of the chromophore may be an overly simplistic representation. Figure 7.3 displays results using a two-ellipsoid model with a center protecting group. See Appendix B for model parameters.

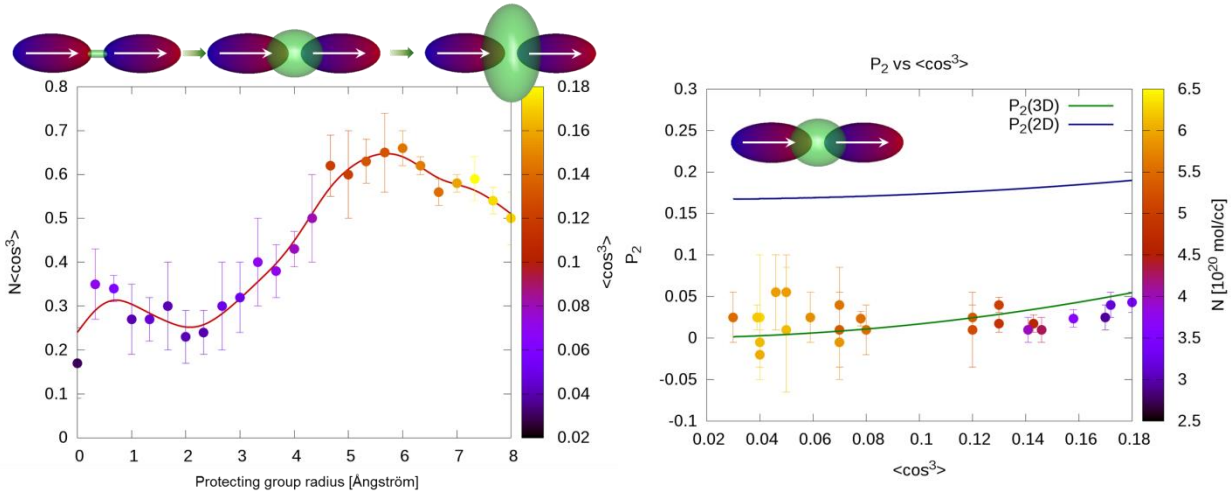

Figure 7.3: Chromophore loading averages as a function of protecting group radius (green center spheroid) for center-protected two-ellipsoid model and average centrosymmetric order parameter $\langle P_2 \rangle$ as a function of average acentric order $\langle \cos^3 \theta \rangle$. Theoretically predicted $\langle P_2(\cos^3 \theta) \rangle$ traces are shown for the two-dimensional (blue line) and three-dimensional (green line) cases of dipole orientational space

Similarly to the results in chapter 3, in which resulting chromophore loading was greatly reduced when a two-ellipsoidal representation was employed, maximum chromophore loading drops by about 36% to a value of $\rho_N \langle \cos^3 \theta \rangle = (0.66 \pm 0.04) \cdot 10^{20}\ molecules/cc$ compared to the

single ellipsoidal representation. Maximum average acentric order drops more than two-fold compared to the single ellipsoid representation to a value of $\langle \cos^3 \theta \rangle = (0.14 \pm 0.01)$. Like the single ellipsoid model, the ordering behavior falls on the three-dimensional curve.

Interestingly, the simulated poling behavior shows an optimal size of around $5 - 6$ Å for the protecting group radius with respect to chromophore loading. Furthermore, in the two-ellipsoid model the protecting group does no longer protect the dipole moments now located at individual ellipsoid centers rather than in the center of the chromophore.[1] A better approach would be to place two protecting groups around the two dipole locations. Figure 7.4 explores this hypothesis.

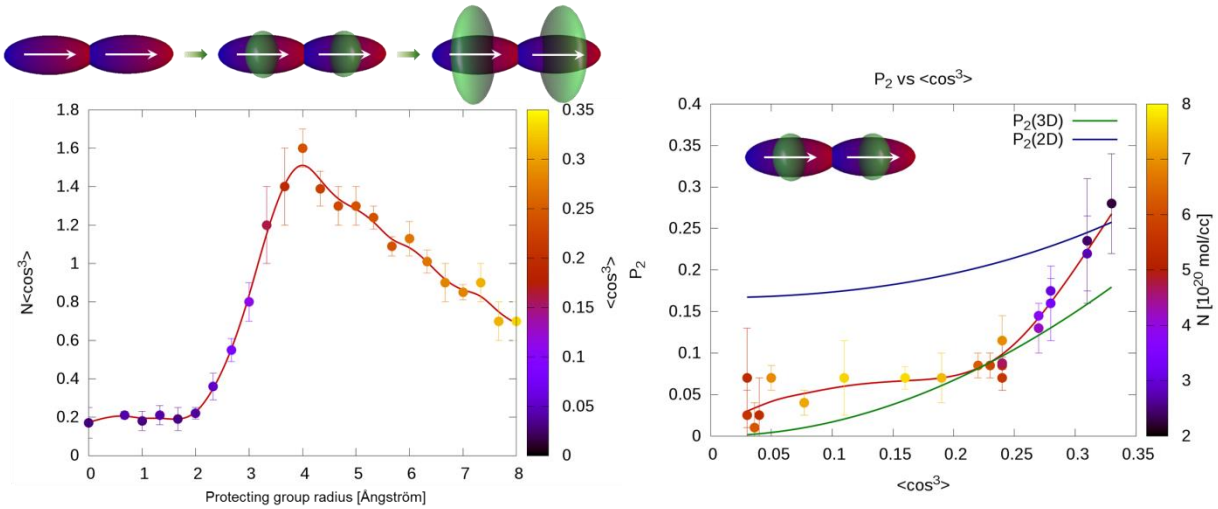

Figure 7.4: Chromophore loading averages as a function of protecting group radius (green center spheroid) for dipole-protected two-ellipsoid model and average centrosymmetric order parameter $\langle P_2 \rangle$ as a function of average acentric order $\langle \cos^3 \theta \rangle$. Theoretically predicted $\langle P_2(\cos^3 \theta) \rangle$ traces are shown for the two-dimensional (blue line) and three-dimensional (green line) cases of dipole orientational space

The resulting improvement in chromophore loading is tremendous. Compared to the single-ellipsoid model of similar dimensions and identical overall dipole moment the two-ellipsoid LoD

[1] The small gap of 2 Å between the chromophore ellipsoids, inaccessible to other chromophores in the simulation due to size, was put in place to visually represent this fact.

representation (see Appendix B for model parameters) improves the optimal chromophore loading by 54% compared to the single ellipsoid results in figure 7.1 and by about 142% compared to the center protected two-ellipsoid results in figure 7.3 to a value of $(1.6 \pm 0.1) \cdot 10^{20}\ molecules/cc$. Furthermore, while maximum simulated acentric order is 0.33 ± 0.05, the acentric order observed at peak chromophore loading is 0.24 ± 0.01. The drop in chromophore loading after its peak is due to a rapid drop in number densities, outpacing the increase seen in acentric order.

The increase in acentric order after peak chromophore loading has been reached is accompanied by an increase in centrosymmetric order so strongly that the chromophore organization switches from three-dimensional to two-dimensional behavior. A much less pronounced decrease in order dimensionality can be observed before peak chromophore loading is reached. For the present linear chromophore system lower dimensionality can be accompanied by both relatively low and relatively large acentric order – the overall optimal value with respect to chromophore loading, however, is observed in the three-dimensional case.

Figure 7.5 displays simulated chromophore loading as a function of protecting group radii and order behavior for an identically shaped system compared to figure 7.4 with a center point dipole instead of the two dipoles at the chromophore ellipsoid centers. This arrangement was chosen to investigate possible shape effects on chromophore behavior as well as its effect on dipole protection. Results show overall peak chromophore loading is reduced to a value of $(1.0 \pm 0.1) \cdot 10^{20}\ molecules/cc$ a decrease of about 38% compared to the two dipole system from figure 7.4. Acentric order maintains a similar range of values and similar peak values within error bars compared to the two dipole arrangement.

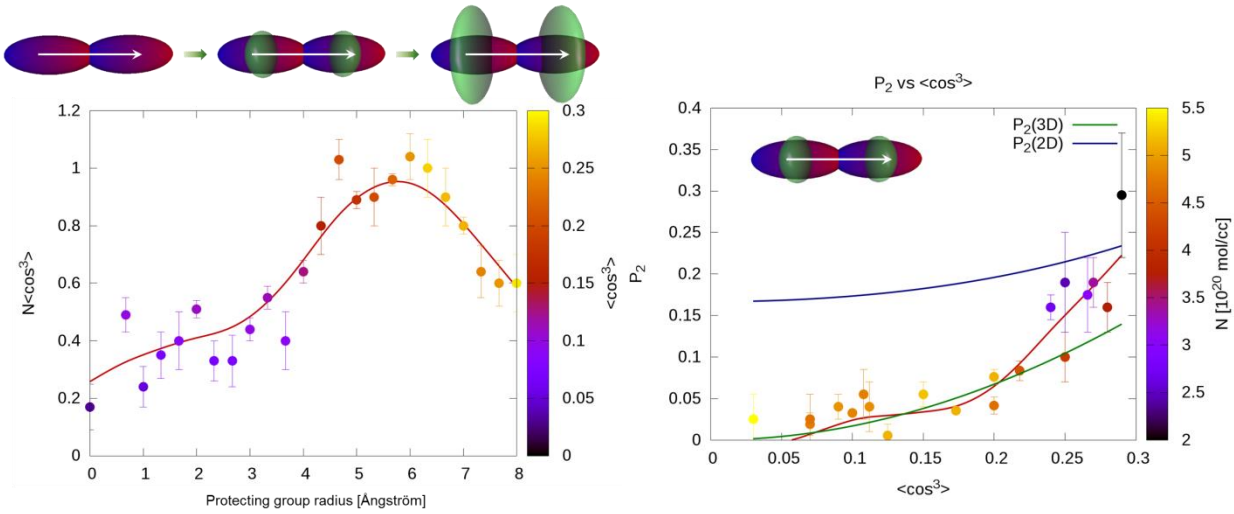

Figure 7.5: Chromophore loading averages as a function of protecting group radius (green center spheroid) for shape-protected two-ellipsoid model and average centrosymmetric order parameter $\langle P_2 \rangle$ as a function of average acentric order $\langle \cos^3 \theta \rangle$. Theoretically predicted $\langle P_2(\cos^3 \theta) \rangle$ traces are shown for the two-dimensional (blue line) and three-dimensional (green line) cases of dipole orientational space

Interestingly, the chromophore loading curve shape resembles that of figure 7.3 with increased chromophore loading due to the increased acentric order in the optimum range. This indicates that the overall chromophore shape including the protecting groups can increase acentric order as evidenced by the increase in order when two protecting groups are used. However, optimal chromophore loading can only be achieved when dipoles are protected.

The resulting design criterion is that individual dipole moments need to be protected. For realistic electro-optic chromophore systems with distributed partial charges not necessarily representing point dipoles the optimum location for the placement of protecting groups can potentially be obtained using theory. To that end, figures 7.6 and 7.7 give an outlook on applying the presented concept of dipole protection to a realistic chromophore system based on a slightly modified YLD124 chromophore[10–12,14–20] using a dimethyl-amine donor instead of the usual TBDMS attachments.

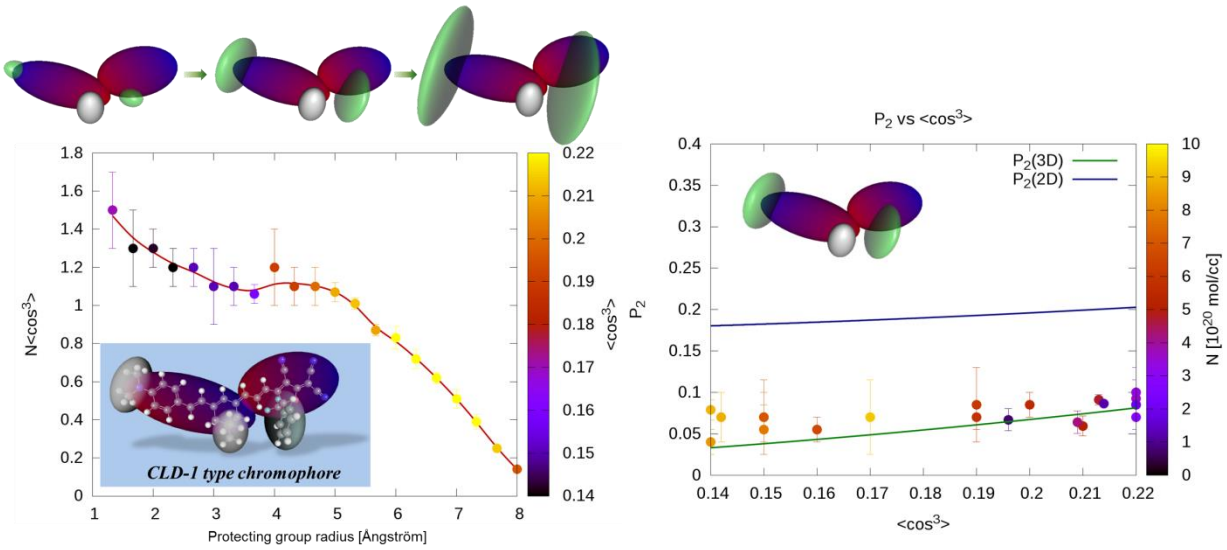

Figure 7.6: Chromophore loading averages as a function of protecting group radius (green center spheroid) for CLD-1 type model and average centrosymmetric order parameter $\langle P_2 \rangle$ as a function of average acentric order $\langle \cos^3 \theta \rangle$. Theoretically predicted $\langle P_2(\cos^3 \theta) \rangle$ traces are shown for the two-dimensional (blue line) and three-dimensional (green line) cases of dipole orientational space. The inset shows underlying LoD model of the CLD-1 type chromophore.

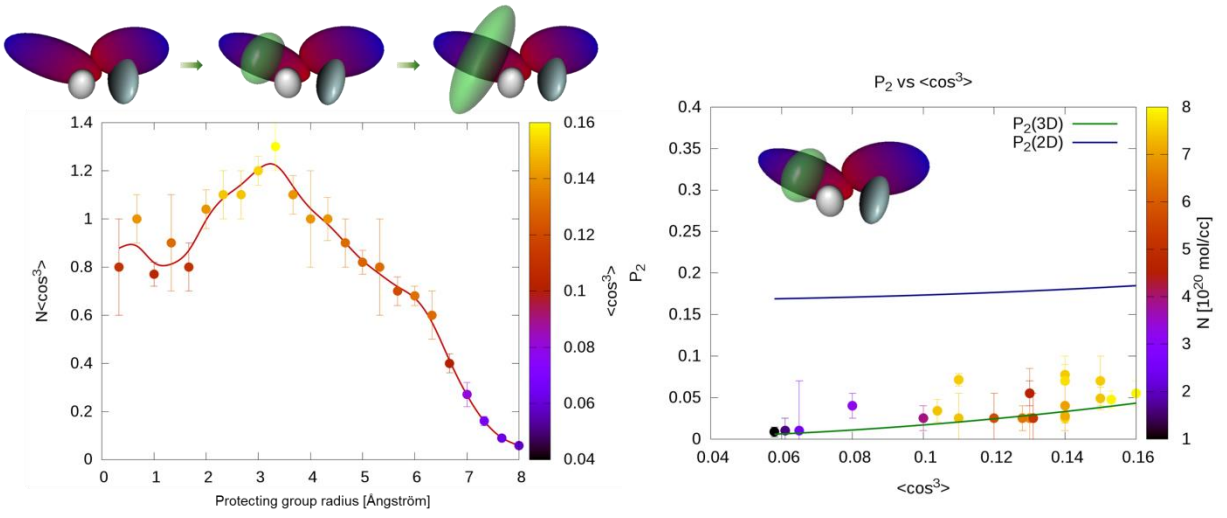

Figure 7.7: Chromophore loading averages as a function of protecting group radius (green center spheroid) for dipole-protected CLD-1 type model and average centrosymmetric order parameter $\langle P_2 \rangle$ as a function of average acentric order $\langle \cos^3 \theta \rangle$. Theoretically predicted $\langle P_2(\cos^3 \theta) \rangle$ traces are shown for the two-dimensional (blue line) and three-dimensional (green line) cases of dipole orientational space

The models in figure 7.6 and 7.7 are based on best-fit values using the current LoD rule set with atomic charges reduced to a point charge and point dipole at the ellipsoid centers (see Appendix B for model parameters). Figure 7.6 displays simulation results for different radii of both ellipsoids representing the donor attachment and the CF_3-phenyl acceptor attachment. In figure 7.7, the donor attachment is replaced with a protection group with varying radius, similar to the ones found in the linear chromophore models in figures 7.1-7.5, is placed at the center of the donor ellipsoid while the acceptor attachment remains unchanged from the original model (inset in figure 7.6). A notable difference to the linear chromophore models in figures 7.1-7.5 is that the individual point dipoles of the donor and acceptor ellipsoids are not facing in the same direction anymore but are almost opposing each other with point charges in both ellipsoids contributing to the overall dipole moment. Furthermore, instead of a linear ellipsoid arrangement there is a notable kink present.

The resulting chromophore loading in Figure 7.6 starts out at relatively large values and then drops to a wide plateau between $3 - 5$ Å with an average chromophore loading value of $(1.1 \pm 0.2) \cdot 10^{20}\ molecules/cc$ after which chromophore loading drops off rapidly. Interestingly, this plateau region is in a protecting group size regime similar to the original chromophore. Based on these results increased chromophore loading could be expected experimentally when both the donor and acceptor attachments are shrunk in size. However, the CF_3-phenyl acceptor attachment cannot simply be replaced without sacrificing electro-optic activity as an almost two-fold improvement of the first-order hyperpolarizability is observed experimentally versus a dimethyl acceptor attachment.[21,22] Therefore, the CF_3-phenyl acceptor attachment is held fixed in the model used for figure 7.7.

The chromophore loading results displayed in figure 7.7 with a fixed CF_3-phenyl acceptor attachment start out chromophore loading of about $(0.8 \pm 0.2) \cdot 10^{20}\ molecules/cc$ similar to the observed theoretical range observed for all chromophores using the CF_3-phenyl-TCF acceptor. Chromophore loading then peaks at a protecting group radius of 3.3 Å at $(1.3 \pm 0.1) \cdot 10^{20}\ molecules/cc$ and drops off afterwards. For both models, order behavior is consistent with the three-dimensional case.

In summary, chromophore protection is important, especially in terms of preventing strong dipole-dipole interactions. Results on a protected two-ellipsoid straight-chromophore system for the first time showed increased chromophore loading compared to single ellipsoid system with a clear dependence on the protecting group size.

Preliminary results using a realistic chromophore system based on the YLD124 chromophore show that while small improvements in chromophore loading are possible, the original chromophore system already possesses a shape and protecting groups that nearly maximize chromophore loading. Future calculations of this kind, in addition to different protecting group locations will also incorporate different ellipsoid alignment angles in order to get a more complete understanding of electro-optic chromophore behavior.

7.3 DESIGN CRITERIA SUMMARY

This section serves as a compilation of the electro-optic chromophore design criteria developed from simulation results in this work. Most of these criteria have been theorized before and they of course cannot represent a complete set of rules as the design of an optimal electro-optic chromophore is one of many compromises and trade-offs with respect to the particular set of desired optical, mechanical, and chemical properties.

7.3.1 OPTIMUM CHROMOPHORE DIPOLE MOMENT

The overall dipole moment of an electro-optic chromophore depends on the relative strengths and separation distance between electron-donating and electron-accepting groups. A larger chromophore dipole moment for an otherwise electronically similar chromophore is indicative of increased first-order hyperpolarizability but it also potentially leads to increased dipole pairing which diminishes the bulk electro-optic response.

In the set of calculations presented in chapter 3 involving a CLD-1[23] based chromophore system with varying dipole strengths it was discovered that at a given density an optimum dipole moment maximizing chromophore loading exists. It was found that for a chromophore represented by a single point dipole the optimum range for a chromophore the size of CLD-1 is on the order of $10 - 15\ Debye$, while for a more realistic representation using two ellipsoids to represent the chromophore core with a more complex electrostatic representation (see figures 3.7 and 7.6) the optimum range is about the experimental dipole moment of CLD-1 of $24\ Debye$.

In general, while additional measures such as the addition of spacing groups can be employed to handle large chromophore dipole moments and prevent dipole pairing it seems the best strategy is

to keep chromophore dipole moments as small as possible without compromising the molecular first-order hyperpolarizability for a given chromophore size. The next design criterion can be employed to find the optimum dipole by focusing solely on the chromophore core.

7.3.2 Chromophore Loading is Determined by the Chromophore Core

A surprising conclusion to the entire simulation work done on TCF-based chromophore systems in chapter 5 and TCP-based chromophore systems in chapter 6 is overall observed chromophore loading stayed within a relatively narrow distribution that depended on the chromophore core being used but not on additional moieties added to the chromophore. For chromophores using the YLD124-type chromophore core the overall average chromophore loading upon poling in an external field of $100\,\frac{V}{\mu m}$ was $\rho_N\langle\cos^3\theta\rangle = (0.8 \pm 0.3)\cdot 10^{20}\ molecules/cc$ while for the short TCP-based chromophore systems under identical conditions the overall average chromophore loading was $\rho_N\langle\cos^3\theta\rangle = (1.5 \pm 0.4)\cdot 10^{20}\ molecules/cc$.

The goal in optimal EO chromophore design could be to stay on the high side of these error bars, however, practical requirements such as chromophore solubility and glass transition temperature may not always permit this as in all of these cases the high end was given by chromophores with little to no attachments. A corollary to this design criterion could be that within reason additional moieties do not strongly influence chromophore and one is thus at liberty to use them as needed.

A practical consequence of this observation is that chromophore screening, experimentally as well as theoretically, could focus on the chromophore core, for example embedded in a proper host material. Indeed, the results shown in chapter 3 for the CLD-1 chromophore core when read

at the respective experimental number densities are in good agreement with the more intricate simulation results presented in chapter 5 of a similar chromophore core with different additional attachments.

7.3.3 MAXIMIZATION OF NUMBER DENSITY

It is certainly feasible to find attachments to electro-optic chromophores that increase acentric order[2]. However, as pointed out above this approach typically does not yield increased chromophore loading as each additional moiety, while maybe increasing acentric order, also adds volume thus lowering chromophore number density.

The results in chapters 3 and 6 as well as in this chapter indicate that number density typically scales much more rapidly than acentric order. In the results in chapters 3 and 6 chromophore number densities increased more than acentric order could decrease. In this chapter, increasing the volume of additional moieties proved to lower number density more rapidly than acentric order could increase. The reason for this behavior is that acentric order is a bounded property and that number density can typically cover a much wider range of values. For example, under an external poling field of $100\frac{V}{\mu m}$ the lowest observed, simulated acentric order was $\langle\cos^3\theta\rangle = 0.04$ (for YLD124 stuck in a traditional NPT simulation). Mathematically, the upper limit of acentric order is $\langle\cos^3\theta\rangle \leq 1$. In real systems at realistic temperatures, however, the Langevin limit in equation (4-36) provides a good "sound barrier" for acentric order.

It is therefore prudent to maximize number density in a given electro-optic chromophore system.

[2] Of course, the converse is true as well.

7.3.4 DIPOLE PROTECTION

The results presented in this chapter provide good insight into the optimal design of protecting groups to prevent unfavorable dipole pairing. It was found that the optimal locations for protecting groups are around strongly dipolar regions of a chromophore. The addition of properly placed protecting groups led to observable increases in acentric order. Furthermore, it could be demonstrated that there is an optimal size, optimizing both number density and acentric order.

The results in chapter 6 provide another strategy for the suppression of unfavorable dipole pairings. Good acentric order and large number densities were observed with minimal and even no additional protecting groups for TCP-based chromophores with slightly tilted planes of donor and acceptor units. However, this may be a risky strategy as strong overall planarity of the conjugated chromophore region typically is a requirement for large first-order hyperpolarizability as observed in TCF-based chromophores.[24]

7.4 REFERENCES FOR CHAPTER 7

[1] Cheng, L. T.; Tam, W.; Stevenson, S. H.; Meredith, G. R.; Rikken, G.; Marder, S. R. Experimental Investigations of Organic Molecular Nonlinear Optical Polarizabilities. 1. Methods and Results on Benzene and Stilbene Derivatives. *J. Phys. Chem.* **1991**, *95* (26), 10631–10643.

[2] Kanis, D. R.; Ratner, M. A.; Marks, T. J. Design and Construction of Molecular Assemblies with Large Second-Order Optical Nonlinearities. Quantum Chemical Aspects. *Chem. Rev.* **1994**, *94* (1), 195–242.

[3] Dalton, L. R.; Harper, A. W.; Robinson, B. H. The Role of London Forces in Defining Noncentrosymmetric Order of High Dipole Moment–high Hyperpolarizability Chromophores in Electrically Poled Polymeric Thin Films. *Proc. Natl. Acad. Sci.* **1997**, *94* (10), 4842–4847.

[4] Dalton, L. R. Rational Design of Organic Electro-Optic Materials. *J. Phys. Condens. Matter* **2003**, *15* (20), R897.

[5] Luo, J.; Haller, M.; Ma, H.; Liu, S.; Kim, T.-D.; Tian, Y.; Chen, B.; Jang, S.-H.; Dalton, L. R.; Jen, A. K.-Y. Nanoscale Architectural Control and Macromolecular Engineering of Nonlinear Optical Dendrimers and Polymers for Electro-Optics †. *J. Phys. Chem. B* **2004**, *108* (25), 8523–8530.

[6] Liao, Y.; Eichinger, B. E.; Firestone, K. A.; Haller, M.; Luo, J.; Kaminsky, W.; Benedict, J. B.; Reid, P. J.; Jen, A. K.-Y.; Dalton, L. R.; Robinson, B. H. Systematic Study of the Structure−Property Relationship of a Series of Ferrocenyl Nonlinear Optical Chromophores. *J. Am. Chem. Soc.* **2005**, *127* (8), 2758–2766.

[7] Liao, Y.; Anderson, C. A.; Sullivan, P. A.; Akelaitis, A. J. P.; Robinson, B. H.; Dalton, L. R. Electro-Optical Properties of Polymers Containing Alternating Nonlinear Optical Chromophores and Bulky Spacers. *Chem. Mater.* **2006**, *18* (4), 1062–1067.

[8] Sullivan, P. A. Theory Guided Design and Molecular Engineering of Organic Materials for Enhanced Second-Order Nonlinear Optical Properties, University of Washington, 2006.

[9] Sullivan, P. A.; Rommel, H.; Liao, Y.; Olbricht, B. C.; Akelaitis, A. J. P.; Firestone, K. A.; Kang, J.-W.; Luo, J.; Davies, J. A.; Choi, D. H.; Eichinger, B. E.; Reid, P. J.; Chen, A.; Jen, A. K.-Y.; Robinson, B. H.; Dalton, L. R. Theory-Guided Design and Synthesis of Multichromophore Dendrimers: An Analysis of the Electro-Optic Effect. *J. Am. Chem. Soc.* **2007**, *129* (24), 7523–7530.

[10] Dalton, L. R.; Sullivan, P. A.; Bale, D. H. Electric Field Poled Organic Electro-Optic Materials: State of the Art and Future Prospects. *Chem. Rev.* **2010**, *110* (1), 25–55.

[11] Dalton, L. R.; Benight, S. J.; Johnson, L. E.; Knorr, D. B.; Kosilkin, I.; Eichinger, B. E.; Robinson, B. H.; Jen, A. K.-Y.; Overney, R. M. Systematic Nanoengineering of Soft Matter Organic Electro-Optic Materials. *Chem. Mater.* **2011**, *23* (3), 430–445.

[12] Jin, W.; Johnston, P. V.; Elder, D. L.; Tillack, A. F.; Olbricht, B. C.; Song, J.; Reid, P. J.; Xu, R.; Robinson, B. H.; Dalton, L. R. Benzocyclobutene Barrier Layer for Suppressing Conductance in Nonlinear Optical Devices during Electric Field Poling. *Appl. Phys. Lett.* **2014**, *104* (24), 243304.

[13] Benight, S. J.; Johnson, L. E.; Barnes, R.; Olbricht, B. C.; Bale, D. H.; Reid, P. J.; Eichinger, B. E.; Dalton, L. R.; Sullivan, P. A.; Robinson, B. H. Reduced Dimensionality in Organic Electro-Optic Materials: Theory and Defined Order. *J. Phys. Chem. B* **2010**, *114* (37), 11949–11956.

[14] Baehr-Jones, T.; Hochberg, M.; Wang, G.; Lawson, R.; Liao, Y.; Sullivan, P. A.; Dalton, L.; Jen, A.-Y.; Scherer, A. Optical Modulation and Detection in Slotted Silicon Waveguides. *Opt. Express* **2005**, *13* (14), 5216–5226.

[15] Pereverzev, Y. V.; Gunnerson, K. N.; Prezhdo, O. V.; Sullivan, P. A.; Liao, Y.; Olbricht, B. C.; Akelaitis, A. J. P.; Jen, A. K.-Y.; Dalton, L. R. Guest−Host Cooperativity in Organic Materials Greatly Enhances the Nonlinear Optical Response. *J. Phys. Chem. C* **2008**, *112* (11), 4355–4363.

[16] Benight, S. J.; Bale, D. H.; Olbricht, B. C.; Dalton, L. R. Organic Electro-Optics: Understanding Material Structure/function Relationships and Device Fabrication Issues. *J. Mater. Chem.* **2009**, *19* (40), 7466.

[17] Sullivan, P. A.; Dalton, L. R. Theory-Inspired Development of Organic Electro-Optic Materials. *Acc. Chem. Res.* **2010**, *43* (1), 10–18.

[18] Kim, S.-K.; Pei, Q.; Fetterman, H. R.; Olbright, B. C.; Dalton, L. R. Photoassisted Corona Poled YLD-124/DR1-Co-PMMA Electrooptic Device Using Photoisomerization. *IEEE Photonics Technol. Lett.* **2011**, *23* (13), 845–847.

[19] Dalton, L.; Benight, S. Theory-Guided Design of Organic Electro-Optic Materials and Devices. *Polymers* **2011**, *3* (4), 1325–1351.

[20] Benight, S. J.; Robinson, B. H.; Dalton, L. R.; Meghea, A. Nano-Engineering of Molecular Interactions in Organic Electro-Optic Materials. *Mol. Interact.* **2012**.

[21] Bale, D. H. Nonlinear Optical Materials Characterization Studies Employing Photostability, Hyper-Rayleigh Scattering, and Electric Field Induced Second Harmonic Generation Techniques, University of Washington, 2008.

[22] Johnson, L. E. Multi-Scale Modeling of Organic Electro-Optic Materials, University of Washington, 2012.

[23] Zhang, C.; Dalton, L. R.; Oh, M.-C.; Zhang, H.; Steier, W. H. Low V_π Electrooptic Modulators from CLD-1: Chromophore Design and Synthesis, Material Processing, and Characterization. *Chem. Mater.* **2001**, *13* (9), 3043–3050.

[24] Planells, M.; Pizzotti, M.; Nichol, G. S.; Tessore, F.; Robertson, N. Effect of Torsional Twist on 2nd Order Non-Linear Optical Activity of Anthracene and Pyrene Tricyanofuran Derivatives. *Phys. Chem. Chem. Phys.* **2014**, *16* (42), 23404–23411.

8 CONCLUSIONS AND OUTLOOK

In conclusion, in this present work an approach for the systematic coarse-graining of all-atom force fields called the Level-of-Detail (LoD) method using ellipsoidal rather than spherical building blocks has been presented. The LoD method's ability to correctly represent underlying force field behavior has been demonstrated on a diverse range of condensed molecular systems relevant to different aspects of the simulation of electro-optic materials such as the accurate simulation of π-π interactions, the incorporation of flexible molecular linkers, and the prediction of dielectric behavior. The major contribution of the LoD method is that it uses a systematic set of rules to determine coarse-graining shapes and interaction potential parameters. This allows for a practically unlimited variety of shapes and sizes of ellipsoids to represent molecular fragments in molecules. All parameters are best-fit to the underlying all-atom force field.

This thesis presents a method, called the adiabatic volume adjustment (AVA) method, to find rapid convergence to equilibrium conditions for the molecular system. The AVA method is employed during the initial stages of a simulation, adjusting the simulation volume in a controllable manner while concurrently adjusting the attractive contribution of the Lennard-Jones potential. This method improves system convergence by enhancing simulation configuration space sampling and overcoming local energetic barriers. In comparison to temperature adjustment approaches such as thermal annealing or replica exchange sampling, a volume adjustment approach like the AVA method does not override small potential contributions such as external poling field interactions with large thermal activity and thus seems more suitable to the requirements for simulating electro-optic materials. In the simulation results presented

throughout all chapters, the AVA method consistently found system configurations with lower overall system energy than obtained by other methods.

Equations for computing the dielectric constant for a system from simulation results have been derived and have been applied to a wide variety of molecules. An enhanced reaction field description consistent with the Onsager reaction field has been introduced that allows the usage of point charges, point dipoles, and is stable for use in systems with ions. In conjunction with the LoD method, fully-atomistic results could be matched as well as experimental dielectric constants.

The simulation of condensed, large electro-optic chromophore systems has been undertaken and the results have been presented in chapters 4-6. The combination of theoretical results and experimental observations force the conclusion that experimentally the YLD124 system is kinetically trapped. Experimental electro-optic chromophore order parameters are well reproduced, within error bars, by the averages of hundreds of simulations over a wide range of electro-optic chromophores. A surprising observation – chromophore loading is fundamentally determined by the chromophore core – has been obtained by averaging over the entire set of simulation results. For the simulated TCF-based electro-optic chromophores the overall chromophore loading parameter, $\rho_N\langle\cos^3\theta\rangle$, was found to be $\rho_N\langle\cos^3\theta\rangle = (0.8 \pm 0.3) \cdot 10^{20}\ molecules/cc$ while the simulated short TCP-based chromophores yielded $\rho_N\langle\cos^3\theta\rangle = (1.5 \pm 0.4) \cdot 10^{20}\ molecules/cc$.

Finally, the observations and conclusions derived from the presented theoretical work have culminated in a set of electro-optic material design criteria which, despite not necessarily being a complete rule set, will guide future theoretical as well as experimental studies and may

potentially lead to an enhanced understanding of the design of optimal electro-optical chromophore systems.

The present work is but the foundation upon which to stand for future accomplishments. Many possible improvements have been conceptualized since the LoD method's inception. A major future feature will be the ability to use different levels of detail dependent on interaction distance for a given simulation. This feature, inherent in the LoD method's name, could reduce computational scaling to $NlogN$-scaling, allowing for large scale system simulations in a fraction of the time that is now possible. Additionally, the LoD method is not limited to ellipsoid shapes but could be extended to other smooth, closed shapes such as hyperellipsoids or toroids.

Future studies on condensed electro-optic materials using the current full LoD rule set which so far has not been applied to large-scale, complex electro-optic chromophore systems may lead to even more insight and understanding of these systems. For example, while theoretical results on C1 and CLD-C1 systems match experimental acentric order well centrosymmetric order is generally underestimated, especially for the coumarin moieties contained in these chromophores. Therefore, future work on C1 and CLD-C1 will focus on improving the interactions between coumarins as the driving force for enhanced centrosymmetric order based on the approach used in section 2.5.1 successfully modeling the π-stacking interactions of benzene and hexafluorobenzene. This same approach in addition to quantum-mechanically calculated torsion potentials, similar to calculations performed already (see figure 6.2 and 6.4), may be beneficial for future simulations of short TCP-based chromophores.

BIBLIOGRAPHY

[1] Cisco Visual Networking Index: Global Mobile Data Traffic Forecast Update 2014–2019 White Paper http://cisco.com/c/en/us/solutions/collateral/service-provider/visual-networking-index-vni/white_paper_c11-520862.html (accessed Jul 15, 2015).

[2] The Zettabyte Era—Trends and Analysis http://cisco.com/c/en/us/solutions/collateral/service-provider/visual-networking-index-vni/VNI_Hyperconnectivity_WP.html (accessed Jul 15, 2015).

[3] Carter, L.; United Nations Environment Programme; World Conservation Monitoring Centre. *Submarine Cables and the Oceans: Connecting the World.*; UNEP World Conservation Monitoring System ; International Cable Protection Committee: Cambridge; Lymington, 2009.

[4] Alferness, R. C. Guided-Wave Devices for Optical Communication. *IEEE J. Quantum Electron.* **1981**, *17*, 946–959.

[5] Becker, R. A. Multigigahertz Lumped-Element Electrooptic Modulators. *IEEE J. Quantum Electron.* **1985**, *21* (8), 1144–1146.

[6] Jackel, J. L. Mach-Zehnder Integrated Optical Modulator. US4709978 A, December 1, 1987.

[7] Takagi, K. Mach-Zehnder Modulator. US6198854 B1, March 6, 2001.

[8] Wang, Z.; Huang, Y.-K.; Ip, E.; Prucnal, P. R.; Wang, T. Performance Investigation of Polarization-Multiplexed 16-QAM Using All-Optical OFDM Transmission and Digital Coherent Detection. In; OSA, 2011; p OMS5.

[9] Voigt, W. Ueber Das Elektrische Analogon Des Zeemaneffectes. *Ann. Phys.* **1901**, *309* (1), 197–208.

[10] Pockels, F. *Lehrbuch Der Kristalloptik*; Teubner: Leipzig und Berlin, 1906.

[11] Singer, K. D.; Kuzyk, M. G.; Sohn, J. E. Second-Order Nonlinear-Optical Processes in Orientationally Ordered Materials: Relationship between Molecular and Macroscopic Properties. *J. Opt. Soc. Am. B* **1987**, *4* (6), 968–976.

[12] Dalton, L. R.; Steier, W. H.; Robinson, B. H.; Zhang, C.; Ren, A.; Garner, S.; Chen, A.; Londergan, T.; Irwin, L.; Carlson, B.; Fifield, L.; Phelan, G.; Kincaid, C.; Amend, J.; Jen, A. From Molecules to Opto-Chips: Organic Electro-Optic Materials. *J. Mater. Chem.* **1999**, *9* (9), 1905–1920.

[13] Sullivan, P. A.; Rommel, H.; Liao, Y.; Olbricht, B. C.; Akelaitis, A. J. P.; Firestone, K. A.; Kang, J.-W.; Luo, J.; Davies, J. A.; Choi, D. H.; Eichinger, B. E.; Reid, P. J.; Chen, A.; Jen, A. K.-Y.; Robinson, B. H.; Dalton, L. R. Theory-Guided Design and Synthesis of

Multichromophore Dendrimers: An Analysis of the Electro-Optic Effect. *J. Am. Chem. Soc.* **2007**, *129* (24), 7523–7530.

[14] Sullivan, P. A.; Dalton, L. R. Theory-Inspired Development of Organic Electro-Optic Materials. *Acc. Chem. Res.* **2010**, *43* (1), 10–18.

[15] Wooten, E. L.; Kissa, K. M.; Yi-Yan, A.; Murphy, E. J.; Lafaw, D. A.; Hallemeier, P. F.; Maack, D.; Attanasio, D. V.; Fritz, D. J.; McBrien, G. J. A Review of Lithium Niobate Modulators for Fiber-Optic Communications Systems. *Sel. Top. Quantum Electron. IEEE J. Of* **2000**, *6* (1), 69–82.

[16] Jundt, D. H. Temperature-Dependent Sellmeier Equation for the Index of Refraction, n_e, in Congruent Lithium Niobate. *Opt. Lett.* **1997**, *22* (20), 1553–1555.

[17] Freude, W.; Leuthold, J.; Alloatti, L.; Vallaitis, T.; Korn, D.; Palmer, R.; Koos, C.; Brosi, J.; Dumon, P.; Baets, R. 100 Gbit/s Electro-Optic Modulator and 56 Gbit/s Wavelength Converter for DQPSK Data in Silicon-Organic Hybrid (SOH) Technology. In *Photonics Society Summer Topical Meeting Series, 2010 IEEE*; 2010; pp 96–97.

[18] Palmer, R.; Koeber, S.; Elder, D. L.; Woessner, M.; Heni, W.; Korn, D.; Lauermann, M.; Bogaerts, W.; Dalton, L.; Freude, W.; Leuthold, J.; Koos, C. High-Speed, Low Drive-Voltage Silicon-Organic Hybrid Modulator Based on a Binary-Chromophore Electro-Optic Material. *J. Light. Technol.* **2014**, *32* (16), 2726–2734.

[19] Haffner, C.; Heni, W.; Fedoryshyn, Y.; Niegemann, J.; Melikyan, A.; Elder, D. L.; Baeuerle, B.; Salamin, Y.; Josten, A.; Koch, U.; Hoessbacher, C.; Ducry, F.; Juchli, L.; Emboras, A.; Hillerkuss, D.; Kohl, M.; Dalton, L. R.; Hafner, C.; Leuthold, J. All-Plasmonic Mach–Zehnder Modulator Enabling Optical High-Speed Communication at the Microscale. *Nat. Photonics* **2015**, *9* (8), 525–528.

[20] Koos, C.; Leuthold, J.; Freude, W.; Kohl, M.; Dalton, L.; Bogaerts, W.; Giesecke, A. L.; Lauermann, M.; Melikyan, A.; Koeber, S.; Wolf, S.; Weimann, C.; Muehlbrandt, S.; Koehnle, K.; Pfeifle, J.; Palmer, R.; Alloatti, L.; Elder, D.; Wahlbrink, T.; Bolten, J. Silicon-Organic Hybrid (SOH) and Plasmonic-Organic Hybrid (POH) Integration. In; OSA, 2015; p Tu2A.1.

[21] Elder, D. L.; Benight, S. J.; Song, J.; Robinson, B. H.; Dalton, L. R. Matrix-Assisted Poling of Monolithic Bridge-Disubstituted Organic NLO Chromophores. *Chem. Mater.* **2014**, *26* (2), 872–874.

[22] Liu, A.; Jones, R.; Liao, L.; Samara-Rubio, D.; Rubin, D.; Cohen, O.; Nicolaescu, R.; Paniccia, M. A High-Speed Silicon Optical Modulator Based on a Metal–oxide–semiconductor Capacitor. *Nature* **2004**, *427* (6975), 615–618.

[23] Yi, H.; Long, Q.; Tan, W.; Li, L.; Wang, X.; Zhou, Z. Demonstration of Low Power Penalty of Silicon Mach–Zehnder Modulator in Long-Haul Transmission. *Opt. Express* **2012**, *20* (25), 27562.

[24] Cao, L.; Aboketaf, A.; Wang, Z.; Preble, S. Hybrid Amorphous Silicon (a-Si:H)–LiNbO3 Electro-Optic Modulator. *Opt. Commun.* **2014**, *330*, 40–44.

[25] Baehr-Jones, T.; Hochberg, M.; Wang, G.; Lawson, R.; Liao, Y.; Sullivan, P. A.; Dalton, L.; Jen, A.-Y.; Scherer, A. Optical Modulation and Detection in Slotted Silicon Waveguides. *Opt. Express* **2005**, *13* (14), 5216–5226.

[26] Pereverzev, Y. V.; Gunnerson, K. N.; Prezhdo, O. V.; Sullivan, P. A.; Liao, Y.; Olbricht, B. C.; Akelaitis, A. J. P.; Jen, A. K.-Y.; Dalton, L. R. Guest−Host Cooperativity in Organic Materials Greatly Enhances the Nonlinear Optical Response. *J. Phys. Chem. C* **2008**, *112* (11), 4355–4363.

[27] Benight, S. J.; Bale, D. H.; Olbricht, B. C.; Dalton, L. R. Organic Electro-Optics: Understanding Material Structure/function Relationships and Device Fabrication Issues. *J. Mater. Chem.* **2009**, *19* (40), 7466.

[28] Dalton, L. R.; Sullivan, P. A.; Bale, D. H. Electric Field Poled Organic Electro-Optic Materials: State of the Art and Future Prospects. *Chem. Rev.* **2010**, *110* (1), 25–55.

[29] Dalton, L. R.; Benight, S. J.; Johnson, L. E.; Knorr, D. B.; Kosilkin, I.; Eichinger, B. E.; Robinson, B. H.; Jen, A. K.-Y.; Overney, R. M. Systematic Nanoengineering of Soft Matter Organic Electro-Optic Materials. *Chem. Mater.* **2011**, *23* (3), 430–445.

[30] Kim, S.-K.; Pei, Q.; Fetterman, H. R.; Olbright, B. C.; Dalton, L. R. Photoassisted Corona Poled YLD-124/DR1-Co-PMMA Electrooptic Device Using Photoisomerization. *IEEE Photonics Technol. Lett.* **2011**, *23* (13), 845–847.

[31] Dalton, L.; Benight, S. Theory-Guided Design of Organic Electro-Optic Materials and Devices. *Polymers* **2011**, *3* (4), 1325–1351.

[32] Benight, S. J.; Robinson, B. H.; Dalton, L. R.; Meghea, A. Nano-Engineering of Molecular Interactions in Organic Electro-Optic Materials. *Mol. Interact.* **2012**.

[33] Jin, W.; Johnston, P. V.; Elder, D. L.; Tillack, A. F.; Olbricht, B. C.; Song, J.; Reid, P. J.; Xu, R.; Robinson, B. H.; Dalton, L. R. Benzocyclobutene Barrier Layer for Suppressing Conductance in Nonlinear Optical Devices during Electric Field Poling. *Appl. Phys. Lett.* **2014**, *104* (24), 243304.

[34] Liao, Y.; Eichinger, B. E.; Firestone, K. A.; Haller, M.; Luo, J.; Kaminsky, W.; Benedict, J. B.; Reid, P. J.; Jen, A. K.-Y.; Dalton, L. R.; Robinson, B. H. Systematic Study of the Structure−Property Relationship of a Series of Ferrocenyl Nonlinear Optical Chromophores. *J. Am. Chem. Soc.* **2005**, *127* (8), 2758–2766.

[35] Hammond, S. R.; Clot, O.; Firestone, K. A.; Bale, D. H.; Lao, D.; Haller, M.; Phelan, G. D.; Carlson, B.; Jen, A. K.-Y.; Reid, P. J.; Dalton, L. R. Site-Isolated Electro-Optic Chromophores Based on Substituted 2,2′-Bis(3,4-Propylenedioxythiophene) π-Conjugated Bridges. *Chem. Mater.* **2008**, *20* (10), 3425–3434.

[36] Bale, D. H. Nonlinear Optical Materials Characterization Studies Employing Photostability, Hyper-Rayleigh Scattering, and Electric Field Induced Second Harmonic Generation Techniques, University of Washington, 2008.

[37] Pan, F.; Wong, M. S.; Bosshard, C.; Günter, P. Crystal Growth and Characterization of the Organic Salt 4-N, N-Dimethylamino-4′-N-Methyl-Stilbazolium Tosylate (dast). *Adv. Mater.* **1996**, *8* (7), 592–595.

[38] Jazbinsek, M.; Mutter, L.; Gunter, P. Photonic Applications With the Organic Nonlinear Optical Crystal DAST. *IEEE J. Sel. Top. Quantum Electron.* **2008**, *14* (5), 1298–1311.

[39] Kwon, O.-P.; Kwon, S.-J.; Jazbinsek, M.; Brunner, F. D. J.; Seo, J.-I.; Hunziker, C.; Schneider, A.; Yun, H.; Lee, Y.-S.; Günter, P. Organic Phenolic Configurationally Locked Polyene Single Crystals for Electro-Optic and Terahertz Wave Applications. *Adv. Funct. Mater.* **2008**, *18* (20), 3242–3250.

[40] Chemla, D. S. *Nonlinear Optical Properties of Organic Molecules and Crystals*; Elsevier, 2012.

[41] Lee, S.-H.; Kang, B.-J.; Kim, J.-S.; Yoo, B.-W.; Jeong, J.-H.; Lee, K.-H.; Jazbinsek, M.; Kim, J. W.; Yun, H.; Kim, J.; Lee, Y. S.; Rotermund, F.; Kwon, O.-P. New Acentric Core Structure for Organic Electrooptic Crystals Optimal for Efficient Optical-to-THz Conversion. *Adv. Opt. Mater.* **2015**, *3* (6), 756–762.

[42] Olbricht, B. C.; Sullivan, P. A.; Wen, G.-A.; Mistry, A. A.; Davies, J. A.; Ewy, T. R.; Eichinger, B. E.; Robinson, B. H.; Reid, P. J.; Dalton, L. R. Laser-Assisted Poling of Binary Chromophore Materials. *J. Phys. Chem. C* **2008**, *112* (21), 7983–7988.

[43] Dalton, L. R.; Günter, P.; Jazbinsek, M.; Kwon, O.-P.; Sullivan, P. A. *Organic Electro-Optics and Photonics: Molecules, Polymers and Crystals*; Cambridge University Press, 2015.

[44] Sullivan, P. A.; Rommel, H. L.; Takimoto, Y.; Hammond, S. R.; Bale, D. H.; Olbricht, B. C.; Liao, Y.; Rehr, J.; Eichinger, B. E.; Jen, A. K.-Y.; Reid, P. J.; Dalton, L. R.; Robinson, B. H. Modeling the Optical Behavior of Complex Organic Media: From Molecules to Materials. *J. Phys. Chem. B* **2009**, *113* (47), 15581–15588.

[45] Bale, D. H.; Eichinger, B. E.; Liang, W.; Li, X.; Dalton, L. R.; Robinson, B. H.; Reid, P. J. Dielectric Dependence of the First Molecular Hyperpolarizability for Electro-Optic Chromophores. *J. Phys. Chem. B* **2011**, *115* (13), 3505–3513.

[46] Johnson, L. E. Multi-Scale Modeling of Organic Electro-Optic Materials, University of Washington, 2012.

[47] Kim, W.-K.; Hayden, L. M. Fully Atomistic Modeling of an Electric Field Poled Guest-Host Nonlinear Optical Polymer. *J. Chem. Phys.* **1999**, *111* (11), 5212–5222.

[48] Tillack, A. F.; Johnson, L. E.; Rawal, M.; Dalton, L. R.; Robinson, B. H. Modeling Chromophore Order: A Guide For Improving EO Performance. In *Symposium II/JJ/KK* –

Materials, Processes and Devices for Nanophotonics, Nonlinear Optics and Resonant Optics; MRS Online Proceedings Library; 2014; Vol. 1698.

[49] Kuzyk, M. G.; Pérez-Moreno, J.; Shafei, S. Sum Rules and Scaling in Nonlinear Optics. *Phys. Rep.* **2013**, *529* (4), 297–398.

[50] Benight, S. J.; Johnson, L. E.; Barnes, R.; Olbricht, B. C.; Bale, D. H.; Reid, P. J.; Eichinger, B. E.; Dalton, L. R.; Sullivan, P. A.; Robinson, B. H. Reduced Dimensionality in Organic Electro-Optic Materials: Theory and Defined Order. *J. Phys. Chem. B* **2010**, *114* (37), 11949–11956.

[51] Benight, S. Nanoengineering of Soft Matter Interactions in Organic Electro-Optic Materials, University of Washington, 2011.

[52] Bale, D. H.; Eichinger, B. E.; Liang, W.; Li, X.; Dalton, L. R.; Robinson, B. H.; Reid, P. J. Dielectric Dependence of the First Molecular Hyperpolarizability for Electro-Optic Chromophores. *J. Phys. Chem. B* **2011**, *115* (13), 3505–3513.

[53] Frisch, M. J.; Trucks, G. W.; Schlegel, H. B.; Scuseria, G. E.; Robb, M. A.; Cheeseman, J. R.; Scalmani, G.; Barone, V.; Mennucci, B.; Petersson, G. A.; Nakatsuji, H.; Caricato, M.; Li, X.; Hratchian, H. P.; Izmaylov, A. F.; Bloino, J.; Zheng, G.; Sonnenberg, J. L.; Hada, M.; Ehara, M.; Toyota, K.; Fukuda, R.; Hasegawa, J.; Ishida, M.; Nakajima, T.; Honda, Y.; Kitao, O.; Nakai, H.; Vreven, T.; Montgomery Jr., J. A.; Peralta, J. E.; Ogliaro, F.; Bearpark, M. J.; Heyd, J.; Brothers, E. N.; Kudin, K. N.; Staroverov, V. N.; Kobayashi, R.; Normand, J.; Raghavachari, K.; Rendell, A. P.; Burant, J. C.; Iyengar, S. S.; Tomasi, J.; Cossi, M.; Rega, N.; Millam, N. J.; Klene, M.; Knox, J. E.; Cross, J. B.; Bakken, V.; Adamo, C.; Jaramillo, J.; Gomperts, R.; Stratmann, R. E.; Yazyev, O.; Austin, A. J.; Cammi, R.; Pomelli, C.; Ochterski, J. W.; Martin, R. L.; Morokuma, K.; Zakrzewski, V. G.; Voth, G. A.; Salvador, P.; Dannenberg, J. J.; Dapprich, S.; Daniels, A. D.; Farkas, Ö.; Foresman, J. B.; Ortiz, J. V.; Cioslowski, J.; Fox, D. J. *Gaussian 09*; Gaussian, Inc.: Wallingford, CT, USA, 2009.

[54] Breneman, C. M.; Wiberg, K. B. Determining Atom-Centered Monopoles from Molecular Electrostatic Potentials. The Need for High Sampling Density in Formamide Conformational Analysis. *J. Comput. Chem.* **1990**, *11* (3), 361–373.

[55] Jorgensen, W. L.; Maxwell, D. S.; Tirado-Rives, J. Development and Testing of the OPLS All-Atom Force Field on Conformational Energetics and Properties of Organic Liquids. *J. Am. Chem. Soc.* **1996**, *118* (45), 11225–11236.

[56] Halgren, T. A. Merck Molecular Force Field. I. Basis, Form, Scope, Parameterization, and Performance of MMFF94. *J. Comput. Chem.* **1996**, *17* (5-6), 490–519.

[57] Ponder, J. W.; Wu, C.; Ren, P.; Pande, V. S.; Chodera, J. D.; Schnieders, M. J.; Haque, I.; Mobley, D. L.; Lambrecht, D. S.; DiStasio, R. A.; Head-Gordon, M.; Clark, G. N. I.; Johnson, M. E.; Head-Gordon, T. Current Status of the AMOEBA Polarizable Force Field. *J. Phys. Chem. B* **2010**, *114* (8), 2549–2564.

[58] Johnson, L. E.; Barnes, R.; Draxler, T. W.; Eichinger, B. E.; Robinson, B. H. Dielectric Constants of Simple Liquids: Stockmayer and Ellipsoidal Fluids. *J. Phys. Chem. B* **2010**, *114* (25), 8431–8440.

[59] Robinson, B. H.; Dalton, L. R. Monte Carlo Statistical Mechanical Simulations of the Competition of Intermolecular Electrostatic and Poling-Field Interactions in Defining Macroscopic Electro-Optic Activity for Organic Chromophore/Polymer Materials. *J. Phys. Chem. A* **2000**, *104* (20), 4785–4795.

[60] Rommel, H. L.; Robinson, B. H. Orientation of Electro-Optic Chromophores under Poling Conditions: A Spheroidal Model. *J. Phys. Chem. C* **2007**, *111* (50), 18765–18777.

[61] Perram, J. W.; Wertheim, M. S. Statistical Mechanics of Hard Ellipsoids. I. Overlap Algorithm and the Contact Function. *J. Comput. Phys.* **1985**, *58* (3), 409–416.

[62] Onsager, L. Electric Moments of Molecules in Liquids. *J. Am. Chem. Soc.* **1936**, *58* (8), 1486–1493.

[63] Robinson, B. H.; Dalton, L. R.; Harper, A. W.; Ren, A.; Wang, F.; Zhang, C.; Todorova, G.; Lee, M.; Aniszfeld, R.; Garner, S.; Chen, A.; Steier, W. H.; Houbrecht, S.; Persoons, A.; Ledoux, I.; Zyss, J.; Jen, A. K. Y. The Molecular and Supramolecular Engineering of Polymeric Electro-Optic Materials. *Chem. Phys.* **1999**, *245* (1–3), 35–50.

[64] Zhang, C.; Dalton, L. R.; Oh, M.-C.; Zhang, H.; Steier, W. H. Low V_π Electrooptic Modulators from CLD-1: Chromophore Design and Synthesis, Material Processing, and Characterization. *Chem. Mater.* **2001**, *13* (9), 3043–3050.

[65] Olbricht, B. C.; Sullivan, P. A.; Dennis, P. C.; Hurst, J. T.; Johnson, L. E.; Benight, S. J.; Davies, J. A.; Chen, A.; Eichinger, B. E.; Reid, P. J.; Dalton, L. R.; Robinson, B. H. Measuring Order in Contact-Poled Organic Electrooptic Materials with Variable-Angle Polarization-Referenced Absorption Spectroscopy (VAPRAS). *J. Phys. Chem. B* **2011**, *115* (2), 231–241.

[66] Sullivan, P. A. Theory Guided Design and Molecular Engineering of Organic Materials for Enhanced Second-Order Nonlinear Optical Properties, University of Washington, 2006.

[67] Rawal, M. Cross-Conjugated Moieties as Design Motifs for a Class of Novel Electro-Optic Chromophores, University of Washington, 2013.

[68] Rawal, M.; Garrett, K.; Tillack, A. F.; Kaminsky, W.; Jucov, E.; Shelton, D. P.; Timofeeva, T. V.; Eichinger, B. E.; Robinson, B. H.; Dalton, L. R. Cross-Conjugation as a Motif for Organic Non-Linear Optical Molecules. In *Symposium II/JJ/KK – Materials, Processes and Devices for Nanophotonics, Nonlinear Optics and Resonant Optics*; MRS Online Proceedings Library; 2014; Vol. 1698.

[69] Gay, J. G.; Berne, B. J. Modification of the Overlap Potential to Mimic a Linear Site–site Potential. *J. Chem. Phys.* **1981**, *74*, 3316.

[70] Allen, M. P.; Tildesley, D. J. *Computer Simulation of Liquids*; Clarendon Press ; Oxford University Press: Oxford [England]; New York, 1989.

[71] Peter, C.; Kremer, K. Multiscale Simulation of Soft Matter Systems – from the Atomistic to the Coarse-Grained Level and Back. *Soft Matter* **2009**, *5* (22), 4357.

[72] Marrink, S. J.; Risselada, H. J.; Yefimov, S.; Tieleman, D. P.; de Vries, A. H. The MARTINI Force Field: Coarse Grained Model for Biomolecular Simulations. *J. Phys. Chem. B* **2007**, *111* (27), 7812–7824.

[73] Izvekov, S.; Voth, G. A. Multiscale Coarse Graining of Liquid-State Systems. *J. Chem. Phys.* **2005**, *123* (13), 134105.

[74] Rudzinski, J. F.; Noid, W. G. The Role of Many-Body Correlations in Determining Potentials for Coarse-Grained Models of Equilibrium Structure. *J. Phys. Chem. B* **2012**, *116* (29), 8621–8635.

[75] Huang, L.; Roux, B. Automated Force Field Parameterization for Nonpolarizable and Polarizable Atomic Models Based on Ab Initio Target Data. *J. Chem. Theory Comput.* **2013**, *9* (8), 3543–3556.

[76] Mladek, B. M.; Fornleitner, J.; Martinez-Veracoechea, F. J.; Dawid, A.; Frenkel, D. Procedure to Construct a Multi-Scale Coarse-Grained Model of DNA-Coated Colloids from Experimental Data. *Soft Matter* **2013**, *9* (30), 7342.

[77] Berendsen, H. J. C.; Postma, J. P. M.; van Gunsteren, W. F.; Hermans, J. Interaction Models for Water in Relation to Protein Hydration. In *Intermolecular Forces*; Pullman, B., Ed.; The Jerusalem Symposia on Quantum Chemistry and Biochemistry; Springer Netherlands, 1981; pp 331–342.

[78] Berendsen, H. J. C.; Grigera, J. R.; Straatsma, T. P. The Missing Term in Effective Pair Potentials. *J. Phys. Chem.* **1987**, *91* (24), 6269–6271.

[79] Grigera, J. R. An Effective Pair Potential for Heavy Water. *J. Chem. Phys.* **2001**, *114* (18), 8064–8067.

[80] Wu, Y.; Tepper, H. L.; Voth, G. A. Flexible Simple Point-Charge Water Model with Improved Liquid-State Properties. *J. Chem. Phys.* **2006**, *124* (2), 024503.

[81] Monticelli, L.; Kandasamy, S. K.; Periole, X.; Larson, R. G.; Tieleman, D. P.; Marrink, S.-J. The MARTINI Coarse-Grained Force Field: Extension to Proteins. *J. Chem. Theory Comput.* **2008**, *4* (5), 819–834.

[82] de Jong, D. H.; Singh, G.; Bennett, W. F. D.; Arnarez, C.; Wassenaar, T. A.; Schäfer, L. V.; Periole, X.; Tieleman, D. P.; Marrink, S. J. Improved Parameters for the Martini Coarse-Grained Protein Force Field. *J. Chem. Theory Comput.* **2013**, *9* (1), 687–697.

[83] Johnson, L. E.; Barnes, R.; Draxler, T. W.; Eichinger, B. E.; Robinson, B. H. Dielectric Constants of Simple Liquids: Stockmayer and Ellipsoidal Fluids. *J. Phys. Chem. B* **2010**, *114* (25), 8431–8440.

[84] Zhang, C.; Dalton, L. R.; Oh, M.-C.; Zhang, H.; Steier, W. H. Low V_π Electrooptic Modulators from CLD-1: Chromophore Design and Synthesis, Material Processing, and Characterization. *Chem. Mater.* **2001**, *13* (9), 3043–3050.

[85] Perram, J. W.; Wertheim, M. S. Statistical Mechanics of Hard Ellipsoids. I. Overlap Algorithm and the Contact Function. *J. Comput. Phys.* **1985**, *58* (3), 409–416.

[86] van Zon, R.; Schofield, J. Constructing Smooth Potentials of Mean Force, Radial Distribution Functions, and Probability Densities from Sampled Data. *J. Chem. Phys.* **2010**, *132* (15), 154110.

[87] Lyubartsev, A.; Mirzoev, A.; Chen, L.; Laaksonen, A. Systematic Coarse-Graining of Molecular Models by the Newton Inversion Method. *Faraday Discuss.* **2010**, *144*, 43.

[88] Klein, P. P. On the Ellipsoid and Plane Intersection Equation. *Appl. Math.* **2012**, *03* (11), 1634–1640.

[89] Patrick, C. R.; Prosser, G. S. A Molecular Complex of Benzene and Hexafluorobenzene. *Nature* **1960**, *187* (4742), 1021–1021.

[90] Overell, J. S. W.; Pawley, G. S. An X-Ray Single-Crystal Study of the Molecular System $C_6F_6.C_6D_6$. *Acta Crystallogr. Sect. B* **1982**, *38* (7), 1966–1972.

[91] Gaw, W. J.; Swinton, F. L. Thermodynamic Properties of Binary Systems Containing Hexafluorobenzene. Part 4.—Excess Gibbs Free Energies of the Three Systems Hexafluorobenzene + Benzene, Touene, and P-Xylene. *Trans. Faraday Soc.* **1968**, *64* (0), 2023–2034.

[92] Bartsch, E.; Bertagnolli, H.; Chieux, P. A Neutron and X-Ray Diffraction Study of the Binary Liquid Aromatic System Benzene-Hexafluorobenzene II. The Mixtures. *Berichte Bunsenges. Für Phys. Chem.* **1986**, *90* (1), 34–46.

[93] Cabaço, M. I.; Danten, Y.; Besnard, M.; Guissani, Y.; Guillot, B. Structural Investigations of Liquid Binary Mixtures: Neutron Diffraction and Molecular Dynamics Studies of Benzene, Hexafluorobenzene, and 1,3,5-Trifluorobenzene. *J. Phys. Chem. B* **1998**, *102* (52), 10712–10723.

[94] Tsuzuki, S.; Uchimaru, T.; Mikami, M. Intermolecular Interaction between Hexafluorobenzene and Benzene: Ab Initio Calculations Including CCSD(T) Level Electron Correlation Correction. *J. Phys. Chem. A* **2006**, *110* (5), 2027–2033.

[95] Gung, B. W.; Amicangelo, J. C. Substituent Effects in $C_6F_6C_6H_5X$ Stacking Interactions. *J. Org. Chem.* **2006**, *71* (25), 9261–9270.

[96] Elola, M. D.; Ladanyi, B. M.; Scodinu, A.; Loughnane, B. J.; Fourkas, J. T. Effects of Molecular Association on Polarizability Relaxation in Liquid Mixtures of Benzene and Hexafluorobenzene. *J. Phys. Chem. B* **2005**, *109* (50), 24085–24099.

[97] Cabaço, M. I.; Danten, Y.; Besnard, M.; Guissani, Y.; Guillot, B. Neutron Diffraction and Molecular Dynamics Study of Liquid Benzene and Its Fluorinated Derivatives as a Function of Temperature. *J. Phys. Chem. B* **1997**, *101* (35), 6977–6987.

[98] Vrbancich, J.; Ritchie, G. L. Quadrupole Moments of Benzene, Hexafluorobenzene and Other Non-Dipolar Aromatic Molecules. *J. Chem. Soc. Faraday Trans. 2 Mol. Chem. Phys.* **1980**, *76*, 648–659.

[99] Hernández-Trujillo, J.; Costas, M.; Vela, A. Quadrupole Interactions in Pure Non-Dipolar Fluorinated or Methylated Benzenes and Their Binary Mixtures. *J. Chem. Soc. Faraday Trans.* **1993**, *89* (14), 2441–2443.

[100] Meyer, E. A.; Castellano, R. K.; Diederich, F. Interactions with Aromatic Rings in Chemical and Biological Recognition. *Angew. Chem. Int. Ed.* **2003**, *42* (11), 1210–1250.

[101] Flory, P. J. *Statistical Mechanics of Chain Molecules*; Interscience Publishers, 1969.

[102] Mark, J. E. *Physical Properties of Polymers Handbook*; Springer Science & Business Media, 2007.

[103] Kirkpatrick, S.; Gelatt, C. D.; Vecchi, M. P. Optimization by Simulated Annealing. *Science* **1983**, *220* (4598), 671–680.

[104] Kawai, H.; Kikuchi, T.; Okamoto, Y. A Prediction of Tertiary Structures of Peptide by the Monte Carlo Simulated Annealing Method. *Protein Eng.* **1989**, *3* (2), 85–94.

[105] *Numerical Recipes in C: The Art of Scientific Computing*, 2nd ed.; Press, W. H., Ed.; Cambridge University Press: Cambridge ; New York, 1992.

[106] Swendsen, R. H.; Wang, J.-S. Replica Monte Carlo Simulation of Spin-Glasses. *Phys. Rev. Lett.* **1986**, *57* (21), 2607–2609.

[107] Hukushima, K.; Nemoto, K. Exchange Monte Carlo Method and Application to Spin Glass Simulations. *J. Phys. Soc. Jpn.* **1996**, *65* (6), 1604–1608.

[108] Falcioni, M.; Deem, M. W. A Biased Monte Carlo Scheme for Zeolite Structure Solution. *J. Chem. Phys.* **1999**, *110* (3), 1754–1766.

[109] Torrie, G. M.; Valleau, J. P. Nonphysical Sampling Distributions in Monte Carlo Free-Energy Estimation: Umbrella Sampling. *J. Comput. Phys.* **1977**, *23* (2), 187–199.

[110] Kumar, S.; Rosenberg, J. M.; Bouzida, D.; Swendsen, R. H.; Kollman, P. A. THE Weighted Histogram Analysis Method for Free-Energy Calculations on Biomolecules. I. The Method. *J. Comput. Chem.* **1992**, *13* (8), 1011–1021.

[111] Frenkel, D.; Smit, B. *Understanding Molecular Simulation: From Algorithms to Applications*; Academic Press, 2001.

[112] Ewald, P. P. Die Berechnung Optischer Und Elektrostatischer Gitterpotentiale. *Ann. Phys.* **1921**, *369* (3), 253–287.

[113] Smith, P. E.; Pettitt, B. M. Ewald Artifacts in Liquid State Molecular Dynamics Simulations. *J. Chem. Phys.* **1996**, *105* (10), 4289–4293.

[114] Hünenberger, P. H.; McCammon, J. A. Effect of Artificial Periodicity in Simulations of Biomolecules under Ewald Boundary Conditions: A Continuum Electrostatics Study. *Biophys. Chem.* **1999**, *78* (1–2), 69–88.

[115] Weber, W.; Hünenberger, P. H.; McCammon, J. A. Molecular Dynamics Simulations of a Polyalanine Octapeptide under Ewald Boundary Conditions: Influence of Artificial Periodicity on Peptide Conformation. *J. Phys. Chem. B* **2000**, *104* (15), 3668–3675.

[116] Tobias, D. J. Electrostatics Calculations: Recent Methodological Advances and Applications to Membranes. *Curr. Opin. Struct. Biol.* **2001**, *11* (2), 253–261.

[117] Fukuda, I.; Nakamura, H. Non-Ewald Methods: Theory and Applications to Molecular Systems. *Biophys. Rev.* **2012**, *4* (3), 161–170.

[118] Barker, J. A.; Watts, R. O. Monte Carlo Studies of the Dielectric Properties of Water-like Models. *Mol. Phys.* **1973**, *26* (3), 789–792.

[119] Neumann, M. Dipole Moment Fluctuation Formulas in Computer Simulations of Polar Systems. *Mol. Phys.* **1983**, *50* (4), 841–858.

[120] Kirkwood, J. G. The Dielectric Polarization of Polar Liquids. *J. Chem. Phys.* **1939**, *7* (10), 911–919.

[121] Fröhlich, H. *Theory of Dielectrics: Dielectric Constant and Dielectric Loss*; Clarendon Press, 1958.

[122] Griffiths, D. J. *Introduction to Electrodynamics*, 4 edition.; Addison-Wesley: Boston, 2012.

[123] Neumann, C. *Hydrodynamische untersuchungen: nebst einem Anhange über die Probleme der Elektrostatik und der magnetischen Induction*; B.G. Teubner, 1883.

[124] Cai, W.; Deng, S.; Jacobs, D. Extending the Fast Multipole Method to Charges inside or Outside a Dielectric Sphere. *J. Comput. Phys.* **2007**, *223* (2), 846–864.

[125] Lin, Y.; Baumketner, A.; Deng, S.; Xu, Z.; Jacobs, D.; Cai, W. An Image-Based Reaction Field Method for Electrostatic Interactions in Molecular Dynamics Simulations of Aqueous Solutions. *J. Chem. Phys.* **2009**, *131* (15), 154103.

[126] Lin, Y.; Baumketner, A.; Song, W.; Deng, S.; Jacobs, D.; Cai, W. Ionic Solvation Studied by Image-Charge Reaction Field Method. *J. Chem. Phys.* **2011**, *134* (4), 044105.

[127] *CRC Handbook of Chemistry and Physics, 96th Edition*; CRC Press, 2014.

[128] Edwards, D. M. F.; Madden, P. A.; McDonald, I. R. A Computer Simulation Study of the Dielectric Properties of a Model of Methyl Cyanide: I. The Rigid Dipole Case. *Mol. Phys.* **1984**, *51* (5), 1141–1161.

[129] Pounds, M. A.; Madden, P. A. Are Dipolar Liquids Ferroelectric? Simulation Studies. *J. Chem. Phys.* **2007**, *126* (10), 104506.

[130] Stockmayer, W. H. Second Virial Coefficients of Polar Gases. *J. Chem. Phys.* **1941**, *9* (5), 398–402.

[131] Goldman, S. Determination of Static Dielectric Constant-Temperature-Density Surfaces of a Stockmayer Fluid by Perturbation Theory. *Mol. Phys.* **1990**, *71* (3), 491–507.

[132] Bartke, J.; Hentschke, R. Dielectric Properties and the Ferroelectric Transition of the Stockmayer-Fluid via Computer Simulation. *Mol. Phys.* **2006**, *104* (19), 3057–3068.

[133] Bartke, J.; Hentschke, R. Phase Behavior of the Stockmayer Fluid via Molecular Dynamics Simulation. *Phys. Rev. E* **2007**, *75* (6).

[134] Tassios, D. *Applied Chemical Engineering Thermodynamics*; Springer, 2013.

[135] JOBACK, K. G.; REID, R. C. Estimation of Pure-Component Properties from Group-Contributions. *Chem. Eng. Commun.* **1987**, *57* (1-6), 233–243.

[136] Stein, S. E.; Brown, R. L. Estimation of Normal Boiling Points from Group Contributions. *J. Chem. Inf. Comput. Sci.* **1994**, *34* (3), 581–587.

[137] Dearden, J. C. Quantitative Structure-Property Relationships for Prediction of Boiling Point, Vapor Pressure, and Melting Point. *Environ. Toxicol. Chem.* **2003**, *22* (8), 1696–1709.

[138] Rebelo, L. P. N.; Canongia Lopes, J. N.; Esperança, J. M. S. S.; Filipe, E. On the Critical Temperature, Normal Boiling Point, and Vapor Pressure of Ionic Liquids. *J. Phys. Chem. B* **2005**, *109* (13), 6040–6043.

[139] Bukowski, R.; Szalewicz, K.; Chabalowski, C. F. Ab Initio Interaction Potentials for Simulations of Dimethylnitramine Solutions in Supercritical Carbon Dioxide with Cosolvents. *J. Phys. Chem. A* **1999**, *103* (36), 7322–7340.

[140] Sum, A. K.; Sandler, S. I.; Bukowski, R.; Szalewicz, K. Prediction of the Phase Behavior of Acetonitrile and Methanol with Ab Initio Pair Potentials. I. Pure Components. *J. Chem. Phys.* **2002**, *116* (17), 7627–7636.

[141] Sum, A. K.; Sandler, S. I.; Bukowski, R.; Szalewicz, K. Prediction of the Phase Behavior of Acetonitrile and Methanol with Ab Initio Pair Potentials. II. The Mixture. *J. Chem. Phys.* **2002**, *116* (17), 7637–7644.

[142] Chernyak, Y. Dielectric Constant, Dipole Moment, and Solubility Parameters of Some Cyclic Acid Esters. *J. Chem. Eng. Data* **2006**, *51* (2), 416–418.

[143] Peppel, W. J. Preparation and Properties of the Alkylene Carbonates. *Ind. Eng. Chem.* **1958**, *50* (5), 767–770.

[144] Walden, P. Ueber Die Molekulargrösse Und Elektrische Leitfähigkeit Einiger Geschmolzenen Salze. *Извуатстія Императорской Акаδеміи Наукъ VI Серія* **1914**, *8* (6), 405–422.

[145] Schurr, J. M. Dielectric Relaxation and Depolarized Dynamic Light Scattering of a Generalized Debye Model Fluid. *Mol. Phys.* **1980**, *40* (5), 1025–1051.

[146] Weingärtner, H.; Knocks, A.; Schrader, W.; Kaatze, U. Dielectric Spectroscopy of the Room Temperature Molten Salt Ethylammonium Nitrate. *J. Phys. Chem. A* **2001**, *105* (38), 8646–8650.

[147] Allen, M.; Evans, D. F.; Lumry, R. Thermodynamic Properties of the Ethylammonium Nitrate + Water System: Partial Molar Volumes, Heat Capacities, and Expansivities. *J. Solut. Chem.* **1985**, *14* (8), 549–560.

[148] Umebayashi, Y.; Chung, W.-L.; Mitsugi, T.; Fukuda, S.; Takeuchi, M.; Fujii, K.; Takamuku, T.; Kanzaki, R.; Ishiguro, S. Liquid Structure and the Ion-Ion Interactions of Ethylammonium Nitrate Ionic Liquid Studied by Large Angle X-Ray Scattering and Molecular Dynamics Simulations. *J. Comput. Chem. Jpn.* **2008**, *7* (4), 125–134.

[149] Liu, S.; Haller, M. A.; Ma, H.; Dalton, L. R.; Jang, S.-H.; Jen, A. K.-Y. Focused Microwave-Assisted Synthesis of 2,5-Dihydrofuran Derivatives as Electron Acceptors for Highly Efficient Nonlinear Optical Chromophores. *Adv. Mater.* **2003**, *15* (7-8), 603–607.

[150] Shi, Y. Low (Sub-1-Volt) Halfwave Voltage Polymeric Electro-Optic Modulators Achieved by Controlling Chromophore Shape. *Science* **2000**, *288* (5463), 119–122.

[151] Dalton, L.; Robinson, B.; Jen, A.; Ried, P.; Eichinger, B.; Sullivan, P.; Akelaitis, A.; Bale, D.; Haller, M.; Luo, J.; Liu, S.; Liao, Y.; Firestone, K.; Bhatambrekar, N.; Bhattacharjee, S.; Sinness, J.; Hammond, S.; Buker, N.; Snoeberger, R.; Lingwood, M.; Rommel, H.; Amend, J.; Jang, S.-H.; Chen, A.; Steier, W. Electro-Optic Coefficients of 500 pm/V and beyond for Organic Materials. In *Proceedings of SPIE*; Eich, M., Ed.; 2005; pp 593502–593502.

[152] Dalton, L. Photonic Integration Improves on Current Technologies. *SPIE Newsroom* **2007**.

[153] Dalton, L. R.; Olbricht, B. C.; Sullivan, P. A. Advances in Organic Materials for Optical Modulation. In *Microwave Photonics, 2007 IEEE International Topical Meeting on*; 2007; pp 1–4.

[154] Anet, R. The Photodimers of Coumarin and Related Compounds. *Can. J. Chem.* **1962**, *40* (7), 1249–1257.

[155] Hammond, G. S.; Stout, C. A.; Lamola, A. A. Mechanisms of Photochemical Reactions in Solution. XXV. The Photodimerization of Coumarin. *J. Am. Chem. Soc.* **1964**, *86* (15), 3103–3106.

[156] Hoffman, R.; Wells, P.; Morrison, H. Organic Photochemistry. XII. Further Studies on the Mechanism of Coumarin Photodimerization. Observation of an Unusual "Heavy Atom" Effect. *J Org Chem* **1971**, *36* (1), 102.

[157] Tian, Y.; Kong, X.; Nagase, Y.; Iyoda, T. Photocrosslinkable Liquid-Crystalline Block Copolymers with Coumarin Units Synthesized with Atom Transfer Radical Polymerization. *J. Polym. Sci. Part Polym. Chem.* **2003**, *41* (14), 2197–2206.

[158] Kim, C.; Trajkovska, A.; Wallace, J. U.; Chen, S. H. New Insight into Photoalignment of Liquid Crystals on Coumarin-Containing Polymer Films. *Macromolecules* **2006**, *39* (11), 3817–3823.

[159] Low, R. J. Measuring Order and Biaxiality. *Eur. J. Phys.* **2002**, *23* (2), 111.

[160] Mottram, N. J.; Newton, C. Introduction to Q-Tensor Theory. *Univ. Strathclyde Dep. Math. Res. Rep.* **2004**, *2004*, 10.

[161] *Visualization and Processing of Tensor Fields*; Laidlaw, D., Weickert, J., Eds.; Farin, G., Hege, H.-C., Hoffman, D., Johnson, C. R., Polthier, K., Rumpf, M., Series Eds.; Mathematics and Visualization; Springer Berlin Heidelberg: Berlin, Heidelberg, 2009.

[162] Majumdar, A.; Zarnescu, A. Landau-De Gennes Theory of Nematic Liquid Crystals: The Oseen-Frank Limit and beyond. *Arch. Ration. Mech. Anal.* **2010**, *196* (1), 227–280.

[163] Lee, K.-S. *Polymers for Photonics Applications I*; Springer, 2003.

[164] Taylor, R. E.; Jr, R. R. B.; Eades, W. D. Polymer Guest-Host Systems and Polymer Electro-Optic Waveguide Systems. US6978069 B1, December 20, 2005.

[165] Allen, N. S. *Photochemistry and Photophysics of Polymeric Materials*; John Wiley & Sons, 2010.

[166] Carboni, R. A. 5-Cyanomethylene-2-Oxo-3-Pyrrolines. US3013013 A, December 12, 1961.

[167] Matumoto, H.; Imai, H.; Tada, S. Pyrroline Derivative. US4845235 A, July 4, 1989.

[168] Jang, S.-H.; Luo, J.; Tucker, N. M.; Leclercq, A.; Zojer, E.; Haller, M. A.; Kim, T.-D.; Kang, J.-W.; Firestone, K.; Bale, D.; Lao, D.; Benedict, J. B.; Cohen, D.; Kaminsky, W.; Kahr, B.; Brédas, J.-L.; Reid, P.; Dalton, L. R.; Jen, A. K.-Y. Pyrroline Chromophores for Electro-Optics. *Chem. Mater.* **2006**, *18* (13), 2982–2988.

[169] Jen, K.-Y.; Jang, S.-H.; Kahr, B. Pyrroline Chromophores. US7307173 B1, December 11, 2007.

[170] Cavanagh, D.; James, M. R.; Meyrick, B. H.; Wight, P. Blue to Green Disperse Dyes for Synthetic Fiber Material. US5865857 A, February 2, 1999.

[171] Brierley, D.; Bullock, J. F.; Leaver, A. Disperse Dye Mixtures. EP1121393 B1, September 4, 2002.

[172] Shuttleworth, L.; McManus, M. J. In Situ Dye Generation for Thermal Transfer Printing. US5011811 A, April 30, 1991.

[173] Shuttleworth, L.; Weber, H. Acylated Dicyanovinylpyrroline Dye-Donor Element for Thermal Dye Transfer. US5166128 A, November 24, 1992.

[174] Leclercq, A.; Zojer, E.; Jang, S.-H.; Barlow, S.; Geskin, V.; Jen, A. K.-Y.; Marder, S. R.; Brédas, J. L. Quantum-Chemical Investigation of Second-Order Nonlinear Optical Chromophores: Comparison of Strong Nitrile-Based Acceptor End Groups and Role of Auxiliary Donors and Acceptors. *J. Chem. Phys.* **2006**, *124* (4), 044510.

[175] Carey, F. A.; Sundberg, R. J. *Advanced Organic Chemistry: Part A: Structure and Mechanisms*; Springer Science & Business Media, 2007.

[176] Cheng, L. T.; Tam, W.; Stevenson, S. H.; Meredith, G. R.; Rikken, G.; Marder, S. R. Experimental Investigations of Organic Molecular Nonlinear Optical Polarizabilities. 1. Methods and Results on Benzene and Stilbene Derivatives. *J. Phys. Chem.* **1991**, *95* (26), 10631–10643.

[177] Kanis, D. R.; Ratner, M. A.; Marks, T. J. Design and Construction of Molecular Assemblies with Large Second-Order Optical Nonlinearities. Quantum Chemical Aspects. *Chem. Rev.* **1994**, *94* (1), 195–242.

[178] Dalton, L. R.; Harper, A. W.; Robinson, B. H. The Role of London Forces in Defining Noncentrosymmetric Order of High Dipole Moment–high Hyperpolarizability Chromophores in Electrically Poled Polymeric Thin Films. *Proc. Natl. Acad. Sci.* **1997**, *94* (10), 4842–4847.

[179] Dalton, L. R. Rational Design of Organic Electro-Optic Materials. *J. Phys. Condens. Matter* **2003**, *15* (20), R897.

[180] Luo, J.; Haller, M.; Ma, H.; Liu, S.; Kim, T.-D.; Tian, Y.; Chen, B.; Jang, S.-H.; Dalton, L. R.; Jen, A. K.-Y. Nanoscale Architectural Control and Macromolecular Engineering of Nonlinear Optical Dendrimers and Polymers for Electro-Optics †. *J. Phys. Chem. B* **2004**, *108* (25), 8523–8530.

[181] Liao, Y.; Anderson, C. A.; Sullivan, P. A.; Akelaitis, A. J. P.; Robinson, B. H.; Dalton, L. R. Electro-Optical Properties of Polymers Containing Alternating Nonlinear Optical Chromophores and Bulky Spacers. *Chem. Mater.* **2006**, *18* (4), 1062–1067.

[182] Sullivan, P. A.; Rommel, H.; Liao, Y.; Olbricht, B. C.; Akelaitis, A. J. P.; Firestone, K. A.; Kang, J.-W.; Luo, J.; Davies, J. A.; Choi, D. H.; Eichinger, B. E.; Reid, P. J.; Chen, A.; Jen, A. K.-Y.; Robinson, B. H.; Dalton, L. R. Theory-Guided Design and Synthesis of Multichromophore Dendrimers: An Analysis of the Electro-Optic Effect. *J. Am. Chem. Soc.* **2007**, *129* (24), 7523–7530.

[183] Planells, M.; Pizzotti, M.; Nichol, G. S.; Tessore, F.; Robertson, N. Effect of Torsional Twist on 2nd Order Non-Linear Optical Activity of Anthracene and Pyrene Tricyanofuran Derivatives. *Phys. Chem. Chem. Phys.* **2014**, *16* (42), 23404–23411.

Appendix A CONTACT FUNCTION CODE

```
/*!
 * Touch, an algorithm designed for determining the closest contact distance between two ellipsoids at arbitrary angles,
 * reducing the three-dimensional problem to a one-dimensional problem in terms of a scalar variable lambda, then iteratively
 * solving a system of linear equations to optimize lambda. Initially written in Matlab by BHR, ported to C++ by RSB in 02/09, then
 * harmonized with current codebase by LEJ in 04/09, and optimized by LEJ in 01/10, finally fixed by AT in 02/11, optimized by AT in 2014
 * Inputs:
 *  kk - the index of the currently active molecule
 *  i - the index of the molecule it is interacting with
 * Return value in distance is the effective LJ sigma for the molecules at their current positions
 */
inline double MC_Elements::touch(const unsigned int kk, const unsigned int i)
{
    double matrices[15];
    // Minimization vectors
    Vec3 V, t;

    // Create lab frame version of A and B matrices (both are symmetric matrices R * L_A/B * R^T)
    // A/B_ij=sum_k L_A/B_k*R_ik*R_jk
    // move into A ellipsoid frame of reference
    // doing so:
    // - replaces 36 multiplication and 12 additions with 36 multiplications and 24 additions once
    // - saves 4 multiplications and 6 additions in loop
    Vec3 z; // multply with kk's transposed (inverse) rotation matrix
    z.vec[0] =
Rmus[i].vec[0]*Elements[kk].rot.mat[0][0]+Rmus[i].vec[1]*Elements[kk].rot.mat[1][0]+Rmus[i].vec[2]*Elements[kk].rot.mat[2][0];
    z.vec[1] =
Rmus[i].vec[0]*Elements[kk].rot.mat[0][1]+Rmus[i].vec[1]*Elements[kk].rot.mat[1][1]+Rmus[i].vec[2]*Elements[kk].rot.mat[2][1];
    z.vec[2] =
Rmus[i].vec[0]*Elements[kk].rot.mat[0][2]+Rmus[i].vec[1]*Elements[kk].rot.mat[1][2]+Rmus[i].vec[2]*Elements[kk].rot.mat[2][2];
    Mat33 irot=Elements[kk].rot.TransMulM3(Elements[i].rot); // new rotation matrix of i in kk's frame

    matrices[0]=Elements[kk].MyType->saxes2.vec[0];
    matrices[1]=Elements[kk].MyType->saxes2.vec[1];
    matrices[2]=Elements[kk].MyType->saxes2.vec[2];
    matrices[3]=(Elements[i].MyType->saxes2.vec[0]*irot.mat[0][0]*irot.mat[0][0]+Elements[i].MyType-
>saxes2.vec[1]*irot.mat[0][1]*irot.mat[0][1]+Elements[i].MyType->saxes2.vec[2]*irot.mat[0][2]*irot.mat[0][2]);
    matrices[4]=(Elements[i].MyType->saxes2.vec[0]*irot.mat[0][0]*irot.mat[1][0]+Elements[i].MyType-
>saxes2.vec[1]*irot.mat[0][1]*irot.mat[1][1]+Elements[i].MyType->saxes2.vec[2]*irot.mat[0][2]*irot.mat[1][2]);
    matrices[5]=(Elements[i].MyType->saxes2.vec[0]*irot.mat[0][0]*irot.mat[2][0]+Elements[i].MyType-
>saxes2.vec[1]*irot.mat[0][1]*irot.mat[2][1]+Elements[i].MyType->saxes2.vec[2]*irot.mat[0][2]*irot.mat[2][2]);
    matrices[6]=(Elements[i].MyType->saxes2.vec[0]*irot.mat[1][0]*irot.mat[1][0]+Elements[i].MyType-
>saxes2.vec[1]*irot.mat[1][1]*irot.mat[1][1]+Elements[i].MyType->saxes2.vec[2]*irot.mat[1][2]*irot.mat[1][2]);
    matrices[7]=(Elements[i].MyType->saxes2.vec[0]*irot.mat[1][0]*irot.mat[2][0]+Elements[i].MyType-
>saxes2.vec[1]*irot.mat[1][1]*irot.mat[2][1]+Elements[i].MyType->saxes2.vec[2]*irot.mat[1][2]*irot.mat[2][2]);
```

```
    matrices[8]=(Elements[i].MyType->saxes2.vec[0]*irot.mat[2][0]*irot.mat[2][0]+Elements[i].MyType-
>saxes2.vec[1]*irot.mat[2][1]*irot.mat[2][1]+Elements[i].MyType->saxes2.vec[2]*irot.mat[2][2]*irot.mat[2][2]);
    if(configuration->vdwtype==6){ // modulate touch
        matrices[0]*=Elements[kk].delta;
        matrices[1]*=Elements[kk].delta;
        matrices[2]*=Elements[kk].delta;
        matrices[3]*=Elements[i].delta;
        matrices[4]*=Elements[i].delta;
        matrices[5]*=Elements[i].delta;
        matrices[6]*=Elements[i].delta;
        matrices[7]*=Elements[i].delta;
        matrices[8]*=Elements[i].delta;
    }
    // d = 1/det(B_LF) (uses the fact that rotations do not change the volume of another matrix)
    double d=Rdist2LJ[i]*Elements[i].MyType->invsaxesvolume;
    double e=d*d;
    if(e>1E10){
        d=1E5;
        e=1E10;
    }
    if(e>Rdist2LJ[i]){
        matrices[0]*=e;
        matrices[1]*=e;
        matrices[2]*=e;

        matrices[3]*=e;
        matrices[4]*=e;
        matrices[5]*=e;
        matrices[6]*=e;
        matrices[7]*=e;
        matrices[8]*=e;
        z*=d;
    }

    double lambda=0.5;
    double xlx=1.0; // x=lambda/(1-lambda) -> do manual calculation with value above
    double Var = 1.0; // trying different forms found 6 loops gives 7 figs for Fx
    double VAV, VBV, det, Vz, V22;
    while(Var > 1E-6){ // loop until variance in distance is sufficiently small
        Var = lambda; // keep lambda around but do CI matrix in terms of x (scale CI by 1/(1-lambda))
        //Populate CI matrix
        matrices[9] = xlx*matrices[3]+matrices[0];
        matrices[10] = xlx*matrices[4];
        matrices[11] = xlx*matrices[5];

        matrices[12] = xlx*matrices[6]+matrices[1];
        matrices[13] = xlx*matrices[7];

        matrices[14] = xlx*matrices[8]+matrices[2];

        // Solve z = CI*V for V using inverse => V=CI^-1*z
```

```
        t.vec[0]=matrices[12]*matrices[14]-matrices[13]*matrices[13];
        t.vec[1]=matrices[13]*matrices[11]-matrices[10]*matrices[14];
        t.vec[2]=matrices[10]*matrices[13]-matrices[11]*matrices[12];

        // do not need to calculate determinant because VAV/VBV will cancel it out anyway
//      det = matrices[9]*t.vec[0] + matrices[10]*t.vec[1] + matrices[11]*t.vec[2];

        V.vec[0] = t.vec[0]*z.vec[0]+t.vec[1]*z.vec[1]+t.vec[2]*z.vec[2];
        t.vec[0] = (matrices[10]*matrices[11]-matrices[9]*matrices[13]); // a_12
        V.vec[1] = t.vec[1]*z.vec[0]+(matrices[9]*matrices[14]-matrices[11]*matrices[11])*z.vec[1]+t.vec[0]*z.vec[2];
        V.vec[2] = t.vec[2]*z.vec[0]+t.vec[0]*z.vec[1]+(matrices[9]*matrices[12]-matrices[10]*matrices[10])*z.vec[2];

        // VAV=V*A_LF*V (uses fact that A_LF is symmetric)
        V22=V.vec[2]*V.vec[2];
        VAV = V.vec[0]*V.vec[0]*matrices[0]+V.vec[1]*V.vec[1]*matrices[1]+V22*matrices[2];
        // denominator=V*B_LF*V (uses fact that B_LF is symmetric)
        VBV = V.vec[0]*(V.vec[0]*matrices[3]+2.0*(V.vec[1]*matrices[4]+V.vec[2]*matrices[5]))
             +V.vec[1]*(V.vec[1]*matrices[6]+2.0*V.vec[2]*matrices[7])+V22*matrices[8];
        //Calculate minimization parameter lambda
        if(VBV < EPS){
            cout << "ERROR: Denominator between oids " << kk << " and " << i << " in touch is too close to zero (" << VBV << ").\n";
            exit(3);
        }
        xlx = sqrt(VAV/VBV); // independent of z-scaling (and determinant) -> also, interesting note: the sqrt is better than anything
else in terms of speed and convergence
        lambda = xlx/(1.0+xlx);
        Var -= lambda;
        Var *= Var;
    }

    //Reconstruct CI and run a final iteration once converged
    matrices[9] = xlx*matrices[3]+matrices[0];
    matrices[10] = xlx*matrices[4];
    matrices[11] = xlx*matrices[5];

    matrices[12] = xlx*matrices[6]+matrices[1];
    matrices[13] = xlx*matrices[7];

    matrices[14] = xlx*matrices[8]+matrices[2];

    t.vec[0]=matrices[12]*matrices[14]-matrices[13]*matrices[13];
    t.vec[1]=matrices[13]*matrices[11]-matrices[10]*matrices[14];
    t.vec[2]=matrices[10]*matrices[13]-matrices[11]*matrices[12];

    det = matrices[9]*t.vec[0] + matrices[10]*t.vec[1] + matrices[11]*t.vec[2];
    if(fabs(det) < EPS){
        cout << "WARNING: Matrix is close to singular. det = " << det << "\n";
        cout << "Distance calculation failed. i = " << i << ", kk = " << kk << ", x = " << xlx << "\n";
        exit(2);
    }
    V22=2.0*z.vec[2];
```

```
    Vz=(z.vec[0]*t.vec[0]+2.0*z.vec[1]*t.vec[1]+V22*t.vec[2])*z.vec[0]+
       ((matrices[9]*matrices[14]-matrices[11]*matrices[11])*z.vec[1]+(matrices[10]*matrices[11]-matrices[9]*matrices[13])*V22)*z.vec[1]+
       (matrices[9]*matrices[12]-matrices[10]*matrices[10])*z.vec[2]*z.vec[2];
    // return (sigma/r)^2
    return det/(lambda*Vz);
}
```

Appendix B MODEL PARAMETERS

B.1 CHAPTER 2 MODELS

Table B.1: Model parameters for Figures 2.2, 2.3, 2.4, and 2.11

Model	Semi-axes [Å] (LJ width [Å])	LJ energy [perg]	Charges	Dipole [*D*]
Sphere	2.33x2.33x2.33 (-)	0.03	-	-
CLD-1 type	2.1x4.3x15.8 (-)	0.24	-	-
CH_3	1.88x1.88x1.56 (-)	0.014	-	-
Benzene	3.3x3.3x1.65 (-)	0.08	-	-
Prolate	12.15x3.14x3.14 (3.0)	0.244	-	(15.0,0,0)

Table B.2: All-atom model parameters for ***Benzene*** in Figures 2.13 and 2.14

Atom	Position [Å]	Partial charge [*e*]	Minimum connectivity	LJ radius and energy
C1	-1.102, 0.858, -0.000	-0.088	2, 9, 10	**1.775 Å, 4.86x10^{-3} perg**
C2	-1.294, -0.525, -0.000	-0.091	3, 4	same as C1
C3	-0.192, -1.383, 0.000	-0.074	5, 6	same as C1
H4	-2.302, -0.934, -0.000	0.087		**1.21 Å, 2.08x10^{-3} perg**
C5	1.102, -0.858, -0.000	-0.088	7, 8	same as C1
H6	-0.342, -2.460, 0.000	0.081		same as H4
C7	1.294, 0.525, 0.000	-0.091	9, 12	same as C1
H8	1.960, -1.526, -0.000	0.086		same as H4
C9	0.192, 1.383, -0.000	-0.074	11	same as C1
H10	-1.960, 1.526, -0.000	0.086		same as H4
H11	0.342, 2.460, -0.000	0.081		same as H4
H12	2.302, 0.934, 0.000	0.087		same as H4

Table B.3: All-atom model parameters for ***Hexafluorobenzene*** in Figures 2.13 and 2.14

Atom	Position [Å]	Partial charge [*e*]	Minimum connectivity	LJ radius and energy
C1	-0.490, -1.305, 0.000	0.088	2, 9, 10	**1.775 Å, 4.86x10^{-3} perg**
C2	-1.375, -0.228, -0.000	0.108	3, 4	same as C1
C3	-0.885, 1.076, 0.000	0.084	5, 6	same as C1

F4	-2.693, -0.446, -0.000	-0.097		**1.425 Å, 4.24x10^{-3} perg**
C5	0.490, 1.305, -0.000	0.088	7, 8	same as C1
F6	-1.734, 2.108, 0.000	-0.091		same as F4
C7	1.375, 0.228, 0.000	0.108	9, 12	same as C1
F8	0.960, 2.555, -0.000	-0.092		same as F4
C9	0.885, -1.076, -0.000	0.084	11	same as C1
F10	-0.960, -2.555, -0.000	-0.092		same as F4
F11	1.734, -2.108, -0.000	-0.091		same as F4
F12	2.693, 0.446, 0.000	-0.097		same as F4

Table B.4: LoD model parameters for ***Benzene*** and ***Hexafluorobenzene*** in Figures 2.13 and 2.14; Note that "all-atom" denotes that charges from the all-atom force-field at original locations are used.

Model	Position [Å] Rotation (Axis,θ)	Semi-axes [Å] (LJ width [Å])	LJ energy [perg]	Charges
Benzene	0, 0, 0 (1, 0, 0, 0)	3.33x3.27x1.66 (2.02)[b]	0.06622[a], 0.08324[b]	All-atom
Hexafluoro-benzene	0, 0, 0 (1, 0, 0, 0)	2.01x.1.71x1.54 (1.58)[b]	0.07099[a], 0.09120[b]	All-atom

[a] "simple touch" LJ potential, equation (2-2), [b] "adjusted-width" LJ potential, equation (2-6)

Table B.5: Quadrupole expansion parameters for ***Benzene*** and ***Hexafluorobenzene*** in Figures 2.13 and 2.14. Overall quadrupole moments in the z-direction are $-1.067\ e\text{Å}^2$ for Benzene and $1.541\ e\text{Å}^2$ for Hexafluorobenzene.

Quadrupole expansion charge [e]	Benzene charges [e] at [Å]	Hexafluorobenzene charges [e] at [Å]
0.8	**-0.8** @ ±0.816 in z-direction 0.402 @ ±0.072 in x-direction 0.795 @ center	**0.8** @ ±0.982 in z-direction 0.399 @ ±0.067 in y-direction -2.397 @ center
1	**-1** @ ±0.730 in z-direction 0.503 @ ±0.064 in x-direction 0.994 @ center	**1** @ ±0.878 in z-direction 0.498 @ ±0.060 in y-direction -2.997 @ center
4	**-4** @ ±0.365 in z-direction 2.012 @ ±0.032 in x-direction 3.977 @ center	**4** @ ±0.439 in z-direction 1.993 @ ±0.030 in y-direction -11.986 @ center
8	**-8** @ ±0.258 in z-direction 4.023 @ ±0.023 in x-direction 7.953 @ center	**8** @ ±0.311 in z-direction 3.986 @ ±0.021 in y-direction -23.973 @ center

16	**-16** @ ±0.182 in z-direction 8.047 @ ±0.016 in x-direction 15.907 @ center	**16** @ ±0.220 in z-direction 7.972 @ ±0.015 in y-direction -47.945 @ center
64	**-64** @ ±0.091 in z-direction 128 @ center	**64** @ ±0.110 in z-direction -128 @ center
256	**-256** @ ±0.046 in z-direction 512 @ center	**256** @ ±0.055 in z-direction -512 @ center
1024	**-1024** @ ±0.023 in z-direction 2048.000 @ center	**1024** @ ±0.027 in z-direction -2048.000 @ center
4096	**-4096** @ ±0.011 in z-direction 8192 @ center	**4096** @ ±0.014 in z-direction -8192 @ center

[a] "simple touch" LJ potential, equation (2-2), [b] "adjusted-width" LJ potential, equation (2-6)

Table B.6: All-atom model parameters for ***Hydrocarbon Chain*** in Figures 2.15, 2.16, and 2.17, line breaks represent LoD ellipsoid partitioning

Atom	Position [Å]	Partial charge [*e*]	Minimum connectivity	LJ radius and energy
C1	19.890, 0.385, -0.000	-0.218	2, 3, 4, 5	**1.65 Å, 4.59x10^{-3} perg**
H2	19.937, 1.032, 0.885	0.045		**1.25 Å, 1.04x10^{-3} perg**
H3	19.937, 1.032, -0.885	0.045		same as H2
H4	20.788, -0.244, -0.000	0.049		same as H2
C5	18.613, -0.461, -0.000	0.160	6, 7, 8	same as C1
H6	18.612, -1.123, 0.878	-0.032		same as H2
H7	18.612, -1.123, -0.878	-0.032		same as H2
C8	17.330, 0.380, -0.000	0.028	9, 10, 11	same as C1
H9	17.332, 1.042, -0.878	-0.010		same as H2
H10	17.332, 1.042, 0.878	-0.010		same as H2
C11	16.045, -0.459, -0.000	-0.056	12, 13, 14	same as C1
H12	16.044, -1.121, 0.878	0.001		same as H2
H13	16.044, -1.121, -0.878	0.000		same as H2
C14	14.763, 0.383, -0.000	0.080	15, 16, 17	same as C1
H15	14.764, 1.046, -0.878	-0.023		same as H2
H16	14.764, 1.046, 0.878	-0.023		same as H2
C17	13.478, -0.455, -0.000	0.037	18, 19, 20	same as C1
H18	13.477, -1.118, 0.878	-0.014		same as H2
H19	13.477, -1.117, -0.878	-0.014		same as H2
C20	12.196, 0.388, 0.000	-0.009	21, 22, 23	same as C1
H21	12.197, 1.050, -0.878	-0.006		same as H2
H22	12.197, 1.050, 0.878	-0.006		same as H2
C23	10.910, -0.450, 0.000	0.031	24, 25, 26	same as C1
H24	10.909, -1.112, 0.878	-0.014		same as H2

H25	10.909, -1.112, -0.878	-0.015		same as H2
C26	9.628, 0.393, 0.000	0.049	27, 28, 29	same as C1
H27	9.630, 1.056, -0.878	-0.019		same as H2
H28	9.630, 1.056, 0.878	-0.019		same as H2
C29	8.343, -0.444, 0.000	0.028	30, 31, 32	same as C1
H30	8.341, -1.106, 0.878	-0.015		same as H2
H31	8.341, -1.106, -0.878	-0.015		same as H2
C32	7.061, 0.400, 0.000	0.014	33, 34, 35	same as C1
H33	7.063, 1.062, -0.878	-0.011		same as H2
H34	7.063, 1.062, 0.878	-0.011		same as H2
C35	5.775, -0.437, 0.000	0.027	36, 37, 38	same as C1
H36	5.774, -1.100, 0.878	-0.013		same as H2
H37	5.774, -1.100, -0.878	-0.013		same as H2
C38	4.494, 0.407, 0.000	0.036	39, 40, 41	same as C1
H39	4.496, 1.069, -0.878	-0.015		same as H2
H40	4.496, 1.069, 0.878	-0.015		same as H2
C41	3.208, -0.430, 0.000	0.025	42, 43, 44	same as C1
H42	3.206, -1.092, 0.878	-0.013		same as H2
H43	3.206, -1.092, -0.878	-0.013		same as H2
C44	1.927, 0.414, 0.000	0.013	45, 46, 47	same as C1
H45	1.929, 1.077, -0.878	-0.011		same as H2
H46	1.929, 1.077, 0.878	-0.011		same as H2
C47	0.641, -0.422, 0.000	0.044	48, 49, 50	same as C1
H48	0.639, -1.085, 0.878	-0.019		same as H2
H49	0.639, -1.085, -0.878	-0.019		same as H2
C50	-0.641, 0.422, 0.000	0.044	51, 52, 53	same as C1
H51	-0.639, 1.085, -0.878	-0.019		same as H2
H52	-0.639, 1.085, 0.878	-0.019		same as H2
C53	-1.927, -0.414, 0.000	0.013	54, 55, 56	same as C1
H54	-1.929, -1.077, 0.878	-0.011		same as H2
H55	-1.929, -1.077, -0.878	-0.011		same as H2
C56	-3.208, 0.430, 0.000	0.025	57, 58, 59	same as C1
H57	-3.206, 1.092, -0.878	-0.013		same as H2
H58	-3.206, 1.092, 0.878	-0.013		same as H2
C59	-4.494, -0.407, 0.000	0.036	60, 61, 62	same as C1
H60	-4.496, -1.069, 0.878	-0.015		same as H2
H61	-4.496, -1.069, -0.878	-0.015		same as H2
C62	-5.775, 0.437, 0.000	0.027	63, 64, 65	same as C1
H63	-5.774, 1.100, -0.878	-0.013		same as H2
H64	-5.774, 1.100, 0.878	-0.013		same as H2
C65	-7.061, -0.400, 0.000	0.014	66, 67, 68	same as C1
H66	-7.063, -1.062, 0.878	-0.011		same as H2
H67	-7.063, -1.062, -0.878	-0.011		same as H2
C68	-8.343, 0.444, -0.000	0.028	69, 70, 71	same as C1
H69	-8.341, 1.106, -0.878	-0.015		same as H2
H70	-8.341, 1.106, 0.878	-0.015		same as H2

C71	-9.628, -0.393, 0.000	0.049	72, 73, 74	same as C1
H72	-9.630, -1.056, 0.878	-0.019		same as H2
H73	-9.630, -1.056, -0.878	-0.019		same as H2
C74	-10.910, 0.450, -0.000	0.031	75, 76, 77	same as C1
H75	-10.909, 1.112, -0.878	-0.015		same as H2
H76	-10.909, 1.112, 0.878	-0.014		same as H2
C77	-12.196, -0.388, -0.000	-0.009	78, 79, 80	same as C1
H78	-12.197, -1.050, 0.878	-0.006		same as H2
H79	-12.197, -1.050, -0.878	-0.006		same as H2
C80	-13.478, 0.455, -0.000	0.037	81, 82, 83	same as C1
H81	-13.477, 1.117, -0.878	-0.014		same as H2
H82	-13.477, 1.118, 0.878	-0.014		same as H2
C83	-14.763, -0.383, -0.000	0.080	84, 85, 86	same as C1
H84	-14.764, -1.046, 0.878	-0.023		same as H2
H85	-14.764, -1.046, -0.878	-0.023		same as H2
C86	-16.045, 0.459, -0.000	-0.056	87, 88, 89	same as C1
H87	-16.044, 1.121, -0.878	0.000		same as H2
H88	-16.044, 1.121, 0.878	0.001		same as H2
C89	-17.330, -0.380, -0.000	0.028	90, 91, 92	same as C1
H90	-17.332, -1.042, 0.878	-0.010		same as H2
H91	-17.332, -1.042, -0.878	-0.010		same as H2
C92	-18.613, 0.461, -0.000	0.160	93, 94, 95	same as C1
H93	-18.612, 1.123, -0.878	-0.032		same as H2
H94	-18.612, 1.123, 0.878	-0.032		same as H2
C95	-19.890, -0.385, -0.000	-0.218	96, 97, 98	same as C1
H96	-20.788, 0.244, -0.000	0.049		same as H2
H97	-19.937, -1.032, 0.885	0.045		same as H2
H98	-19.937, -1.032, -0.885	0.045		same as H2

Table B.7: ***Hydrocarbon Chain LoD model 1*** parameters for Figures 2.15, 2.16, and 2.17; Note that "all-atom" denotes that charges from the all-atom force-field at original locations are used.

Ellipsoid #	Position [Å] Rotation (Axis,θ)	Semi-axes [Å] (LJ width [Å])	LJ energy [perg]	Charges
1	20.085, 0.515, 0.000 (0.354, 0.661, 0.661, 2.461)	1.90x1.90x1.59 (1.55)[b]	0.01066[a], 0.01317[b]	All-atom
2	18.612, -0.784, 0.000 (-0.001, -1.000, -0.001, 1.571)	2.01x1.71x1.54 (1.58)[b]	0.00857[a], 0.01007[b]	All-atom
3	17.331, 0.703, 0.000 (-0.001, -1.000, -0.001, 1.571)	2.01x1.71x1.54 (1.58)[b]	0.00857[a], 0.01007[b]	All-atom
4	16.045, -0.782, 0.000 (-0.001, -1.000, -0.001, 1.571)	2.01x1.71x1.54 (1.58)[b]	0.00857[a], 0.01007[b]	All-atom
5	14.763, 0.707, 0.000 (-0.001, -1.000, -0.001, 1.571)	2.01x1.71x1.54 (1.58)[b]	0.00857[a], 0.01007[b]	All-atom

6	13.477, -0.778, 0.000 (-0.001, -1.000, -0.001, 1.571)	2.01x1.71x1.54 (1.58)[b]	0.00857[a], 0.01007[b]	All-atom
7	12.196, 0.711, 0.000 (-0.001, -1.000, -0.001, 1.571)	2.01x1.71x1.54 (1.58)[b]	0.00857[a], 0.01007[b]	All-atom
8	10.910, -0.773, 0.000 (-0.001, -1.000, -0.001, 1.571)	2.01x1.71x1.54 (1.58)[b]	0.00857[a], 0.01007[b]	All-atom
9	9.629, 0.717, 0.000 (-0.001, -1.000, -0.001, 1.571)	2.01x1.71x1.54 (1.58)[b]	0.00857[a], 0.01007[b]	All-atom
10	8.342, -0.767, 0.000 (-0.001, -1.000, -0.001, 1.571)	2.01x1.71x1.54 (1.58)[b]	0.00857[a], 0.01007[b]	All-atom
11	7.062, 0.723, 0.000 (-0.001, -1.000, -0.001, 1.571)	2.01x1.71x1.54 (1.58)[b]	0.00857[a], 0.01007[b]	All-atom
12	5.774, -0.760, 0.000 (-0.001, -1.000, -0.001, 1.571)	2.01x1.71x1.54 (1.58)[b]	0.00857[a], 0.01007[b]	All-atom
13	4.495, 0.730, 0.000 (-0.001, -1.000, -0.001, 1.571)	2.01x1.71x1.54 (1.58)[b]	0.00857[a], 0.01007[b]	All-atom
14	3.207, -0.753, 0.000 (-0.001, -1.000, -0.001, 1.571)	2.01x1.71x1.54 (1.58)[b]	0.00857[a], 0.01007[b]	All-atom
15	1.928, 0.738, 0.000 (-0.001, -1.000, -0.001, 1.571)	2.01x1.71x1.54 (1.58)[b]	0.00857[a], 0.01007[b]	All-atom
16	0.640, -0.745, 0.000 (-0.001, -1.000, -0.001, 1.571)	2.01x1.71x1.54 (1.58)[b]	0.00857[a], 0.01007[b]	All-atom
17	-0.640, 0.745, 0.000 (-0.001, -1.000, -0.001, 1.571)	2.01x1.71x1.54 (1.58)[b]	0.00857[a], 0.01007[b]	All-atom
18	-1.928, -0.738, 0.000 (0.707, -0.001, 0.707, 3.139)	2.01x1.71x1.54 (1.58)[b]	0.00857[a], 0.01007[b]	All-atom
19	-3.207, 0.753, 0.000 (0.707, -0.001, 0.707, 3.140)	2.01x1.71x1.54 (1.58)[b]	0.00857[a], 0.01007[b]	All-atom
20	-4.495, -0.730, 0.000 (0.707, -0.001, 0.707, 3.140)	2.01x1.71x1.54 (1.58)[b]	0.00857[a], 0.01007[b]	All-atom
21	-5.774, 0.760, 0.000 (0.707, -0.001, 0.707, 3.140)	2.01x1.71x1.54 (1.58)[b]	0.00857[a], 0.01007[b]	All-atom
22	-7.062, -0.723, 0.000 (0.707, -0.001, 0.707, 3.140)	2.01x1.71x1.54 (1.58)[b]	0.00857[a], 0.01007[b]	All-atom
23	-8.342, 0.767, 0.000 (0.707, -0.001, 0.707, 3.140)	2.01x1.71x1.54 (1.58)[b]	0.00857[a], 0.01007[b]	All-atom
24	-9.629, -0.717, 0.000 (0.707, -0.001, 0.707, 3.140)	2.01x1.71x1.54 (1.58)[b]	0.00857[a], 0.01007[b]	All-atom
25	-10.910, 0.773, 0.000 (0.707, -0.001, 0.707, 3.140)	2.01x1.71x1.54 (1.58)[b]	0.00857[a], 0.01007[b]	All-atom
26	-12.196, -0.711, 0.000 (0.707, -0.001, 0.707, 3.140)	2.01x1.71x1.54 (1.58)[b]	0.00857[a], 0.01007[b]	All-atom
27	-13.477, 0.778, 0.000 (0.707, -0.001, 0.707, 3.140)	2.01x1.71x1.54 (1.58)[b]	0.00857[a], 0.01007[b]	All-atom

28	-14.763, -0.707, 0.000 (0.707, -0.001, 0.707, 3.141)	2.01x1.71x1.54 (1.58)[b]	0.00857[a], 0.01007[b]	All-atom
29	-16.045, 0.782, 0.000 (0.707, 0.000, 0.707, 3.141)	2.01x1.71x1.54 (1.58)[b]	0.00857[a], 0.01007[b]	All-atom
30	-17.331, -0.703, 0.000 (0.707, -0.001, 0.707, 3.140)	2.01x1.71x1.54 (1.58)[b]	0.00857[a], 0.01007[b]	All-atom
31	-18.612, 0.784, 0.000 (0.707, -0.001, 0.707, 3.140)	2.01x1.71x1.54 (1.58)[b]	0.00857[a], 0.01007[b]	All-atom
32	-20.085, -0.515, 0.000 (0.797, -0.427, -0.427, 1.795)	1.90x1.90x1.59 (1.55)[b]	0.01066[a], 0.01317[b]	All-atom

[a] "simple touch" LJ potential, equation (2-2), [b] "adjusted-width" LJ potential, equation (2-6)

Table B.8: ***Hydrocarbon Chain LoD model 2*** parameters for Figures 2.15, 2.16, and 2.17; Note that "all-atom" denotes that charges from the all-atom force-field at original locations are used.

Ellipsoid #	Position [Å] Rotation (Axis,θ)	Semi-axes [Å] (LJ width [Å])	LJ energy [perg]	Charges
1	19.429, -0.064, 0.000 (0.851, 0.371, 0.371, 1.731)	2.57x1.85x1.78 (1.74)	0.02476	All-atom
2	16.688, -0.040, 0.000 (0.802, 0.422, 0.422, 1.789)	2.59x1.88x1.66 (1.74)	0.02209	All-atom
3	14.120, -0.036, 0.000 (0.802, 0.422, 0.422, 1.789)	2.59x1.88x1.66 (1.74)	0.02209	All-atom
4	11.553, -0.031, 0.000 (0.348, -0.663, -0.663, 2.471)	2.59x1.88x1.66 (1.74)	0.02209	All-atom
5	8.986, -0.025, 0.000 (0.803, 0.422, 0.422, 1.789)	2.59x1.88x1.66 (1.74)	0.02209	All-atom
6	6.418, -0.019, 0.000 (0.803, 0.422, 0.422, 1.789)	2.59x1.88x1.66 (1.74)	0.02209	All-atom
7	3.851, -0.011, 0.000 (0.803, 0.422, 0.422, 1.789)	2.59x1.88x1.66 (1.74)	0.02209	All-atom
8	1.284, -0.004, 0.000 (0.803, 0.422, 0.422, 1.789)	2.59x1.88x1.66 (1.74)	0.02209	All-atom
9	-1.284, 0.004, 0.000 (0.803, 0.422, 0.422, 1.789)	2.59x1.88x1.66 (1.74)	0.02209	All-atom
10	-3.851, 0.011, 0.000 (0.348, -0.663, -0.663, 2.472)	2.59x1.88x1.66 (1.74)	0.02209	All-atom
11	-6.418, 0.019, 0.000 (0.348, -0.663, -0.663, 2.471)	2.59x1.88x1.66 (1.74)	0.02209	All-atom
12	-8.986, 0.025, 0.000 (0.348, -0.663, -0.663, 2.471)	2.59x1.88x1.66 (1.74)	0.02209	All-atom
13	-11.553, 0.031, 0.000 (0.348, -0.663, -0.663, 2.471)	2.59x1.88x1.66 (1.74)	0.02209	All-atom

14	-14.120, 0.036, 0.000 (0.349, -0.663, -0.663, 2.471)	2.59x1.88x1.66 (1.74)	0.02209	All-atom
15	-16.688, 0.040, 0.000 (0.349, -0.663, -0.663, 2.471)	2.59x1.88x1.66 (1.74)	0.02209	All-atom
16	-19.429, 0.064, 0.000 (0.294, -0.676, -0.676, 2.569)	2.57x1.85x1.78 (1.74)	0.02476	All-atom

Table B.9: ***Hydrocarbon Chain LoD model 3*** parameters for Figures 2.15, 2.16, and 2.17; Note that "all-atom" denotes that charges from the all-atom force-field at original locations are used.

Ellipsoid #	Position [Å] Rotation (Axis,θ)	Semi-axes [Å] (LJ width [Å])	LJ energy [perg]	Charges
1	20.085, 0.515, 0.000 (0.354, 0.661, 0.661, 2.461)	1.90x1.90x1.59 (1.55)	0.01317	All-atom
2	17.329, -0.288, 0.000 (0.014, 0.002, 1.000, 0.001)	2.97x2.04x1.81 (1.95)	0.03157	All-atom
3	13.479, 0.213, 0.000 (0.004, 0.002, -1.000, 0.002)	2.97x2.04x1.81 (1.95)	0.03157	All-atom
4	9.627, -0.275, 0.000 (0.004, 0.001, -1.000, 0.002)	2.97x2.04x1.81 (1.95)	0.03157	All-atom
5	5.777, 0.231, 0.000 (0.000, 0.000, 1.000, 3.139)	2.97x2.04x1.81 (1.95)	0.03157	All-atom
6	1.925, -0.254, 0.000 (0.001, 0.000, -1.000, 0.003)	2.97x2.04x1.81 (1.95)	0.03157	All-atom
7	-1.925, 0.254, 0.000 (0.000, 0.000, 1.000, 3.139)	2.97x2.04x1.81 (1.95)	0.03157	All-atom
8	-5.777, -0.231, 0.000 (0.000, 0.000, 1.000, 3.139)	2.97x2.04x1.81 (1.95)	0.03157	All-atom
9	-9.627, 0.275, 0.000 (0.000, 0.000, 1.000, 3.139)	2.97x2.04x1.81 (1.95)	0.03157	All-atom
10	-13.479, -0.213, 0.000 (0.000, 0.000, 1.000, 3.140)	2.97x2.04x1.81 (1.95)	0.03157	All-atom
11	-17.329, 0.288, 0.000 (0.000, 0.000, -1.000, 3.141)	2.97x2.04x1.81 (1.95)	0.03157	All-atom
12	-20.085, -0.515, 0.000 (0.797, -0.427, -0.427, 1.795)	1.90x1.90x1.59 (1.55)	0.01317	All-atom

Table B.10: ***Hydrocarbon Chain LoD model 4*** parameters for Figures 2.15, 2.16, and 2.17; Note that "all-atom" denotes that charges from the all-atom force-field at original locations are used.

Ellipsoid #	Position [Å] Rotation (Axis,θ)	Semi-axes [Å] (LJ width [Å])	LJ energy [perg]	Charges
1	18.137, -0.052, 0.000 (0.000, 0.000, 1.000, 0.253)	3.91x2.09x1.81 (2.06)	0.04265	All-atom
2	12.837, -0.033, 0.000 (0.000, 0.000, 1.000, 0.367)	3.80x2.12x1.81 (2.05)	0.04052	All-atom
3	7.702, -0.022, 0.000 (0.000, 0.000, -1.000, 2.776)	3.80x2.12x1.81 (2.05)	0.04051	All-atom
4	2.567, -0.008, 0.000 (0.000, 0.000, -1.000, 2.776)	3.80x2.12x1.81 (2.05)	0.04051	All-atom
5	-2.567, 0.008, 0.000 (0.000, 0.000, -1.000, 2.776)	3.80x2.12x1.81 (2.05)	0.04051	All-atom
6	-7.702, 0.022, 0.000 (0.000, 0.000, 1.000, 0.366)	3.80x2.12x1.81 (2.05)	0.04051	All-atom
7	-12.837, 0.033, 0.000 (0.000, 0.000, 1.000, 0.367)	3.80x2.12x1.81 (2.05)	0.04052	All-atom
8	-18.137, 0.052, 0.000 (0.000, 0.000, 1.000, 0.253)	3.91x2.09x1.81 (2.06)	0.04262	All-atom

B.2 CHAPTER 3 MODELS

Table B.11: LoD model parameters for Chapter 3

Model	Position [Å] Rotation (Axis,θ)	Semi-axes [Å]	LJ energy [perg]	Center Charge [e] (Center Dipole[a] [D])
Single ellipsoid CLD-1	0, 0, 0 (1, 0, 0, 0)	15.79x4.30x2.22	0.2430	no charge (-23.648,-7.283,-0.428)
2-ellipsoid CLD-1 (Donor)	-8.002, 0.775,-0.080 (0.806,-0.156, 0.572, 0.400)	6.78x3.63x2.03	0.0772	0.208 (0.344,1.445,0.046)
2-ellipsoid CLD-1 (Acceptor)	4.182,-0.591, 0.063 (0.087, 0.156, 0.984, 0.435)	10.09x3.70x2.36	0.1632	-0.208 (-11.792,-10.096,-0.332)
3-ellipsoid CLD-1 (Donor)	-8.097, 0.763,-0.078 (0.721,-0.151,-0.678, 0.474)	6.21x3.69x1.99	0.0766	0.083 (-3.953,1.408,-0.033)
3-ellipsoid CLD-1 (Acceptor)	6.590, 0.580,-0.077 (0.239, 0.027, 0.971, 0.381)	5.79x4.12x2.16	0.1151	-0.319 (-5.794,-6.150,-0.335)

3-ellipsoid CLD-1 (Bridge)	-0.438,-2.441, 0.335 (0.552,-0.578,-0.601, 1.860)	3.61x2.64x2.68	0.0454	0.236 (-0.067,0.808,-0.527)
TCP-Me (Donor)	-8.097, 0.763,-0.078 (0.721,-0.151,-0.678, 0.474)	5.06x3.79x2.20	0.0716	0.295 (1.193,-0.488,-0.028)
TCP-Me (Acceptor)	-8.097, 0.763,-0.078 (0.721,-0.151,-0.678, 0.474)	4.52x4.06x1.93	0.1085	-0.450 (-0.578,-3.176,0.371)
TCP-Me (C=O)	-8.097, 0.763,-0.078 (0.721,-0.151,-0.678, 0.474)	2.08x1.70x1.70	0.0185	0.253 (0.489,-1.639,-3.607)
TCP-Me (Methyl)	-8.097, 0.763,-0.078 (0.721,-0.151,-0.678, 0.474)	2.01x1.99x1.60	0.0070	-0.097 (-0.019,0.449,-0.314)

[a]Dipole vectors are given in the lab frame

B.3 CHAPTERS 4 & 5 MODELS

Table B.12: All-atom model parameters for ***Acetonitrile (OPLS-AA)***, line breaks represent LoD ellipsoid partitioning

Atom	Position [Å]	Partial charge [*e*]	Minimum connectivity	LJ radius and energy
C1	0.000, 0.000, -1.190	-0.08	2, 3, 4, 5	**1.65 Å, 4.59x10^{-3} perg**
H2	1.026, 0.000, -1.555	0.06		**1.25 Å, 1.04x10^{-3} perg**
H3	-0.513, 0.889, -1.555	0.06		same as H2
H4	-0.513, -0.889, -1.555	0.06		same as H2
C5	0.000, 0.000, 0.278	0.46	1, 6	same as C1
N6	0.000, 0.000, 1.434	-0.56		**1.6 Å, 11.81x10^{-3} perg**

Table B.13: LoD model parameters for ***Acetonitrile (OPLS-AA)***. Note that "all-atom" denotes that charges from the all-atom force-field at original locations are used.

Model	Position [Å] Rotation (Axis,θ)	Semi-axes [Å] (LJ width [Å])	LJ energy [perg]	Charges
Single ellipsoid	0.000, 0.000,-0.166 (-0.577,-0.577,-0.577, 2.094)	2.97x1.75x1.75 (1.69)[b]	0.03917[b]	All-atom
2-ellipsoid (Methyl)	0.000, 0.000,-1.405 (0.000,-1.000,0.000, 1.571)	1.54x1.87x1.87 (1.47)[b]	0.01447[b]	All-atom
2-ellipsoid (Cyano)	0.000, 0.000, 0.990 (-0.357,-0.863,-0.357, 1.718)	2.17x1.61x1.61 (1.65)[b]	0.02242[b]	All-atom

[a] "simple touch" LJ potential, equation (2-2), [b] "adjusted-width" LJ potential, equation (2-6)

Table B.14: All-atom model parameters for ***Acetonitrile (CCSD DFT, calculated by Dr. Lewis E. Johnson, reproduced with permission)***, line breaks represent LoD ellipsoid partitioning

Atom	Position [Å]	Partial charge [*e*]	Minimum connectivity	LJ radius and energy
H1	-1.546, -0.001, 1.025	0.127		**1.25 Å, 1.04x10^{-3} perg**
C2	-1.182, 0.000, 0.000	-0.259	1, 3, 4, 5	**1.65 Å, 4.59x10^{-3} perg**
H3	-1.546, -0.887, -0.513	0.127		same as H1
H4	-1.546, 0.887, -0.512	0.127		same as H1
C5	0.281, 0.000, 0.000	0.460	2, 6	same as C2
N6	1.435, 0.000, 0.000	-0.581		**1.6 Å, 11.81x10^{-3} perg**

Table B.15: LoD model parameters for ***Acetonitrile (CCSD DFT, calculated by Dr. Lewis E. Johnson, reproduced with permission)***.

Model	Position [Å] Rotation (Axis,θ)	Semi-axes [Å] (LJ width [Å])	LJ energy [perg]	Center Charge [*e*] (Center Dipole[a] [*D*])
Single ellipsoid	0.000, 0.000,-0.166 (-0.577,-0.577,-0.577, 2.094)	2.97x1.75x1.75 (1.69)[b]	0.03103[b]	no charge (-4.742,0.000,0.003)
2-ellipsoid (Methyl)	0.000, 0.000,-1.405 (0.000,-1.000,0.000, 1.571)	1.54x1.87x1.87 (1.47)[b]	0.01447[b]	0.122 (-0.539,0.000,0.002)
2-ellipsoid (Cyano)	0.000, 0.000, 0.990 (-0.357,-0.863,-0.357, 1.718)	2.17x1.61x1.61 (1.65)[b]	0.02242[b]	-0.122 (-2.808,0.000,0.000)

[a]Dipole vectors are given in the lab frame, [b] "adjusted-width" LJ potential, equation (2-6)

Table B.16: All-atom model parameters for ***Ethylene Carbonate***, coloring represents LoD ellipsoid partitioning.

Atom	Position [Å]	Partial charge [*e*]	Minimum connectivity	LJ radius and energy
C1	-1.310, -0.756, 0.112	0.18	2, 6, 7, 8	**1.75 Å, 4.59x10^{-3} perg**
C2	-1.310, 0.756, -0.112	0.18	3, 4, 5	same as C1
O3	0.082, 1.107, 0.101	-0.481	9	**1.5 Å, 11.81x10^{-3} perg**
H4	-1.916, 1.305, 0.603	0.067		**1.21 Å, 1.04x10^{-3} perg**
H5	-1.577, 1.036, -1.132	0.063		same as H4
O6	0.082, -1.107, -0.101	-0.481	9	same as O3
H7	-1.916, -1.305, -0.603	0.067		same as H4
H8	-1.577, -1.036, 1.132	0.063		same as H4
C9	0.842, 0.000, 0.000	1.033	10	**1.875 Å, 7.30x10^{-3} perg**
O10	2.043, -0.000, -0.000	-0.691		**1.48 Å, 14.59x10^{-3} perg**

Table B.17: LoD model parameters for ***Ethylene Carbonate***. Note that "all-atom" denotes that charges from the all-atom force-field at original locations are used.

Model	Position [Å] Rotation (Axis,θ)	Semi-axes [Å] (LJ width [Å])	LJ energy [perg]	Charges
Single ellipsoid	-0.097, 0.000, 0.000 (0.000, 0.060, 1.000, 3.142)	3.26x2.41x1.81 (1.72)[b]	0.08020[a], 0.09819[b]	All-atom
2-ellipsoid (CH_2-CH_2)	-1.523, 0.000, 0.000 (0.522, 0.674, 0.522, 1.955)	2.53x1.97x1.70 (1.62)[b]	0.01926[a], 0.02625[b]	All-atom
2-ellipsoid (CO_3)	0.794, 0.000, 0.000 (1.000, 0.000, 0.000, 0.091)	2.39x2.35x1.61 (1.68)[b]	0.06212[a], 0.07071[b]	All-atom

[a] "simple touch" LJ potential, equation (2-2), [b] "adjusted-width" LJ potential, equation (2-6)

Table B.18: All-atom model parameters for ***Ethyl ammonium Cation***, coloring represents LoD ellipsoid partitioning

Atom	Position [Å]	Partial charge [*e*]	Minimum connectivity	LJ radius and energy
C1	-1.298, -0.271, -0.000	-0.329	2, 3, 4, 5	**1.65 Å, 4.59x10^{-3} perg**
C2	-0.061, 0.610, 0.000	0.221	6, 7, 8	same as C1
H3	-2.181, 0.375, -0.000	0.144		**1.25 Å, 1.04x10^{-3} perg**
H4	-1.353, -0.902, 0.893	0.119		same as H3
H5	-1.353, -0.902, -0.893	0.119		same as H3
N6	1.211, -0.245, 0.000	-0.447	9, 10, 11	**1.6 Å, 11.81x10^{-3} perg**
H7	0.007, 1.242, 0.889	0.066		same as H3
H8	0.007, 1.242, -0.889	0.066		same as H3
H9	1.247, -0.854, 0.827	0.347		same as H3
H10	2.063, 0.330, -0.000	0.346		same as H3
H11	1.247, -0.855, -0.827	0.347		same as H3

Table B.19: All-atom model parameters for ***Nitrate Anion***, coloring represent LoD ellipsoid partitioning

Atom	Position [Å]	Partial charge [*e*]	Minimum connectivity	LJ radius and energy
N1	-0.000, -0.000, 0.000	0.914	2, 3, 4	**1.60 Å, 11.81x10^{-3} perg**
O2	-0.621, 1.101, -0.000	-0.638		**1.48 Å, 14.59x10^{-3} perg**
O3	-0.644, -1.088, -0.000	-0.638		same as O2
O4	1.264, -0.013, -0.000	-0.638		same as O2

Table B.20: LoD model parameters for ***Ethyl ammonium nitrate***. Note that "all-atom" denotes that charges from the all-atom force-field at original locations are used.

Model	Position [Å] Rotation (Axis,θ)	Semi-axes [Å] (LJ width [Å])	LJ energy [perg]	Center Charge [*e*] (Center Dipole[a] [*D*])
EtNH3$^+$ (Ethyl)	-0.840, 0.192, 0.000 (0.294,-0.676,-0.676, 2.570)	2.49x1.96x1.78 (1.53)[b]	0.02760[b]	0.407 (0.573,0.719,0.000)
EtNH3$^+$ (NH_3^+)	1.356,-0.346, 0.000 (0.348,-0.663,-0.663, 2.470)	1.79x1.79x1.54 (1.46)[b]	0.02540[b]	0.593 (1.123,-0.789,0.000)
Nitrate	0.000, 0.000, 0.000 (0.000, 0.000, 1.000, 0.001)	2.34x2.33x1.48 (1.62)[b]	0.08171[b]	-1.000 (0.000,0.000,0.000)

[a]Dipole vectors are given in the lab frame, [b] "adjusted-width" LJ potential, equation (2-6)

Table B.21: All-atom model parameters for ***YLD124***, coloring represents LoD ellipsoid partitioning

Atom	Position [Å]	Partial charge [*e*]	Minimum connectivity	LJ radius and energy
C1	-1.283, -1.535, -0.825	-0.158	2, 4, 9	**1.65 Å, 4.59x10^{-3} perg**
C2	-0.135, -0.799, -0.812	-0.174	3, 16	same as C1
H3	-0.201, 0.278, -0.963	0.11		**1.25 Å, 1.04x10^{-3} perg**
H4	-1.205, -2.612, -0.687	0.117		same as H3
N5	-6.670, 0.204, -1.546	-0.478	6, 60, 61	**1.6 Å, 11.81x10^{-3} perg**
C6	-5.361, -0.206, -1.356	0.384	7, 11	same as C1
C7	-4.283, 0.720, -1.363	-0.278	8, 12	same as C1
C8	-2.974, 0.305, -1.201	-0.102	9, 13	same as C1
C9	-2.635, -1.052, -1.011	0.127	10	same as C1
C10	-3.709, -1.965, -0.994	-0.148	11, 14	same as C1
C11	-5.026, -1.569, -1.155	-0.249	15	same as C1
H12	-4.470, 1.778, -1.496	0.176		same as H3
H13	-2.194, 1.061, -1.220	0.099		same as H3
H14	-3.499, -3.022, -0.845	0.105		same as H3
H15	-5.799, -2.326, -1.119	0.158		same as H3
C16	1.198, -1.306, -0.629	0.131	17, 18	same as C1
C17	2.262, -0.435, -0.679	-0.299	19, 24	same as C1
C18	1.450, -2.782, -0.403	0.001	20, 21, 59	same as C1
H19	2.058, 0.624, -0.831	0.129		same as H3
C20	2.794, -3.089, 0.298	0.312	22, 118, 122	same as C1
H21	0.634, -3.219, 0.184	0.01		same as H3
C22	3.918, -2.304, -0.417	0.132	23, 24, 58	same as C1
H23	4.041, -2.713, -1.432	-0.012		same as H3
C24	3.628, -0.823, -0.540	0.094	25	same as C1
C25	4.616, 0.147, -0.561	-0.194	26, 27	same as C1
H26	4.294, 1.181, -0.681	0.119		same as H3
C27	6.007, -0.074, -0.441	0.029	28, 29	same as C1
C28	6.933, 0.948, -0.443	-0.299	30, 57	same as C1
H29	6.356, -1.094, -0.333	0.063		same as H3
C30	8.331, 0.823, -0.288	0.248	31, 32	same as C1
C31	9.234, 1.877, -0.202	-0.281	33, 34	same as C1
C32	9.146, -0.467, -0.162	-0.098	35, 36, 37	same as C1
C33	10.556, 1.354, 0.012	0.527	35, 38	same as C1
C34	8.856, 3.241, -0.290	0.39	39	same as C1
O35	10.499, 0.002, 0.089	-0.351		**1.48 Å, 14.59x10^{-3} perg**
C36	9.260, -1.176, -1.539	0.618	40, 41, 42	same as C1
C37	8.728, -1.371, 0.997	0.253	43, 44	same as C1
C38	11.778, 1.970, 0.165	-0.451	45, 46	same as C1
N39	8.449, 4.330, -0.369	-0.429		same as N5
F40	9.623, -0.300, -2.488	-0.2		**1.42 Å, 4.24x10^{-3} perg**

F41	10.177, -2.156, -1.511	-0.158		same as F40
F42	8.083, -1.724, -1.913	-0.193		same as F40
C43	8.551, -0.766, 2.250	-0.159	47, 48	same as C1
C44	8.553, -2.756, 0.883	-0.163	49, 50	same as C1
C45	11.931, 3.386, 0.114	0.447	51	same as C1
C46	12.950, 1.186, 0.384	0.491	52	same as C1
H47	8.691, 0.306, 2.356	0.085		same as H3
C48	8.200, -1.523, 3.364	-0.074	53, 54	same as C1
C49	8.191, -3.512, 2.000	-0.056	54, 55	same as C1
H50	8.699, -3.261, -0.063	0.099		same as H3
N51	12.101, 4.537, 0.080	-0.455		same as N5
N52	13.914, 0.558, 0.566	-0.481		same as N5
H53	8.071, -1.036, 4.326	0.111		same as H3
C54	8.014, -2.902, 3.241	-0.107	56	same as C1
H55	8.061, -4.585, 1.895	0.096		same as H3
H56	7.738, -3.496, 4.108	0.104		same as H3
H57	6.568, 1.969, -0.543	0.159		same as H3
H58	4.866, -2.479, 0.101	-0.052		same as H3
H59	1.427, -3.294, -1.378	-0.003		same as H3
C60	-6.997, 1.615, -1.736	0.199	63, 115, 116	same as C1
C61	-7.765, -0.760, -1.562	0.115	62, 111, 114	same as C1
C62	-8.277, -1.158, -0.170	0.306	65, 112, 113	same as C1
C63	-7.070, 2.423, -0.431	0.286	64, 110, 117	same as C1
O64	-7.266, 3.779, -0.780	-0.607	108	same as O35
O65	-9.285, -2.134, -0.350	-0.6	109	same as O35
C66	-11.322, -4.084, -0.031	0.267	72, 84, 88, 109	same as C1
C67	-6.148, 5.808, 1.064	0.369	68, 76, 80, 108	same as C1
C68	-6.549, 7.044, 1.899	-0.324	69, 70, 71	same as C1
H69	-7.251, 6.791, 2.704	0.054		same as H3
H70	-5.661, 7.488, 2.372	0.07		same as H3
H71	-7.012, 7.826, 1.285	0.052		same as H3
C72	-12.157, -4.894, 0.986	-0.317	73, 74, 75	same as C1
H73	-12.852, -5.563, 0.458	0.072		same as H3
H74	-11.529, -5.522, 1.630	0.06		same as H3
H75	-12.761, -4.247, 1.634	0.058		same as H3
C76	-5.136, 6.238, -0.020	-0.261	77, 78, 79	same as C1
H77	-4.828, 5.393, -0.647	0.042		same as H3
H78	-5.549, 7.009, -0.682	0.042		same as H3
H79	-4.231, 6.656, 0.443	0.048		same as H3
C80	-5.473, 4.778, 1.995	-0.257	81, 82, 83	same as C1
H81	-4.596, 5.224, 2.487	0.047		same as H3
H82	-6.147, 4.430, 2.788	0.031		same as H3
H83	-5.119, 3.898, 1.445	0.052		same as H3
C84	-12.274, -3.250, -0.917	-0.204	85, 86, 87	same as C1

H85	-12.888, -2.562, -0.324	0.027		same as H3
H86	-11.723, -2.657, -1.655	0.032		same as H3
H87	-12.962, -3.911, -1.464	0.047		same as H3
C88	-10.530, -5.060, -0.927	-0.249	89, 90, 91	same as C1
H89	-9.862, -5.703, -0.340	0.038		same as H3
H90	-11.218, -5.720, -1.474	0.056		same as H3
H91	-9.920, -4.527, -1.665	0.048		same as H3
C92	-8.891, -3.883, 1.964	-0.41	93, 94, 95, 109	same as C1
H93	-8.335, -4.627, 1.382	0.091		same as H3
H94	-8.159, -3.214, 2.432	0.091		same as H3
H95	-9.407, -4.412, 2.774	0.07		same as H3
C96	-11.022, -1.658, 1.959	-0.459	97, 98, 99, 109	same as C1
H97	-10.320, -0.970, 2.445	0.098		same as H3
H98	-11.723, -1.056, 1.369	0.103		same as H3
H99	-11.593, -2.151, 2.755	0.086		same as H3
C100	-8.519, 6.297, -0.933	-0.494	101, 102, 103, 108	same as C1
H101	-7.851, 6.574, -1.756	0.112		same as H3
H102	-9.423, 5.862, -1.375	0.114		same as H3
H103	-8.812, 7.216, -0.413	0.095		same as H3
C104	-8.954, 4.456, 1.514	-0.484	105, 106, 107, 108	same as C1
H105	-9.829, 4.013, 1.023	0.117		same as H3
H106	-8.540, 3.705, 2.197	0.1		same as H3
H107	-9.314, 5.291, 2.127	0.088		same as H3
Si108	-7.704, 5.059, 0.228	0.763		**2.0 Å, $6.95x10^{-3}$ perg**
Si109	-10.115, -2.925, 0.887	0.748		same as Si108
H110	-7.895, 2.047, 0.192	-0.01		same as H3
H111	-8.597, -0.329, -2.127	0.058		same as H3
H112	-7.447, -1.548, 0.437	-0.046		same as H3
H113	-8.674, -0.270, 0.345	-0.012		same as H3
H114	-7.465, -1.666, -2.099	0.024		same as H3
H115	-6.268, 2.090, -2.401	-0.002		same as H3
H116	-7.963, 1.680, -2.244	0.031		same as H3
H117	-6.141, 2.288, 0.140	-0.066		same as H3
C118	2.728, -2.691, 1.787	-0.185	119, 120, 121	same as C1
H119	1.952, -3.267, 2.306	0.047		same as H3
H120	3.683, -2.895, 2.285	0.028		same as H3
H121	2.502, -1.629, 1.918	0.007		same as H3
C122	3.087, -4.595, 0.196	-0.348	123, 124, 125	same as C1
H123	2.296, -5.183, 0.678	0.075		same as H3
H124	3.159, -4.921, -0.849	0.072		same as H3
H125	4.033, -4.845, 0.692	0.078		same as H3

Table B.22: LoD model parameters for ***YLD124***, coloring represents LoD ellipsoid partitioning: **(67,..,71,76,..,83|108|100,..,103|104,..,107|64|63,110,117|60,115,116|61,111,114|62,112,113|65|109|92,..,95|96,..,99|66,72,..,75,84,..,91|1,..,24,58,59|118,..,125|25,..,35,38,39,45,46,51,52,57|36,40,..,42|37,43,44,47,..,50,53,..,56)**

#	Position [Å] Rotation (Axis,θ)	Semi-axes [Å]	LJ energy [perg]	Center Charge [*e*] (Center Dipole[a] [*D*])
1	-5.713, 6.024, 1.324 (0.476, 0.246, 0.844, 3.115)	2.88x2.91x1.91	0.02582[b]	-0.035 (-0.305,-0.291,-0.291)
2	-7.704, 5.059, 0.228 (1.000, 0.000, 0.000, 0.000)	2.00x2.00x2.00	0.00695[b]	0.763 (0.000,0.000,0.000)
3	-8.597, 6.408, -1.043 (0.444, -0.205, 0.873, 2.183)	1.84x1.84x1.52	0.00687[b]	-0.174 (-0.332,0.424,-0.537)
4	-9.074, 4.403, 1.635 (0.443, -0.892, -0.091, 0.843)	1.84x1.84x1.52	0.00688[b]	-0.178 (-0.548,-0.302,0.416)
5	-7.266, 3.779, -0.780 (1.000, 0.000, 0.000, 0.000)	1.48x1.48x1.48	0.01459[b]	-0.607 (0.000,0.000,0.000)
6	-7.054, 2.343, -0.237 (0.025, -0.547, -0.837, 3.011)	1.96x1.66x1.50	0.00600[b]	0.210 (-0.272,0.141,-0.406)
7	-7.033, 1.699, -1.925 (0.024, -0.531, -0.847, 2.893)	1.95x1.66x1.50	0.00600[b]	0.228 (-0.111,-0.086,0.138)
8	-7.848, -0.834, -1.740 (0.714, -0.343, -0.610, 1.289)	1.95x1.66x1.50	0.00600[b]	0.196 (-0.117,0.085,-0.049)
9	-8.209, -1.080, 0.013 (0.751, -0.361, -0.553, 1.274)	1.96x1.66x1.50	0.00600[b]	0.249 (-0.241,-0.057,-0.380)
10	-9.285, -2.134, -0.350 (1.000, 0.000, 0.000, 0.000)	1.48x1.48x1.48	0.01459[b]	-0.600 (0.000,0.000,0.000)
11	-10.115, -2.925, 0.887 (1.000, 0.000, 0.000, 0.000)	2.00x2.00x2.00	0.00695[b]	0.748 (0.000,0.000,0.000)
12	-8.778, -3.971, 2.068 (0.487, -0.111, 0.866, 2.360)	2.88x2.91x1.91	0.02582[b]	-0.158 (0.474,-0.277,0.302)
13	-11.105, -1.541, 2.063 (-0.412, 0.265, 0.872, 2.479)	1.84x1.84x1.52	0.00688[b]	-0.171 (-0.322,0.515,0.350)
14	-11.659, -4.407, -0.317 (-0.312, 0.782, 0.539, 1.290)	2.91x2.87x1.91	0.02582[b]	-0.065 (0.140,0.137,-0.017)
15	-1.052, -1.163, -0.860 (-0.043, 0.056, 0.998, 2.937)	9.01x3.13x1.66	0.08401[b]	0.129 (15.303,-4.983,2.852)
16	2.919, -3.698, 1.077 (0.328, -0.264, 0.907, 1.856)	3.48x1.89x1.78	0.01435[b]	-0.227 (0.029,-0.506,0.356)
17	9.507, 1.734, -0.109 (0.059, -0.033, -0.998, 2.890)	7.33x3.83x1.71	0.10602[b]	-0.566 (-4.766,-1.104,-0.688)

18	9.285, -1.344, -1.875 (0.013, -0.234, -0.972, 2.904)	2.22x2.22x1.40	0.01724[b]	0.066 (0.038,0.464,1.346)
19	8.348, -2.195, 2.212 (0.633, 0.270, 0.726, 2.301)	3.44x3.04x1.66	0.03077[b]	0.190 (0.137,0.211,-0.446)

[a]Dipole vectors are given in the lab frame, [b] "simple touch" LJ potential, equation (2-2)

Table B.23: All-atom model parameters for ***YLD124 (2nd enantiomer)***, coloring represents LoD ellipsoid partitioning

Atom	Position [Å]	Partial charge [*e*]	Minimum connectivity	LJ radius and energy
C1	1.182, -1.496, 0.293	-0.15	2, 4, 9	**1.65 Å, 4.59x10^{-3} perg**
C2	0.045, -0.742, 0.275	-0.191	3, 16	same as C1
H3	0.117, 0.323, 0.491	0.123		**1.25 Å, 1.04x10^{-3} perg**
H4	1.094, -2.563, 0.095	0.112		same as H3
N5	6.538, 0.079, 1.472	-0.506	6, 47, 48	**1.6 Å, 11.81x10^{-3} perg**
C6	5.241, -0.287, 1.153	0.404	7, 11	same as C1
C7	4.188, 0.667, 1.106	-0.281	8, 12	same as C1
C8	2.886, 0.292, 0.832	-0.113	9, 13	same as C1
C9	2.531, -1.049, 0.572	0.132	10	same as C1
C10	3.583, -1.987, 0.593	-0.14	11, 14	same as C1
C11	4.892, -1.632, 0.868	-0.265	15	same as C1
H12	4.391, 1.715, 1.284	0.178		same as H3
H13	2.125, 1.067, 0.815	0.099		same as H3
H14	3.360, -3.032, 0.388	0.104		same as H3
H15	5.648, -2.407, 0.860	0.161		same as H3
C16	-1.286, -1.226, 0.030	0.101	17, 18	same as C1
C17	-2.347, -0.353, 0.113	-0.304	19, 24	same as C1
C18	-1.542, -2.686, -0.281	0.096	20, 21, 46	same as C1
H19	-2.140, 0.695, 0.326	0.125		same as H3
C20	-2.882, -2.949, -1.007	0.409	22, 105, 109	same as C1
H21	-0.723, -3.090, -0.889	-0.021		same as H3
C22	-4.008, -2.200, -0.255	-0.014	23, 24, 45	same as C1
H23	-4.141, -2.666, 0.734	-0.022		same as H3
C24	-3.714, -0.730, -0.047	0.179	25	same as C1
C25	-4.700, 0.237, 0.042	-0.277	26, 27	same as C1
H26	-4.376, 1.263, 0.214	0.132		same as H3
C27	-6.094, 0.021, -0.054	0.141	28, 29	same as C1
C28	-7.020, 1.037, 0.065	-0.328	30, 44	same as C1
H29	-6.447, -0.991, -0.211	-0.027		same as H3
C30	-8.425, 0.916, -0.001	0.261	31, 32	same as C1
C31	-9.336, 1.948, 0.194	-0.288	33, 34	same as C1

C32	-9.243, -0.347, -0.288	-0.057	35, 36, 37	same as C1
C33	-10.673, 1.428, 0.088	0.509	35, 38	same as C1
C34	-8.956, 3.285, 0.474	0.397	39	same as C1
O35	-10.622, 0.095, -0.147	-0.366		**1.48 Å, $14.59x10^{-3}$ perg**
C36	-9.007, -1.495, 0.692	0.254	113, 114	same as C1
C37	-9.141, -0.733, -1.789	0.598	123, 124, 125	same as C1
C38	-11.907, 2.029, 0.202	-0.432	40, 41	same as C1
N39	-8.547, 4.351, 0.704	-0.43		same as N5
C40	-12.057, 3.422, 0.463	0.437	42	same as C1
C41	-13.095, 1.251, 0.059	0.492	43	same as C1
N42	-12.226, 4.554, 0.676	-0.452		same as N5
N43	-14.072, 0.628, -0.053	-0.483		same as N5
H44	-6.652, 2.045, 0.248	0.157		same as H3
H45	-4.953, -2.340, -0.790	0.04		same as H3
H46	-1.524, -3.253, 0.663	-0.024		same as H3
C47	6.879, 1.466, 1.775	0.24	50, 102, 103	same as C1
C48	7.605, -0.915, 1.535	0.114	49, 98, 101	same as C1
C49	8.224, -1.266, 0.174	0.3	52, 99, 100	same as C1
C50	7.135, 2.334, 0.533	0.286	51, 97, 104	same as C1
O51	7.354, 3.659, 0.974	-0.612	95	same as O35
O52	9.179, -2.287, 0.393	-0.6	96	same as O35
C53	11.225, -4.245, 0.167	0.275	59, 71, 75, 96	same as C1
C54	6.820, 5.855, -0.938	0.359	55, 63, 67, 95	same as C1
C55	7.515, 7.018, -1.681	-0.338	56, 57, 58	same as C1
H56	8.297, 6.663, -2.364	0.059		same as H3
H57	6.784, 7.574, -2.286	0.076		same as H3
H58	7.973, 7.735, -0.990	0.056		same as H3
C59	12.216, -4.937, -0.794	-0.312	60, 61, 62	same as C1
H60	12.808, -5.689, -0.253	0.071		same as H3
H61	11.705, -5.458, -1.613	0.059		same as H3
H62	12.925, -4.228, -1.239	0.056		same as H3
C63	5.702, 6.425, -0.039	-0.28	64, 65, 66	same as C1
H64	5.192, 5.634, 0.525	0.048		same as H3
H65	6.087, 7.154, 0.684	0.047		same as H3
H66	4.944, 6.938, -0.649	0.055		same as H3
C67	6.186, 4.906, -1.979	-0.273	68, 69, 70	same as C1
H68	5.470, 5.454, -2.608	0.053		same as H3
H69	6.934, 4.465, -2.650	0.035		same as H3
H70	5.635, 4.086, -1.503	0.062		same as H3
C71	12.015, -3.559, 1.302	-0.203	72, 73, 74	same as C1
H72	12.720, -2.811, 0.919	0.028		same as H3
H73	11.348, -3.059, 2.013	0.031		same as H3
H74	12.602, -4.302, 1.862	0.045		same as H3
C75	10.290, -5.309, 0.782	-0.267	76, 77, 78	same as C1

H76	9.729, -5.855, 0.013	0.041		same as C1
H77	10.874, -6.051, 1.346	0.059		same as H3
H78	9.566, -4.861, 1.472	0.055		same as H3
C79	9.154, -3.728, -2.154	-0.411	80, 81, 82, 96	same as C1
H80	8.479, -4.499, -1.765	0.094		same as H3
H81	8.539, -2.977, -2.665	0.091		same as H3
H82	9.789, -4.195, -2.917	0.07		same as H3
C83	11.275, -1.586, -1.525	-0.46	84, 85, 86, 96	same as C1
H84	10.671, -0.833, -2.045	0.1		same as H3
H85	11.860, -1.068, -0.757	0.102		same as H3
H86	11.978, -1.996, -2.260	0.087		same as H3
C87	8.792, 6.030, 1.497	-0.477	88, 89, 90, 95	same as C1
H88	8.010, 6.337, 2.200	0.107		same as H3
H89	9.560, 5.498, 2.070	0.107		same as H3
H90	9.251, 6.937, 1.088	0.09		same as H3
C91	9.514, 4.237, -0.916	-0.47	92, 93, 94, 95	same as C1
H92	10.204, 3.643, -0.305	0.112		same as H3
H93	9.169, 3.602, -1.741	0.098		same as H3
H94	10.095, 5.055, -1.357	0.083		same as H3
Si95	8.101, 4.921, 0.141	0.77		**2.0 Å, 6.95x10^{-3} perg**
Si96	10.194, -2.948, -0.781	0.74		same as Si95
H97	8.005, 1.944, -0.015	-0.017		same as H3
H98	8.395, -0.532, 2.187	0.058		same as H3
H99	7.441, -1.599, -0.521	-0.04		same as H3
H100	8.693, -0.370, -0.259	-0.008		same as H3
H101	7.240, -1.835, 2.004	0.028		same as H3
H102	6.089, 1.931, 2.373	-0.012		same as H3
H103	7.778, 1.472, 2.397	0.021		same as H3
H104	6.271, 2.282, -0.144	-0.065		same as H3
C105	-2.805, -2.470, -2.470	-0.299	106, 107, 108	same as C1
H106	-2.026, -3.018, -3.015	0.067		same as H3
H107	-3.756, -2.645, -2.986	0.072		same as H3
H108	-2.576, -1.402, -2.544	0.028		same as H3
C109	-3.180, -4.457, -0.990	-0.428	110, 111, 112	same as C1
H110	-2.388, -5.020, -1.499	0.09		same as H3
H111	-3.258, -4.840, 0.035	0.091		same as H3
H112	-4.124, -4.677, -1.503	0.09		same as H3
C113	-8.942, -1.177, 2.057	-0.159	115, 116	same as C1
C114	-8.911, -2.838, 0.306	-0.147	117, 118	same as C1
C115	-8.778, -2.174, 3.014	-0.066	119, 120	same as C1
H116	-9.022, -0.141, 2.373	0.08		same as H3
C117	-8.738, -3.836, 1.268	-0.091	119, 122	same as C1
H118	-8.975, -3.125, -0.736	0.099		same as H3
C119	-8.672, -3.510, 2.622	-0.099	121	same as C1

H120	-8.733, -1.906, 4.066	0.105	same as H3
H121	-8.542, -4.290, 3.367	0.102	same as H3
H122	-8.665, -4.872, 0.952	0.105	same as H3
F123	-9.314, 0.348, -2.564	-0.199	**1.42 Å, 4.24x10^{-3} perg**
F124	-10.076, -1.635, -2.129	-0.154	same as F123
F125	-7.933, -1.263, -2.084	-0.186	same as F123

Table B.24: LoD model parameters for ***YLD124 (2nd enantiomer)***, coloring represents LoD ellipsoid partitioning:
(54,..,58,63,..,70|95|87,..,90|91,..,94|51|50,97,104|47,102,103|48,98,101|49,99,100|52|96|79,..,82|83,..,86|53,71,..,78,59,..,62|1,..,24,45,46|105,..,112|25,..,35,38,39,40,..,44|37,123,..,125|36,113,..,122)

#	Position [Å] Rotation (Axis,θ)	Semi-axes [Å]	LJ energy [perg]	Center Charge [*e*] (Center Dipole[a] [*D*])
1	6.462, 6.121, -1.261 (0.660, 0.732, 0.170, 0.998)	2.90x2.90x1.91	0.02582[b]	-0.041 (0.141,-0.323,0.303)
2	8.101, 4.921, 0.141 (0.000, 0.000, 0.000, 0.000)	2.00x2.00x2.00	0.00695[b]	0.770 (0.000,0.000,0.000)
3	8.857, 6.129, 1.627 (-0.358, -0.200, -0.912, 2.243)	1.84x1.84x1.52	0.00688[b]	-0.172 (0.263,0.391,0.620)
4	9.649, 4.177, -1.014 (-0.448, 0.169, 0.878, 3.030)	1.84x1.84x1.53	0.00688[b]	-0.176 (0.597,-0.361,-0.343)
5	7.354, 3.659, 0.974 (0.000, 0.000, 0.000, 0.000)	1.48x1.48x1.48	0.01459[b]	-0.612 (0.000,0.000,0.000)
6	7.136, 2.265, 0.335 (0.984, -0.146, -0.100, 1.236)	1.97x1.66x1.50	0.00600[b]	0.203 (0.195,0.154,0.549)
7	6.896, 1.539, 1.971 (0.973, -0.139, -0.186, 1.215)	1.96x1.67x1.50	0.00600[b]	0.249 (0.101,-0.163,-0.328)
8	7.671, -0.999, 1.716 (0.257, -0.455, -0.853, 2.461)	1.96x1.67x1.50	0.00600[b]	0.200 (0.072,0.109,-0.017)
9	8.175, -1.178, -0.008 (0.262, -0.465, -0.845, 2.552)	1.97x1.66x1.50	0.00599[b]	0.251 (0.227,-0.136,0.484)
10	9.179, -2.287, 0.393 (0.000, 0.000, 0.000, 0.000)	1.48x1.48x1.48	0.01459[b]	-0.600 (0.000,0.000,0.000)
11	10.194, -2.948, -0.781 (0.000, 0.000, 0.000, 0.000)	2.00x2.00x2.00	0.00695[b]	0.740 (0.000,0.000,0.000)
12	9.058, -3.799, -2.286 (-0.171, 0.690, 0.703, 1.087)	1.84x1.84x1.53	0.00688[b]	-0.156 (-0.453,-0.250,-0.434)

13	11.375, -1.460, -1.602 (0.398, -0.755, 0.521, 1.395)	1.84x1.84x1.53	0.00688[b]	-0.171 (0.402,0.583,-0.257)
14	11.513, -4.609, 0.456 (0.435, 0.731, -0.525, 1.255)	2.92x2.88x1.91	0.02582[b]	-0.060 (-0.150,0.153,-0.010)
15	0.949, -1.140, 0.391 (0.539, -0.481, 0.691, 0.275)	8.98x3.13x1.66	0.08405[b]	0.234 (-18.572,-5.279,-4.963)
16	-3.004, -3.515, -1.818 (-0.284, 0.358, 0.889, 1.496)	3.49x1.89x1.78	0.01435[b]	-0.289 (-0.151,-0.591,-0.597)
17	-9.618, 1.801, 0.200 (0.593, 0.020, -0.805, 0.312)	7.32x3.83x1.70	0.10602[b]	-0.613 (3.276,-0.797,-0.263)
18	-9.114, -0.824, -2.159 (-0.054, 0.113, 0.992, 2.762)	2.22x2.22x1.65	0.01724[b]	0.059 (-0.230,0.136,1.354)
19	-8.830, -2.580, 1.740 (0.676, -0.232, -0.700, 2.523)	3.44x3.05x1.66	0.03077[b]	0.184 (-0.078,0.339,-0.493)

[a]Dipole vectors are given in the lab frame, [b] "simple touch" LJ potential, equation (2-2)

Table B.25: All-atom model parameters for ***JRD1***, coloring represents LoD ellipsoid partitioning

Atom	Position [Å]	Partial charge [*e*]	Minimum connectivity	LJ radius and energy
C1	1.079, -1.772, -1.130	-0.178	2, 4, 9	**1.65 Å, 4.59x10^{-3} perg**
C2	2.186, -0.986, -1.006	-0.144	3, 16	same as C1
H3	2.071, 0.096, -1.058	0.101		**1.25 Å, 1.04x10^{-3} perg**
H4	1.207, -2.852, -1.088	0.122		same as H3
N5	-4.359, -0.240, -1.926	-0.385	6, 60, 61	**1.6 Å, 11.81x10^{-3} perg**
C6	-3.040, -0.602, -1.711	0.301	7, 11	same as C1
C7	-2.012, 0.373, -1.598	-0.205	8, 12	same as C1
C8	-0.690, 0.010, -1.417	-0.156	9, 13	same as C1
C9	-0.289, -1.340, -1.324	0.164	10	same as C1
C10	-1.315, -2.303, -1.423	-0.18	11, 14	same as C1
C11	-2.644, -1.958, -1.604	-0.206	15	same as C1
H12	-2.249, 1.427, -1.659	0.141		same as H3
H13	0.051, 0.801, -1.346	0.115		same as H3
H14	-1.056, -3.357, -1.348	0.11		same as H3
H15	-3.379, -2.752, -1.651	0.152		same as H3
C16	3.537, -1.444, -0.828	0.084	17, 18	same as C1
C17	4.558, -0.523, -0.760	-0.27	19, 24	same as C1
C18	3.859, -2.922, -0.741	0.036	20, 21, 59	same as C1
H19	4.306, 0.535, -0.814	0.125		same as H3
C20	5.196, -3.232, -0.029	0.347	22, 106, 110	same as C1
H21	3.050, -3.455, -0.227	-0.002		same as H3

C22	6.298, -2.329, -0.631	0.183	23, 24, 58	same as C1
H23	6.471, -2.633, -1.675	-0.026		same as H3
C24	5.938, -0.859, -0.623	0.063	25	same as C1
C25	6.878, 0.154, -0.532	-0.207	26, 27	same as C1
H26	6.508, 1.179, -0.561	0.125		same as H3
C27	8.276, -0.011, -0.410	0.06	28, 29	same as C1
C28	9.151, 1.050, -0.307	-0.326	30, 57	same as C1
H29	8.673, -1.019, -0.391	0.048		same as H3
C30	10.553, 0.981, -0.154	0.25	31, 32	same as C1
C31	11.401, 2.067, 0.029	-0.286	33, 34	same as C1
C32	11.433, -0.272, -0.141	0	35, 36, 37	same as C1
C33	12.749, 1.595, 0.199	0.51	35, 38	same as C1
C34	10.954, 3.413, 0.062	0.393	39	same as C1
O35	12.760, 0.240, 0.156	-0.365		**1.48 Å, 14.59×10^{-3} perg**
C36	11.584, -0.852, -1.574	0.604	40, 41, 42	same as C1
C37	11.064, -1.295, 0.933	0.171	43, 44	same as C1
C38	13.939, 2.256, 0.408	-0.439	45, 46	same as C1
N39	10.493, 4.482, 0.079	-0.429		same as N5
F40	11.909, 0.121, -2.439	-0.206		**1.42 Å, 4.24×10^{-3} perg**
F41	12.547, -1.786, -1.623	-0.161		same as F40
F42	10.436, -1.421, -2.005	-0.19		same as F40
C43	10.896, -0.818, 2.242	-0.119	47, 48	same as C1
C44	10.920, -2.667, 0.689	-0.125	49, 50	same as C1
C45	14.020, 3.676, 0.484	0.446	51	same as C1
C46	15.149, 1.515, 0.559	0.49	52	same as C1
H47	11.011, 0.242, 2.448	0.073		same as H3
C48	10.586, -1.689, 3.282	-0.076	53, 54	same as C1
C49	10.602, -3.537, 1.734	-0.061	54, 55	same as C1
H50	11.057, -3.073, -0.305	0.089		same as H3
N51	14.132, 4.834, 0.553	-0.456		same as N5
N52	16.143, 0.923, 0.687	-0.482		same as N5
H53	10.464, -1.300, 4.289	0.108		same as H3
C54	10.435, -3.054, 3.031	-0.109	56	same as C1
H55	10.496, -4.599, 1.528	0.094		same as H3
H56	10.193, -3.736, 3.841	0.106		same as H3
H57	8.737, 2.057, -0.317	0.163		same as H3
H58	7.239, -2.507, -0.100	-0.068		same as H3
H59	3.890, -3.333, -1.762	-0.014		same as H3
C60	-4.761, 1.164, -1.958	0.05	63, 103, 104	same as C1
C61	-5.386, -1.246, -2.178	0.141	62, 99, 102	same as C1
C62	-6.057, -1.800, -0.914	0.439	65, 100, 101	same as C1
C63	-4.890, 1.814, -0.572	0.42	64, 98, 105	same as C1
O64	-5.279, 3.159, -0.781	-0.5	96	same as O35
O65	-6.968, -2.807, -1.331	-0.502	97	same as O35

C66	-8.638, -5.106, -1.378	0.163	72, 84, 88, 97	same as C1
C67	-4.120, 5.071, 1.149	0.476	68, 76, 80, 96	same as C1
C68	-4.450, 6.349, 1.954	-0.174	69, 70, 71	same as C1
H69	-5.100, 6.153, 2.815	0.027		same as H3
H70	-3.524, 6.794, 2.344	0.023		same as H3
H71	-4.942, 7.105, 1.332	0.005		same as H3
C72	-9.693, -5.925, -0.604	-0.019	73, 74, 75	same as C1
H73	-9.996, -6.802, -1.192	0.017		same as H3
H74	-9.306, -6.292, 0.355	-0.03		same as H3
H75	-10.600, -5.342, -0.403	-0.033		same as H3
C76	-3.161, 5.461, 0.000	-0.216	77, 78, 79	same as C1
H77	-2.872, 4.592, -0.603	0.047		same as H3
H78	-3.611, 6.199, -0.674	0.019		same as H3
H79	-2.242, 5.903, 0.410	0.025		same as H3
C80	-3.403, 4.056, 2.066	-0.292	81, 82, 83	same as C1
H81	-2.497, 4.507, 2.494	0.051		same as H3
H82	-4.030, 3.724, 2.900	0.022		same as H3
H83	-3.088, 3.161, 1.516	0.06		same as H3
C84	-9.249, -4.616, -2.710	-0.016	85, 86, 87	same as C1
H85	-10.125, -3.978, -2.547	-0.037		same as H3
H86	-8.522, -4.047, -3.301	-0.007		same as H3
H87	-9.572, -5.475, -3.315	0.002		same as H3
C88	-7.427, -6.011, -1.689	-0.16	89, 90, 91	same as C1
H89	-6.995, -6.443, -0.779	0		same as H3
H90	-7.739, -6.847, -2.330	0.034		same as H3
H91	-6.638, -5.464, -2.217	0.042		same as H3
C92	-7.267, -4.008, 1.290	-0.061	97, 114, 115	same as C1
C93	-9.564, -2.403, -0.102	-0.052	97, 124, 125	same as C1
C94	-6.607, 5.616, -0.677	-0.054	96, 144, 145	same as C1
C95	-6.915, 3.536, 1.582	-0.014	96, 134, 135	same as C1
Si96	-5.707, 4.324, 0.358	0.246		**2.0 Å, 6.95x10^{-3} perg**
Si97	-8.101, -3.577, -0.354	0.327		same as Si96
H98	-5.637, 1.277, 0.028	-0.066		same as H3
H99	-6.157, -0.800, -2.816	0.03		same as H3
H100	-5.304, -2.217, -0.231	-0.119		same as H3
H101	-6.574, -0.991, -0.379	-0.064		same as H3
H102	-4.964, -2.079, -2.749	-0.006		same as H3
H103	-4.062, 1.752, -2.563	0.026		same as H3
H104	-5.731, 1.230, -2.458	0.057		same as H3
H105	-3.933, 1.753, -0.037	-0.078		same as H3
C106	5.069, -2.983, 1.487	-0.201	107, 108, 109	same as C1
H107	4.306, -3.639, 1.924	0.049		same as H3
H108	6.018, -3.193, 1.994	0.029		same as H3
H109	4.791, -1.949, 1.711	0.009		same as H3

C110	5.566, -4.706, -0.265	-0.404	111, 112, 113	same as C1
H111	4.792, -5.373, 0.133	0.087		same as H3
H112	5.681, -4.925, -1.334	0.082		same as H3
H113	6.510, -4.958, 0.233	0.09		same as H3
C114	-6.032, -4.689, 1.287	0.004	116, 117	same as C1
C115	-7.797, -3.642, 2.541	-0.034	118, 119	same as C1
C116	-5.369, -5.005, 2.473	-0.158	120, 121	same as C1
H117	-5.573, -4.972, 0.343	0.086		same as H3
C118	-7.141, -3.959, 3.732	-0.136	120, 122	same as C1
H119	-8.730, -3.088, 2.592	0.02		same as H3
C120	-5.926, -4.644, 3.702	-0.038	123	same as C1
H121	-4.418, -5.530, 2.440	0.098		same as H3
H122	-7.576, -3.665, 4.684	0.108		same as H3
H123	-5.413, -4.890, 4.628	0.085		same as H3
C124	-9.639, -1.218, -0.858	-0.022	126, 127	same as C1
C125	-10.635, -2.682, 0.769	-0.035	128, 129	same as C1
C126	-10.725, -0.346, -0.744	-0.114	130, 131	same as C1
H127	-8.842, -0.980, -1.558	0.07		same as H3
C128	-11.722, -1.814, 0.890	-0.148	130, 132	same as C1
H129	-10.631, -3.592, 1.364	0.096		same as H3
C130	-11.769, -0.642, 0.134	-0.021	133	same as C1
H131	-10.759, 0.558, -1.347	0.087		same as H3
H132	-12.535, -2.056, 1.571	0.099		same as H3
H133	-12.617, 0.033, 0.223	0.077		same as H3
C134	-6.914, 3.749, 2.972	-0.082	136, 137	same as C1
C135	-7.913, 2.687, 1.060	-0.068	138, 139	same as C1
C136	-7.861, 3.145, 3.803	-0.114	140, 141	same as C1
H137	-6.168, 4.395, 3.425	0.081		same as H3
C138	-8.857, 2.074, 1.883	-0.073	140, 142	same as C1
H139	-7.954, 2.504, -0.012	0.073		same as H3
C140	-8.832, 2.304, 3.261	-0.073	143	same as C1
H141	-7.836, 3.330, 4.874	0.095		same as H3
H142	-9.608, 1.418, 1.452	0.049		same as H3
H143	-9.567, 1.830, 3.906	0.093		same as H3
C144	-7.548, 6.485, -0.096	-0.038	146, 147	same as C1
C145	-6.345, 5.759, -2.053	-0.018	148, 149	same as C1
C146	-8.195, 7.464, -0.851	-0.128	150, 151	same as C1
H147	-7.793, 6.390, 0.960	0.034		same as H3
C148	-6.992, 6.735, -2.814	-0.14	150, 153	same as C1
H149	-5.637, 5.090, -2.534	0.061		same as H3
C150	-7.916, 7.592, -2.213	-0.053	152	same as C1
H151	-8.920, 8.123, -0.379	0.102		same as H3
H152	-8.419, 8.353, -2.804	0.083		same as H3
H153	-6.776, 6.825, -3.875	0.099		same as H3

Table B.26: LoD model parameters for ***JRD1***, coloring represents LoD ellipsoid partitioning: **(66,72,..,75,84,..,87,88,..,91|97|92,114,..,123|93,124,..,133|65|62,100,101|61,99,102|67,..,71,76,.., 83|96|95,134,..,143|94,144,..,153|64|63,98,105|60,103,104|1,..,24,58,59|110,..,113|106,..,109|25,.. ,35,38,39,45,46,51,52,57|36,40,..,42|37,43,44,47,..,50,53,..,56)**

#	Position [Å] Rotation (Axis,θ)	Semi-axes [Å]	LJ energy [perg]	Center Charge [*e*] (Center Dipole[a] [*D*])
1	-8.791, -5.520, -1.677 (-0.406, -0.337, -0.850, 2.236)	3.06x3.05x2.03	0.02587[b]	-0.043 (0.281,0.112,-0.248)
2	-8.101, -3.577, -0.354 (1.000, 0.000, 0.000, 0.000)	2.00x2.00x2.00	0.00695[b]	0.327 (0.000,0.000,0.000)
3	-6.538, -4.345, 2.595 (0.885, 0.016, -0.465, 1.801)	3.51x3.14x1.75	0.03081[b]	-0.026 (0.930,-0.482,0.417)
4	-10.758, -1.455, 0.022 (-0.222, 0.624, 0.750, 1.176)	3.51x3.14x1.75	0.03080[b]	0.038 (-0.505,0.267,0.119)
5	-6.968, -2.807, -1.331 (1.000, 0.000, 0.000, 0.000)	1.48x1.48x1.48	0.01459[b]	-0.502 (0.000,0.000,0.000)
6	-6.019, -1.738, -0.714 (0.809, -0.384, -0.446, 1.388)	2.11x1.74x1.57	0.00604[b]	0.255 (-0.315,-0.090,-0.800)
7	-5.442, -1.307, -2.376 (0.780, -0.366, -0.508, 1.382)	2.10x1.74x1.57	0.00604[b]	0.165 (-0.080,0.138,0.081)
8	-3.670, 5.288, 1.371 (0.293, 0.581, 0.759, 2.081)	3.06x3.05x2.03	0.02588[b]	0.073 (-0.703,-0.469,-0.535)
9	-5.707, 4.324, 0.358 (1.000, 0.000, 0.000, 0.000)	2.00x2.00x2.00	0.00695[b]	0.246 (0.000,0.000,0.000)
10	-7.952, 2.871, 2.495 (0.772, -0.104, 0.627, 2.039)	3.51x3.14x1.75	0.03081[b]	-0.032 (-0.279,-0.136,0.514)
11	-7.317, 6.679, -1.512 (-0.498, -0.384, -0.777, 3.041)	3.51x3.14x1.75	0.03080[b]	-0.053 (-0.309,0.571,-0.755)
12	-5.279, 3.159, -0.781 (1.000, 0.000, 0.000, 0.000)	1.48x1.48x1.48	0.01459[b]	-0.500 (0.000,0.000,0.000)
13	-4.857, 1.719, -0.385 (0.053, -0.506, -0.861, 2.888)	2.11x1.74x1.57	0.00604[b]	0.276 (-0.166,0.320,-0.638)
14	-4.804, 1.268, -2.139 (0.047, -0.483, -0.875, 2.846)	2.10x1.74x1.57	0.00604[b]	0.132 (-0.152,0.025,-0.097)
15	1.271, -1.382, -1.140 (-0.056, 0.009, 0.998, 2.981)	7.32x3.29x1.92	0.08520[b]	0.212 (15.471,-4.724,2.979)
16	5.608, -4.874, -0.278 (-0.475, -0.649, -0.594, 1.901)	2.00x1.99x1.61	0.00692[b]	-0.145 (0.162,-0.591,-0.049)
17	5.056, -2.958, 1.666 (-0.002, -0.096, -0.995, 2.119)	2.00x1.99x1.61	0.00693[b]	-0.114 (-0.069,-0.125,0.281)
18	11.678, 1.924, 0.105 (0.084, -0.412, 0.907, 0.326)	6.20x3.48x1.85	0.10587[b]	-0.507 (-4.787,-2.048,-0.892)
19	11.619, -0.988, -1.924 (0.029, -0.191, -0.981, 2.870)	2.32x2.31x1.79	0.01724[b]	0.047 (-0.023,0.311,1.366)

20	10.729, -2.241, 2.069 (0.645, 0.243, 0.724, 2.387)	3.51x3.13x1.75	0.03080[b]	0.150 (0.032,0.000,-0.121)

[a]Dipole vectors are given in the lab frame, [b] "simple touch" LJ potential, equation (2-2)

Table B.27: All-atom model parameters for ***JRD1 (2nd enantiomer)***, coloring represents LoD ellipsoid partitioning

Atom	Position [Å]	Partial charge [*e*]	Minimum connectivity	LJ radius and energy
C1	1.121, -1.803, -1.021	-0.189	2, 4, 9	**1.65 Å, 4.59x10^{-3} perg**
C2	2.217, -1.004, -0.876	-0.15	3, 16	same as C1
H3	2.090, 0.076, -0.924	0.108		**1.25 Å, 1.04x10^{-3} perg**
H4	1.261, -2.881, -0.969	0.122		same as H3
N5	-4.324, -0.357, -1.921	-0.401	6, 47, 48	**1.6 Å, 11.81x10^{-3} perg**
C6	-3.003, -0.695, -1.681	0.331	7, 11	same as C1
C7	-1.984, 0.292, -1.607	-0.238	8, 12	same as C1
C8	-0.661, -0.049, -1.400	-0.132	9, 13	same as C1
C9	-0.248, -1.391, -1.245	0.174	10	same as C1
C10	-1.265, -2.366, -1.309	-0.193	11, 14	same as C1
C11	-2.596, -2.043, -1.512	-0.204	15	same as C1
H12	-2.230, 1.341, -1.718	0.15		same as H3
H13	0.073, 0.750, -1.363	0.104		same as H3
H14	-0.997, -3.413, -1.187	0.114		same as H3
H15	-3.323, -2.845, -1.527	0.152		same as H3
C16	3.568, -1.450, -0.671	0.088	17, 18	same as C1
C17	4.577, -0.520, -0.560	-0.297	19, 24	same as C1
C18	3.903, -2.926, -0.604	0.085	20, 21, 46	same as C1
H19	4.314, 0.536, -0.600	0.122		same as H3
C20	5.228, -3.237, 0.131	0.417	22, 93, 97	same as C1
H21	3.089, -3.476, -0.116	-0.019		same as H3
C22	6.333, -2.310, -0.427	-0.015	23, 24, 45	same as C1
H23	6.532, -2.590, -1.473	-0.022		same as H3
C24	5.956, -0.844, -0.394	0.181	25	same as C1
C25	6.883, 0.174, -0.245	-0.276	26, 27	same as C1
H26	6.503, 1.196, -0.247	0.132		same as H3
C27	8.278, 0.016, -0.086	0.151	28, 29	same as C1
C28	9.144, 1.078, 0.078	-0.374	30, 44	same as C1
H29	8.685, -0.988, -0.102	-0.03		same as H3
C30	10.543, 1.006, 0.250	0.281	31, 32	same as C1
C31	11.402, 2.094, 0.360	-0.305	33, 34	same as C1
C32	11.409, -0.253, 0.350	0.043	35, 36, 37	same as C1
C33	12.754, 1.621, 0.491	0.502	35, 38	same as C1
C34	10.966, 3.442, 0.324	0.403	39	same as C1
O35	12.765, 0.267, 0.444	-0.393		**1.48 Å, 14.59x10^{-3} perg**

C36	11.334, -1.174, -0.867	0.204	141, 142	same as C1
C37	11.198, -0.956, 1.719	0.572	151, 152, 153	same as C1
C38	13.954, 2.284, 0.625	-0.418	40, 41	same as C1
N39	10.513, 4.515, 0.278	-0.432		same as N5
C40	14.040, 3.705, 0.670	0.428	42	same as C1
C41	15.170, 1.544, 0.725	0.489	43	same as C1
N42	14.156, 4.863, 0.711	-0.449		same as N5
N43	16.170, 0.953, 0.805	-0.482		same as N5
H44	8.729, 2.084, 0.068	0.171		same as H3
H45	7.263, -2.490, 0.122	0.036		same as H3
H46	3.958, -3.318, -1.631	-0.024		same as H3
C47	-4.742, 1.039, -2.017	0.093	50, 90, 91	same as C1
C48	-5.344, -1.384, -2.106	0.088	49, 86, 89	same as C1
C49	-5.995, -1.867, -0.803	0.466	52, 87, 88	same as C1
C50	-4.890, 1.747, -0.662	0.433	51, 85, 92	same as C1
O51	-5.306, 3.074, -0.927	-0.525	83	same as O35
O52	-6.862, -2.943, -1.133	-0.509	84	same as O35
C53	-8.469, -5.278, -0.920	0.13	59, 71, 75, 84	same as C1
C54	-4.272, 5.039, 1.019	0.468	55, 63, 67, 83	same as C1
C55	-4.658, 6.326, 1.782	-0.19	56, 57, 58	same as C1
H56	-5.338, 6.134, 2.620	0.028		same as H3
H57	-3.756, 6.796, 2.201	0.028		same as H3
H58	-5.138, 7.060, 1.126	0.007		same as H3
C59	-9.585, -5.984, -0.121	-0.006	60, 61, 62	same as C1
H60	-9.815, -6.958, -0.576	0.016		same as H3
H61	-9.290, -6.170, 0.919	-0.031		same as H3
H62	-10.514, -5.403, -0.113	-0.034		same as H3
C63	-3.267, 5.421, -0.093	-0.181	64, 65, 66	same as C1
H64	-2.938, 4.545, -0.665	0.039		same as H3
H65	-3.697, 6.138, -0.802	0.007		same as H3
H66	-2.375, 5.886, 0.348	0.017		same as H3
C67	-3.582, 4.055, 1.989	-0.311	68, 69, 70	same as C1
H68	-2.708, 4.534, 2.454	0.055		same as H3
H69	-4.243, 3.724, 2.797	0.025		same as H3
H70	-3.219, 3.158, 1.473	0.065		same as H3
C71	-8.956, -5.029, -2.366	-0.058	72, 73, 74	same as C1
H72	-9.846, -4.389, -2.394	-0.028		same as H3
H73	-8.180, -4.554, -2.976	0.006		same as H3
H74	-9.219, -5.984, -2.843	0.017		same as H3
C75	-7.227, -6.194, -0.965	-0.134	76, 77, 78	same as C1
H76	-6.886, -6.467, 0.040	-0.006		same as H3
H77	-7.470, -7.128, -1.492	0.03		same as H3
H78	-6.392, -5.722, -1.496	0.036		same as H3
C79	-7.320, -3.717, 1.623	-0.081	84, 101, 102	same as C1

C80	-9.542, -2.435, -0.158	-0.067	84, 111, 112	same as C1
C81	-6.675, 5.509, -0.937	-0.069	83, 131, 132	same as C1
C82	-7.062, 3.464, 1.344	-0.046	83, 121, 122	same as C1
Si83	-5.808, 4.252, 0.167	0.318		**2.0 Å, 6.95x10^{-3} perg**
Si84	-8.042, -3.589, -0.122	0.384		same as Si83
H85	-5.626, 1.219, -0.041	-0.066		same as H3
H86	-6.121, -0.983, -2.764	0.048		same as H3
H87	-5.226, -2.196, -0.091	-0.12		same as H3
H88	-6.546, -1.041, -0.331	-0.077		same as H3
H89	-4.918, -2.246, -2.629	0.004		same as H3
H90	-4.045, 1.608, -2.643	0.012		same as H3
H91	-5.709, 1.071, -2.528	0.048		same as H3
H92	-3.933, 1.730, -0.124	-0.089		same as H3
C93	5.064, -3.022, 1.649	-0.287	94, 95, 96	same as C1
H94	4.298, -3.695, 2.054	0.064		same as H3
H95	6.003, -3.232, 2.174	0.069		same as H3
H96	4.769, -1.995, 1.889	0.023		same as H3
C97	5.619, -4.702, -0.127	-0.413	98, 99, 100	same as C1
H98	4.843, -5.385, 0.239	0.085		same as H3
H99	5.760, -4.897, -1.197	0.088		same as H3
H100	6.553, -4.955, 0.387	0.085		same as H3
C101	-6.083, -4.366, 1.822	0.01	103, 104	same as C1
C102	-7.938, -3.150, 2.753	-0.039	105, 106	same as C1
C103	-5.503, -4.460, 3.088	-0.156	107, 108	same as C1
H104	-5.557, -4.800, 0.976	0.084		same as H3
C105	-7.364, -3.244, 4.023	-0.126	107, 109	same as C1
H106	-8.875, -2.613, 2.644	0.024		same as H3
C107	-6.147, -3.903, 4.194	-0.053	110	same as C1
H108	-4.549, -4.967, 3.210	0.099		same as H3
H109	-7.866, -2.796, 4.877	0.105		same as H3
H110	-5.698, -3.975, 5.181	0.091		same as H3
C111	-9.585, -1.380, -1.090	-0.016	113, 114	same as C1
C112	-10.666, -2.608, 0.673	-0.032	115, 116	same as C1
C113	-10.689, -0.530, -1.182	-0.101	117, 118	same as C1
H114	-8.746, -1.231, -1.764	0.058		same as H3
C115	-11.773, -1.761, 0.588	-0.137	117, 119	same as C1
H116	-10.688, -3.417, 1.400	0.09		same as H3
C117	-11.787, -0.718, -0.339	-0.034	120	same as C1
H118	-10.696, 0.273, -1.915	0.084		same as H3
H119	-12.627, -1.919, 1.243	0.097		same as H3
H120	-12.649, -0.060, -0.410	0.078		same as H3
C121	-7.137, 3.703, 2.728	-0.092	123, 124	same as C1
C122	-8.017, 2.588, 0.788	-0.057	125, 126	same as C1
C123	-8.116, 3.099, 3.520	-0.098	127, 128	same as C1

H124	-6.427, 4.372, 3.206	0.088		same as H3
C125	-8.993, 1.974, 1.573	-0.058	127, 129	same as C1
H126	-8.000, 2.382, -0.281	0.064		same as H3
C127	-9.044, 2.231, 2.945	-0.095	130	same as C1
H128	-8.150, 3.305, 4.587	0.091		same as H3
H129	-9.711, 1.298, 1.116	0.047		same as H3
H130	-9.804, 1.757, 3.562	0.101		same as H3
C131	-7.650, 6.381, -0.418	-0.052	133, 134	same as C1
C132	-6.356, 5.622, -2.302	-0.031	135, 136	same as C1
C133	-8.273, 7.335, -1.224	-0.101	137, 138	same as C1
H134	-7.939, 6.309, 0.629	0.038		same as H3
C135	-6.978, 6.572, -3.114	-0.12	137, 140	same as C1
H136	-5.621, 4.949, -2.736	0.065		same as H3
C137	-7.936, 7.433, -2.575	-0.073	139	same as C1
H138	-9.024, 7.996, -0.800	0.095		same as H3
H139	-8.421, 8.173, -3.206	0.086		same as H3
H140	-6.717, 6.639, -4.167	0.094		same as H3
C141	11.372, -0.575, -2.135	-0.136	143, 144	same as C1
C142	11.286, -2.572, -0.781	-0.135	145, 146	same as C1
C143	11.357, -1.351, -3.290	-0.087	147, 148	same as C1
H144	11.416, 0.507, -2.219	0.075		same as H3
C145	11.261, -3.347, -1.942	-0.088	147, 149	same as C1
H146	11.275, -3.071, 0.179	0.093		same as H3
C147	11.297, -2.743, -3.198	-0.089	150	same as C1
H148	11.391, -0.867, -4.262	0.111		same as H3
H149	11.224, -4.429, -1.858	0.103		same as H3
H150	11.283, -3.350, -4.098	0.1		same as H3
F151	11.238, -0.059, 2.717	-0.199		**1.42 Å, 4.24x10^{-3} perg**
F152	12.151, -1.872, 1.953	-0.151		same as F151
F153	10.002, -1.585, 1.778	-0.184		same as F151

Table B.28: LoD model parameters for ***JRD1 (2nd enantiomer)***, coloring represents LoD ellipsoid partitioning:
(54,..,58,63,..,70|83|82,121,..,130|81,131,..,140|51|50,85,92|47,90,91|53,59,..,62,71,..,78|84|80,111,..,120|79,101,..,110|52|49,87,88|48,86,89|1,..,24,45,46|97,..,100|93,..,96|25,..,34,35,38,..,44|37,151,..,153|36,141,..,150)

#	Position [Å] Rotation (Axis,θ)	Semi-axes [Å]	LJ energy [perg]	Center Charge [*e*] (Center Dipole[a] [*D*])
1	-8.791, -5.520, -1.677 (-0.406, -0.337, -0.850, 2.236)	3.06x3.05x2.03	0.02588[b]	0.059 (-0.612,-0.500,-0.560)
2	-8.101, -3.577, -0.354 (0.000, 0.000, 0.000, 0.000)	2.00x2.00x2.00	0.00695[b]	0.318 (0.000,0.000,0.000)

3	-6.538, -4.345, 2.595 (0.885, 0.016, -0.465, 1.801)	3.51x3.14x1.75	0.03081[b]	-0.056 (-0.470,-0.224,0.683)
4	-10.758, -1.455, 0.022 (-0.222, 0.624, 0.750, 1.176)	3.51x3.14x1.75	0.03080[b]	-0.068 (-0.347,0.643,-0.852)
5	-6.968, -2.807, -1.331 (0.000, 0.000, 0.000, 0.000)	1.48x1.48x1.48	0.01459[b]	-0.525 (0.000,0.000,0.000)
6	-6.019, -1.738, -0.714 (0.809, -0.384, -0.446, 1.388)	2.11x1.74x1.57	0.00604[b]	0.278 (-0.223,0.291,-0.682)
7	-5.442, -1.307, -2.376 (0.780, -0.366, -0.508, 1.382)	2.10x1.74x1.57	0.00604[b]	0.153 (-0.152,-0.030,-0.016)
8	-3.670, 5.288, 1.371 (0.293, 0.581, 0.759, 2.081)	3.06x3.05x2.03	0.02587[b]	-0.063 (0.277,-0.041,-0.271)
9	-5.707, 4.324, 0.358 (0.000, 0.000, 0.000, 0.000)	2.00x2.00x2.00	0.00695[b]	0.384 (0.000,0.000,0.000)
10	-7.952, 2.871, 2.495 (0.772, -0.104, 0.627, 2.039)	3.51x3.14x1.75	0.03080[b]	0.020 (-0.653,0.340,0.065)
11	-7.317, 6.679, -1.512 (-0.498, -0.384, -0.777, 3.041)	3.51x3.14x1.75	0.03080[b]	-0.041 (0.953,-0.389,0.688)
12	-5.279, 3.159, -0.781 (0.000, 0.000, 0.000, 0.000)	1.48x1.48x1.48	0.01459[b]	-0.509 (0.000,0.000,0.000)
13	-4.857, 1.719, -0.385 (0.053, -0.506, -0.861, 2.888)	2.11x1.74x1.57	0.00604[b]	0.269 (-0.283,-0.219,-0.834)
14	-4.804, 1.268, -2.139 (0.047, -0.483, -0.875, 2.846)	2.10x1.74x1.57	0.00604[b]	0.140 (-0.133,0.125,-0.032)
15	1.271, -1.382, -1.140 (-0.056, 0.009, 0.998, 2.981)	7.32x3.29x1.92	0.08518[b]	0.300 (16.653,-4.781,3.965)
16	5.608, -4.874, -0.278 (-0.475, -0.649, -0.594, 1.901)	2.00x1.99x1.61	0.00692[b]	-0.155 (0.161,-0.589,-0.105)
17	5.056, -2.958, 1.666 (-0.002, -0.096, -0.995, 2.119)	2.00x1.99x1.61	0.00693[b]	-0.132 (0.033,-0.150,0.437)
18	11.678, 1.924, 0.105 (0.084, -0.412, 0.907, 0.326)	6.21x3.49x1.85	0.10587[b]	-0.558 (-3.645,-1.394,-0.291)
19	11.619, -0.988, -1.924 (0.029, -0.191, -0.981, 2.870)	2.32x2.31x1.79	0.01724[b]	0.037 (0.333,0.395,-1.235)
20	10.729, -2.241, 2.069 (0.645, 0.243, 0.724, 2.387)	3.51x3.13x1.75	0.03080[b]	0.150 (0.008,0.057,0.269)

[a]Dipole vectors are given in the lab frame, [b] "simple touch" LJ potential, equation (2-2)

Table B.29: All-atom model parameters for ***C1***, coloring represents LoD ellipsoid partitioning

Atom	Position [Å]	Partial charge [*e*]	Minimum connectivity	LJ radius and energy
C1	-5.026, -9.181, 0.022	0.163	2, 5, 14	**1.65 Å, 4.59x10^{-3} perg**
C2	-6.132, -9.871, 0.495	-0.222	3, 6	same as C1

C3	-5.986, -11.271, 0.189	0.465	4, 8	same as C1
O4	-4.803, -11.472, -0.436	-0.354	5	**1.48 Å, 14.59x10^{-3} perg**
C5	-4.122, -10.207, -0.665	0.063	15, 16	same as C1
C6	-7.198, -9.247, 1.192	0.379	7	same as C1
N7	-8.011, -8.635, 1.758	-0.423		**1.6 Å, 11.81x10^{-3} perg**
C8	-6.796, -12.355, 0.441	-0.416	9, 11	same as C1
C9	-8.049, -12.229, 1.108	0.435	10	same as C1
N10	-9.078, -12.167, 1.650	-0.447		same as N7
C11	-6.390, -13.660, 0.031	0.491	12	same as C1
N12	-6.070, -14.731, -0.296	-0.478		same as N7
C13	-3.687, -7.093, -0.200	-0.048	14, 20, 103	same as C1
C14	-4.814, -7.788, 0.177	-0.269	104	same as C1
C15	-2.714, -10.308, -0.079	0.153	98, 102	same as C1
C16	-4.181, -10.041, -2.209	0.584	17, 18, 19	same as C1
F17	-3.545, -8.918, -2.611	-0.182		**1.42 Å, 4.24x10^{-3} perg**
F18	-5.456, -9.959, -2.619	-0.199		same as F17
F19	-3.612, -11.082, -2.834	-0.162		same as F17
C20	-3.435, -5.703, -0.048	0.025	21, 24	same as C1
C21	-4.212, -4.639, 0.449	-0.073	22, 38	same as C1
C22	-3.540, -3.410, 0.419	-0.196	23, 105	same as C1
C23	-2.246, -3.465, -0.102	0.168	24, 25	same as C1
S24	-1.858, -5.099, -0.555	-0.107		**2.47 Å, 4.24x10^{-3} perg**
C25	-1.279, -2.417, -0.291	-0.196	26, 106	same as C1
C26	-1.509, -1.100, -0.040	-0.178	27, 107	same as C1
C27	-0.587, 0.005, -0.207	0.164	28, 32	same as C1
C28	0.764, -0.140, -0.592	-0.13	29, 108	same as C1
C29	1.602, 0.949, -0.747	-0.234	30, 109	same as C1
C30	1.137, 2.274, -0.535	0.281	31, 33	same as C1
C31	-0.213, 2.424, -0.134	-0.182	32, 110	same as C1
C32	-1.036, 1.320, 0.022	-0.183	111	same as C1
N33	1.952, 3.375, -0.709	-0.33	34, 35	same as N7
C34	3.322, 3.256, -1.188	0.092	36, 112, 113	same as C1
C35	1.459, 4.706, -0.379	0.018	114, 115, 116	same as C1
C36	4.324, 3.040, -0.052	0.337	37, 117, 118	same as C1
O37	5.623, 2.940, -0.665	-0.536	43	same as O4
C38	-5.621, -4.790, 0.967	0.543	39, 119, 120	same as C1
O39	-6.167, -3.528, 1.381	-0.532	40	same as O4
C40	-7.115, -2.967, 0.574	0.739	41, 42	same as C1
O41	-7.489, -3.454, -0.467	-0.519		same as O4
C42	-7.611, -1.669, 1.177	-0.269	58, 121, 122	same as C1
C43	6.673, 2.842, 0.190	0.846	44, 51	same as C1
C44	7.980, 2.731, -0.570	-0.388	45, 123, 124	same as C1
C45	9.204, 2.743, 0.348	0.117	46, 125, 126	same as C1
C46	10.517, 2.602, -0.430	0.116	47, 127, 128	same as C1

C47	11.741, 2.633, 0.488	-0.304	48, 129, 130	same as C1
C48	13.044, 2.475, -0.265	0.78	49, 52	same as C1
O49	14.097, 2.620, 0.607	-0.474	50	same as O4
C50	15.418, 2.501, 0.191	0.411	53, 57	same as C1
O51	6.549, 2.841, 1.394	-0.548		same as O4
O52	13.163, 2.258, -1.445	-0.527		same as O4
C53	16.313, 3.401, 0.774	-0.211	54, 131	same as C1
C54	17.668, 3.314, 0.478	-0.039	55, 132	same as C1
C55	18.132, 2.326, -0.403	-0.132	56, 65	same as C1
C56	17.219, 1.428, -0.975	-0.018	57, 133	same as C1
C57	15.861, 1.505, -0.683	-0.259	134	same as C1
C58	-8.776, -1.054, 0.398	0.083	59, 135, 136	same as C1
C59	-9.243, 0.270, 1.013	0.057	60, 137, 138	same as C1
C60	-10.419, 0.884, 0.251	-0.246	61, 139, 140	same as C1
C61	-10.878, 2.198, 0.844	0.766	62, 63	same as C1
O62	-10.394, 2.758, 1.796	-0.525		same as O4
O63	-11.944, 2.682, 0.121	-0.472	64	same as O4
C64	-12.577, 3.872, 0.458	0.421	79, 83	same as C1
C65	19.562, 2.176, -0.768	0.669	66, 67	same as C1
O66	20.004, 1.344, -1.526	-0.493		same as O4
O67	20.340, 3.111, -0.122	-0.408	68	same as O4
C68	21.712, 3.177, -0.323	0.41	69, 73	same as C1
C69	22.301, 3.100, -1.594	-0.276	70, 141	same as C1
C70	23.674, 3.260, -1.701	-0.096	71, 142	same as C1
C71	24.475, 3.502, -0.570	-0.075	72, 74	same as C1
C72	23.846, 3.580, 0.688	0.364	73, 77	same as C1
C73	22.468, 3.417, 0.819	-0.349	143	same as C1
C74	25.904, 3.679, -0.608	0.022	75, 144	same as C1
C75	26.602, 3.911, 0.527	-0.368	76, 145	same as C1
C76	25.947, 3.993, 1.828	0.765	77, 78	same as C1
O77	24.557, 3.815, 1.827	-0.391		same as O4
O78	26.485, 4.197, 2.889	-0.521		same as O4
C79	-12.897, 4.224, 1.772	-0.263	80, 146	same as C1
C80	-13.600, 5.402, 1.996	-0.01	81, 147	same as C1
C81	-13.986, 6.226, 0.929	-0.133	82, 84	same as C1
C82	-13.663, 5.851, -0.384	-0.028	83, 148	same as C1
C83	-12.958, 4.676, -0.618	-0.239	149	same as C1
C84	-14.729, 7.468, 1.254	0.663	85, 86	same as C1
O85	-15.029, 7.828, 2.370	-0.49		same as O4
O86	-15.047, 8.171, 0.114	-0.406	87	same as O4
C87	-15.726, 9.380, 0.167	0.41	88, 92	same as C1
C88	-15.426, 10.386, 1.099	-0.27	89, 150	same as C1
C89	-16.108, 11.590, 1.019	-0.095	90, 151	same as C1
C90	-17.078, 11.821, 0.027	-0.074	91, 93	same as C1

C91	-17.345, 10.790, -0.896	0.37	92, 96	same as C1
C92	-16.676, 9.569, -0.830	-0.359	152	same as C1
C93	-17.822, 13.046, -0.115	0.014	94, 153	same as C1
C94	-18.736, 13.189, -1.101	-0.36	95, 154	same as C1
C95	-19.008, 12.120, -2.057	0.759	96, 97	same as C1
O96	-18.267, 10.944, -1.887	-0.39		same as O4
O97	-19.800, 12.159, -2.967	-0.519		same as O4
C98	-1.548, -10.323, -0.854	-0.134	99, 155	same as C1
C99	-0.300, -10.449, -0.240	-0.074	100, 156	same as C1
C100	-0.201, -10.571, 1.144	-0.097	101, 157	same as C1
C101	-1.362, -10.567, 1.921	-0.078	102, 158	same as C1
C102	-2.607, -10.434, 1.314	-0.126	159	same as C1
H103	-2.880, -7.657, -0.657	0.116		**1.25 Å, 1.04x10^{-3} perg**
H104	-5.631, -7.270, 0.664	0.144		same as H103
H105	-3.990, -2.495, 0.783	0.13		same as H103
H106	-0.309, -2.727, -0.674	0.177		same as H103
H107	-2.497, -0.816, 0.318	0.132		same as H103
H108	1.176, -1.130, -0.761	0.088		same as H103
H109	2.633, 0.766, -1.022	0.16		same as H103
H110	-0.624, 3.409, 0.049	0.125		same as H103
H111	-2.069, 1.480, 0.326	0.117		same as H103
H112	3.398, 2.442, -1.914	0.02		same as H103
H113	3.584, 4.171, -1.729	0.054		same as H103
H114	2.266, 5.427, -0.511	0.066		same as H103
H115	1.118, 4.767, 0.662	0.029		same as H103
H116	0.626, 5.004, -1.031	0.037		same as H103
H117	4.107, 2.125, 0.509	-0.028		same as H103
H118	4.312, 3.874, 0.656	0		same as H103
H119	-6.275, -5.226, 0.206	-0.025		same as H103
H120	-5.643, -5.426, 1.859	-0.033		same as H103
H121	-6.761, -0.975, 1.226	0.084		same as H103
H122	-7.887, -1.866, 2.221	0.088		same as H103
H123	7.943, 1.808, -1.164	0.108		same as H103
H124	8.021, 3.548, -1.302	0.102		same as H103
H125	9.208, 3.674, 0.929	-0.01		same as H103
H126	9.110, 1.934, 1.083	-0.006		same as H103
H127	10.519, 1.665, -1.001	-0.005		same as H103
H128	10.604, 3.405, -1.173	-0.006		same as H103
H129	11.789, 3.569, 1.060	0.091		same as H103
H130	11.693, 1.834, 1.241	0.09		same as H103
H131	15.933, 4.155, 1.455	0.135		same as H103
H132	18.367, 4.009, 0.927	0.099		same as H103
H133	17.591, 0.666, -1.651	0.1		same as H103
H134	15.160, 0.814, -1.132	0.169		same as H103

H135	-9.606, -1.771, 0.369	0.011	same as H103
H136	-8.472, -0.903, -0.645	-0.003	same as H103
H137	-9.534, 0.118, 2.060	0.006	same as H103
H138	-8.415, 0.990, 1.034	0.004	same as H103
H139	-10.164, 1.061, -0.803	0.08	same as H103
H140	-11.281, 0.204, 0.231	0.08	same as H103
H141	21.694, 2.909, -2.468	0.175	same as H103
H142	24.148, 3.201, -2.677	0.119	same as H103
H143	21.999, 3.481, 1.794	0.184	same as H103
H144	26.412, 3.622, -1.568	0.105	same as H103
H145	27.677, 4.049, 0.536	0.152	same as H103
H146	-12.597, 3.595, 2.599	0.17	same as H103
H147	-13.861, 5.701, 3.006	0.097	same as H103
H148	-13.962, 6.479, -1.215	0.098	same as H103
H149	-12.701, 4.365, -1.625	0.144	same as H103
H150	-14.687, 10.215, 1.870	0.171	same as H103
H151	-15.890, 12.379, 1.734	0.118	same as H103
H152	-16.894, 8.787, -1.548	0.187	same as H103
H153	-17.633, 13.855, 0.587	0.107	same as H103
H154	-19.314, 14.096, -1.238	0.15	same as H103
H155	-1.593, -10.243, -1.932	0.096	same as H103
H156	0.596, -10.458, -0.855	0.102	same as H103
H157	0.772, -10.673, 1.616	0.101	same as H103
H158	-1.299, -10.666, 3.001	0.107	same as H103
H159	-3.503, -10.433, 1.928	0.076	same as H103

Table B.30: LoD model parameters for ***C1***, coloring represents LoD ellipsoid partitioning: **(68,..,78,141,..,145|67,65,66|50,53,..,57,131,..,134|49,48,52|47,129,130|46,127,128|45,125,126|44,123,124|43,51,37|36,117,118|34,112,113|35,114,..,116|33,20,..,32,105,..,111|1,..,14,103,..,104|16,..,19|15,98,..,102,155,..,159|38,119,120|39,40,41|42,121,122|58,135,136|59,137,138|60,139,140|61,62,63|64,79,..,83,146,..,149|84,85,86|87,..,97,150,..,154)**

#	Position [Å] Rotation (Axis,θ)	Semi-axes [Å]	LJ energy [perg]	Center Charge [*e*] (Center Dipole[a] [*D*])
1	24.487, 3.621, 0.361 (0.909, -0.206, 0.362, 1.580)	5.09x3.45x1.69	0.07284[b]	0.221 (-4.717,-1.302,-5.442)
2	20.039, 2.216, -0.812 (0.415, -0.244, 0.876, 1.581)	2.58x1.72x1.59	0.03459[b]	-0.232 (-2.040,0.186,0.483)
3	16.767, 2.412, -0.102 (0.420, -0.236, 0.876, 1.561)	3.63x2.84x1.67	0.03006[b]	0.255 (-2.836,0.022,0.488)
4	13.502, 2.447, -0.385 (0.708, -0.458, 0.538, 1.725)	2.59x1.72x1.59	0.03460[b]	-0.221 (-2.215,0.188,0.872)
5	11.741, 2.667, 0.811 (0.577, 0.607, 0.546, 2.002)	2.01x1.69x1.52	0.00618[b]	-0.123 (0.000,0.085,0.766)

6	10.539, 2.569, -0.751 (0.561, 0.594, 0.576, 1.970)	2.02x1.69x1.52	0.00618[b]	0.106 (-0.014,0.016,0.197)
7	9.182, 2.773, 0.669 (0.566, 0.588, 0.577, 1.971)	2.02x1.69x1.52	0.00618[b]	0.101 (0.013,-0.035,-0.203)
8	7.981, 2.705, -0.893 (0.578, 0.598, 0.555, 2.021)	2.01x1.69x1.52	0.00618[b]	-0.178 (0.001,-0.103,-0.945)
9	6.215, 2.880, 0.327 (-0.384, 0.667, 0.638, 2.306)	2.57x1.72x1.59	0.03458[b]	-0.238 (2.506,-0.207,-0.812)
10	4.268, 3.020, 0.258 (0.603, 0.485, 0.633, 1.970)	2.02x1.68x1.52	0.00617[b]	0.309 (0.112,0.150,-0.534)
11	3.404, 3.281, -1.497 (0.586, 0.458, 0.668, 1.941)	2.01x1.69x1.52	0.00618[b]	0.166 (0.009,0.137,0.038)
12	1.387, 4.918, -0.329 (-0.466, 0.475, 0.747, 2.440)	1.90x1.90x1.55	0.00698[b]	0.151 (0.111,0.137,-0.049)
13	-0.889, -0.788, -0.220 (0.233, 0.214, 0.949, 1.039)	8.21x3.28x1.78	0.07667[b]	-0.242 (-1.571,-1.685,0.466)
14	-6.153, -10.683, 0.400 (0.338, 0.298, 0.893, 1.154)	6.16x3.94x1.77	0.09999[b]	-0.401 (4.167,4.006,-1.623)
15	-4.199, -10.000, -2.565 (0.116, -0.006, 0.993, 1.050)	2.27x2.27x1.66	0.01724[b]	0.041 (0.222,-0.257,1.301)
16	-1.327, -10.457, 0.596 (-0.407, -0.606, -0.684, 2.381)	3.51x3.09x1.66	0.03081[b]	0.127 (0.075,-0.006,-0.097)
17	-5.786, -5.052, 0.999 (-0.542, 0.201, 0.816, 2.735)	2.03x1.67x1.52	0.00617[b]	0.485 (0.467,0.761,-0.124)
18	-6.891, -3.376, 0.483 (0.469, -0.863, 0.189, 1.080)	2.58x1.72x1.59	0.03459[b]	-0.312 (-1.152,2.035,0.397)
19	-7.471, -1.548, 1.444 (0.799, 0.601, 0.040, 1.551)	2.01x1.69x1.52	0.00618[b]	-0.097 (-0.290,0.253,0.586)
20	-8.904, -1.192, 0.136 (0.786, 0.616, 0.049, 1.493)	2.02x1.69x1.52	0.00618[b]	0.091 (0.010,0.022,0.127)
21	-9.112, 0.409, 1.273 (0.782, 0.621, 0.046, 1.501)	2.02x1.69x1.52	0.00618[b]	0.067 (-0.033,-0.034,-0.054)
22	-10.567, 0.761, -0.011 (0.796, 0.605, 0.017, 1.553)	2.01x1.69x1.52	0.00618[b]	-0.086 (-0.295,-0.245,-0.520)
23	-11.105, 2.606, 0.934 (0.495, -0.836, 0.235, 0.949)	2.59x1.72x1.59	0.03460[b]	-0.231 (0.943,-2.055,-0.662)
24	-13.280, 5.040, 0.692 (-0.165, 0.924, 0.346, 1.625)	3.63x2.84x1.67	0.03006[b]	0.257 (1.452,-2.454,-0.274)
25	-14.970, 7.883, 1.244 (-0.176, 0.925, 0.336, 1.620)	2.58x1.72x1.59	0.03459[b]	-0.233 (1.054,-1.752,-0.415)
26	-17.529, 11.463, -0.714 (0.571, -0.741, -0.354, 0.988)	5.09x3.45x1.69	0.07284[b]	0.218 (5.091,-1.857,4.890)

[a]Dipole vectors are given in the lab frame, [b] "simple touch" LJ potential, equation (2-2)

Table B.31: All-atom model parameters for ***CLD-C1***, coloring represents LoD ellipsoid partitioning.

Atom	Position [Å]	Partial charge [*e*]	Minimum connectivity	LJ radius and energy
C1	-2.972, -3.369, -2.706	-0.203	2, 6, 99, 100	**1.65 Å, 4.59x10^{-3} perg**
C2	-2.449, -3.193, -1.317	0.262	3, 19	same as C1
C3	-3.144, -3.717, -0.278	-0.285	4, 9	same as C1
C4	-4.351, -4.499, -0.557	0.233	5, 23	same as C1
C5	-5.181, -4.119, -1.740	-0.357	6, 101, 102	same as C1
C6	-4.497, -3.196, -2.761	0.455	7, 8	same as C1
C7	-4.989, -3.554, -4.164	-0.492	103, 104, 105	same as C1
C8	-4.859, -1.739, -2.469	-0.329	106, 107, 108	same as C1
C9	-2.714, -3.568, 1.145	-0.090	10, 109, 110	same as C1
C10	-3.459, -2.400, 1.790	0.261	39, 111, 112	same as C1
C11	3.062, 0.362, -1.402	0.308	12, 16, 17	same as C1
C12	2.504, -0.430, -0.385	-0.326	13, 113	same as C1
C13	1.314, -1.105, -0.596	-0.082	14, 114	same as C1
C14	0.644, -1.011, -1.821	0.116	15, 18	same as C1
C15	1.196, -0.221, -2.834	-0.174	16, 115	same as C1
C16	2.387, 0.458, -2.629	-0.238	116	same as C1
N17	4.243, 1.152, -1.139	-0.265	20, 22	**1.6 Å, 11.81x10^{-3} perg**
C18	-0.608, -1.716, -2.051	-0.159	19, 117	same as C1
C19	-1.196, -2.481, -1.119	-0.299	118	same as C1
C20	5.151, 0.658, -0.070	-0.140	21, 119, 120	same as C1
C21	6.041, -0.516, -0.509	0.225	69, 121, 122	same as C1
C22	4.997, 1.670, -2.305	-0.213	123, 124, 125	same as C1
C23	-4.682, -5.552, 0.224	-0.308	24, 126	same as C1
C24	-5.793, -6.425, -0.078	0.055	25, 127	same as C1
C25	-6.341, -7.239, 0.841	-0.257	26, 128	same as C1
C26	-7.445, -8.134, 0.622	0.076	27, 30	same as C1
C27	-8.129, -8.492, -0.697	0.150	28, 32, 33	same as C1
O28	-9.166, -9.453, -0.340	-0.310	29	**1.48 Å, 14.59x10^{-3} perg**
C29	-9.150, -9.647, 1.035	0.443	30, 31	same as C1
C30	-8.082, -8.825, 1.615	-0.239	168	same as C1
C31	-10.054, -10.497, 1.587	-0.460	169, 170	same as C1
C32	-7.173, -9.349, -1.657	0.408	171, 172, 173	same as C1
C33	-8.779, -7.308, -1.381	0.146	34, 38	same as C1
C34	-8.109, -6.573, -2.361	-0.200	35, 129	same as C1
C35	-8.721, -5.489, -2.979	-0.074	36, 130	same as C1
C36	-10.017, -5.126, -2.629	-0.123	37, 131	same as C1
C37	-10.689, -5.844, -1.646	-0.090	38, 132	same as C1
C38	-10.074, -6.924, -1.021	-0.167	133	same as C1
O39	-2.960, -2.257, 3.115	-0.449	40	same as O28
C40	-2.975, -1.023, 3.699	0.781	41, 42	same as C1

O41	-2.512, -1.119, 4.815	-0.510		same as O28
C42	-3.491, 0.227, 3.024	-0.578	43, 134, 135	same as C1
C43	-4.972, 0.417, 3.314	0.095	44, 136, 137	same as C1
C44	-5.509, 1.641, 2.590	0.066	45, 138, 139	same as C1
C45	-6.983, 1.851, 2.905	-0.417	46, 140, 141	same as C1
C46	-7.536, 2.994, 2.083	0.726	47, 48	same as C1
O47	-7.851, 2.986, 0.913	-0.501		same as O28
O48	-7.670, 4.149, 2.815	-0.437	49	same as O28
C49	-8.147, 5.296, 2.178	0.385	50, 54	same as C1
C50	-7.229, 6.214, 1.661	-0.198	51, 142	same as C1
C51	-7.697, 7.416, 1.144	-0.097	52, 143	same as C1
C52	-9.067, 7.694, 1.148	-0.166	53, 55	same as C1
C53	-9.975, 6.767, 1.663	-0.052	54, 144	same as C1
C54	-9.520, 5.560, 2.181	-0.233	145	same as C1
C55	-9.530, 8.983, 0.570	0.737	56, 57	same as C1
O56	-9.079, 9.571, -0.389	-0.503		same as O28
O57	-10.590, 9.529, 1.260	-0.457	58	same as O28
C58	-11.142, 10.723, 0.794	0.512	59, 63	same as C1
C59	-10.625, 11.943, 1.261	-0.335	60, 146	same as C1
C60	-11.252, 13.124, 0.906	-0.079	61, 147	same as C1
C61	-12.392, 13.105, 0.091	-0.190	62, 64	same as C1
C62	-12.892, 11.871, -0.363	0.489	63, 67	same as C1
C63	-12.271, 10.660, -0.018	-0.500	148	same as C1
C64	-13.072, 14.322, -0.303	0.072	65, 149	same as C1
C65	-14.162, 14.249, -1.085	-0.444	66, 150	same as C1
C66	-14.649, 12.937, -1.529	0.740	67, 68	same as C1
O67	-14.007, 11.771, -1.161	-0.359		same as O28
O68	-15.601, 12.650, -2.222	-0.513		same as O28
O69	7.019, -0.817, 0.467	-0.417	70	same as O28
C70	8.223, -0.161, 0.439	0.731	71, 72	same as C1
O71	8.884, -0.541, 1.381	-0.499		same as O28
C72	8.593, 0.843, -0.626	-0.464	73, 151, 152	same as C1
C73	10.093, 0.924, -0.844	0.076	74, 153, 154	same as C1
C74	10.425, 1.941, -1.925	0.198	75, 155, 156	same as C1
C75	11.928, 2.047, -2.119	-0.276	76, 157, 158	same as C1
C76	12.303, 3.013, -3.212	0.680	77, 78	same as C1
O77	11.591, 3.672, -3.936	-0.487		same as O28
O78	13.609, 3.291, -3.545	-0.382	79	same as O28
C79	14.625, 2.638, -2.855	0.350	80, 84	same as C1
C80	15.362, 3.368, -1.916	-0.212	81, 159	same as C1
C81	16.455, 2.770, -1.301	-0.091	82, 160	same as C1
C82	16.807, 1.457, -1.621	-0.124	83, 85	same as C1
C83	16.074, 0.741, -2.571	-0.119	84, 161	same as C1
C84	14.977, 1.326, -3.191	-0.199	162	same as C1

C85	17.980, 0.801, -0.985	0.720	86, 87	same as C1
O86	18.775, 0.043, -1.498	-0.496		same as O28
O87	18.111, 1.119, 0.348	-0.459	88	same as O28
C88	19.198, 0.599, 1.053	0.502	89, 93	same as C1
C89	19.036, -0.612, 1.747	-0.335	90, 163	same as C1
C90	20.061, -1.069, 2.556	-0.067	91, 164	same as C1
C91	21.248, -0.334, 2.683	-0.204	92, 94	same as C1
C92	21.385, 0.876, 1.979	0.461	93, 97	same as C1
C93	20.360, 1.359, 1.150	-0.475	165	same as C1
C94	22.341, -0.785, 3.518	0.093	95, 166	same as C1
C95	23.458, -0.041, 3.607	-0.464	96, 167	same as C1
C96	23.552, 1.217, 2.857	0.759	97, 98	same as C1
O97	22.515, 1.654, 2.055	-0.356		same as O28
O98	24.451, 2.028, 2.800	-0.517		same as O28
H99	-2.484, -2.645, -3.398	0.055		**1.25 Å, 1.04x10^{-3} perg**
H100	-2.686, -4.376, -3.071	0.067		same as H99
H101	-5.532, -5.058, -2.232	0.138		same as H99
H102	-6.107, -3.634, -1.362	0.104		same as H99
H103	-6.086, -3.505, -4.224	0.117		same as H99
H104	-4.585, -2.863, -4.916	0.118		same as H99
H105	-4.688, -4.570, -4.455	0.111		same as H99
H106	-5.941, -1.569, -2.552	0.084		same as H99
H107	-4.552, -1.449, -1.455	0.058		same as H99
H108	-4.365, -1.056, -3.173	0.081		same as H99
H109	-2.911, -4.516, 1.697	0.075		same as H99
H110	-1.614, -3.402, 1.198	0.063		same as H99
H111	-3.327, -1.467, 1.198	0.011		same as H99
H112	-4.545, -2.599, 1.860	0.035		same as H99
H113	3.010, -0.515, 0.590	0.186		same as H99
H114	0.874, -1.728, 0.199	0.111		same as H99
H115	0.683, -0.133, -3.799	0.132		same as H99
H116	2.796, 1.080, -3.440	0.155		same as H99
H117	-1.077, -1.600, -3.044	0.140		same as H99
H118	-0.722, -2.594, -0.121	0.173		same as H99
H119	5.771, 1.522, 0.248	0.099		same as H99
H120	4.538, 0.371, 0.813	0.100		same as H99
H121	5.475, -1.462, -0.575	0.057		same as H99
H122	6.502, -0.309, -1.507	0.007		same as H99
H123	5.781, 0.966, -2.641	0.076		same as H99
H124	4.330, 1.882, -3.155	0.115		same as H99
H125	5.484, 2.608, -2.009	0.103		same as H99
H126	-4.078, -5.766, 1.123	0.167		same as H99
H127	-6.162, -6.383, -1.124	0.076		same as H99
H128	-5.946, -7.239, 1.869	0.175		same as H99

H129	-7.073, -6.819, -2.637	0.115		same as H99
H130	-8.173, -4.920, -3.740	0.109		same as H99
H131	-10.504, -4.278, -3.123	0.126		same as H99
H132	-11.708, -5.561, -1.360	0.129		same as H99
H133	-10.628, -7.469, -0.247	0.136		same as H99
H134	-2.910, 1.101, 3.379	0.164		same as H99
H135	-3.313, 0.162, 1.926	0.154		same as H99
H136	-5.536, -0.486, 3.003	0.013		same as H99
H137	-5.136, 0.515, 4.406	0.048		same as H99
H138	-4.927, 2.539, 2.880	0.046		same as H99
H139	-5.364, 1.528, 1.496	0.022		same as H99
H140	-7.565, 0.936, 2.672	0.125		same as H99
H141	-7.123, 2.032, 3.990	0.130		same as H99
H142	-6.155, 5.993, 1.661	0.147		same as H99
H143	-6.991, 8.143, 0.725	0.137		same as H99
H144	-11.050, 6.983, 1.662	0.129		same as H99
H145	-10.230, 4.829, 2.584	0.162		same as H99
H146	-9.733, 11.958, 1.897	0.182		same as H99
H147	-10.860, 14.084, 1.260	0.140		same as H99
H148	-12.667, 9.704, -0.381	0.228		same as H99
H149	-12.673, 15.279, 0.052	0.117		same as H99
H150	-14.719, 15.131, -1.418	0.191		same as H99
H151	8.072, 0.582, -1.577	0.143		same as H99
H152	8.187, 1.831, -0.324	0.154		same as H99
H153	10.600, 1.193, 0.105	0.014		same as H99
H154	10.491, -0.072, -1.121	0.021		same as H99
H155	9.936, 1.659, -2.879	-0.034		same as H99
H156	10.007, 2.933, -1.660	-0.025		same as H99
H157	12.419, 2.366, -1.176	0.072		same as H99
H158	12.360, 1.053, -2.364	0.060		same as H99
H159	15.089, 4.403, -1.678	0.152		same as H99
H160	17.039, 3.337, -0.565	0.140		same as H99
H161	16.370, -0.282, -2.835	0.141		same as H99
H162	14.407, 0.770, -3.944	0.152		same as H99
H163	18.109, -1.187, 1.647	0.183		same as H99
H164	19.952, -2.013, 3.103	0.139		same as H99
H165	20.479, 2.302, 0.602	0.226		same as H99
H166	22.227, -1.730, 4.061	0.114		same as H99
H167	24.319, -0.327, 4.219	0.196		same as H99
C168	-7.767, -8.767, 2.990	0.402	176	same as C1
C169	-10.118, -10.763, 2.982	0.450	174	same as C1
C170	-11.015, -11.191, 0.798	0.488	175	same as C1
F171	-6.882, -10.569, -1.158	-0.130		**1.42 Å, 4.24x10^{-3} perg**
F172	-7.713, -9.584, -2.868	-0.137		same as F171

F173	-5.966, -8.801, -1.911	-0.151	same as F171
N174	-10.207, -11.007, 4.112	-0.426	same as N17
N175	-11.802, -11.758, 0.164	-0.451	same as N17
N176	-7.485, -8.695, 4.113	-0.407	same as N17

Table B.32: LoD model parameters for ***CLD-C1***, coloring represents LoD ellipsoid partitioning: **(88,..,98,163,..,167|79,..,87,159,..,162|76,..,78|75,157,158|74,155,156|73,153,154|72,151,152|69,..,71|21,121,122|20,119,120,22,123,124,125|1,..,6,11,..,19,23,..,31,99,..,102,113,..,118,126,..,128,168,..,170,174,..,176|7,103,..,105,8,106,..,108|9,109,110|10,111,112|32,171,..,173|33,..,38,129,..,133|39,..,41|42,134,135|43,136,137|44,138,139|45,140,141|46,..,48|49,..,57,142,..,145|58,..,68,146,..,150)**

#	Position [Å] Rotation (Axis,θ)	Semi-axes [Å]	LJ energy [perg]	Center Charge [*e*] (Center Dipole[a] [*D*])
1	21.705, 0.426, 2.428 (0.190, -0.277, -0.942, 3.013)	4.61x3.56x1.80	0.07294[b]	0.256 (-6.405,-3.400,-1.091)
2	16.679, 1.531, -1.667 (0.611, -0.710, -0.349, 0.861)	3.98x3.38x1.85	0.06555[b]	-0.046 (-6.554,3.591,-4.170)
3	12.535, 3.379, -3.625 (-0.043, 0.408, 0.912, 2.924)	2.41x1.88x1.73	0.03437[b]	-0.188 (-0.521,-1.720,1.929)
4	12.153, 1.882, -1.949 (0.560, -0.031, -0.828, 2.099)	2.13x1.72x1.59	0.00620[b]	-0.144 (0.451,-0.289,0.374)
5	10.203, 2.114, -2.093 (0.566, -0.027, -0.824, 2.129)	2.13x1.72x1.59	0.00620[b]	0.139 (0.278,-0.188,0.237)
6	10.314, 0.747, -0.680 (0.559, -0.024, -0.829, 2.146)	2.13x1.72x1.59	0.00620[b]	0.110 (-0.043,0.014,-0.050)
7	8.366, 1.020, -0.784 (0.557, -0.009, -0.831, 2.148)	2.13x1.72x1.59	0.00620[b]	-0.167 (-0.840,0.695,-0.557)
8	8.011, -0.566, 0.818 (-0.226, 0.408, 0.884, 3.103)	2.41x1.87x1.73	0.03438[b]	-0.184 (0.635,1.864,-1.978)
9	6.015, -0.696, -0.768 (0.674, 0.684, 0.280, 1.359)	2.15x1.71x1.58	0.00619[b]	0.289 (-0.104,-0.002,0.310)
10	5.132, 1.330, -1.275 (-0.183, -0.859, -0.479, 1.597)	3.38x1.94x1.80	0.01342[b]	0.141 (0.113,0.543,0.066)
11	-4.361, -5.295, -0.196 (0.119, -0.608, -0.785, 2.434)	11.96x3.54x1.97	0.19473[b]	-0.130 (3.457,7.886,-10.197)
12	-4.990, -2.561, -3.402 (0.525, -0.107, 0.844, 1.883)	3.40x1.98x1.86	0.01441[b]	-0.251 (-0.449,0.569,-0.584)
13	-2.493, -3.759, 1.293 (-0.049, -0.293, -0.955, 2.393)	2.14x1.72x1.59	0.00620[b]	0.049 (0.210,-0.248,0.181)
14	-3.692, -2.221, 1.663 (-0.101, -0.290, -0.952, 2.342)	2.14x1.71x1.58	0.00620[b]	0.306 (0.167,-0.250,0.169)
15	-6.936, -9.573, -1.896 (-0.372, 0.257, 0.892, 2.853)	2.31x2.30x1.81	0.01724[b]	-0.010 (-0.691,0.512,0.655)

16	-9.461, -6.096, -2.065 (-0.255, -0.296, -0.920, 2.813)	3.52x3.13x1.75	0.03080[b]	0.108 (-0.518,0.127,0.190)
17	-2.788, -1.542, 3.907 (0.583, -0.101, -0.806, 2.536)	2.41x1.87x1.73	0.03439[b]	-0.179 (-1.006,2.452,-1.297)
18	-3.306, 0.424, 2.843 (0.721, -0.018, 0.693, 2.228)	2.13x1.72x1.58	0.00620[b]	-0.260 (0.819,0.887,-0.758)
19	-5.149, 0.220, 3.504 (0.719, 0.009, 0.695, 2.216)	2.13x1.72x1.59	0.00620[b]	0.157 (0.060,0.112,0.088)
20	-5.332, 1.833, 2.394 (0.725, 0.012, 0.689, 2.199)	2.13x1.72x1.58	0.00620[b]	0.135 (0.030,0.064,0.075)
21	-7.159, 1.672, 3.113 (0.718, 0.035, 0.695, 2.155)	2.13x1.72x1.58	0.00620[b]	-0.162 (-0.574,-0.576,0.699)
22	-7.712, 3.442, 1.912 (0.638, -0.076, -0.766, 2.517)	2.47x1.83x1.72	0.03463[b]	-0.211 (0.862,-1.949,1.107)
23	-9.031, 7.565, 1.223 (-0.087, 0.264, 0.961, 1.937)	3.98x3.38x1.84	0.06553[b]	-0.010 (3.075,-7.867,3.081)
24	-12.988, 12.577, -0.375 (0.247, -0.842, -0.480, 0.712)	4.60x3.55x1.79	0.07294[b]	0.252 (6.019,-0.577,4.212)

[a]Dipole vectors are given in the lab frame, [b] "simple touch" LJ potential, equation (2-2)

Table B.33: All-atom model parameters for ***PSLD41***, last column gives LoD ellipsoid number

Atom	Position [Å]	Partial charge [*e*]	Minimum connectivity	LJ radius and energy	#
C1	-12.326,-2.472,2.820	0.268	2, 76, 212, 348	**1.65 Å, 4.59x10^{-3} perg**	1
C2	-13.857,-2.472,2.820	-0.03	3, 4, 5	same as C1	2
H3	-14.256,-1.461,2.674	0.01		**1.25 Å, 1.04x10^{-3} perg**	2
H4	-14.256,-2.850,3.769	0.01		same as H3	2
H5	-14.256,-3.104,2.018	0.01		same as H3	2
F6	-19.251,8.407,14.312	-0.199	9	**1.42 Å, 4.24x10^{-3} perg**	7
F7	-20.300,10.256,13.875	-0.159	9	same as F6	7
F8	-18.131,10.254,14.053	-0.18	9	same as F6	7
C9	-19.194,9.547,13.606	0.582	21	same as C1	7
H10	-3.899,13.357,14.682	0.028	15	same as H3	4
C11	-5.405,16.021,13.581	0.026	13, 62, 63, 64	same as C1	3
H12	-19.160,11.999,12.703	0.099	26	same as H3	8
N13	-5.247,14.575,13.586	-0.218	15, 16	**1.6 Å, 11.81x10^{-3} perg**	5
C14	-7.632,14.296,13.161	-0.215	16, 17, 18	same as C1	5
C15	-3.929,13.995,13.788	0.084	117, 49	same as C1	4
C16	-6.336,13.758,13.382	0.264	20	same as C1	5
C17	-8.724,13.473,12.959	-0.122	22, 25	same as C1	5
H18	-7.780,15.369,13.143	0.131		same as H3	5
S19	-13.752,11.232,12.530	-0.096	29, 33	**2.47 Å, 4.24x10^{-3} perg**	5
C20	-6.214,12.346,13.382	-0.228	24, 34	same as C1	5
C21	-19.077,9.237,12.089	0.021	32, 35, 45	same as C1	6

C22	-8.611,12.066,12.964	0.125	24, 28	same as C1	5
C23	-11.032,11.484,12.597	-0.164	27, 28, 29	same as C1	5
C24	-7.320,11.539,13.179	-0.129	38	same as C1	5
H25	-9.690,13.940,12.788	0.092		same as H3	5
C26	-19.078,11.783,11.646	-0.137	45, 48	same as C1	8
H27	-11.307,12.535,12.650	0.163		same as H3	5
C28	-9.720,11.155,12.762	-0.175	43	same as C1	5
C29	-12.133,10.585,12.382	0.08	39	same as C1	5
H30	-16.482,10.456,12.307	0.117	31	same as H3	6
C31	-15.908,9.553,12.127	-0.056	33, 37	same as C1	6
O32	-20.306,8.516,11.799	-0.341	42	**1.48 Å, $14.59x10^{-3}$ perg**	6
C33	-14.492,9.686,12.159	0.081	40	same as C1	5
H34	-5.250,11.879,13.543	0.135		same as H3	5
C35	-17.981,8.199,11.830	0.172	37, 46	same as C1	6
N36	-23.536,7.240,11.386	-0.476	41	same as N13	6
C37	-16.578,8.379,11.883	-0.254	50	same as C1	6
H38	-7.186,10.460,13.186	0.108		same as H3	5
C39	-12.187,9.219,12.048	-0.143	40, 92	same as C1	5
C40	-13.499,8.735,11.934	-0.123	61	same as C1	5
C41	-22.439,6.854,11.342	0.482	47	same as C1	6
C42	-20.045,7.217,11.522	0.467	46, 47	same as C1	6
H43	-9.438,10.106,12.773	0.121		same as H3	5
H44	-19.091,13.865,11.120	0.105	48	same as H3	8
C45	-19.015,10.464,11.181	0.168	55	same as C1	8
C46	-18.620,7.008,11.517	-0.236	51	same as C1	6
C47	-21.099,6.366,11.282	-0.408	52	same as C1	6
C48	-19.040,12.848,10.743	-0.084	56	same as C1	8
H49	-3.613,13.392,12.926	0.029		same as H3	4
H50	-15.999,7.478,11.693	0.154		same as H3	6
C51	-17.929,5.804,11.224	0.384	53	same as C1	6
C52	-20.911,4.988,10.970	0.435	54	same as C1	6
N53	-17.270,4.872,10.996	-0.424		same as N13	6
N54	-20.800,3.858,10.712	-0.449		same as N13	6
C55	-18.925,10.233,9.800	-0.125	57, 58	same as C1	8
C56	-18.950,12.611,9.373	-0.092	57, 59	same as C1	8
C57	-18.895,11.297,8.903	-0.083	60	same as C1	8
H58	-18.883,9.215,9.423	0.077		same as H3	8
H59	-18.925,13.442,8.674	0.1		same as H3	8
H60	-18.829,11.098,7.837	0.111		same as H3	8
H61	-13.713,7.708,11.667	0.14		same as H3	5
H62	-4.437,16.487,13.772	0.062		same as H3	3
H63	-6.101,16.355,14.361	0.022		same as H3	3
H64	-5.773,16.389,12.613	0.021		same as H3	3
H65	-9.237,-0.376,8.181	-0.016	69	same as H3	16

H66	-8.559,1.995,8.553	0.046	68	same as H3	15
H67	-9.143,1.214,10.021	0.019	68	same as H3	15
C68	-9.460,1.602,9.043	-0.142	69, 84	same as C1	15
C69	-9.984,0.430,8.223	0.308	72, 77	same as C1	16
H70	-10.822,-1.764,7.195	0.114	71	same as H3	18
C71	-11.010,-1.326,6.222	-0.261	73, 75	same as C1	18
O72	-10.259,0.904,6.906	-0.422	73	same as O32	17
C73	-10.756,0.029,5.980	0.397	78	same as C1	18
H74	-9.050,4.329,9.505	0.012	80	same as H3	13
C75	-11.518,-2.124,5.192	-0.043	76, 82	same as C1	18
C76	-11.773,-1.592,3.930	-0.154	81	same as C1	18
H77	-10.900,0.019,8.673	-0.019		same as H3	16
C78	-11.010,0.571,4.711	-0.264	81, 85	same as C1	18
H79	-9.564,3.581,11.003	0.007	80	same as H3	13
C80	-9.925,3.916,10.022	0.004	84, 90	same as C1	13
C81	-11.515,-0.236,3.698	-0.034	86	same as C1	18
H82	-11.714,-3.175,5.389	0.09		same as H3	18
O83	-9.256,6.426,11.246	-0.545	89	same as O32	11
C84	-10.485,2.727,9.232	0.165	87, 88	same as C1	14
H85	-10.805,1.625,4.548	0.134		same as H3	18
H86	-11.709,0.196,2.719	0.089		same as H3	18
H87	-10.829,3.065,8.247	-0.016		same as H3	14
H88	-11.371,2.326,9.747	-0.028		same as H3	14
C89	-10.410,6.242,10.927	0.801	90, 93	same as C1	11
C90	-10.962,5.024,10.217	-0.277	91, 94	same as C1	12
H91	-11.362,5.360,9.250	0.084		same as H3	12
C92	-10.974,8.365,11.804	0.601	93, 95, 96	same as C1	9
O93	-11.395,7.150,11.162	-0.573		same as O32	10
H94	-11.832,4.663,10.781	0.092		same as H3	12
H95	-10.247,8.878,11.163	-0.059		same as H3	9
H96	-10.455,8.110,12.736	-0.053		same as H3	9
F97	2.499,22.192,21.958	-0.104	99	same as F6	19
F98	1.516,20.182,20.432	-0.125	101	same as F6	19
C99	1.531,22.439,21.070	0.07	101, 102	same as C1	19
F100	1.513,24.720,21.682	-0.097	102	same as F6	19
C101	1.012,21.415,20.281	0.22	103	same as C1	19
C102	1.026,23.730,20.931	0.131	105	same as C1	19
C103	0.010,21.645,19.338	-0.333	106, 107	same as C1	19
H104	0.209,19.763,18.332	-0.03	106	same as H3	20
C105	0.020,23.991,20.003	0.07	107, 108	same as C1	19
C106	-0.559,20.524,18.512	0.512	109, 112	same as C1	20
C107	-0.480,22.947,19.228	0.22	115	same as C1	19
F108	-0.461,25.231,19.870	-0.104		same as F6	19
H109	-0.908,20.907,17.547	-0.03		same as H3	20

H110	-1.209,18.717,16.804	0.097	113	same as H3	22
O111	-1.512,17.138,14.933	-0.497	116	same as O32	26
O112	-1.651,19.956,19.240	-0.381	114	same as O32	21
C113	-2.017,18.357,17.428	-0.228	114, 118	same as C1	22
C114	-2.322,18.910,18.668	0.327	120	same as C1	22
F115	-1.447,23.224,18.342	-0.125		same as F6	19
C116	-2.423,16.722,15.622	0.673	118, 119	same as C1	26
C117	-2.915,15.113,13.976	0.054	119, 140, 141	same as C1	28
C118	-2.789,17.281,16.958	-0.069	122	same as C1	22
O119	-3.218,15.694,15.253	-0.321		same as O32	27
C120	-3.383,18.404,19.438	-0.336	121, 123	same as C1	22
H121	-3.578,18.870,20.396	0.135		same as H3	22
C122	-3.843,16.767,17.706	-0.234	123, 125	same as C1	22
C123	-4.137,17.337,18.955	0.35	127	same as C1	22
H124	-4.693,17.214,21.591	-0.043	128	same as H3	24
H125	-4.439,15.938,17.346	0.113		same as H3	22
F126	-5.285,14.943,22.474	-0.126	130	same as F6	25
O127	-5.187,16.769,19.622	-0.382	128	same as O32	23
C128	-5.539,17.301,20.900	0.54	129, 131	same as C1	24
H129	-5.811,18.359,20.808	-0.043		same as H3	24
C130	-6.525,15.348,22.165	0.239	131, 133	same as C1	25
C131	-6.709,16.513,21.419	-0.355	134	same as C1	25
F132	-7.393,13.485,23.348	-0.1	133	same as F6	25
C133	-7.599,14.591,22.626	0.041	136	same as C1	25
C134	-8.022,16.885,21.125	0.238	135, 137	same as C1	25
F135	-8.256,17.994,20.408	-0.125		same as F6	25
C136	-8.898,14.992,22.321	0.175	137, 138	same as C1	25
C137	-9.115,16.147,21.572	0.035	139	same as C1	25
F138	-9.936,14.274,22.755	-0.106		same as F6	25
F139	-10.362,16.533,21.285	-0.097		same as F6	25
H140	-1.897,14.715,13.966	0.069		same as H3	28
H141	-3.012,15.858,13.182	0.069		same as H3	28
F142	-4.375,12.038,-2.139	-0.199	145	same as F6	33
F143	-5.209,14.042,-2.122	-0.159	145	same as F6	33
F144	-5.540,12.743,-3.835	-0.18	145	same as F6	33
C145	-5.442,12.773,-2.487	0.582	157	same as C1	33
H146	-9.344,6.540,-16.471	0.028	151	same as H3	30
C147	-10.972,9.348,-16.262	0.026	149, 198, 199, 200	same as C1	29
H148	-7.164,14.506,-3.415	0.099	162	same as H3	34
N149	-10.473,8.132,-15.638	-0.218	151, 152	same as N13	31
C150	-10.212,9.307,-13.518	-0.215	152, 153, 154	same as C1	31
C151	-10.377,6.910,-16.419	0.084	253, 185	same as C1	30
C152	-10.110,8.133,-14.311	0.264	156	same as C1	31

C153	-9.844,9.306,-12.185	-0.122	158, 161	same as C1	31
H154	-10.588,10.226,-13.951	0.131		same as H3	31
S155	-8.268,10.576,-7.048	-0.096	165, 169	same as S19	31
C156	-9.620,6.965,-13.676	-0.228	160, 170	same as C1	31
C157	-6.724,12.217,-1.809	0.021	168, 171, 181	same as C1	32
C158	-9.350,8.147,-11.548	0.125	160, 164	same as C1	31
C159	-8.917,9.118,-9.266	-0.164	163, 164, 165	same as C1	31
C160	-9.256,6.984,-12.340	-0.129	174	same as C1	31
H161	-9.950,10.230,-11.625	0.092		same as H3	31
C162	-8.057,14.119,-2.942	-0.137	181, 184	same as C1	34
H163	-9.192,10.109,-9.620	0.163		same as H3	31
C164	-8.946,8.087,-10.157	-0.175	179	same as C1	31
C165	-8.531,9.061,-7.882	0.08	175	same as C1	31
H166	-7.564,11.609,-4.491	0.117	167	same as H3	32
C167	-7.526,10.530,-4.388	-0.056	169, 173	same as C1	32
O168	-6.442,12.364,-0.389	-0.341	178	same as O32	32
C169	-7.867,9.772,-5.542	0.081	176	same as C1	31
H170	-9.523,6.039,-14.230	0.135		same as H3	31
C171	-6.826,10.701,-2.001	0.172	173, 182	same as C1	32
N172	-5.613,13.286,2.881	-0.476	177	same as N13	32
C173	-7.163,9.990,-3.177	-0.254	186	same as C1	32
H174	-8.884,6.067,-11.888	0.108		same as H3	31
C175	-8.320,7.982,-7.003	-0.143	176, 228	same as C1	31
C176	-7.947,8.391,-5.715	-0.123	197	same as C1	31
C177	-5.760,12.308,2.266	0.482	183	same as C1	32
C178	-6.275,11.154,0.193	0.467	182, 183	same as C1	32
H179	-8.616,7.104,-9.834	0.121		same as H3	31
H180	-9.293,15.655,-3.795	0.105	184	same as H3	34
C181	-8.008,12.983,-2.124	0.168	191	same as C1	34
C182	-6.527,10.119,-0.777	-0.236	187	same as C1	32
C183	-5.940,11.101,1.527	-0.408	188	same as C1	32
C184	-9.271,14.775,-3.158	-0.084	192	same as C1	34
H185	-11.005,6.110,-16.003	0.029		same as H3	30
H186	-7.136,8.908,-3.075	0.154		same as H3	32
C187	-6.506,8.717,-0.563	0.384	189	same as C1	32
C188	-5.759,9.868,2.218	0.435	190	same as C1	32
N189	-6.520,7.555,-0.490	-0.424		same as N13	32
N190	-5.603,8.884,2.820	-0.449		same as N13	32
C191	-9.189,12.528,-1.521	-0.125	193, 194	same as C1	34
C192	-10.441,14.316,-2.556	-0.092	193, 195	same as C1	34
C193	-10.395,13.189,-1.732	-0.083	196	same as C1	34
H194	-9.165,11.654,-0.877	0.077		same as H3	34
H195	-11.381,14.833,-2.724	0.1		same as H3	34

H196	-11.299,12.824,-1.253	0.111		same as H3	34
H197	-7.762,7.684,-4.916	0.14		same as H3	31
H198	-11.190,9.148,-17.311	0.062		same as H3	29
H199	-10.232,10.159,-16.219	0.022		same as H3	29
H200	-11.896,9.703,-15.785	0.021		same as H3	29
H201	-8.960,-1.876,-2.747	-0.016	205	same as H3	42
H202	-9.648,-0.394,-4.631	0.046	204	same as H3	41
H203	-7.905,-0.406,-4.374	0.019	204	same as H3	41
C204	-8.857,-0.069,-3.942	-0.142	205, 220	same as C1	41
C205	-9.048,-0.789,-2.613	0.308	208, 213	same as C1	42
H206	-8.981,-2.141,-0.436	0.114	207	same as H3	44
C207	-9.976,-1.842,-0.129	-0.261	209, 211	same as C1	44
O208	-10.347,-0.465,-2.121	-0.422	209	same as O32	43
C209	-10.750,-0.987,-0.924	0.397	214	same as C1	44
H210	-9.534,1.867,-5.843	0.012	216	same as H3	39
C211	-10.498,-2.316,1.080	-0.043	212, 218	same as C1	44
C212	-11.773,-1.950,1.503	-0.155	217	same as C1	44
H213	-8.284,-0.474,-1.887	-0.019		same as H3	42
C214	-12.035,-0.616,-0.502	-0.264	217, 221	same as C1	44
H215	-7.791,1.843,-5.667	0.007	216	same as H3	39
C216	-8.717,2.165,-5.174	0.004	220, 226	same as C1	39
C217	-12.539,-1.095,0.702	-0.034	222	same as C1	44
H218	-9.890,-2.978,1.691	0.09		same as H3	44
O219	-8.685,3.897,-7.464	-0.545	225	same as O32	37
C220	-8.866,1.460,-3.820	0.165	223, 224	same as C1	40
H221	-12.615,0.048,-1.135	0.134		same as H3	44
H222	-13.535,-0.799,1.018	0.089		same as H3	44
H223	-9.801,1.773,-3.340	-0.016		same as H3	40
H224	-8.053,1.774,-3.149	-0.028		same as H3	40
C225	-8.643,4.408,-6.367	0.801	226, 229	same as C1	37
C226	-8.712,3.689,-5.037	-0.277	227, 230	same as C1	38
H227	-9.616,4.039,-4.520	0.084		same as H3	38
C228	-8.503,6.539,-7.385	0.601	229, 231, 232	same as C1	35
O229	-8.540,5.752,-6.183	-0.573		same as O32	36
H230	-7.873,4.032,-4.418	0.092		same as H3	38
H231	-9.434,6.389,-7.944	-0.059		same as H3	35
H232	-7.686,6.174,-8.020	-0.053		same as H3	35
F233	-7.473,10.647,-28.783	-0.104	235	same as F6	45
F234	-7.889,9.445,-26.392	-0.125	237	same as F6	45
C235	-8.147,11.286,-27.821	0.07	237, 238	same as C1	45
F236	-8.428,13.163,-29.227	-0.097	238	same as F6	45
C237	-8.364,10.684,-26.585	0.22	239	same as C1	45
C238	-8.632,12.573,-28.048	0.131	241	same as C1	45

C239	-9.073,11.322,-25.566	-0.333	242, 243	same as C1	45
H240	-9.334,9.580,-24.345	-0.03	242	same as H3	46
C241	-9.337,13.240,-27.048	0.07	243, 244	same as C1	45
C242	-9.277,10.668,-24.227	0.512	245, 248	same as C1	46
C243	-9.539,12.612,-25.822	0.22	251	same as C1	45
F244	-9.804,14.473,-27.269	-0.104		same as F6	45
H245	-10.209,11.022,-23.774	-0.03		same as H3	46
H246	-10.007,9.391,-22.120	0.097	249	same as H3	48
O247	-11.047,8.050,-20.329	-0.497	252	same as O32	52
O248	-8.165,11.015,-23.398	-0.381	250	same as O32	47
C249	-9.129,9.707,-21.572	-0.228	250, 254	same as C1	48
C250	-8.145,10.522,-22.122	0.327	256	same as C1	48
F251	-10.222,13.275,-24.877	-0.125		same as F6	45
C252	-10.066,8.397,-19.699	0.673	254, 255	same as C1	52
C253	-10.848,7.185,-17.838	0.054	255, 276, 277	same as C1	54
C254	-8.983,9.270,-20.244	-0.069	258	same as C1	48
O255	-9.841,8.027,-18.420	-0.321		same as O32	53
C256	-7.023,10.904,-21.365	-0.336	257, 259	same as C1	48
H257	-6.287,11.539,-21.840	0.135		same as H3	48
C258	-7.881,9.637,-19.480	-0.234	259, 261	same as C1	48
C259	-6.897,10.460,-20.050	0.35	263	same as C1	48
H260	-4.348,11.132,-20.620	-0.043	264	same as H3	50
H261	-7.766,9.302,-18.457	0.113		same as H3	48
F262	-2.583,9.878,-19.354	-0.126	266	same as F6	51
O263	-5.849,10.771,-19.229	-0.382	264	same as O32	49
C264	-4.812,11.605,-19.748	0.54	265, 267	same as C1	50
H265	-5.222,12.576,-20.049	-0.043		same as H3	50
C266	-2.729,10.901,-18.499	0.239	267, 269	same as C1	51
C267	-3.789,11.795,-18.662	-0.355	270	same as C1	51
F268	-0.781,10.180,-17.355	-0.1	269	same as F6	51
C269	-1.793,11.046,-17.480	0.041	272	same as C1	51
C270	-3.894,12.838,-17.740	0.238	271, 273	same as C1	51
F271	-4.894,13.724,-17.847	-0.125		same as F6	51
C272	-1.921,12.102,-16.580	0.175	273, 274	same as C1	51
C273	-2.972,13.007,-16.711	0.035	275	same as C1	51
F274	-1.031,12.252,-15.597	-0.106		same as F6	51
F275	-3.091,14.023,-15.850	-0.097		same as F6	51
H276	-10.941,6.253,-18.402	0.069		same as H3	54
H277	-11.816,7.693,-17.831	0.069		same as H3	54
F278	-11.188,-13.236,16.281	-0.199	281	same as F6	59
F279	-10.048,-	-0.159	281	same as F6	59

	12.918,18.100				
F280	-9.087,-13.792,16.355	-0.18	281	same as F6	59
C281	-9.989,-12.871,16.761	0.582	293	same as C1	59
H282	-0.089,-19.751,6.550	0.028	287	same as H3	56
C283	1.731,-18.863,9.095	0.026	285, 334, 335, 336	same as C1	55
H284	-7.681,-12.620,17.959	0.099	298	same as H3	60
N285	0.650,-18.586,8.163	-0.218	287, 288	same as N13	57
C286	-0.546,-17.350,9.891	-0.215	288, 289, 290	same as C1	57
C287	0.738,-19.070,6.794	0.084	389, 321	same as C1	56
C288	-0.443,-17.854,8.567	0.264	292	same as C1	57
C289	-1.647,-16.617,10.295	-0.122	294, 297	same as C1	57
H290	0.247,-17.533,10.606	0.131		same as H3	57
S291	-5.663,-14.058,13.089	-0.096	301, 305	same as S19	57
C292	-1.512,-17.569,7.681	-0.228	296, 306	same as C1	57
C293	-9.619,-11.448,16.261	0.021	304, 307, 317	same as C1	58
C294	-2.718,-16.334,9.419	0.125	296, 300	same as C1	57
C295	-4.196,-15.070,11.018	-0.164	299, 300, 301	same as C1	57
C296	-2.606,-16.833,8.105	-0.129	310	same as C1	57
H297	-1.670,-16.251,11.317	0.092		same as H3	57
C298	-7.423,-11.628,17.611	-0.137	317, 320	same as C1	60
H299	-3.507,-15.271,11.835	0.163		same as H3	57
C300	-3.897,-15.576,9.788	-0.175	315	same as C1	57
C301	-5.357,-14.305,11.384	0.08	311	same as C1	57
H302	-7.495,-12.780,14.853	0.117	303	same as H3	58
C303	-7.877,-12.595,13.855	-0.056	305, 309	same as C1	58
O304	-10.670,-10.613,16.821	-0.341	314	same as O32	58
C305	-7.111,-13.119,12.777	0.081	312	same as C1	57
H306	-1.487,-17.924,6.659	0.135		same as H3	57
C307	-9.831,-11.331,14.749	0.172	309, 318	same as C1	58
N308	-13.068,-8.881,18.686	-0.476	313	same as N13	58
C309	-9.042,-11.881,13.711	-0.254	322	same as C1	58
H310	-3.407,-16.635,7.396	0.108		same as H3	57
C311	-6.349,-13.666,10.617	-0.143	312, 364	same as C1	57
C312	-7.315,-13.020,11.402	-0.123	333	same as C1	57
C313	-12.839,-9.112,17.568	0.482	319	same as C1	58
C314	-11.481,-10.145,15.842	0.467	318, 319	same as C1	58
H315	-4.605,-15.436,8.976	0.121		same as H3	57
H316	-5.571,-11.622,18.700	0.105	320	same as H3	60
C317	-8.273,-10.919,16.755	0.168	327	same as C1	60
C318	-10.969,-10.560,14.561	-0.236	323	same as C1	58

C319	-12.571,-9.383,16.193	-0.408	324	same as C1	58
C320	-6.220,-11.059,18.035	-0.084	328	same as C1	60
H321	0.725,-18.245,6.069	0.029		same as H3	56
H322	-9.416,-11.689,12.708	0.154		same as H3	58
C323	-11.494,-10.241,13.282	0.384	325	same as C1	58
C324	-13.466,-8.842,15.225	0.435	326	same as C1	58
N325	-11.841,-10.033,12.190	-0.424		same as N13	58
N326	-14.220,-8.381,14.467	-0.449		same as N13	58
C327	-7.903,-9.630,16.343	-0.125	329, 330	same as C1	60
C328	-5.858,-9.779,17.621	-0.092	329, 331	same as C1	60
C329	-6.707,-9.063,16.773	-0.083	332	same as C1	60
H330	-8.556,-9.064,15.685	0.077		same as H3	60
H331	-4.924,-9.339,17.957	0.1		same as H3	60
H332	-6.439,-8.063,16.447	0.111		same as H3	60
H333	-8.138,-12.468,10.965	0.14		same as H3	57
H334	2.492,-19.462,8.593	0.062		same as H3	55
H335	1.379,-19.426,9.969	0.022		same as H3	55
H336	2.209,-17.940,9.453	0.021		same as H3	55
H337	-11.175,-8.879,2.280	-0.016	341	same as H3	68
H338	-9.098,-9.989,3.102	0.046	340	same as H3	67
H339	-10.543,-10.962,3.369	0.019	340	same as H3	67
C340	-10.021,-10.051,3.694	-0.142	341, 356	same as C1	67
C341	-10.902,-8.858,3.345	0.308	344, 349	same as C1	68
H342	-12.670,-7.136,2.652	0.114	343	same as H3	70
C343	-12.048,-6.284,2.902	-0.261	345, 347	same as C1	70
O344	-10.166,-7.671,3.632	-0.422	345	same as O32	69
C345	-10.756,-6.458,3.410	0.397	350	same as C1	70
H346	-7.821,-11.238,4.947	0.012	352	same as H3	65
C347	-12.545,-4.989,2.715	-0.043	348, 354	same as C1	70
C348	-11.773,-3.873,3.027	-0.155	353	same as C1	70
H349	-11.831,-8.875,3.933	-0.019		same as H3	68
C350	-9.974,-5.337,3.726	-0.264	353, 357	same as C1	70
H351	-9.217,-12.269,5.179	0.007	352	same as H3	65
C352	-8.758,-11.329,5.510	0.004	356, 362	same as C1	65
C353	-10.482,-4.057,3.535	-0.034	358	same as C1	70
H354	-13.550,-4.863,2.321	0.09		same as H3	70
O355	-6.891,-13.248,6.547	-0.545	361	same as O32	63
C356	-9.680,-10.148,5.186	0.165	359, 360	same as C1	66
H357	-8.975,-5.497,4.120	0.134		same as H3	70
H358	-9.867,-3.197,3.785	0.089		same as H3	70
H359	-9.208,-9.211,5.505	-0.016		same as H3	66
H360	-10.611,-10.236,5.765	-0.028		same as H3	66

C361	-7.466,-12.535,7.338	0.801	362, 365	same as C1	63
C362	-8.437,-11.423,7.003	-0.277	363, 366	same as C1	64
H363	-8.000,-10.484,7.370	0.084		same as H3	64
C364	-6.364,-13.643,9.114	0.601	365, 367, 368	same as C1	61
O365	-7.296,-12.637,8.684	-0.573		same as O32	62
H366	-9.347,-11.571,7.599	0.092		same as H3	64
H367	-5.372,-13.413,8.708	-0.059		same as H3	61
H368	-6.667,-14.609,8.690	-0.053		same as H3	61
F369	7.305,-30.550,7.363	-0.104	371	same as F6	71
F370	5.799,-28.368,6.812	-0.125	373	same as F6	71
C371	7.373,-29.474,8.153	0.07	373, 374	same as C1	71
F372	8.961,-30.552,9.531	-0.097	374	same as F6	71
C373	6.602,-28.347,7.886	0.22	375	same as C1	71
C374	8.217,-29.477,9.262	0.131	377	same as C1	71
C375	6.660,-27.205,8.687	-0.333	378, 379	same as C1	71
H376	5.623,-25.918,7.323	-0.03	378	same as H3	72
C377	8.292,-28.356,10.086	0.07	379, 380	same as C1	71
C378	5.801,-26.004,8.400	0.512	381, 384	same as C1	72
C379	7.509,-27.242,9.794	0.22	387	same as C1	71
F380	9.105,-28.359,11.147	-0.104		same as F6	71
H381	6.299,-25.094,8.750	-0.03		same as H3	72
H382	4.682,-23.811,7.664	0.097	385	same as H3	74
O383	3.970,-21.635,6.744	-0.497	388	same as O32	78
O384	4.560,-26.181,9.090	-0.381	386	same as O32	73
C385	3.781,-24.034,8.219	-0.228	386, 390	same as C1	74
C386	3.619,-25.196,8.967	0.327	392	same as C1	74
F387	7.601,-26.175,10.601	-0.125		same as F6	71
C388	2.951,-21.871,7.363	0.673	390, 391	same as C1	78
C389	2.041,-19.832,6.616	0.054	391, 412, 413	same as C1	80
C390	2.729,-23.102,8.180	-0.069	394	same as C1	74
O391	1.889,-21.036,7.384	-0.321		same as O32	79
C392	2.426,-25.436,9.672	-0.336	393, 395	same as C1	74
H393	2.351,-26.356,10.238	0.135		same as H3	74
C394	1.542,-23.322,8.870	-0.234	395, 397	same as C1	74
C395	1.396,-24.500,9.619	0.35	399	same as C1	74
H396	0.057,-26.704,10.413	-0.043	400	same as H3	76
H397	0.730,-22.607,8.841	0.113		same as H3	74
F398	-2.365,-26.796,9.770	-0.126	402	same as F6	77
O399	0.197,-24.635,10.265	-0.382	400	same as O32	75
C400	-0.018,-25.812,11.045	0.54	401, 403	same as C1	76
H401	0.733,-25.880,11.841	-0.043		same as H3	76
C402	-2.514,-26.198,10.961	0.239	403, 405	same as C1	77
C403	-1.394,-25.721,11.643	-0.355	406	same as C1	77
F404	-4.852,-26.568,10.817	-0.1	405	same as F6	77

C405	-3.799,-26.092,11.488	0.041	408	same as C1	77
C406	-1.610,-25.105,12.877	0.238	407, 409	same as C1	77
F407	-0.570,-24.625,13.574	-0.125		same as F6	77
C408	-3.981,-25.478,12.725	0.175	409, 410	same as C1	77
C409	-2.883,-24.985,13.428	0.035	411	same as C1	77
F410	-5.206,-25.368,13.241	-0.106		same as F6	77
F411	-3.059,-24.400,14.617	-0.097		same as F6	77
H412	2.209,-20.068,5.562	0.069		same as H3	80
H413	2.885,-19.244,6.987	0.069		same as H3	80

Table B.34: LoD model parameters for ***PSLD41***

#	Position [Å] Rotation (Axis,θ)	Semi-axes [Å]	LJ energy [perg]	Center Charge [*e*] (Center Dipole[a] [*D*])
1	0.765, 0.000, 0.000 (1.000, 0.000, 0.000, 0.000)	1.65x1.65x1.65	0.00459[b]	0.268 (0.000,0.000,0.000)
2	-0.941, 0.000, -0.005 (0.341, 0.876, 0.341, 1.701)	1.99x1.99x1.61	0.00693[b]	0.000 (-0.057,-0.001,-0.002)
3	7.671, 18.686, 10.762 (-0.641, 0.517, 0.568, 2.057)	2.00x1.99x1.61	0.00696[b]	0.131 (0.188,0.089,0.038)
4	9.239, 16.192, 10.975 (-0.644, -0.097, -0.759, 2.951)	1.69x1.47x1.41	0.00604[b]	0.141 (-0.003,0.017,-0.008)
5	3.176, 14.195, 9.966 (-0.260, 0.966, 0.013, 2.988)	7.21x3.39x1.95	0.07730[b]	-0.174 (-2.223,-1.585,-0.400)
6	-6.350, 9.472, 8.645 (-0.259, 0.960, 0.108, 3.057)	5.47x3.59x1.87	0.09997[b]	-0.413 (4.039,4.193,1.196)
7	-6.126, 12.087, 11.131 (-0.212, 0.972, -0.100, 3.102)	2.32x2.31x1.79	0.01724[b]	0.044 (-0.013,-0.075,-1.339)
8	-5.891, 14.093, 7.386 (-0.316, -0.895, 0.314, 1.752)	3.51x3.13x1.75	0.03080[b]	0.137 (-0.016,0.004,0.110)
9	2.363, 10.888, 9.040 (-0.586, 0.329, 0.741, 1.922)	2.12x1.73x1.58	0.00611[b]	0.489 (-0.915,-0.201,-0.189)
10	1.697, 9.622, 8.342 (-0.367, 0.903, 0.225, 3.013)	1.48x1.48x1.48	0.01459[b]	-0.573 (0.000,0.000,0.000)
11	3.358, 8.821, 8.293 (-0.065, 0.994, -0.089, 2.861)	2.07x1.71x1.71	0.01879[b]	0.256 (-3.851,-0.614,-1.065)
12	1.880, 7.490, 7.318 (-0.619, 0.377, 0.689, 1.760)	2.11x1.73x1.58	0.00611[b]	-0.100 (-0.668,-0.026,-0.178)
13	3.410, 6.404, 7.292 (-0.638, 0.333, 0.694, 1.765)	2.11x1.73x1.58	0.00611[b]	0.023 (0.037,0.012,-0.008)
14	2.364, 5.185, 6.321 (-0.644, 0.337, 0.687, 1.752)	2.12x1.73x1.58	0.00611[b]	0.121 (0.286,0.035,0.062)
15	3.872, 4.075, 6.317 (-0.639, 0.336, 0.692, 1.703)	2.12x1.73x1.58	0.00611[b]	-0.078 (0.316,0.053,0.015)

16	3.075, 2.661, 5.484 (-0.092, -0.985, 0.149, 2.829)	2.13x1.72x1.58	0.00610[b]	0.273 (0.072,0.415,-0.145)
17	2.833, 3.375, 4.086 (-0.367, 0.903, 0.225, 3.013)	1.48x1.48x1.48	0.01459[b]	-0.422 (0.000,0.000,0.000)
18	1.828, 1.692, 2.137 (0.253, -0.778, -0.575, 1.641)	2.40x1.97x1.45	0.02960[b]	0.069 (0.956,1.697,1.793)
19	13.692, 25.329, 17.445 (0.304, 0.925, 0.228, 2.483)	3.83x3.39x1.89	0.04849[b]	-0.178 (0.458,0.961,0.750)
20	12.611, 22.926, 15.480 (0.126, 0.757, 0.641, 2.282)	2.12x1.72x1.58	0.00608[b]	0.452 (-0.228,0.206,0.625)
21	11.440, 22.428, 16.420 (-0.243, 0.491, -0.837, 2.612)	1.48x1.48x1.48	0.01459[b]	-0.381 (0.000,0.000,0.000)
22	10.011, 20.314, 15.370 (0.062, 0.689, -0.722, 1.740)	3.18x3.17x1.79	0.02908[b]	0.154 (-0.690,0.795,2.142)
23	7.905, 19.241, 16.801 (-0.243, 0.491, -0.837, 2.612)	1.48x1.48x1.48	0.01459[b]	-0.382 (0.000,0.000,0.000)
24	7.659, 19.953, 18.191 (0.346, -0.658, -0.669, 0.956)	2.12x1.72x1.58	0.00608[b]	0.454 (-0.351,-0.591,-0.366)
25	5.110, 18.100, 19.123 (-0.147, 0.274, 0.951, 2.296)	3.83x3.39x1.89	0.04849[b]	-0.181 (-1.076,-0.759,0.426)
26	11.182, 19.428, 12.414 (-0.935, -0.158, 0.318, 2.991)	2.07x1.71x1.71	0.01889[b]	0.176 (-2.611,-1.192,1.975)
27	9.874, 18.166, 12.433 (-0.243, 0.491, -0.837, 2.612)	1.48x1.48x1.48	0.01459[b]	-0.321 (0.000,0.000,0.000)
28	10.380, 17.661, 10.978 (-0.054, 0.468, 0.882, 2.254)	1.69x1.47x1.41	0.00604[b]	0.193 (0.119,0.045,-0.104)
29	2.054, 11.980, -19.170 (0.030, -0.868, -0.495, 2.770)	2.00x1.99x1.61	0.00696[b]	0.131 (-0.041,-0.040,-0.204)
30	2.804, 9.123, -19.159 (-0.113, -0.164, -0.980, 2.854)	1.69x1.47x1.41	0.00604[b]	0.141 (-0.013,0.014,-0.003)
31	4.004, 11.123, -13.131 (0.070, -0.983, 0.170, 1.335)	7.21x3.39x1.95	0.07730[b]	-0.174 (0.726,0.068,2.661)
32	6.708, 13.079, -2.950 (-0.068, -0.994, 0.081, 1.321)	5.47x3.59x1.87	0.09997[b]	-0.413 (-1.376,0.969,-5.700)
33	7.941, 15.368, -5.462 (0.151, -0.926, 0.347, 1.216)	2.32x2.31x1.79	0.01724[b]	0.044 (-1.178,-0.265,0.584)
34	3.773, 16.175, -5.175 (-0.397, 0.412, 0.820, 1.194)	3.51x3.13x1.75	0.03080[b]	0.137 (0.102,0.031,-0.034)
35	4.566, 8.909, -10.440 (0.064, 0.835, 0.547, 3.111)	2.12x1.73x1.58	0.00611[b]	0.489 (0.112,0.374,0.873)
36	4.551, 8.224, -9.003 (-0.093, -0.981, -0.171, 1.436)	1.48x1.48x1.48	0.01459[b]	-0.573 (0.000,0.000,0.000)
37	4.424, 6.580, -9.830 (0.050, -0.884, 0.466, 1.539)	2.07x1.71x1.71	0.01879[b]	0.256 (0.139,1.709,3.661)

38	4.368, 6.296, -7.634 (-0.012, 0.872, 0.490, 3.089)	2.11x1.73x1.58	0.00611[b]	-0.100 (0.001,0.359,0.591)
39	4.395, 4.515, -8.223 (-0.020, 0.857, 0.516, 3.049)	2.11x1.73x1.58	0.00611[b]	0.023 (-0.020,-0.015,-0.030)
40	4.203, 4.055, -6.414 (-0.028, 0.859, 0.511, 3.048)	2.12x1.73x1.58	0.00611[b]	0.121 (-0.022,-0.138,-0.260)
41	4.265, 2.272, -6.983 (-0.033, 0.867, 0.497, 3.012)	2.12x1.73x1.58	0.00611[b]	-0.078 (-0.078,-0.150,-0.273)
42	4.212, 1.530, -5.316 (-0.168, -0.608, 0.776, 1.200)	2.13x1.72x1.58	0.00610[b]	0.273 (-0.300,0.254,-0.210)
43	2.745, 2.007, -4.941 (-0.093, -0.981, -0.171, 1.436)	1.48x1.48x1.48	0.01459[b]	-0.422 (0.000,0.000,0.000)
44	1.831, 1.004, -2.533 (0.072, 0.526, 0.847, 2.600)	2.40x1.97x1.45	0.02960[b]	0.068 (0.780,1.020,-2.320)
45	4.276, 14.521, -29.829 (-0.346, -0.820, 0.456, 2.341)	3.83x3.39x1.89	0.04849[b]	-0.178 (0.219,0.585,-1.142)
46	3.631, 13.004, -26.985 (-0.470, -0.882, 0.042, 2.723)	2.12x1.72x1.58	0.00608[b]	0.452 (0.540,0.400,-0.183)
47	4.927, 13.486, -26.218 (0.848, -0.248, 0.468, 2.333)	1.48x1.48x1.48	0.01459[b]	-0.381 (0.000,0.000,0.000)
48	5.080, 12.554, -23.626 (0.549, -0.606, 0.576, 2.920)	3.18x3.17x1.79	0.02908[b]	0.154 (1.796,1.385,-0.743)
49	7.242, 13.243, -22.049 (0.848, -0.248, 0.468, 2.333)	1.48x1.48x1.48	0.01459[b]	-0.382 (0.000,0.000,0.000)
50	8.290, 14.169, -22.785 (-0.680, 0.596, -0.427, 1.518)	2.12x1.72x1.58	0.00608[b]	0.454 (-0.033,-0.303,0.717)
51	10.388, 14.445, -20.272 (0.501, 0.743, 0.444, 2.975)	3.83x3.39x1.89	0.04849[b]	-0.181 (0.907,0.139,1.036)
52	2.474, 10.673, -22.874 (0.297, -0.181, -0.938, 2.950)	2.07x1.71x1.71	0.01889[b]	0.176 (2.811,0.994,1.803)
53	3.251, 10.499, -21.240 (0.848, -0.248, 0.468, 2.333)	1.48x1.48x1.48	0.01459[b]	-0.321 (0.000,0.000,0.000)
54	2.009, 9.563, -20.781 (0.488, 0.039, -0.872, 1.231)	1.69x1.47x1.41	0.00604[b]	0.193 (-0.137,-0.054,-0.072)
55	14.970, -16.432, 6.396 (0.495, 0.524, 0.694, 1.304)	2.00x1.99x1.61	0.00696[b]	0.131 (0.147,-0.117,-0.098)
56	13.644, -16.567, 3.760 (0.132, -0.501, -0.855, 2.076)	1.69x1.47x1.41	0.00604[b]	0.141 (0.015,0.005,0.011)
57	9.547, -13.193, 7.448 (0.356, 0.699, 0.620, 3.079)	7.21x3.39x1.95	0.07730[b]	-0.174 (-2.172,1.461,0.873)
58	1.745, -7.769, 12.400 (0.352, 0.632, 0.691, 3.029)	5.47x3.59x1.87	0.09997[b]	-0.413 (4.820,-3.387,-0.784)
59	3.017, -10.724, 14.051 (-0.333, -0.744, -0.579, 2.967)	2.32x2.31x1.79	0.01724[b]	0.044 (0.431,1.248,-0.235)

60	6.119, -7.831, 14.404 (-0.042, -0.506, -0.861, 1.371)	3.51x3.13x1.75	0.03080[b]	0.137 (-0.045,-0.097,0.032)
61	6.864, -11.316, 6.130 (0.655, 0.245, 0.714, 1.007)	2.12x1.73x1.58	0.00611[b]	0.489 (-0.525,0.520,0.607)
62	5.796, -10.166, 5.864 (0.302, 0.591, 0.748, 2.732)	1.48x1.48x1.48	0.01459[b]	-0.573 (0.000,0.000,0.000)
63	5.963, -10.481, 4.054 (-0.504, -0.698, -0.509, 2.931)	2.07x1.71x1.71	0.01879[b]	0.256 (-1.922,2.380,2.642)
64	4.560, -8.797, 4.372 (0.722, 0.385, 0.574, 1.023)	2.11x1.73x1.58	0.00611[b]	-0.100 (-0.272,0.388,0.504)
65	4.429, -9.024, 2.514 (0.718, 0.378, 0.585, 0.950)	2.11x1.73x1.58	0.00611[b]	0.023 (0.030,-0.007,-0.025)
66	3.320, -7.510, 2.542 (0.721, 0.394, 0.571, 0.951)	2.12x1.73x1.58	0.00611[b]	0.121 (0.141,-0.159,-0.205)
67	3.151, -7.746, 0.693 (0.754, 0.390, 0.529, 0.950)	2.12x1.73x1.58	0.00611[b]	-0.078 (0.187,-0.130,-0.227)
68	1.952, -6.395, 0.430 (-0.428, -0.648, -0.629, 2.314)	2.13x1.72x1.58	0.00610[b]	0.273 (0.419,0.014,0.150)
69	2.926, -5.199, 0.812 (0.302, 0.591, 0.748, 2.732)	1.48x1.48x1.48	0.01459[b]	-0.422 (0.000,0.000,0.000)
70	1.828, -2.696, 0.399 (0.187, -0.034, -0.982, 2.751)	2.40x1.97x1.45	0.02960[b]	0.068 (1.145,-2.350,0.437)
71	20.656, -26.055, 6.202 (-0.830, -0.308, -0.465, 3.042)	3.83x3.39x1.89	0.04849[b]	-0.178 (0.707,-1.058,0.276)
72	18.952, -23.348, 5.445 (0.808, 0.073, 0.584, 2.483)	2.12x1.72x1.58	0.00608[b]	0.452 (-0.175,-0.544,0.397)
73	17.652, -23.709, 6.270 (-0.099, -0.959, 0.267, 2.792)	1.48x1.48x1.48	0.01459[b]	-0.381 (0.000,0.000,0.000)
74	15.675, -21.792, 6.100 (-0.576, -0.754, 0.315, 3.120)	3.18x3.17x1.79	0.02908[b]	0.154 (-0.485,-1.917,1.337)
75	13.289, -22.163, 7.445 (-0.099, -0.959, 0.267, 2.792)	1.48x1.48x1.48	0.01459[b]	-0.382 (0.000,0.000,0.000)
76	13.227, -23.518, 8.255 (0.472, 0.110, -0.875, 2.455)	2.12x1.72x1.58	0.00608[b]	0.454 (-0.503,0.586,-0.099)
77	10.194, -23.108, 9.452 (0.636, -0.347, 0.689, 1.613)	3.83x3.39x1.89	0.04849[b]	-0.181 (-1.274,0.138,0.522)
78	16.616, -19.267, 4.195 (-0.877, 0.284, 0.387, 1.269)	2.07x1.71x1.71	0.01889[b]	0.176 (-2.921,-0.676,1.775)
79	14.981, -18.564, 4.564 (-0.099, -0.959, 0.267, 2.792)	1.48x1.48x1.48	0.01459[b]	-0.321 (0.000,0.000,0.000)
80	15.356, -17.283, 3.646 (0.727, -0.174, 0.664, 1.894)	1.69x1.47x1.41	0.00604[b]	0.193 (0.131,0.046,-0.088)

[a]Dipole vectors are given in the lab frame, [b] "simple touch" LJ potential, equation (2-2)

B.4 CHAPTER 6 MODELS

Table B.35: All-atom model parameters for ***TCP-1***, coloring represents LoD ellipsoid partitioning

Atom	Position [Å]	Partial charge [*e*]	Minimum connectivity	LJ radius and energy
C1	0.180, -0.803, -0.077	-0.109	2, 3, 7	**1.65 Å, 4.59x10^{-3} perg**
C2	-0.858, 0.093, 0.012	-0.185	29, 43	same as C1
H3	-0.080, -1.853, -0.178	0.125		**1.25 Å, 1.04x10^{-3} perg**
C4	4.412, -0.027, -0.007	0.379	5, 9, 14	same as C1
C5	3.880, -1.340, -0.135	-0.245	6, 10	same as C1
C6	2.517, -1.556, -0.155	-0.141	7, 11	same as C1
C7	1.581, -0.500, -0.050	0.131	8	same as C1
C8	2.114, 0.806, 0.076	-0.104	9, 12	same as C1
C9	3.472, 1.041, 0.096	-0.257	13	same as C1
H10	4.541, -2.195, -0.198	0.154		same as H3
H11	2.149, -2.575, -0.248	0.12		same as H3
H12	1.445, 1.658, 0.152	0.106		same as H3
H13	3.816, 2.064, 0.172	0.159		same as H3
N14	5.764, 0.204, 0.014	-0.412	15, 16	**1.6 Å, 11.81x10^{-3} perg**
C15	6.737, -0.865, -0.223	0.214	17, 18, 19	same as C1
C16	6.322, 1.536, 0.266	0.234	20, 21, 22	same as C1
H17	6.341, -1.550, -0.980	-0.008		same as H3
C18	7.137, -1.629, 1.044	-0.165	23, 24, 25	same as C1
H19	7.622, -0.402, -0.671	0.027		same as H3
H20	5.701, 2.055, 1.001	-0.012		same as H3
C21	6.490, 2.385, -1.000	-0.173	26, 27, 28	same as C1
H22	7.296, 1.391, 0.746	0.022		same as H3
H23	6.274, -2.118, 1.506	0.037		same as H3
H24	7.578, -0.955, 1.786	0.053		same as H3
H25	7.879, -2.399, 0.803	0.047		same as H3
H26	6.932, 3.356, -0.750	0.048		same as H3
H27	5.528, 2.561, -1.492	0.039		same as H3
H28	7.149, 1.889, -1.721	0.053		same as H3
C29	-2.226, -0.266, -0.020	0.021	30, 31	same as C1
C30	-2.770, -1.667, -0.151	0.668	32, 33	same as C1
C31	-3.325, 0.584, 0.061	-0.227	34, 35	same as C1
N32	-4.155, -1.519, -0.135	-0.644	34, 36	same as N14
O33	-2.184, -2.727, -0.251	-0.482		**1.48 Å, 14.59x10^{-3} perg**
C34	-4.543, -0.200, -0.011	0.4	37	same as C1
C35	-3.227, 1.991, 0.193	0.39	38	same as C1
H36	-4.794, -2.301, -0.206	0.401		same as H3

C37	-5.870, 0.182, 0.026	-0.369	39, 40	same as C1
N38	-3.043, 3.136, 0.300	-0.435		same as N14
C39	-6.872, -0.828, -0.068	0.454	41	same as C1
C40	-6.296, 1.535, 0.153	0.442	42	same as C1
N41	-7.640, -1.701, -0.149	-0.466		same as N14
N42	-6.696, 2.623, 0.255	-0.44		same as N14
H43	-0.656, 1.157, 0.115	0.149		same as H3

Table B.36: LoD model parameters for ***TCP-1***, coloring represents LoD ellipsoid partitioning: **(1,3,..,28|2,29,..,43)**

#	**Position** [Å] **Rotation (Axis,θ)**	**Semi-axes** [Å]	**LJ energy [perg]**	**Center Charge** [e] **(Center Dipole**[a] [D])
1	4.673, -0.009, -0.009 (0.018,-0.102,-0.995, 2.907)	5.07x3.78x2.20	0.07158[b]	0.321 (0.360,-0.429,-0.050)
2	-4.243, 0.005, 0.008 (0.835,-0.018, 0.550, 0.112)	4.73x4.01x1.89	0.10890[b]	-0.321 (1.785,-2.486,-0.229)

[a]Dipole vectors are given in the lab frame, [b] "simple touch" LJ potential, equation (2-2)

Table B.37: All-atom model parameters for ***TCP-Me***, coloring represents LoD ellipsoid partitioning

Atom	**Position** [Å]	**Partial charge** [e]	**Minimum connectivity**	**LJ radius and energy**
C1	0.240, -0.713, -0.144	-0.149	2, 3, 7	**1.65 Å, 4.59x10^{-3} perg**
C2	-0.819, 0.164, -0.003	-0.173	16, 33	same as C1
H3	-0.031, -1.746, -0.337	0.125		**1.25 Å, 1.04x10^{-3} perg**
C4	4.523, -0.241, -0.008	0.368	5, 9, 14	same as C1
C5	3.887, -1.405, -0.525	-0.252	6, 10	same as C1
C6	2.512, -1.515, -0.540	-0.131	7, 11	same as C1
C7	1.657, -0.485, -0.073	0.135	8	same as C1
C8	2.296, 0.661, 0.466	-0.077	9, 12	same as C1
C9	3.670, 0.782, 0.498	-0.277	13	same as C1
H10	4.476, -2.237, -0.889	0.155		same as H3
H11	2.066, -2.426, -0.931	0.12		same as H3
H12	1.709, 1.458, 0.905	0.088		same as H3
H13	4.092, 1.684, 0.921	0.166		same as H3
N14	5.887, -0.116, 0.017	-0.379	17, 18	**1.6 Å, 11.81x10^{-3} perg**
C15	-0.194, 2.461, -1.031	-0.313	16, 32, 47, 48	same as C1
C16	-0.592, 1.661, 0.191	0.774	31	same as C1
C17	6.769, -1.117, -0.591	0.213	19, 20, 21	same as C1
C18	6.553, 1.020, 0.663	0.186	22, 23, 24	same as C1

H19	6.304, -1.499, -1.504	-0.009		same as H3
C20	7.139, -2.267, 0.353	-0.171	25, 26, 27	same as C1
H21	7.676, -0.594, -0.912	0.027		same as H3
H22	6.001, 1.296, 1.567	0.002		same as H3
C23	6.732, 2.233, -0.257	-0.18	28, 29, 30	same as C1
H24	7.531, 0.666, 1.006	0.035		same as H3
H25	6.251, -2.818, 0.677	0.041		same as H3
H26	7.647, -1.892, 1.249	0.052		same as H3
H27	7.815, -2.968, -0.150	0.05		same as H3
H28	7.252, 3.038, 0.275	0.054		same as H3
H29	5.767, 2.617, -0.602	0.045		same as H3
H30	7.326, 1.972, -1.140	0.057		same as H3
O31	-0.741, 2.160, 1.289	-0.522		**1.48 Å, 14.59x10^{-3} perg**
H32	0.096, 3.471, -0.733	0.096		same as H3
C33	-2.166, -0.317, 0.002	-0.042	34, 35	same as C1
C34	-2.542, -1.785, 0.082	0.689	36, 37	same as C1
C35	-3.367, 0.388, -0.037	-0.187	38, 39	same as C1
N36	-3.931, -1.808, 0.088	-0.64	38, 40	same as N14
O37	-1.840, -2.776, 0.136	-0.479		same as O31
C38	-4.480, -0.547, 0.026	0.373	41	same as C1
C39	-3.523, 1.787, -0.203	0.379	42	same as C1
H40	-4.464, -2.666, 0.155	0.398		same as H3
C41	-5.844, -0.337, 0.025	-0.34	43, 44	same as C1
N42	-3.610, 2.935, -0.381	-0.417		same as N14
C43	-6.701, -1.477, 0.082	0.453	45	same as C1
C44	-6.460, 0.946, -0.021	0.425	46	same as C1
N45	-7.343, -2.448, 0.129	-0.462		same as N14
N46	-7.026, 1.963, -0.055	-0.427		same as N14
H47	0.617, 1.972, -1.580	0.04		same as H3
H48	-1.056, 2.529, -1.706	0.08		same as H3

Table B.38: All-atom model parameters for ***TCP-Me (2nd rotamer)***, coloring represents LoD ellipsoid partitioning

Atom	Position [Å]	Partial charge [*e*]	Minimum connectivity	LJ radius and energy
C1	0.237, -0.729, 0.037	-0.159	2, 3, 7	**1.65 Å, 4.59x10^{-3} perg**
C2	-0.819, 0.162, 0.012	-0.174	16, 33	same as C1
H3	-0.037, -1.778, 0.096	0.128		**1.25 Å, 1.04x10^{-3} perg**
C4	4.520, -0.248, -0.036	0.4	5, 9, 14	same as C1
C5	3.883, -1.467, 0.326	-0.258	6, 10	same as C1
C6	2.509, -1.579, 0.323	-0.145	7, 11	same as C1
C7	1.654, -0.497, -0.008	0.147	8	same as C1
C8	2.295, 0.709, -0.394	-0.078	9, 12	same as C1

C9	3.668, 0.831, -0.410	-0.289	13	same as C1
H10	4.471, -2.327, 0.623	0.158		same as H3
H11	2.061, -2.529, 0.605	0.124		same as H3
H12	1.708, 1.551, -0.740	0.087		same as H3
H13	4.093, 1.766, -0.753	0.17		same as H3
N14	5.884, -0.120, -0.041	-0.407	17, 18	**1.6 Å, 11.81x10^{-3} perg**
C15	-0.173, 2.307, 1.320	-0.319	16, 32, 47, 48	same as C1
C16	-0.588, 1.670, 0.010	0.793	31	same as C1
C17	6.772, -1.257, 0.220	0.196	19, 20, 21	same as C1
C18	6.545, 1.164, -0.296	0.216	22, 23, 24	same as C1
H19	6.341, -2.160, -0.224	0		same as H3
C20	7.075, -1.473, 1.707	-0.181	25, 26, 27	same as C1
H21	7.703, -1.071, -0.325	0.034		same as H3
H22	5.949, 1.969, 0.142	-0.005		same as H3
C23	6.817, 1.433, -1.781	-0.195	28, 29, 30	same as C1
H24	7.491, 1.154, 0.257	0.029		same as H3
H25	6.162, -1.680, 2.274	0.042		same as H3
H26	7.548, -0.587, 2.144	0.058		same as H3
H27	7.759, -2.320, 1.835	0.053		same as H3
H28	7.336, 2.390, -1.903	0.056		same as H3
H29	5.886, 1.472, -2.356	0.048		same as H3
H30	7.446, 0.648, -2.214	0.06		same as H3
O31	-0.750, 2.308, -1.012	-0.529		**1.48 Å, 14.59x10^{-3} perg**
H32	0.137, 3.339, 1.147	0.094		same as H3
C33	-2.167, -0.311, -0.050	-0.04	34, 35	same as C1
C34	-2.548, -1.754, -0.322	0.687	36, 37	same as C1
C35	-3.366, 0.385, 0.091	-0.197	38, 39	same as C1
N36	-3.938, -1.774, -0.321	-0.646	38, 40	same as N14
O37	-1.850, -2.731, -0.512	-0.479		same as O31
C38	-4.482, -0.532, -0.088	0.397	41	same as C1
C39	-3.517, 1.749, 0.443	0.378	42	same as C1
H40	-4.474, -2.615, -0.498	0.399		same as H3
C41	-5.846, -0.321, -0.048	-0.359	43, 44	same as C1
N42	-3.600, 2.863, 0.774	-0.416		same as N14
C43	-6.707, -1.442, -0.248	0.453	45	same as C1
C44	-6.459, 0.945, 0.173	0.433	46	same as C1
N45	-7.351, -2.398, -0.417	-0.461		same as N14
N46	-7.021, 1.949, 0.346	-0.428		same as N14
H47	-1.035, 2.310, 1.999	0.082		same as H3
H48	0.627, 1.738, 1.805	0.039		same as H3

Table B.39: LoD model parameters for ***TCP-Me (A.1)***, coloring represents LoD ellipsoid partitioning:
(1,3,..,14,17,..,30|2,33,..,46|16,31|15,32,47,48)

#	Position [Å] Rotation (Axis,θ)	Semi-axes [Å]	LJ energy [perg]	Center Charge [*e*] (Center Dipole[a] [*D*])
1	4.781, -0.247, -0.003 (0.599,-0.106, 0.793, 0.213)	5.06x3.79x2.20	0.07159[b]	0.295 (1.193,-0.488,-0.028)
2	-4.326, -0.360, -0.005 (0.002, 0.036, 0.999, 2.981)	4.52x4.06x1.93	0.10850[b]	-0.450 (-0.578,-3.176,0.371)
3	-0.688, 1.981, 0.895 (-0.591,-0.688,-0.421, 2.381)	2.08x1.70x1.70	0.01854[b]	0.253 (0.489,-1.639,-3.607)
4	-0.147, 2.577, -1.213 (0.409, 0.141,-0.902, 1.611)	2.01x1.99x1.60	0.00699[b]	-0.097 (-0.019,0.449,-0.314)

[a]Dipole vectors are given in the lab frame, [b] "simple touch" LJ potential, equation (2-2)

Table B.40: LoD model parameters for ***TCP-Me (A.2)***, coloring represents LoD ellipsoid partitioning:
(1,3,..,14,17,..,30|2,33,..,46|16,31|15,32,47,48)

#	Position [Å] Rotation (Axis,θ)	Semi-axes [Å]	LJ energy [perg]	Center Charge [*e*] (Center Dipole[a] [*D*])
1	4.782, -0.252, -0.032 (0.012,-0.301,-0.953, 2.980)	5.07x3.78x2.20	0.07159[b]	0.291 (1.277,-0.493,-0.019)
2	-4.327, -0.351, -0.033 (0.782, 0.053,-0.621, 0.262)	4.52x4.06x1.93	0.10850[b]	-0.452 (-0.609,-3.106,-0.794)
3	-0.692, 2.079, -0.645 (0.636,-0.749, 0.189, 2.043)	2.08x1.70x1.70	0.01854[b]	0.264 (0.541,-2.137,3.429)
4	-0.124, 2.398, 1.515 (-0.075, 0.336, 0.939, 1.712)	2.01x1.99x1.60	0.00699[b]	-0.104 (-0.021,0.407,0.376)

[a]Dipole vectors are given in the lab frame, [b] "simple touch" LJ potential, equation (2-2)

Table B.41: LoD model parameters for ***TCP-Me (B.1)***, coloring represents LoD ellipsoid partitioning:
(1,3,..,14|17,19,..,21,25,..,27|18,22,..,24,28,..,30|2,33,..,46|16,31|15,32,47,48)

#	Position [Å] Rotation (Axis,θ)	Semi-axes [Å]	LJ energy [perg]	Center Charge [*e*] (Center Dipole[a] [*D*])
1	3.103, -0.424, -0.042 (0.772,-0.068, 0.632, 0.555)	4.33x3.24x1.69	0.04765[b]	-0.108 (-3.748,-1.021,-0.153)
2	7.055, -1.834, -0.124 (-0.119,-0.690,-0.714, 1.480)	2.63x1.97x1.78	0.01320[b]	0.203 (-0.077,0.756,-0.415)

3	6.715, 1.785, 0.213 (-0.174,0.618, 0.767, 1.595)	2.63x1.97x1.78	0.01320[b]	0.200 (0.072,-0.714,0.430)
4	-4.326, -0.360, -0.005 (0.002, 0.036, 0.999, 2.981)	5.10x4.38x1.78	0.10827[b]	-0.450 (-0.578,-3.176,0.371)
5	-0.688, 1.981, 0.895 (-0.591,-0.688,-0.421, 2.381)	2.11x1.59x1.59	0.01854[b]	0.253 (0.489,-1.639,-3.607)
6	-0.147, 2.577, -1.213 (0.409, 0.141,-0.902, 1.611)	1.90x1.90x1.54	0.00696[b]	-0.097 (-0.019,0.449,-0.314)

[a]Dipole vectors are given in the lab frame, [b] "simple touch" LJ potential, equation (2-2)

Table B.42: All-atom model parameters for ***TCP-Ph***, coloring represents LoD ellipsoid partitioning

Atom	Position [Å]	Partial charge [e]	Minimum connectivity	LJ radius and energy
C1	0.024, -1.751, 0.285	-0.116	2, 3, 7	**1.65 Å, 4.59x10^{-3} perg**
C2	1.020, -0.907, -0.165	-0.178	16, 32	same as C1
H3	0.356, -2.617, 0.850	0.115		**1.25 Å, 1.04x10^{-3} perg**
C4	-4.269, -1.676, -0.094	0.4	5, 9, 14	same as C1
C5	-3.591, -2.489, 0.856	-0.277	6, 10	same as C1
C6	-2.214, -2.489, 0.937	-0.115	7, 11	same as C1
C7	-1.401, -1.674, 0.111	0.111	8	same as C1
C8	-2.080, -0.889, -0.856	-0.06	9, 12	same as C1
C9	-3.456, -0.888, -0.957	-0.293	13	same as C1
H10	-4.147, -3.146, 1.514	0.159		same as H3
H11	-1.733, -3.136, 1.666	0.116		same as H3
H12	-1.517, -0.297, -1.567	0.066		same as H3
H13	-3.911, -0.263, -1.715	0.171		same as H3
N14	-5.638, -1.664, -0.186	-0.4	17, 18	**1.6 Å, 11.81x10^{-3} perg**
C15	0.076, 1.462, -0.063	-0.348	16, 46, 47	same as C1
C16	0.708, 0.402, -0.874	0.806	31	same as C1
C17	-6.485, -2.385, 0.767	0.201	19, 20, 21	same as C1
C18	-6.340, -0.932, -1.244	0.199	22, 23, 24	same as C1
H19	-6.029, -2.339, 1.761	-0.005		same as H3
C20	-6.769, -3.837, 0.366	-0.165	25, 26, 27	same as C1
H21	-7.427, -1.831, 0.845	0.03		same as H3
H22	-5.769, -1.007, -2.175	0		same as H3
C23	-6.624, 0.534, -0.897	-0.143	28, 29, 30	same as C1
H24	-7.282, -1.459, -1.429	0.027		same as H3
H25	-5.845, -4.419, 0.296	0.039		same as H3
H26	-7.269, -3.884, -0.608	0.054		same as H3
H27	-7.422, -4.315, 1.105	0.047		same as H3
H28	-7.169, 1.018, -1.715	0.043		same as H3

H29	-5.696, 1.089, -0.726	0.019		same as H3
H30	-7.234, 0.611, 0.009	0.05		same as H3
O31	1.011, 0.542, -2.053	-0.535		**1.48 Å, 14.59x10^{-3} perg**
C32	2.399, -1.251, 0.006	-0.059	33, 34	same as C1
C33	2.879, -2.624, 0.432	0.715	35, 36	same as C1
C34	3.544, -0.482, -0.185	-0.184	37, 38	same as C1
N35	4.266, -2.541, 0.452	-0.681	37, 39	same as N14
O36	2.250, -3.627, 0.709	-0.488		same as O31
C37	4.722, -1.294, 0.087	0.419	40	same as C1
C38	3.606, 0.899, -0.503	0.365	41	same as C1
H39	4.860, -3.327, 0.687	0.408		same as H3
C40	6.068, -0.992, 0.031	-0.365	42, 43	same as C1
N41	3.635, 2.041, -0.727	-0.419		same as N14
C42	7.001, -2.015, 0.378	0.453	44	same as C1
C43	6.598, 0.271, -0.358	0.437	45	same as C1
N44	7.709, -2.892, 0.674	-0.464		same as N14
N45	7.102, 1.274, -0.668	-0.432		same as N14
C46	-0.012, 2.721, -0.542	-0.065	48, 49	same as C1
H47	-0.251, 1.196, 0.938	0.078		same as H3
C48	-0.560, 3.899, 0.123	0.192	50, 51	same as C1
H49	0.392, 2.881, -1.541	0.117		same as H3
C50	-1.201, 3.850, 1.378	-0.152	52, 53	same as C1
C51	-0.449, 5.147, -0.519	-0.187	54, 55	same as C1
C52	-1.704, 5.006, 1.964	-0.076	56, 57	same as C1
H53	-1.307, 2.900, 1.893	0.114		same as H3
C54	-0.951, 6.305, 0.069	-0.046	56, 58	same as C1
H55	0.046, 5.199, -1.486	0.118		same as H3
C56	-1.580, 6.238, 1.313	-0.096	59	same as C1
H57	-2.194, 4.950, 2.932	0.092		same as H3
H58	-0.850, 7.259, -0.442	0.09		same as H3
H59	-1.973, 7.139, 1.775	0.097		same as H3

Table B.43: All-atom model parameters for ***TCP-Ph (2nd rotamer)***, coloring represents LoD ellipsoid partitioning

Atom	Position [Å]	Partial charge [*e*]	Minimum connectivity	LJ radius and energy
C1	-0.954, -1.468, -0.036	-0.178	2, 3, 7	**1.65 Å, 4.59x10^{-3} perg**
C2	0.263, -0.881, 0.281	-0.127	16, 32	same as C1
H3	-0.856, -2.447, -0.494	0.132		**1.25 Å, 1.04x10^{-3} perg**
C4	-5.137, -0.443, 0.020	0.413	5, 9, 14	same as C1
C5	-4.621, -1.597, -0.631	-0.257	6, 10	same as C1
C6	-3.273, -1.881, -0.601	-0.146	7, 11	same as C1

C7	-2.323, -1.048, 0.050	0.166	8	same as C1
C8	-2.848, 0.092, 0.716	-0.115	9, 12	same as C1
C9	-4.196, 0.382, 0.700	-0.276	13	same as C1
H10	-5.278, -2.262, -1.177	0.152		same as H3
H11	-2.918, -2.768, -1.120	0.125		same as H3
H12	-2.187, 0.729, 1.287	0.123		same as H3
H13	-4.535, 1.247, 1.256	0.167		same as H3
N14	-6.475, -0.145, 0.006	-0.444	17, 18	**1.6 Å, 11.81x10^{-3} perg**
C15	1.210, 1.452, -0.004	-0.316	16, 46, 47	same as C1
C16	0.395, 0.531, 0.815	0.665	31	same as C1
C17	-7.467, -1.056, -0.571	0.223	19, 20, 21	same as C1
C18	-7.000, 1.104, 0.564	0.265	22, 23, 24	same as C1
H19	-7.169, -2.089, -0.370	-0.005		same as H3
C20	-7.702, -0.840, -2.071	-0.164	25, 26, 27	same as C1
H21	-8.404, -0.902, -0.024	0.023		same as H3
H22	-6.284, 1.910, 0.377	-0.024		same as H3
C23	-7.344, 1.018, 2.056	-0.195	28, 29, 30	same as C1
H24	-7.898, 1.361, -0.009	0.018		same as H3
H25	-6.786, -1.006, -2.645	0.036		same as H3
H26	-8.044, 0.181, -2.272	0.052		same as H3
H27	-8.469, -1.532, -2.438	0.046		same as H3
H28	-7.755, 1.972, 2.405	0.05		same as H3
H29	-6.459, 0.785, 2.656	0.05		same as H3
H30	-8.091, 0.239, 2.242	0.058		same as H3
O31	-0.194, 0.892, 1.830	-0.502		**1.48 Å, 14.59x10^{-3} perg**
C32	1.466, -1.627, 0.049	-0.008	33, 34	same as C1
C33	1.571, -2.828, -0.875	0.638	35, 36	same as C1
C34	2.744, -1.430, 0.570	-0.167	37, 38	same as C1
N35	2.903, -3.220, -0.820	-0.584	37, 39	same as N14
O36	0.728, -3.370, -1.565	-0.478		same as O31
C37	3.652, -2.425, 0.018	0.312	40	same as C1
C38	3.120, -0.504, 1.576	0.377	41	same as C1
H39	3.268, -3.997, -1.357	0.387		same as H3
C40	5.002, -2.636, 0.216	-0.305	42, 43	same as C1
N41	3.408, 0.243, 2.422	-0.42		same as N14
C42	5.620, -3.727, -0.466	0.439	44	same as C1
C43	5.834, -1.826, 1.041	0.414	45	same as C1
N44	6.061, -4.631, -1.054	-0.462		same as N14
N45	6.573, -1.202, 1.688	-0.429		same as N14
C46	1.389, 2.734, 0.382	-0.066	48, 49	same as C1
H47	1.641, 1.061, -0.921	0.075		same as H3
C48	2.127, 3.786, -0.309	0.207	50, 51	same as C1
H49	0.930, 3.015, 1.329	0.111		same as H3
C50	2.738, 3.604, -1.566	-0.166	52, 53	same as C1

C51	2.234, 5.047, 0.307	-0.198	54, 55	same as C1
C52	3.430, 4.644, -2.176	-0.061	56, 57	same as C1
H53	2.669, 2.644, -2.068	0.116		same as H3
C54	2.929, 6.088, -0.303	-0.042	56, 58	same as C1
H55	1.770, 5.200, 1.279	0.119		same as H3
C56	3.529, 5.890, -1.547	-0.103	59	same as C1
H57	3.896, 4.486, -3.145	0.091		same as H3
H58	3.004, 7.052, 0.192	0.089		same as H3
H59	4.073, 6.700, -2.027	0.099		same as H3

Table B.44: LoD model parameters for ***TCP-Ph (A.1)***, coloring represents LoD ellipsoid partitioning:
(1,3,..,14,17,..,30|2,32,..,45|16,31|15,46,..,59)

#	**Position** [Å] **Rotation (Axis,θ)**	**Semi-axes** [Å]	**LJ energy [perg]**	**Center Charge** [e] **(Center Dipole**[a] [D])
1	-4.529, -1.698, -0.097 (-0.043, 0.267, 0.963, 3.044)	5.07x3.78x2.20	0.07159[b]	0.272 (-1.041,-0.692, 0.294)
2	4.560, -1.123, 0.050 (-0.006,-0.138,-0.990, 2.900)	4.52x4.05x1.93	0.10849[b]	-0.472 (0.905,-3.122, 0.758)
3	0.902, 0.492, -1.629 (-0.389,-0.709,-0.588, 2.060)	2.08x1.70x1.70	0.01854[b]	0.271 (-1.032,-0.475, 4.011)
4	-0.821, 4.380, 0.499 (0.434, 0.397, 0.809, 2.223)	4.37x3.36x1.76	0.04159[b]	-0.071 (-0.901, 3.539, 0.293)

[a]Dipole vectors are given in the lab frame, [b] "simple touch" LJ potential, equation (2-2)

Table B.45: LoD model parameters for ***TCP-Ph (A.2)***, coloring represents LoD ellipsoid partitioning:
(1,3,..,14,17,..,30|2,32,..,45|16,31|15,46,..,59)

#	**Position** [Å] **Rotation (Axis,θ)**	**Semi-axes** [Å]	**LJ energy [perg]**	**Center Charge** [e] **(Center Dipole**[a] [D])
1	-5.401, -0.413, 0.003 (0.949,-0.095,-0.301, 0.926)	5.07x3.79x2.20	0.07161[b]	0.294 (-1.118,-0.172,-0.067)
2	3.537, -2.259, 0.145 (0.956,-0.270,-0.115, 0.726)	4.52x4.05x1.93	0.10850[b]	-0.413 (-0.949,-1.960,-2.020)
3	0.018, 0.763, 1.465 (-0.405,-0.801,-0.440, 2.450)	2.09x1.70x1.70	0.01854[b]	0.163 (1.716,-1.053,-2.957)
4	2.484, 4.201, -0.686 (0.573, 0.568, 0.591, 1.405)	4.37x3.37x1.76	0.04159[b]	-0.044 (1.232,3.020,-0.448)

[a]Dipole vectors are given in the lab frame, [b] "simple touch" LJ potential, equation (2-2)

Table B.46: All-atom model parameters for ***TCP-PhF***, coloring represents LoD ellipsoid partitioning

Atom	Position [Å]	Partial charge [*e*]	Minimum connectivity	LJ radius and energy
C1	-0.185, -1.961, -0.326	-0.124	2, 3, 7	**1.65 Å, 4.59x10^{-3} perg**
C2	-1.138, -1.087, 0.158	-0.178	16, 32	same as C1
H3	-0.558, -2.781, -0.932	0.115		**1.25 Å, 1.04x10^{-3} perg**
C4	4.103, -2.140, 0.081	0.38	5, 9, 14	same as C1
C5	3.388, -2.875, -0.906	-0.264	6, 10	same as C1
C6	2.014, -2.795, -0.994	-0.135	7, 11	same as C1
C7	1.241, -1.969, -0.141	0.131	8	same as C1
C8	1.954, -1.261, 0.859	-0.075	9, 12	same as C1
C9	3.328, -1.341, 0.969	-0.271	13	same as C1
H10	3.912, -3.535, -1.586	0.158		same as H3
H11	1.504, -3.385, -1.752	0.121		same as H3
H12	1.420, -0.665, 1.590	0.067		same as H3
H13	3.810, -0.772, 1.753	0.166		same as H3
N14	5.469, -2.209, 0.182	-0.391	17, 18	**1.6 Å, 11.81x10^{-3} perg**
C15	-0.076, 1.234, 0.179	-0.359	16, 46, 47	same as C1
C16	-0.765, 0.168, 0.932	0.804	31	same as C1
C17	6.282, -2.940, -0.794	0.197	19, 20, 21	same as C1
C18	6.201, -1.561, 1.274	0.197	22, 23, 24	same as C1
H19	5.844, -2.820, -1.789	-0.004		same as H3
C20	6.468, -4.424, -0.456	-0.159	25, 26, 27	same as C1
H21	7.258, -2.445, -0.835	0.031		same as H3
H22	5.620, -1.641, 2.197	-0.002		same as H3
C23	6.569, -0.100, 0.987	-0.128	28, 29, 30	same as C1
H24	7.112, -2.146, 1.442	0.026		same as H3
H25	5.509, -4.950, -0.429	0.038		same as H3
H26	6.946, -4.547, 0.522	0.053		same as H3
H27	7.104, -4.907, -1.207	0.045		same as H3
H28	7.134, 0.320, 1.827	0.041		same as H3
H29	5.675, 0.512, 0.834	0.014		same as H3
H30	7.190, -0.021, 0.088	0.046		same as H3
O31	-1.069, 0.264, 2.116	-0.534		**1.48 Å, 14.59x10^{-3} perg**
C32	-2.533, -1.348, -0.037	-0.045	33, 34	same as C1
C33	-3.082, -2.671, -0.531	0.699	35, 36	same as C1
C34	-3.636, -0.528, 0.186	-0.197	37, 38	same as C1
N35	-4.463, -2.513, -0.554	-0.661	37, 39	same as N14
O36	-2.505, -3.692, -0.854	-0.483		same as O31
C37	-4.854, -1.263, -0.130	0.407	40	same as C1
C38	-3.626, 0.837, 0.569	0.376	41	same as C1
H39	-5.096, -3.254, -0.829	0.403		same as H3
C40	-6.182, -0.892, -0.066	-0.351	42, 43	same as C1

N41	-3.593, 1.967, 0.846	-0.424		same as N14
C42	-7.167, -1.844, -0.466	0.444	44	same as C1
C43	-6.646, 0.378, 0.382	0.437	45	same as C1
N44	-7.919, -2.667, -0.806	-0.461		same as N14
N45	-7.096, 1.391, 0.738	-0.433		same as N14
C46	0.066, 2.462, 0.721	-0.037	48, 49	same as C1
H47	0.247, 1.001, -0.832	0.076		same as H3
C48	0.675, 3.645, 0.122	0.133	50, 51	same as C1
H49	-0.339, 2.591, 1.724	0.11		same as H3
C50	1.323, 3.630, -1.130	-0.112	52, 53	same as C1
C51	0.618, 4.863, 0.826	-0.149	54, 55	same as C1
C52	1.889, 4.783, -1.659	-0.221	56, 57	same as C1
H53	1.389, 2.705, -1.695	0.126		same as H3
C54	1.178, 6.028, 0.309	-0.186	56, 58	same as C1
H55	0.118, 4.894, 1.790	0.129		same as H3
C56	1.806, 5.967, -0.929	0.328	59	same as C1
H57	2.390, 4.783, -2.622	0.14		same as H3
H58	1.133, 6.970, 0.844	0.135		same as H3
F59	2.355, 7.085, -1.441	-0.189		**1.42 Å, 4.24x10^{-3} perg**

Table B.47: All-atom model parameters for ***TCP-PhF (2nd rotamer)***, coloring represents LoD ellipsoid partitioning

Atom	Position [Å]	Partial charge [*e*]	Minimum connectivity	LJ radius and energy
C1	-1.233, -1.582, -0.091	-0.186	2, 3, 7	**1.65 Å, 4.59x10^{-3} perg**
C2	0.025, -1.124, 0.276	-0.129	16, 32	same as C1
H3	-1.212, -2.536, -0.607	0.13		**1.25 Å, 1.04x10^{-3} perg**
C4	-5.309, -0.192, -0.020	0.378	5, 9, 14	same as C1
C5	-4.885, -1.342, -0.743	-0.246	6, 10	same as C1
C6	-3.569, -1.748, -0.714	-0.156	7, 11	same as C1
C7	-2.561, -1.048, 0.005	0.189	8	same as C1
C8	-2.996, 0.086, 0.741	-0.142	9, 12	same as C1
C9	-4.312, 0.496, 0.728	-0.242	13	same as C1
H10	-5.588, -1.907, -1.341	0.154		same as H3
H11	-3.284, -2.627, -1.287	0.126		same as H3
H12	-2.291, 0.619, 1.365	0.128		same as H3
H13	-4.583, 1.347, 1.341	0.159		same as H3
N14	-6.614, 0.226, -0.032	-0.417	17, 18	**1.6 Å, 11.81x10^{-3} perg**
C15	1.181, 1.127, 0.141	-0.318	16, 46, 47	same as C1
C16	0.271, 0.239, 0.893	0.651	31	same as C1
C17	-7.672, -0.547, -0.689	0.214	19, 20, 21	same as C1
C18	-7.037, 1.474, 0.612	0.25	22, 23, 24	same as C1

H19	-7.474, -1.615, -0.554	-0.005		same as H3
C20	-7.849, -0.211, -2.174	-0.16	25, 26, 27	same as C1
H21	-8.603, -0.344, -0.149	0.025		same as H3
H22	-6.251, 2.225, 0.491	-0.023		same as H3
C23	-7.410, 1.310, 2.090	-0.176	28, 29, 30	same as C1
H24	-7.900, 1.849, 0.051	0.019		same as H3
H25	-6.936, -0.419, -2.740	0.034		same as H3
H26	-8.093, 0.849, -2.310	0.052		same as H3
H27	-8.664, -0.804, -2.603	0.045		same as H3
H28	-7.738, 2.270, 2.505	0.048		same as H3
H29	-6.559, 0.954, 2.678	0.044		same as H3
H30	-8.228, 0.591, 2.212	0.052		same as H3
O31	-0.301, 0.595, 1.919	-0.496		**1.48 Å, 14.59x10^{-3} perg**
C32	1.163, -1.958, 0.017	0.019	33, 34	same as C1
C33	1.182, -3.106, -0.977	0.615	35, 36	same as C1
C34	2.443, -1.904, 0.567	-0.185	37, 38	same as C1
N35	2.473, -3.618, -0.925	-0.572	37, 39	same as N14
O36	0.310, -3.529, -1.712	-0.471		same as O31
C37	3.271, -2.942, -0.029	0.332	40	same as C1
C38	2.877, -1.074, 1.632	0.378	41	same as C1
H39	2.780, -4.392, -1.501	0.382		same as H3
C40	4.594, -3.282, 0.176	-0.333	42, 43	same as C1
N41	3.211, -0.404, 2.524	-0.42		same as N14
C42	5.128, -4.382, -0.559	0.444	44	same as C1
C43	5.475, -2.595, 1.059	0.425	45	same as C1
N44	5.501, -5.286, -1.193	-0.46		same as N14
N45	6.252, -2.074, 1.753	-0.429		same as N14
C46	1.465, 2.363, 0.607	-0.037	48, 49	same as C1
H47	1.594, 0.753, -0.791	0.07		same as H3
C48	2.308, 3.384, -0.003	0.141	50, 51	same as C1
H49	1.012, 2.626, 1.562	0.101		same as H3
C50	2.929, 3.228, -1.259	-0.116	52, 53	same as C1
C51	2.516, 4.590, 0.694	-0.151	54, 55	same as C1
C52	3.724, 4.231, -1.797	-0.221	56, 57	same as C1
H53	2.787, 2.312, -1.824	0.128		same as H3
C54	3.311, 5.605, 0.170	-0.199	56, 58	same as C1
H55	2.048, 4.727, 1.665	0.129		same as H3
C56	3.904, 5.407, -1.071	0.339	59	same as C1
H57	4.207, 4.120, -2.762	0.141		same as H3
H58	3.478, 6.534, 0.704	0.139		same as H3
F59	4.673, 6.381, -1.592	-0.19		**1.42 Å, 4.24x10^{-3} perg**

Table B.48: LoD model parameters for ***TCP-PhF (A.1)***, coloring represents LoD ellipsoid partitioning:
(1,3,..,14,17,..,30|2,32,..,45|16,31|15,46,..,59)

#	Position [Å] Rotation (Axis,θ)	Semi-axes [Å]	LJ energy [perg]	Center Charge [*e*] (Center Dipole[a] [*D*])
1	4.359, -2.177, 0.085 (0.979,-0.191, 0.076, 0.589)	5.06x3.79x2.20	0.07159[b]	0.271 (1.092,-0.753,-0.319)
2	-4.682, -1.102, -0.084 (0.742, 0.009,-0.670, 0.439)	4.52x4.05x1.93	0.10849[b]	-0.466 (-1.020,-3.056,-0.918)
3	-0.960, 0.229, 1.691 (-0.457,-0.713,-0.532, 2.185)	2.08x1.70x1.70	0.01854[b]	0.270 (1.032,-0.326,-4.018)
4	1.023, 4.260, -0.281 (0.556, 0.538, 0.634, 1.505)	4.45x3.39x1.79	0.04512[b]	-0.076 (0.590, 2.551, 0.363)

[a]Dipole vectors are given in the lab frame, [b] "simple touch" LJ potential, equation (2-2)

Table B.49: LoD model parameters for ***TCP-PhF (A.2)***, coloring represents LoD ellipsoid partitioning:
(1,3,..,14,17,..,30|2,32,..,45|16,31|15,46,..,59)

#	Position [Å] Rotation (Axis,θ)	Semi-axes [Å]	LJ energy [perg]	Center Charge [*e*] (Center Dipole[a] [*D*])
1	-5.567, -0.138, -0.038 (0.927,-0.132,-0.351, 1.025)	5.06x3.79x2.20	0.07161[b]	0.293 (-1.215,-0.040,-0.086)
2	3.169, -2.773, 0.105 (0.930,-0.301,-0.210, 0.801)	4.52x4.06x1.93	0.10850[b]	-0.405 (-1.144,-1.738,-2.156)
3	-0.095, 0.467, 1.550 (-0.410,-0.797,-0.443, 2.438)	2.09x1.70x1.70	0.01854[b]	0.155 (1.636,-1.018,-2.935)
4	2.795, 3.901, -0.401 (0.638, 0.524, 0.564, 1.375)	4.45x3.39x1.78	0.04513[b]	-0.044 (0.783, 2.010, 0.251)

[a]Dipole vectors are given in the lab frame, [b] "simple touch" LJ potential, equation (2-2)

Table B.50: All-atom model parameters for ***TCP-PhF$_5$***, coloring represents LoD ellipsoid partitioning

Atom	Position [Å]	Partial charge [*e*]	Minimum connectivity	LJ radius and energy
C1	0.786, -2.415, 0.291	-0.142	2, 3, 7	**1.65 Å, 4.59x10^{-3} perg**
C2	1.581, -1.390, -0.184	-0.139	16, 32	same as C1
H3	1.285, -3.160, 0.903	0.12		**1.25 Å, 1.04x10^{-3} perg**
C4	-3.409, -3.277, -0.179	0.372	5, 9, 14	same as C1
C5	-2.611, -3.862, 0.845	-0.234	6, 10	same as C1
C6	-1.269, -3.568, 0.954	-0.168	7, 11	same as C1

C7	-0.615, -2.658, 0.085	0.161	8	same as C1
C8	-1.405, -2.106, -0.954	-0.076	9, 12	same as C1
C9	-2.746, -2.401, -1.085	-0.275	13	same as C1
H10	-3.044, -4.572, 1.539	0.152		same as H3
H11	-0.691, -4.045, 1.741	0.13		same as H3
H12	-0.948, -1.466, -1.700	0.059		same as H3
H13	-3.291, -1.947, -1.903	0.17		same as H3
N14	-4.745, -3.559, -0.300	-0.386	17, 18	**1.6 Å, 11.81x10^{-3} perg**
C15	0.083, 0.680, -0.192	-0.393	16, 46, 47	same as C1
C16	1.004, -0.208, -0.943	0.784	31	same as C1
C17	-5.458, -4.375, 0.687	0.203	19, 20, 21	same as C1
C18	-5.546, -3.064, -1.423	0.179	22, 23, 24	same as C1
H19	-5.061, -4.162, 1.684	-0.005		same as H3
C20	-5.411, -5.879, 0.393	-0.171	25, 26, 27	same as C1
H21	-6.498, -4.031, 0.699	0.03		same as H3
H22	-4.943, -3.087, -2.336	0.005		same as H3
C23	-6.134, -1.667, -1.194	-0.139	28, 29, 30	same as C1
H24	-6.356, -3.785, -1.583	0.033		same as H3
H25	-4.382, -6.252, 0.389	0.04		same as H3
H26	-5.852, -6.101, -0.585	0.055		same as H3
H27	-5.975, -6.432, 1.153	0.05		same as H3
H28	-6.738, -1.364, -2.057	0.044		same as H3
H29	-5.345, -0.923, -1.049	0.02		same as H3
H30	-6.777, -1.652, -0.308	0.052		same as H3
O31	1.334, -0.002, -2.103	-0.524		**1.48 Å, 14.59x10^{-3} perg**
C32	3.000, -1.414, 0.014	-0.087	33, 34	same as C1
C33	3.766, -2.650, 0.438	0.706	35, 36	same as C1
C34	3.943, -0.404, -0.144	-0.157	37, 38	same as C1
N35	5.100, -2.258, 0.486	-0.639	37, 39	same as N14
O36	3.369, -3.770, 0.691	-0.487		same as O31
C37	5.270, -0.935, 0.143	0.386	40	same as C1
C38	3.686, 0.960, -0.432	0.362	41	same as C1
H39	5.851, -2.893, 0.725	0.396		same as H3
C40	6.511, -0.334, 0.118	-0.36	42, 43	same as C1
N41	3.435, 2.080, -0.626	-0.418		same as N14
C42	7.648, -1.120, 0.473	0.458	44	same as C1
C43	6.742, 1.023, -0.249	0.433	45	same as C1
N44	8.533, -1.817, 0.774	-0.462		same as N14
N45	7.001, 2.120, -0.540	-0.425		same as N14
C46	-0.271, 1.864, -0.733	0.116	48, 49	same as C1
H47	-0.228, 0.366, 0.796	0.102		same as H3
C48	-1.104, 2.914, -0.160	-0.081	50, 51	same as C1
H49	0.128, 2.080, -1.721	0.085		same as H3
C50	-1.714, 2.870, 1.107	0.156	52, 53	same as C1

C51	-1.332, 4.083, -0.912	0.081	54, 55	same as C1
C52	-2.491, 3.913, 1.596	0.066	56, 57	same as C1
F53	-1.563, 1.799, 1.901	-0.105		**1.42 Å, 4.24x10^{-3} perg**
C54	-2.107, 5.138, -0.444	0.128	56, 58	same as C1
F55	-0.794, 4.204, -2.132	-0.084		same as F53
C56	-2.689, 5.053, 0.818	0.127	59	same as C1
F57	-3.052, 3.828, 2.806	-0.098		same as F53
F58	-2.297, 6.226, -1.195	-0.109		same as F53
F59	-3.436, 6.055, 1.281	-0.096		same as F53

Table B.51: All-atom model parameters for ***TCP-PhF$_5$ (2nd rotamer)***, coloring represents LoD ellipsoid partitioning

Atom	Position [Å]	Partial charge [*e*]	Minimum connectivity	LJ radius and energy
C1	-2.013, 1.677, -0.006	-0.183	2, 3, 7	**1.65 Å, 4.59x10^{-3} perg**
C2	-0.685, 1.446, -0.346	-0.092	16, 32	same as C1
H3	-2.173, 2.651, 0.444	0.13		**1.25 Å, 1.04x10^{-3} perg**
C4	-5.775, -0.416, 0.083	0.405	5, 9, 14	same as C1
C5	-5.571, 0.861, 0.678	-0.26	6, 10	same as C1
C6	-4.347, 1.487, 0.601	-0.14	7, 11	same as C1
C7	-3.222, 0.908, -0.049	0.163	8	same as C1
C8	-3.439, -0.356, -0.661	-0.094	9, 12	same as C1
C9	-4.660, -0.991, -0.594	-0.279	13	same as C1
H10	-6.371, 1.351, 1.218	0.155		same as H3
H11	-4.229, 2.455, 1.081	0.125		same as H3
H12	-2.644, -0.818, -1.229	0.114		same as H3
H13	-4.768, -1.937, -1.110	0.167		same as H3
N14	-6.984, -1.055, 0.146	-0.427	17, 18	**1.6 Å, 11.81x10^{-3} perg**
C15	0.971, -0.471, -0.168	-0.337	16, 46, 47	same as C1
C16	-0.176, 0.133, -0.891	0.607	31	same as C1
C17	-8.174, -0.412, 0.712	0.222	19, 20, 21	same as C1
C18	-7.169, -2.423, -0.350	0.247	22, 23, 24	same as C1
H19	-8.163, 0.651, 0.456	-0.006		same as H3
C20	-8.319, -0.608, 2.226	-0.181	25, 26, 27	same as C1
H21	-9.044, -0.836, 0.198	0.026		same as H3
H22	-6.262, -3.001, -0.156	-0.019		same as H3
C23	-7.554, -2.493, -1.833	-0.181	28, 29, 30	same as C1
H24	-7.955, -2.882, 0.259	0.021		same as H3
H25	-7.470, -0.176, 2.766	0.041		same as H3
H26	-8.374, -1.672, 2.481	0.058		same as H3
H27	-9.236, -0.126, 2.583	0.052		same as H3
H28	-7.701, -3.536, -2.136	0.049		same as H3

H29	-6.776, -2.057, -2.467	0.046		same as H3
H30	-8.486, -1.951, -2.024	0.055		same as H3
O31	-0.721, -0.434, -1.833	-0.479		**1.48 Å, 14.59x10^{-3} perg**
C32	0.265, 2.502, -0.130	-0.026	33, 34	same as C1
C33	0.057, 3.661, 0.830	0.637	35, 36	same as C1
C34	1.522, 2.693, -0.697	-0.16	37, 38	same as C1
N35	1.218, 4.421, 0.747	-0.585	37, 39	same as N14
O36	-0.879, 3.920, 1.562	-0.473		same as O31
C37	2.130, 3.893, -0.138	0.324	40	same as C1
C38	2.102, 1.940, -1.751	0.381	41	same as C1
H39	1.368, 5.254, 1.302	0.387		same as H3
C40	3.356, 4.483, -0.371	-0.312	42, 43	same as C1
N41	2.548, 1.325, -2.633	-0.423		same as N14
C42	3.666, 5.691, 0.324	0.433	44	same as C1
C43	4.351, 3.956, -1.244	0.419	45	same as C1
N44	3.855, 6.671, 0.925	-0.453		same as N14
N45	5.209, 3.574, -1.932	-0.426		same as N14
C46	1.479, -1.644, -0.599	0.112	48, 49	same as C1
H47	1.359, 0.047, 0.699	0.097		same as H3
C48	2.578, -2.419, -0.039	-0.08	50, 51	same as C1
H49	1.020, -2.070, -1.487	0.08		same as H3
C50	3.334, -2.065, 1.094	0.135	52, 53	same as C1
C51	2.942, -3.627, -0.666	0.094	54, 55	same as C1
C52	4.377, -2.850, 1.569	0.096	56, 57	same as C1
F53	3.066, -0.935, 1.766	-0.104		**1.42 Å, 4.24x10^{-3} perg**
C54	3.981, -4.429, -0.209	0.121	56, 58	same as C1
F55	2.270, -4.042, -1.749	-0.092		same as F53
C56	4.704, -4.037, 0.916	0.12	59	same as C1
F57	5.066, -2.474, 2.650	-0.104		same as F53
F58	4.287, -5.568, -0.836	-0.109		same as F53
F59	5.702, -4.795, 1.368	-0.096		same as F53

Table B.52: LoD model parameters for ***TCP-PhF$_5$ (A.1)***, coloring represents LoD ellipsoid partitioning:
(1,3,..,14,17,..,30|2,32,..,45|16,31|15,46,..,59)

#	**Position** [Å] **Rotation (Axis,θ)**	**Semi-axes** [Å]	**LJ energy [perg]**	**Center Charge** [*e*] **(Center Dipole[a]** [***D***]**)**
1	-3.656, -3.353, -0.187 (0.086,-0.295,-0.952, 3.040)	5.06x3.79x2.20	0.07159[b]	0.279 (-1.113,-0.972, 0.380)
2	5.066, -0.801, 0.108 (0.021,-0.134,-0.991, 2.685)	4.52x4.06x1.93	0.10850[b]	-0.432 (1.256,-2.877, 0.677)
3	1.215, -0.076, -1.686 (-0.349,-0.723,-0.596, 2.033)	2.08x1.70x1.70	0.01854[b]	0.260 (-1.095,-0.684, 3.849)
4	-1.627, 3.557, 0.232 (0.350, 0.471, 0.810, 2.391)	4.60x3.62x1.86	0.05894[b]	-0.107 (-0.944, 2.194,-0.360)

[a]Dipole vectors are given in the lab frame, [b] "simple touch" LJ potential, equation (2-2)

Table B.53: LoD model parameters for ***TCP-PhF$_5$ (A.2)***, coloring represents LoD ellipsoid partitioning:
(1,3,..,14,17,..,30|2,32,..,45|16,31|15,46,..,59)

#	**Position** [Å] **Rotation (Axis,θ)**	**Semi-axes** [Å]	**LJ energy [perg]**	**Center Charge** [*e*] **(Center Dipole[a]** [***D***]**)**
1	-6.021, -0.513, 0.110 (0.827, 0.229, 0.514, 1.004)	5.06x3.79x2.20	0.07161[b]	0.308 (-1.233,-0.203, 0.124)
2	2.061, 3.701, -0.269 (0.821, 0.387, 0.419, 0.846)	4.52x4.06x1.93	0.10850[b]	-0.371 (-1.656, 1.356, 2.144)
3	-0.525, -0.230, -1.495 (0.581,-0.439, 0.685, 1.410)	2.08x1.70x1.70	0.01854[b]	0.128 (1.467, 1.528, 2.537)
4	3.278, -2.880, 0.334 (0.704,-0.454,-0.546, 1.152)	4.60x3.62x1.86	0.05894[b]	-0.065 (0.904,-1.464,-0.260)

[a]Dipole vectors are given in the lab frame, [b] "simple touch" LJ potential, equation (2-2)

B.5 CHAPTER 7 MODELS

Table B.54: LoD model parameters for figures 7.1 and 7.2, ***r*** ranges from 0-8 Å

#	Position [Å] Rotation (Axis,θ)	Semi-axes [Å] (LJ width [Å])	LJ energy [perg]	Center Charge [*e*] (Center Dipole[a] [*D*])
1	0, 0, 0 (1, 0, 0, 0)	1.8x3.8x12.8 (2.0)[b]	0.285[b]	no charge (0,0,24)
2	0, 0, 0 (1, 0, 0, 0)	***r*** x ***r*** x4.8 (2.0)[b]	0.1[b]	no charge (0,0,0)

[a]Dipole vectors are given in the lab frame, [b] "adjusted-width" LJ potential, equation (2-6)

Table B.55: LoD model parameters for figure 7.3, ***r*** ranges from 0-8 Å

#	Position [Å] Rotation (Axis,θ)	Semi-axes [Å] (LJ width [Å])	LJ energy [perg]	Center Charge [*e*] (Center Dipole[a] [*D*])
1	0, 0, -7.8 (1, 0, 0, 0)	1.5x3.4x6.8 (2.0)[b]	0.2[b]	no charge (0,0,12)
2	0, 0, 7.8 (1, 0, 0, 0)	1.5x3.4x6.8 (2.0)[b]	0.2[b]	no charge (0,0,12)
3	0, 0, 0 (1, 0, 0, 0)	***r*** x ***r*** x4.8 (2.0)[b]	0.1[b]	no charge (0,0,0)

[a]Dipole vectors are given in the lab frame, [b] "adjusted-width" LJ potential, equation (2-6)

Table B.56: LoD model parameters for figure 7.4, ***r*** ranges from 0-8 Å

#	Position [Å] Rotation (Axis,θ)	Semi-axes [Å] (LJ width [Å])	LJ energy [perg]	Center Charge [*e*] (Center Dipole[a] [*D*])
1	0, 0, -6.8 (1, 0, 0, 0)	1.5x3.4x7.8 (2.0)[b]	0.2[b]	no charge (0,0,12)
2	0, 0, 6.8 (1, 0, 0, 0)	1.5x3.4x7.8 (2.0)[b]	0.2[b]	no charge (0,0,12)
3	0, 0, -6.8 (1, 0, 0, 0)	***r*** x ***r*** x2.8 (2.0)[b]	0.1[b]	no charge (0,0,0)
4	0, 0, 6.8 (1, 0, 0, 0)	***r*** x ***r*** x2.8 (2.0)[b]	0.1[b]	no charge (0,0,0)

[a]Dipole vectors are given in the lab frame, [b] "adjusted-width" LJ potential, equation (2-6)

Table B.57: LoD model parameters for figure 7.5, ***r*** ranges from 0-8 Å

#	**Position** [Å] **Rotation (Axis,θ)**	**Semi-axes** [Å] **(LJ width** [Å]**)**	**LJ energy** **[perg]**	**Center Charge** [e] **(Center Dipole**[a] [D]**)**
1	0, 0, -6.8 (1, 0, 0, 0)	1.5x3.4x7.8 (2.0)[b]	0.2[b]	no charge point dipole (0,0,24) at (0,0,0)
2	0, 0, 6.8 (1, 0, 0, 0)	1.5x3.4x7.8 (2.0)[b]	0.2[b]	
3	0, 0, -6.8 (1, 0, 0, 0)	***r*** x ***r*** x2.8 (2.0)[b]	0.1[b]	no charge (0,0,0)
4	0, 0, 6.8 (1, 0, 0, 0)	***r*** x ***r*** x2.8 (2.0)[b]	0.1[b]	no charge (0,0,0)

[a]Dipole vectors are given in the lab frame, [b] "adjusted-width" LJ potential, equation (2-6)

Table B.58: LoD model parameters for figure 7.6, ***r*** ranges from 1.33-8 Å

#	**Position** [Å] **Rotation (Axis,θ)**	**Semi-axes** [Å] **(LJ width** [Å]**)**	**LJ energy** **[perg]**	**Center Charge** [e] **(Center Dipole**[a] [D]**)**
1	-5.687, 0.190, 0.160 (0.501,-0.108, 0.859, 0.316)	7.22x3.01x1.55 (2.34)[b]	0.14193[b]	0.299 (10.799, 5.097,-0.145)
2	-1.717, 3.406, -0.633 (0.460, 0.360,-0.812, 1.881)	3.17x1.88x1.74 (1.62)[b]	0.02699[b]	-0.238 (0.016, 0.580,-0.194)
3	5.215, -1.720, -0.206 (0.823, 0.131,-0.553, 0.292)	5.96x3.72x1.49 (2.37)[b]	0.13500[b]	-0.478 (-4.837, 2.217, 0.905)
4	4.103, 1.929, -0.270 (0.371,-0.921,-0.117, 1.574)	***r*** x ***r*** x1.72 (2.02)[b]	0.07699[b]	0.161 (0.132, 0.175,-1.743)
5	-11.958, -1.871, -0.162 (0.458, 0.569, 0.683, 2.389)	***r*** x ***r*** x1.80 (1.64)[b]	0.02661[b]	0.255 (-0.388,-0.194,-0.033)

[a]Dipole vectors are given in the lab frame, [b] "adjusted-width" LJ potential, equation (2-6)

Table B.59: LoD model parameters for figure 7.7, ***r*** ranges from 0.33-8 Å

#	**Position** [Å] **Rotation (Axis,θ)**	**Semi-axes** [Å] **(LJ width** [Å]**)**	**LJ energy** **[perg]**	**Center Charge** [e] **(Center Dipole**[a] [D]**)**
1	-5.687, 0.190, 0.160 (0.501,-0.108, 0.859, 0.316)	7.22x3.01x1.55 (2.34)[b]	0.14193[b]	0.299 (10.799, 5.097,-0.145)
2	-1.717, 3.406, -0.633 (0.460, 0.360,-0.812, 1.881)	3.17x1.88x1.74 (1.62)[b]	0.02699[b]	-0.238 (0.016, 0.580,-0.194)
3	5.215, -1.720, -0.206 (0.823, 0.131,-0.553, 0.292)	5.96x3.72x1.49 (2.37)[b]	0.13500[b]	-0.478 (-4.837, 2.217, 0.905)
4	4.103, 1.929, -0.270 (0.371,-0.921,-0.117, 1.574)	4.78x3.72x1.49 (2.02)[b]	0.07699[b]	0.161 (0.132, 0.175,-1.743)
5	-11.958, -1.871, -0.162 (0.458, 0.569, 0.683, 2.389)	***r*** x ***r*** x1.80 (1.64)[b]	0.02661[b]	0.255 (-0.388,-0.194,-0.033)

[a]Dipole vectors are given in the lab frame, [b] "adjusted-width" LJ potential, equation (2-6)

VITA

Andreas F. Tillack was born in Suhl, Germany in former East Germany. After moving to Berlin, he and his parents witnessed the Fall of the Wall on November 9, 1989 at the Brandenburg Gate when the entire world suddenly opened up to him to be explored. In 2004 he won a green card and subsequently became a permanent resident of the United States of America. Andreas knew from a young age that he wanted to become a scientist. He attended Humboldt-University in Berlin where he developed and built a flow cytometer using the optical pickup unit of a commercial DVD burner and received a Master of Science (Diplom) in Physics in March 2007 mentored by Dr. Stefan Kirstein in Prof. Jürgen P. Rabe's group. He worked in Dr. Kirstein's company, Riegler & Kirstein GmbH, after his graduation in Berlin and then moved to Seattle for graduate school at the University of Washington. He first worked for Prof. David S. Ginger's group where he conducted experimental research on the plasmonic emission enhancement of nanoprisms and was responsible for NEXAFS measurements of organic solar cell material blends at the Stanford Synchrotron Radiation Lightsource (SSRL). Ultimately, he decided to join Prof. Bruce H. Robinson in the quest for understanding and improving organic non-linear electro-optical materials through advanced statistical mechanics theory. His work in both groups included collaborations with research groups in chemistry, physics, and material sciences. During graduate school he co-authored numerous papers and attended multiple conferences. He was a speaker at the 2014 MRS Spring Meeting in San Francisco, which led to an invited talk at the 2014 Symposium on Applications of Sum Rules and Scaling in Nonlinear Optics at Washington State University in Pullman organized by Prof. Mark G. Kuzyk. Andreas graduated with a Doctor of Philosophy in Chemistry in August 2015.